Molecular response to ultra-intense x-rays studied with ion and electron momentum imaging

by

Xiang Li

B.S., South China Normal University, China, 2014

AN ABSTRACT OF A DISSERTATION

submitted in partial fulfillment of the
requirements for the degree

DOCTOR OF PHILOSOPHY

Department of Physics
College of Arts and Sciences

KANSAS STATE UNIVERSITY
Manhattan, Kansas

2019

Abstract

A new era in ultrafast science has started in the last decade with the advent of x-ray free-electron lasers (XFELs). These machines, which deliver ultra-intense (up to 10^{20} W/cm^2) and ultrashort (down to hundreds of attoseconds) x-ray pulses, have enabled numerous exciting spectroscopic and imaging techniques for exploring structures and dynamics of atoms, molecules, nanomaterials and biological objects. This thesis aims at advancing our understanding of the fundamental interactions between XFEL pulses and molecules by employing experimental techniques based on coincident momentum spectroscopy of the resulting ions and electrons. The work presented here describes the dependence of molecular response on basic x-ray pulse parameters such as wavelength, pulse energy and pulse duration, which is essential for all XFEL applications, and explores the potential of the employed experimental approach for imaging of ultrafast molecular dynamics.

More specifically, the dominant x-ray induced processes including sequential photoionization, ultrafast charge rearrangement and molecular fragmentation are studied. And it is observed that because of the charge rearrangement, molecules exposed to ultra-intense x-rays can be ionized more heavily than the isolated atoms with similar photoabsorption cross sections. While the pulse energy mainly determines what interaction products are created (i.e., what is the charge state distribution of the resulting ionic fragments), the pulse duration is found to be the key parameter which determines how fast a particular charge state is reached, and, thus, how large is the kinetic energy of the corresponding ion. With shorter pulses, a certain pair of ionic fragments is created faster and, thus, at a shorter internuclear distance, resulting in more efficient charge rearrangement. This, in turn, results in the enhancement of sequential ionization for shorter pulses. Moreover, signatures of resonance-enhanced x-ray multiple ionization, which were previously reported for atoms, are presented here for molecules.

In addition to the fundamental investigations of x-ray – molecule interactions, two imaging schemes for studying molecular dynamics with free-electrons lasers are explored in proof-of-principle experiments. One is the so-called "Coulomb explosion imaging" method. The fragment momentum distribution from iodomethane molecules exploded by XFEL pulses is found to resemble the one expected from the instantaneous explosion of a molecule at equilibrium geometry, potentially providing a robust tool for ultrafast imaging of evolving molecular structures. A time-dependent explosion model is implemented to account for the charge buildup process. The other method is based on ion and electron coincidence measurement, which can fix the ejected electrons with respect to the molecular frame. Combining this method with a sequential two-photon absorption from a single XFEL pulse, a one-pulse pump-probe experiment is carried out on N_2 molecules. The transition from the molecular ion N_2^{2+} created by the first absorbed photon to two isolated atomic ions N^+ and N^+ is observed from the perspective of core-shell electrons, demonstrating the feasibility of time-resolved x-ray electron spectroscopy in the molecular frame.

Molecular response to ultra-intense x-rays studied with ion and electron momentum imaging

by

Xiang Li

B.S., South China Normal University, China, 2014

A DISSERTATION

submitted in partial fulfillment of the
requirements for the degree

DOCTOR OF PHILOSOPHY

Department of Physics
College of Arts and Sciences

KANSAS STATE UNIVERSITY
Manhattan, Kansas

2019

Approved by:

Major Professor
Artem Rudenko

Copyright

Abstract

A new era in ultrafast science has started in the last decade with the advent of x-ray free-electron lasers (XFELs). These machines, which deliver ultra-intense (up to 10^{20} W/cm^2) and ultrashort (down to hundreds of attoseconds) x-ray pulses, have enabled numerous exciting spectroscopic and imaging techniques for exploring structures and dynamics of atoms, molecules, nanomaterials and biological objects. This thesis aims at advancing our understanding of the fundamental interactions between XFEL pulses and molecules by employing experimental techniques based on coincident momentum spectroscopy of the resulting ions and electrons. The work presented here describes the dependence of molecular response on basic x-ray pulse parameters such as wavelength, pulse energy and pulse duration, which is essential for all XFEL applications, and explores the potential of the employed experimental approach for imaging of ultrafast molecular dynamics.

More specifically, the dominant x-ray induced processes including sequential photoionization, ultrafast charge rearrangement and molecular fragmentation are studied. And it is observed that because of the charge rearrangement, molecules exposed to ultra-intense x-rays can be ionized more heavily than the isolated atoms with similar photoabsorption cross sections. While the pulse energy mainly determines what interaction products are created (i.e., what is the charge state distribution of the resulting ionic fragments), the pulse duration is found to be the key parameter which determines how fast a particular charge state is reached, and, thus, how large is the kinetic energy of the corresponding ion. With shorter pulses, a certain pair of ionic fragments is created faster and, thus, at a shorter internuclear distance, resulting in more efficient charge rearrangement. This, in turn, results in the enhancement of sequential ionization for shorter pulses. Moreover, signatures of resonance-enhanced x-ray multiple ionization, which were previously reported for atoms, are presented here for molecules.

In addition to the fundamental investigations of x-ray – molecule interactions, two imaging schemes for studying molecular dynamics with free-electrons lasers are explored in proof-of-principle experiments. One is the so-called "Coulomb explosion imaging" method. The fragment momentum distribution from iodomethane molecules exploded by XFEL pulses is found to resemble the one expected from the instantaneous explosion of a molecule at equilibrium geometry, potentially providing a robust tool for ultrafast imaging of evolving molecular structures. A time-dependent explosion model is implemented to account for the charge buildup process. The other method is based on ion and electron coincidence measurement, which can fix the ejected electrons with respect to the molecular frame. Combining this method with a sequential two-photon absorption from a single XFEL pulse, a one-pulse pump-probe experiment is carried out on N_2 molecules. The transition from the molecular ion N_2^{2+} created by the first absorbed photon to two isolated atomic ions N^+ and N^+ is observed from the perspective of core-shell electrons, demonstrating the feasibility of time-resolved x-ray electron spectroscopy in the molecular frame.

Table of Contents

List of Figures

Acknowledgments

This thesis only becomes possible with the dedicated teamwork contributed by my extraordinary colleagues. I am lucky to work with so many wonderful people during the PhD studies.

My supervisor, Artem Rudenko, has provided the most crucial guidance and support. I have worked with Artem since I was an undergraduate in 2013. From him, I learned how to spot a physics problem and propose a feasible experiment to solve it. I learned to be both optimistic and critical with the experimental findings and became more efficient in communicating them to others. I learned scientific research was not a one-step process, and perseverance was needed in order to get as close to truth as possible.

Many improvements in my work were made possible by Daniel Rolles. Daniel's insightful criticism and suggestions have led me to think deeper and further with my research, which eventually resulted in more exciting findings.

One part of the thesis work was done during my visit to the LCLS in 2018, thanks to the great support from Peter Walter and Michael Minitti. With that visit, I gained more experience of working at large research facilities, and had the valuable opportunity to participate in several cutting-edge soft x-ray experiments, which broadened my scope in the field related to x-ray free-electron lasers.

Another part of the thesis work was done during my stay at the European XFEL in 2019. Thanks to the nice coordination of Rebecca Boll and Michael Meyer, I had a great experience through a series of successful ion and electron momentum imaging experiments. I also would like to thank Benjamin Erk for his kind help and discussions, and Thommaso Mazza for providing the xenon charge state distributions.

Much of the work in this thesis were done in close collaboration with the theory colleagues Ludger Inhester, Sang-Kil Son and Robin Santra at the Center for Free-Electron Laser Science. Their ab initio model calculations are successful in supporting our interpretations

of the experimental data. Only by this joint effort, did a better understanding of ultra-intense x-ray interaction with molecules become possible.

The five-year PhD study at K-State couldn't have been filled with tremendous amount of fun without my colleagues in the Rudenko and Rolles group: Jeffrey Powell, Yubaraj Malakar, Balram Kaderiya, Javad Robatjazi, Keyu Chen, Farzaneh Ziaee, Shashank Pathak, Kurtis Borne and Anbu Venkatachalam. They have helped me with my research and encouraged me through their enthusiasm with physics.

Apart from Artem Rudenko and Daniel Rolles, I would like to thank my committee members: Loren Greenman, Stefan Bossmann and SunGo Kim, for devoting their precious time to my PhD work.

Dedication

To my parents, Chunlian Liang and Xiutao Li.

Chapter 1

Introduction

Light-matter interaction is the fundamental driver for many of nature's phenomena. Understanding and utilizing light-matter interactions involving different quantum systems is at the heart of ultrafast science. The advent of x-ray free-electron lasers (XFELs) in the last decade has opened up a new frontier to study light-matter interactions in a hitherto uncharted territory. Compared with those from synchrotron facilities which are previously most powerful x-ray sources, the pulses from x-ray free-electron lasers are three orders of magnitude shorter (few tens of fs), and one to ten billion times brighter (with peak brightness on the order of 10^{33} $(photons/s/mrad^2/mm^2/0.1\% - BW)$). This makes XFEL pulses interact with matter in a drastically different way from what has been observed before. Even though photoabsorption and scattering are the two underlying processes accounting for interactions between matter and x-rays from all kinds of sources, XFEL pulses with their ultrahigh intensity (up to 10^{20} W/cm^2) take such interactions from the linear regime to nonlinear. Sequential multiphoton absorption [1] was found to be the major electronic response of atoms to such intense x-rays. Other less likely nonlinear processes such as direct two-photon absorption [2], stimulated Raman scattering [3] and nonlinear Compton scattering [4] have also been observed. If the photon energy is high enough, inner-shell electrons of the atom are sequentially ejected into the continuum via multiple photoabsorption and Auger decay steps on the ultrashort time scale defined by the pulse duration, leaving the remaining part of the atom in a very

high charge state. For heavy atoms, resonance and relativistic effects [5–8] were found to be important to describe the ionization process. With molecules, novel phenomena such as the production of double-core-hole states in molecules [9–12] have been observed. For polyatomic molecules, sequential x-ray absorption is localized at particular elements which have the largest photoabsorption cross sections. This localized interaction, which can make these particular sites highly charged, induces charge rearrangements and nuclear dynamics [13–19]. With larger molecules containing several tens of atoms, apart from molecular Auger process and charge transfer which also play a role in the ionization of small molecules, the effects of secondary ionization by photo- and Auger electrons, electron-ion recombination and chemical bonding were found to be important to describe their interaction with ultra-intense XFEL pulses [20, 21].

Some of the above findings which are relevant to the work of this thesis will be discussed in more detail in Chapter 2, where the theory of ultra-intense x-ray interaction with atoms and molecules will be presented in a self-contained manner. Despite the dramatic progress made in our understanding of ultra-intense x-ray interaction with matter at the atomic and molecular levels, many open questions still remain. The work in this thesis aims to address some of these open questions through the experiments made possible by the combination of the x-ray free-electron laser and the "ion and electron momentum imaging" technique, both of which will be discussed in Chapter 3, with the data analysis aspect of such experiments presented in Chapter 4. Some of these to-be-addressed questions are general for both atoms and molecules, including how the ultra-intense x-ray ionization of atoms or molecules scales with the photon flux and what determines the average ionization rate leading to a particular ion charge state. Other questions are molecule-specific, including how charge-rearrangement and resonance effects influence the ionization of molecules compared with the independent-atom model, whether there is an interplay among the three key processes in the interaction: photoionization, charge rearrangement, and fragmentation, and how theses processes depend on pulse parameters such as pulse energy and duration.

Chapter 5 addresses these questions through the results of two experiments with gas-phase iodomethane (CH_3I) molecules, one using hard x-rays (8.3 keV) from the Linac Coherent

Light Source (LCLS) and the other using soft x-rays (1.2 keV, 1.5 keV and 2 keV) from the European X-Ray Free-Electron Laser Facility (EuXFEL). A simple sequential multiphoton ionization model is developed which can explain the experimental data and answer the first two general questions raised in previous paragraph. The probability to obtain a certain interaction product is found to be proportional to $e^{-bf}f^n$, with b the constant depending on the pulse duration and photoabsorption cross section, f the photon flux, and n the number of photoabsorptions needed to reach this interaction product. This model also indicates that the average ionization rate leading to a particular ion charge state is only proportional to the inverse of the pulse duration, and independent of all other XFEL pulse parameters. Such dependence is confirmed with the measurement of ion kinetic energy which shows no dependence on pulse energy, but increases with shorter pulses because of their larger ionization rates. Charge rearrangement effect is found to greatly enhance the ionization of molecules compared with the independent-atom model. Resonance effect is observed for the first time for ionization of molecules by XFEL pulses. Compared with the atomic case [5], new resonance structures appear in the charge state distributions of ionic fragments from molecules, which can be attributed to the effect of charge rearrangement. The three processes: photoionization, charge rearrangement, and fragmentation are shown to be interdependent through their dependence on pulse duration. With the larger ionization rate of shorter pulses, a particular total molecular charge state is reached faster at shorter internuclear distances before the atoms can move farther apart through fragmentation. The shorter distance makes it easier for electrons to be transferred from the low-charged site of the molecule to the highly charged site where photoionization is localized. These transferred electrons can enhance further ionizations of the highly charged site and hence increase the yield of high-charge-state ions.

The operation of high-repetition-rate XFEL facilities such as the EuXFEL enables new experimental capabilities in ultrafast science. One of them is to shorten the experimental time needed for coincidence measurement of multiple charged particles, which requires low interaction rate ($<$ 1) and needs pulses at high-repetition rates in order to accumulate enough statistics in a reasonably short time window.

Multiple-ion coincidence measurement is explored in Chapter 6 where the "Coulomb Explosion Imaging" technique is used to study the charge buildup, electron redistribution and fragmentation processes in the interaction of CH_3I molecules with 2 keV x-rays from the EuXFEL. Thanks to the ultrashort and ultra-intense x-ray pulses, which charge up molecules on a ultrafast time scale before the nuclei can move further apart, the relative momentum distribution of the coincidently detected ionic fragments resembles the one expected from the explosion of a molecule which is instantaneously charged up. This makes it possible to retrieve the initial structure of the molecule before its interaction with x-rays, making "Coulomb Explosion Imaging" of molecules with XFEL pulses a promising time-resolved technique, which complements the imaging methods based on x-ray [22, 23] or electron [24, 25] scattering as well as those based on photoelectron diffraction with table-top lasers [26–28] and XFELs [29–31]. The small discrepancy between the measured relative momentum distribution and the one expected from the instantaneous charge-up model is due to the neglected charge buildup and redistribution processes. A model taking into account of these two processes [18], developed by Motomura and Kukk et al., is implemented in the Coulomb explosion simulation and a better match with the experimental momentum distribution is achieved.

The first ion-electron coincidence measurement with an x-ray free-electron laser is presented in Chapter 7, applied to studying the interaction between N_2 molecules and 506 eV, 100 fs x-rays. This proof-of-principle experiment was done at the LCLS with 120 Hz repetition rate, as a preparation for the future ion-electron coincidence experiment at high-repetition-rate facilities such as the LCLS-II. By sorting the detected electrons according to the kinetic energy release (KER) of coincident ionic fragments and establishing the relation between the measured KER and the internuclear separation in the molecular ion prior to the Coulomb explosion (larger KERs correspond to smaller internuclear distances and vice versa), the change of core electron binding energy (or corresponding photoelectron energy) in a dissociating molecular ion is observed. The observation of such "dynamic line shift" is supported by calculations. It is worth noting that the combination of ion-electron coincidence technique with an XFEL enables such time-resolved observation with a single x-ray

pulse configuration. When applicable, this single-pulse x-ray-pump and x-ray-probe scheme, where one photon in the pulse initiates the dynamics which are then probed by a time-delayed second photon within the same pulse, can be a simple alternative to the two-pulses x-ray-pump and x-ray-probe method [32].

From the general perspective of x-ray interaction with matter, the work in this thesis focuses on the photoabsorption by molecules and the processes it induces, because photoabsorption is the mostly likely process in such interactions, with a probability typically orders of magnitude larger than x-ray scattering. However, the findings of this thesis are still relevant to x-ray scattering-based applications such as coherent imaging of biomolecules [33–35], nano-sized clusters [36–38] and droplets [39]. In a typical imaging experiment, photoabsorption causes radiation damage to the being-imaged structure. For XFEL pulses with their ultrashort duration, even though this issue can be mitigated through the concept of "diffraction before destruction" [40], radiation damage is still present [41, 42]. The findings on the molecular response to ultra-intense x-rays can help understand the mechanisms of such radiation damage in XFEL imaging applications.

Most of the findings in this thesis are also reported in [43–47]. The results presented in Chapter 5 originate from the coordinated analysis of the hard x-ray data acquired in the experiment at the Coherent X-ray Imaging (CXI) instrument of the LCLS and recent soft x-ray data obtained using the Small Quantum Systems (SQS) instrument at the EuXFEL. These results are to a large extent reflected in [43, 44] and [45] for hard and soft x-rays, respectively. The "Coulomb explosion imaging" results presented in Chapter 6 were obtained during the same SQS experiment and will be reported in [46]. Finally, the ion-electron coincidence data presented in Chapter 7 are from the experiment performed at the Atomic, Molecular and Optical (AMO) physics instrument of the LCLS and are summarized in [47].

Chapter 2

Theory of ultra-intense x-ray interaction with molecules

The basics of ultra-intense x-ray interaction with atoms and molecules will be presented in this chapter. Starting with the first three sections, which introduce the formulations for describing x-rays, atoms and molecules, the physical processes important for the ultra-intense x-ray interaction with molecules will be discussed in the framework of quantum state evolution in the last section. Some of the most recent findings on such processes relevant to the work of this thesis will also be briefly reviewed. The physical variables of this chapter are in atomic units.

2.1 X-rays

X-rays are a kind of electromagnetic radiation with wavelength ranging from 0.01 nm to 10 nm or with photon energy from 100 eV to 100 keV. X-rays with photon energies below 5 keV are typically called soft x-rays, and above 5 keV hard x-rays. It can be described by either the classical or quantum electromagnetic field theory. The subsections below only consider the field in empty space.

2.1.1 Classical representation

Electromagnetic field

The electric field $\mathbf{E}$ and magnetic field $\mathbf{B}$ in empty space satisfy the Maxwell equations (Gaussian units)

$$\begin{cases} \bigtriangledown \cdot \mathbf{E} = 0 & (2.1) \\ \bigtriangledown \times \mathbf{E} = -\alpha \dfrac{\partial B}{\partial t} & (2.2) \\ \bigtriangledown \cdot \mathbf{B} = 0 & (2.3) \\ \bigtriangledown \times \mathbf{B} = \alpha \dfrac{\partial E}{\partial t}, & (2.4) \end{cases}$$

and can be calculated from the vector potential $\mathbf{A}$ (assuming Coulomb gauge $\nabla \cdot \mathbf{A} = 0$ from hereon)

$$\begin{cases} \mathbf{E} = -\alpha \dfrac{\partial \mathbf{A}}{\partial t} & (2.5) \\ \mathbf{B} = \bigtriangledown \times \mathbf{A}, & (2.6) \end{cases}$$

with the vector potential $\mathbf{A}$ given by the wave equation

$$\bigtriangledown^2 \mathbf{A} - \alpha^2 \frac{\partial^2 \mathbf{A}}{\partial^2 t} = 0, \tag{2.7}$$

where $\alpha = \frac{e^2}{4\pi\epsilon_0 \hbar c}$ is the fine structure constant, and in atomic units the speed of light $c = \frac{1}{\alpha} \approx 137$.

A solution to Eq. (2.7) is

$$\begin{aligned} \boldsymbol{A}(\boldsymbol{r},\ t;\ \omega) &= \boldsymbol{\epsilon} A_0(\omega) cos(\boldsymbol{k} \cdot \boldsymbol{r} - \omega t + \delta(\omega)) & (2.8) \\ &= \boldsymbol{\epsilon} A_0(\omega) e^{i(\boldsymbol{k} \cdot \boldsymbol{r} - \omega t + \delta(\omega))} + cc., & (2.9) \end{aligned}$$

which describes a plane wave with frequency ω, amplitude $A_0(w)$ and polarization in the direction of the unit vector $\boldsymbol{\epsilon}$. It propagates along the direction of the wave vector $\boldsymbol{k}$, which

is related to ω by the relation $\omega = |\boldsymbol{k}|c$. The constant phase offset for this wave is $\delta(\omega)$.

According to Eqs. (2.5), (2.6) and (2.9), a solution for the electromagnetic field is

$$\begin{cases} \boldsymbol{E}(\boldsymbol{r},\ t;\ \omega) = \boldsymbol{\epsilon}|\boldsymbol{k}|A_0(\omega)e^{i(\boldsymbol{k}\cdot\boldsymbol{r} - \omega t + \delta(\omega) + \frac{\pi}{2})} + cc. & (2.10) \\ \boldsymbol{B}(\boldsymbol{r},\ t;\ \omega) = (\boldsymbol{k} \times \boldsymbol{\epsilon})A_0(\omega)e^{i(\boldsymbol{k}\cdot\boldsymbol{r} - \omega t + \delta(\omega) + \frac{\pi}{2})} + cc.. & (2.11) \end{cases}$$

The electromagnetic field $\boldsymbol{E}_g(\boldsymbol{r},\ t)$ and $\boldsymbol{B}_g(\boldsymbol{r},\ t)$ of a general x-ray pulse can be expressed by a linear superposition of different monochromatic wave components (all have the same polarization and propagation directions) as

$$\begin{cases} \boldsymbol{E}_g(\boldsymbol{r},\ t) = \int \boldsymbol{E}(\boldsymbol{r},\ t;\ \omega)\ d\omega & (2.12) \\ \boldsymbol{B}_g(\boldsymbol{r},\ t) = \int \boldsymbol{B}(\boldsymbol{r},\ t;\ \omega)\ d\omega, & (2.13) \end{cases}$$

or in complex representation

$$\begin{cases} \widetilde{\boldsymbol{E}}_g(\boldsymbol{r},\ t) = \int \widetilde{\boldsymbol{E}}(\boldsymbol{r},\ t;\ \omega)\ d\omega & (2.14) \\ \widetilde{\boldsymbol{B}}_g(\boldsymbol{r},\ t) = \int \widetilde{\boldsymbol{B}}(\boldsymbol{r},\ t;\ \omega)\ d\omega, & (2.15) \end{cases}$$

where $\widetilde{\boldsymbol{E}}(\boldsymbol{r},\ t;\ \omega)$ and $\widetilde{\boldsymbol{B}}(\boldsymbol{r},\ t;\ \omega)$ are the first terms respectively in Eqs. (2.10) and (2.11). $\boldsymbol{E}_g$ and $\boldsymbol{B}_g$ are respectively the real parts of $\widetilde{\boldsymbol{E}}_g$ and $\widetilde{\boldsymbol{B}}_g$.

The energy density u and flux (Poynting vector) $\boldsymbol{S}$ are given by

$$u = \frac{|\boldsymbol{E}_g|^2 + |\boldsymbol{B}_g|^2}{8\pi} \text{ and } \boldsymbol{S} = \frac{1}{4\pi\alpha}\boldsymbol{E}_g \times \boldsymbol{B}_g. \quad (2.16)$$

Ultrashort x-ray pulse

X-rays used in typical ultrafast science experiments have very narrow extents in both space and time domain. It's convenient to utilize the complex representation in Eq. (2.14), and describe the x-ray beam in space and time separately as $U_s(\boldsymbol{r}) = U_s^m(\boldsymbol{r})e^{i\varphi_s(\boldsymbol{r})}$ and $U_{time}(t) = U_{time}^m(t)e^{i\varphi_{time}(t)}$, where $U_s^m(\boldsymbol{r})$ and $U_{time}^m(t)$ are respectively the magnitude

of $U_s(\boldsymbol{r})$ and $U_{time}(t)$. $\varphi_s(t)$ and $\varphi_{time}(t)$ are respectively the space- and time-dependent phases. With a Fourier transform of $U_{time}(t)$, x-rays can also be represented spectrally as $U_f(\omega) = U_f^m(\omega)e^{i\varphi_f(\omega)}$, with $U_f^m(\omega)$ being the magnitude of $U_f(\omega)$ and $\varphi_f(\omega)$ the spectral phase.

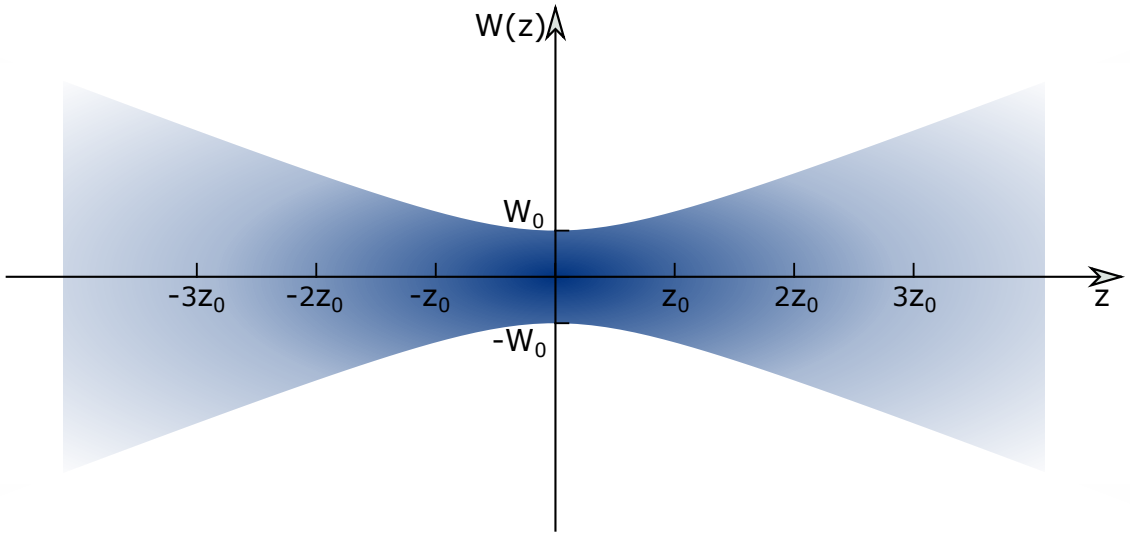

Figure 2.1: Sketch of a Gaussian beam.

In space, assuming the x-rays to be a Gaussian beam [48] (propagating in $\boldsymbol{z}$ direction) as shown in Fig. 2.1:

$$U_s(\boldsymbol{r}) = U_s^0 \frac{W_0}{W(z)} e^{-\frac{\rho^2}{W^2(z)}} e^{-ikz - ik\frac{\rho^2}{2R(z)} + i\zeta(z)}. \tag{2.17}$$

U_s^0 is the square root of the x-ray peak intensity. W_0 is the beam waist radius or half the focal spot size. Together with the wavelength λ_0, it determines the Rayleigh range $z_0 = \frac{\pi^2 W_0}{\lambda}$. $\rho = \sqrt{x^2 + y^2}$ is the distance of the point (x, y, z) from the beam center axis $z = 0$. $W(z) = W_0\sqrt{(1 + (\frac{z}{z_0})^2)}$ is the beam radius at z. $R(z) = z[1 + (\frac{z_0}{z})^2]$ is the radius of curvature of the wavefront at z. $\zeta(z) = tan^{-1}(\frac{z}{z_0})$ is the Gouy phase, which changes from $-\frac{\pi}{2}$ at $z = -\infty$ to $\frac{\pi}{2}$ at $z = \infty$. It causes an excess delay of the wavefront defined by the first two phase terms $-ikz - ik\frac{\rho^2}{2R(z)}$, which is called the Gouy effect.

Also assuming the x-ray pulse in the time domain is a Gaussian, at a fixed location $\boldsymbol{r}$

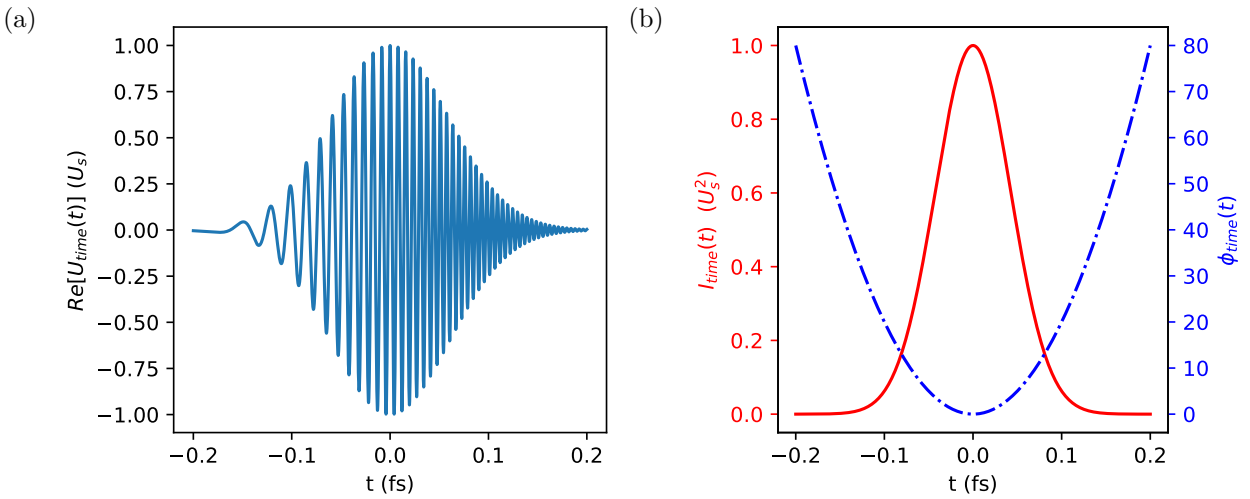

Figure 2.2: Temporal representation of an up-chirped (the instantaneous frequency increases with time) 500 eV (the photon energy corresponding to the center frequency) x-ray pulse ($\tau = 100\ as$). (a) Real part of $U_{time}(t)$. (b) Pulse intensity $I_{time}(t)$ and temporal phase $\phi_{time}(t)$.

and with peak intensity given by $U_s(\boldsymbol{r})$, the x-ray can be expressed as

$$U_{time}(t) = U_s(\boldsymbol{r}) e^{-2ln2(\frac{t}{\tau})^2} e^{i[\omega_0 t + \phi_{time}(t)]}, \tag{2.18}$$

where ω_0 is the center frequency and $\phi_{time}(t)$ is the general time-dependent phase. τ is the pulse duration, which is defined as the full width at half maximum (FWHM) of the time-dependent x-ray intensity,

$$I_{time}(t) = [U_{time}(t)]^2 = U_s^2(\boldsymbol{r}) e^{-4ln2(\frac{t}{\tau})^2}. \tag{2.19}$$

The real part of $U_{time}(t)$, $I_{time}(t)$ and $\phi_{time}(t)$ are plotted in Fig. 2.2 for an up-chirped (the instantaneous frequency increases with time.) 500 eV x-ray pulse ($\tau = 100\ as$). If $\phi_{time}(t) = 0$, the spectral representation obtained by the Fourier transform of Eq. (2.18) is also a Gaussian, which centers around ω_0 and has a FWHM (bandwidth) $\Delta\ \omega$ related to the pulse duration τ by $\Delta\ \omega = \frac{4ln2}{\tau}$. It's worth noting that most of the discussion in this section also applies to ultrashort pulses at other wavelengths after corresponding changes.

2.1.2 Quantized electromagnetic field

In the description of x-ray interaction with atoms and molecules, the "photon picture" is often very convenient, which requires the quantization of electromagnetic field. The total energy of electromagnetic field ($\boldsymbol{E},\ \boldsymbol{B}$) confined in a cube with length L and volume $V\ =\ L^3$ is

$$H_{classical}\ =\ \int_V \frac{|\boldsymbol{E}|^2\ +\ |\boldsymbol{B}|^2}{8\pi}\ d^3r. \tag{2.20}$$

Upon decomposing the field into different modes characterized by the wave vector $\boldsymbol{k}$ and polarization vector $\boldsymbol{\epsilon}_{\boldsymbol{k},\xi}$ ($\xi\ =\ 1,\ 2$), and introducing the creation and annihilation operators $\hat{a}^\dagger_{\mathbf{k},\xi}$ and $\hat{a}_{\mathbf{k},\xi}$ in analogy to the ones used in solving the quantum harmonic oscillator problem, the electromagnetic field Hamiltonian can be shown to become (see e.g. [49])

$$\hat{H}\ =\ \sum_{\mathbf{k},\xi}\ \omega_{\boldsymbol{k}}(\hat{a}^\dagger_{\mathbf{k},\xi}\hat{a}_{\mathbf{k},\xi}\ +\ \frac{1}{2}). \tag{2.21}$$

The vector potential operator in this quantized formulation is given by

$$\hat{\boldsymbol{A}}(\boldsymbol{r},\ t)\ =\sum_{\boldsymbol{k},\xi}\sqrt{\frac{2\pi}{V\omega_{\boldsymbol{k}}\alpha^2}}[\hat{a}_{\boldsymbol{k},\xi}\boldsymbol{\epsilon}_{\boldsymbol{k},\xi}e^{i(\boldsymbol{k}\cdot\boldsymbol{r}\ -\ \omega_{\boldsymbol{k}}t)}\ +\ \hat{a}^\dagger_{\boldsymbol{k},\xi}\boldsymbol{\epsilon}^*_{\boldsymbol{k},\xi}e^{-i(\mathbf{k}\cdot\boldsymbol{r}\ -\ \omega_{\boldsymbol{k}}t)}]. \tag{2.22}$$

From Eqs. (2.5), (2.6) and (2.22), the electric and magnetic field operators are

$$\begin{cases} \hat{\boldsymbol{E}}\ =\ \sum_{\boldsymbol{k},\xi} i\sqrt{\frac{2\pi\omega_{\boldsymbol{k}}}{V}}[\hat{a}_{\boldsymbol{k},\xi}\boldsymbol{\epsilon}_{\boldsymbol{k},\xi}e^{i(\boldsymbol{k}\cdot\boldsymbol{r}\ -\ \omega_{\boldsymbol{k}}t)}\ -\ \hat{a}^\dagger_{\boldsymbol{k},\xi}\boldsymbol{\epsilon}^*_{\boldsymbol{k},\xi}e^{-i(\mathbf{k}\cdot\boldsymbol{r}\ -\ \omega_{\boldsymbol{k}}t)}] & (2.23) \\ \hat{\boldsymbol{B}}\ =\ \sum_{\boldsymbol{k},\xi} i\sqrt{\frac{2\pi}{V\omega_{\boldsymbol{k}}\alpha^2}}[\hat{a}_{\boldsymbol{k},\xi}(\boldsymbol{k}\ \times\ \boldsymbol{\epsilon}_{\boldsymbol{k},\xi})e^{i(\boldsymbol{k}\cdot\boldsymbol{r}\ -\ \omega_{\boldsymbol{k}}t)}\ -\ \hat{a}^\dagger_{\boldsymbol{k},\xi}(\boldsymbol{k}\ \times\ \boldsymbol{\epsilon}^*_{\boldsymbol{k},\xi})e^{-i(\mathbf{k}\cdot\boldsymbol{r}\ -\ \omega_{\boldsymbol{k}}t)}] & (2.24) \end{cases}$$

$\hat{n}_{\boldsymbol{k},\xi}\ =\hat{a}^\dagger_{\mathbf{k},\xi}\hat{a}_{\mathbf{k},\xi}$ is the photon number operator and its eigenstate is the photon number state $|n_{\boldsymbol{k},\xi}\rangle$:

$$\hat{n}_{\boldsymbol{k},\xi}\,|n_{\boldsymbol{k},\xi}\rangle\ =\ n_{\boldsymbol{k},\xi}\,|n_{\boldsymbol{k},\xi}\rangle\,, \tag{2.25}$$

where $n_{\boldsymbol{k},\xi}$ is the number of photons in the mode $(\boldsymbol{k}, \xi)$.

For multiple modes, the photon number state becomes

$$\left|n_{\boldsymbol{k_1},\xi_1},\ n_{\boldsymbol{k_2},\xi_2},\ \ldots,\ n_{\boldsymbol{k_j},\xi_j},\ \ldots\right\rangle\ =\ \left|n_{\boldsymbol{k_1},\xi_1}\right\rangle \bigotimes \left|n_{\boldsymbol{k_2},\xi_2}\right\rangle \bigotimes \cdots \bigotimes \left|n_{\boldsymbol{k_j},\xi_j}\right\rangle \bigotimes \cdots . \tag{2.26}$$

which is still an eigenstate of the photon number operator $\hat{n}_{\boldsymbol{k_j},\xi_j}$:

$$\hat{n}_{\boldsymbol{k_j},\xi_j}\left|n_{\boldsymbol{k_1},\xi_1},\ n_{\boldsymbol{k_2},\xi_2},\ \ldots,\ n_{\boldsymbol{k_j},\xi_j},\ \ldots\right\rangle\ =\ n_{\boldsymbol{k_j},\xi_j}\left|n_{\boldsymbol{k_1},\xi_1},\ n_{\boldsymbol{k_2},\xi_2},\ \ldots,\ n_{\boldsymbol{k_j},\xi_j},\ \ldots\right\rangle . \tag{2.27}$$

And the multi-mode state can be changed by the creation and annihilation operators according to

$$\hat{a}^{\dagger}_{\mathbf{k}_j,\xi_j}\left|n_{\boldsymbol{k_1},\xi_1},\ n_{\boldsymbol{k_2},\xi_2},\ \ldots,\ n_{\boldsymbol{k_j},\xi_j},\ \ldots\right\rangle\ =\ \sqrt{n_{\boldsymbol{k_j},\xi_j}\ +\ 1}\left|n_{\boldsymbol{k_1},\xi_1},\ n_{\boldsymbol{k_2},\xi_2},\ \ldots,\ (n_{\boldsymbol{k_j},\xi_j}\ +\ 1),\ \ldots\right\rangle , \tag{2.28}$$

and

$$\hat{a}_{\mathbf{k}_j,\xi_j}\left|n_{\boldsymbol{k_1},\xi_1},\ n_{\boldsymbol{k_2},\xi_2},\ \ldots,\ n_{\boldsymbol{k_j},\xi_j},\ \ldots\right\rangle\ =\ \sqrt{n_{\boldsymbol{k_j},\xi_j}}\left|n_{\boldsymbol{k_1},\xi_1},\ n_{\boldsymbol{k_2},\xi_2},\ \ldots,\ (n_{\boldsymbol{k_j},\xi_j}\ -\ 1),\ \ldots\right\rangle . \tag{2.29}$$

2.2 Atom

2.2.1 Hydrogenic atoms and ions

For hydrogenic atoms and ions with atomic number Z, the electronic eigenstate $\Phi(\boldsymbol{r})$ and energy E satisfy the Schrödinger equation

$$(-\frac{1}{2}\bigtriangledown^2\ -\frac{Z}{r})\phi(\boldsymbol{r})\ =\ E\phi(\boldsymbol{r}). \tag{2.30}$$

After separation of variables with $\phi(\boldsymbol{r}) = R(r)Y(\theta,\phi)$ and $Y(\theta,\phi) = f(\theta)g(\phi)$ (r, θ and ϕ are respectively the radial distance, polar angle and azimuthal angle) and solving each of the three separated ordinary differential equations, the eigenstates are obtained as

$$\phi_{n,\ l,\ m}(\boldsymbol{r}) = \sqrt{(\frac{2Z}{n})^3\frac{(n\ -\ l\ -\ 1)!}{2n[(n\ +\ l)!]}}(\frac{2Zr}{n})^l e^{-\frac{Zr}{n}}L^{2l+1}_{n-l-1}(\frac{2Zr}{n})Y^m_l(\theta,\ \phi), \tag{2.31}$$

with eigen energy

$$E_n = -\frac{Z^2}{2n^2} \tag{2.32}$$

where $L^{2l+1}_{n-l-1}(x)$ are associated Laguerre polynomials and $Y^m_l(\theta\,\phi)$ are spherical harmonics. The eigenstate is uniquely defined by the three quantum numbers n, l, and m and can be represented by the "ket" notation $|n,\ l,\ m\rangle$, with

$$n = 1,\ 2,\ \ldots \tag{2.33}$$

$$l = 0,\ 1,\ \ldots,\ n-1 \tag{2.34}$$

$$m = 0,\ \pm1,\ \ldots,\ \pm l. \tag{2.35}$$

Since the Hamiltonian in Eq. (2.30) commutes with the squared angular momentum operator $\mathcal{L}^2$ and $\boldsymbol{z}$ direction angular momentum operator $\mathcal{L}_{\boldsymbol{z}}$, $\phi_{n,\ l,\ m}(\boldsymbol{r})$ is also an eigenfunction of these two angular momentum operators:

$$\begin{cases} \mathcal{L}^2\phi_{n,\ l,\ m}(\boldsymbol{r}) = l(l+1)\phi_{n,\ l,\ m}(\boldsymbol{r}) & (2.36) \\ \mathcal{L}_{\boldsymbol{z}}\phi_{n,\ l,\ m}(\boldsymbol{r}) = m\phi_{n,\ l,\ m}(\boldsymbol{r}). & (2.37) \end{cases}$$

So the magnitude of angular momentum of an electron in hydrogenic atoms or ions at state $|n,\ l,\ m\rangle$ is $\sqrt{l(l+1)}$, and the $\boldsymbol{z}$ direction angular momentum is m.

2.2.2 Many-electron atoms

When there are more than one electrons in the atom, simple analytical solution to the Schrödinger equation doesn't exist anymore, and numerical methods or approximations are required. With the independent-particle model, the many-electron state $\Psi(q_1,\ q_2,\ \ldots,\ q_i,\ \ldots, q_n)$, which is antisymmetric upon exchange of two electrons as required by the Fermi-Dirac statistics, can be expressed by the Slater determinant:

$$\Psi(q_1,\ q_2,\ \ldots,\ q_i,\ \ldots,\ q_n) = \frac{1}{\sqrt{n!}} \begin{vmatrix} \psi_{\alpha_1}(q_1) & \psi_{\alpha_1}(q_2) & \cdots & \psi_{\alpha_1}(q_i) & \cdots & \psi_{\alpha_1}(q_n) \\ \psi_{\alpha_2}(q_1) & \psi_{\alpha_2}(q_2) & \cdots & \psi_{\alpha_2}(q_i) & \cdots & \psi_{\alpha_2}(q_n) \\ \vdots & \vdots & \vdots\!\vdots & \vdots & \vdots\!\vdots & \vdots \\ \psi_{\alpha_s}(q_1) & \psi_{\alpha_s}(q_2) & \cdots & \psi_{\alpha_s}(q_i) & \cdots & \psi_{\alpha_s}(q_n) \\ \vdots & \vdots & \vdots\!\vdots & \vdots & \vdots\!\vdots & \vdots \\ \psi_{\alpha_n}(q_1) & \psi_{\alpha_n}(q_2) & \cdots & \psi_{\alpha_n}(q_i) & \cdots & \psi_{\alpha_n}(q_n) \end{vmatrix}, \quad (2.38)$$

where $\psi_{\alpha_s}(q_i) = \phi_{\alpha_s}(\boldsymbol{r_i})\chi^{\sigma}_{\alpha_s}$ is the single particle state, with the subscript α_s representing the spin quantum number $\sigma = \pm\frac{1}{2}$, as well as the quantum numbers n, l, and m which have analogous meanings as the corresponding quantum numbers specified for hydrogenic atoms in the last subsection. $\phi_{\alpha_s}(\boldsymbol{r_i})$ and $\chi^{\sigma}_{\alpha_s}$ are the spatial and spin parts of the wave function respectively, and $\psi_{\alpha_s}(q_i)$ is also called the spin orbital.

The Hartree-Fock method, which is an independent-particle model approximating the effect on one electron from the other electrons to be an averaged repulsion (mean field) from these other electrons, can be used to solve for the spin orbitals $\psi_{\alpha_s}(q)$, with the Hartree-Fock equation (see e.g. [50] for a derivation)

$$\Big[-\frac{1}{2}\ \bigtriangledown^2\ -\ \frac{Z}{r}\Big]\psi_{\alpha_s}(q)\ +\ \Big[\mathcal{J}\ -\ \mathcal{K}\Big]\psi_{\alpha_s}(q)\ =\ \varepsilon_{\alpha_s}\psi_{\alpha_s}(q) \quad (2.39)$$

where the Coulomb and Exchange operators $\mathcal{J}$ and $\mathcal{K}$ act on $\psi_{\alpha_s}(q)$ according to

$$\begin{cases} \mathcal{J}\psi_{\alpha_s}(q) &= \Big[\sum_{\alpha_t}\int \phi^*_{\alpha_t}(\boldsymbol{r}')\frac{1}{|\boldsymbol{r}\ -\ \boldsymbol{r}'|}\phi_{\alpha_t}(\boldsymbol{r}')\ d^3r'\Big]\psi_{\alpha_s}(q) & (2.40)\\ \mathcal{K}\psi_{\alpha_s}(q) &= \Big[\sum_{\alpha_t}\langle\chi_{\alpha_t^\sigma}|\chi_{\alpha_s^\sigma}\rangle\int \phi^*_{\alpha_t}(\boldsymbol{r}')\frac{1}{|\boldsymbol{r}\ -\ \boldsymbol{r}'|}\phi_{\alpha_s}(\boldsymbol{r}'))\ d^3r'\Big]\phi_{\alpha_t}(\boldsymbol{r}). & (2.41)\end{cases}$$

From Eqs. (2.40) and (2.41), the Coulomb operator $\mathcal{J}$ represents the averaged effect of all the other electrons has on the electron occupying spin orbital $\psi_{\alpha_s}(q)$, whereas the Exchange operator $\mathcal{K}$ is non-local and attributable to the exchange effects between $\psi_{\alpha_s}(q)$ and other spin orbitals.

The Hartree-Fock equation (2.39) looks similar in form to the time-independent Schrödinger equation if rewritten with the Hartree-Fock operator $\mathcal{H}_{HF} = \Big[-\frac{1}{2}\ \bigtriangledown^2\ -\frac{Z}{r}\ +\ \mathcal{J}\ -\ \mathcal{K}\Big]$:

$$\mathcal{H}_{HF}\psi_{\alpha_s}(q)\ =\ \varepsilon_{\alpha_s}\psi_{\alpha_s}(q). \tag{2.42}$$

ε_{α_s} in Eqs. (2.39) and (2.42) can be taken as the eigen value of the spin orbital $\psi_{\alpha_s}(q)$. It's often the case that the n spin orbitals $\psi_{\alpha_{s0}}(q)$ which can be used to construct the many-electron ground state $\Psi_0(q_1,\ q_2,\ \ldots,\ q_i,\ \ldots,\ q_n)$ with Eq. (2.38) are these orbitals with the n lowest eigenvalues $\varepsilon_{\alpha_{s0}}$. The approximate value to the total ground state energy is given by

$$E_0\ =\ \langle\Psi_0|\,\mathcal{H}_{HF}\,|\Psi_0\rangle\ =\ \sum_{\alpha_{s0}}\varepsilon_{\alpha_{s0}}\ +\ \frac{1}{2}\sum_{\alpha_{s0},\alpha_{t0}}\Big[\mathcal{J}_{\alpha_{s0},\alpha_{t0}}\ -\ \mathcal{K}_{\alpha_{s0},\alpha_{t0}}\Big], \tag{2.43}$$

where $\mathcal{J}_{\alpha_{s0},\alpha_{t0}} = \langle\psi_{\alpha_{s0}}(q)\psi_{\alpha_{t0}}(q')|\,\frac{1}{|\boldsymbol{r}\ -\ \boldsymbol{r}'|}\,|\psi_{\alpha_{s0}}(q)\psi_{\alpha_{t0}}(q')\rangle$ and $\mathcal{K}_{\alpha_{s0},\alpha_{t0}} = \langle\psi_{\alpha_{s0}}(q)\psi_{\alpha_{t0}}(q')|\,\frac{1}{|\boldsymbol{r}\ -\ \boldsymbol{r}'|}\,|\psi_{\alpha_{t0}}(q)\psi_{\alpha_{s0}}(q')\rangle$.

If the electron occupying spin orbital $\langle\psi_{\alpha_s}(q)|$ is removed, the ionic state $\langle\Psi_{ion}|$ can be constructed accordingly with Eq. (2.38) assuming all the other orbitals are unchanged, with

its energy given by

$$E_{ion} \;=\; \langle \Psi_{ion} | \, \mathcal{H}_{HF} \, | \Psi_{ion} \rangle \;=\; E_0 \; - \varepsilon_{\alpha_s}. \tag{2.44}$$

So the binding energy of the electron occupying spin orbital $\langle \psi_{\alpha_s}|$ is $E_{ion} \;-\; E_0 \;=\; -\varepsilon_{\alpha_s}$.

If the electron occupying spin orbital $\langle \psi_{\alpha_s}(q)|$ is excited to an unoccupied spin orbital $\langle \psi_{\alpha_w}(q)|$, the singly-excited state $\langle \Psi_{exc}|$ can be constructed according to Eq. (2.38) by replacing $\langle \psi_{\alpha_s}(q)|$ with $\langle \psi_{\alpha_w}(q)|$ and assuming all the other orbitals are unchanged, with its energy given by

$$E_{exc} \;=\; \langle \Psi_{exc} | \, \mathcal{H}_{HF} \, | \Psi_{exc} \rangle \;=\; E_0 \; + \varepsilon_{\alpha_w} \; - \varepsilon_{\alpha_s} \; + \; \Big[\mathcal{J}_{\alpha_s,\alpha_w} \; - \; \mathcal{K}_{\alpha_s,\alpha_w} \Big]. \tag{2.45}$$

So if the terms in square brackets can be neglected, the excitation energy needed for the transition between the two spin orbitals is $E_{exc} \;-\; E_0 \;=\; \varepsilon_{\alpha_w} \;- \varepsilon_{\alpha_s}$.

The Hartree-Fock equation (2.39) consists of a set of coupled differential equations which are nonlinear since the operator $\mathcal{H}_{HF}$ itself contains the to-be-solved spin orbitals $\langle \psi_{\alpha_s}(q)|$. An iterative procedure can be used to get these spin orbitals:

1. Make an educated guess on the set of spin orbitals in Eq. (2.38).

2. Construct the Coulomb and Exchange operators with the guessed spin orbitals and solve for the spin orbitals with Eq. (2.39).

3. Construct the Coulomb and Exchange operators with the spin orbitals solved with Eq. (2.39), and solve for the spin orbitals with the new operators.

4. If the orbitals solved in step 3 are not identical to the ones used to construct the Coulomb and Exchange operators, repeat step 3. if they are identical, a self-consistent solution is obtained.

Due to the mean-field approximation, the electron correlations are not properly accounted for by the Hartree-Fock method. One way to mitigate this problem is the "Configuration

Interaction" (CI) approach. Instead of only optimizing on one electronic configuration described by $\Psi(q_1,\ q_2,\ \ldots,\ q_i,\ \ldots,\ q_n)$ as discussed above, the CI method works with multiple electronic configurations:

$$\langle\Psi_{CI}|\ =\ c_0\,\langle\Psi_0|\ +\ c_2\,\langle\Psi_1|\ +\ \ldots+\ c_i\,\langle\Psi_i|\ +\ \ldots, \tag{2.46}$$

where $\langle\Psi_i|$ represents the i^{th} electronic configuration and c_i is its weight to be solved. Based on the ground state Ψ_0, the excited state $\langle\Psi_i|$ (with $i\ >\ 0$) can be constructed with Eq. (2.38) by replacing one or more occupied orbitals with unoccupied ones.

2.3 Molecule

[1] The time-independent Schrödinger equation for a molecule is

$$\Big[\mathcal{H}_{nuc}\ +\ \mathcal{H}_{ele}\Big]\Phi(\{\boldsymbol{R}\},\ \{\boldsymbol{r}\})\ =\ E\Phi(\{\boldsymbol{R}\},\ \{\boldsymbol{r}\}), \tag{2.47}$$

where $\{\boldsymbol{R}\}\ =\ \boldsymbol{R_1},\ \boldsymbol{R_2},\ \ldots,\ \boldsymbol{R_s},\ \ldots$ are the nuclear positions, and $\{\boldsymbol{r}\}\ =\ \boldsymbol{r_1},\ \boldsymbol{r_2},\ \ldots,\ \boldsymbol{r_i},\ \ldots$ are the electron positions. The nulcear Hamiltonian is

$$\mathcal{H}_{nuc}\ =\ -\sum_s \frac{\nabla^2_{R_s}}{2M_s}\ +\ \frac{1}{2}\sum_{s\neq t}\frac{Z_sZ_t}{|\boldsymbol{R}_s\ -\ \boldsymbol{R}_t|}, \tag{2.48}$$

where M_s is the mass of the nucleus labeled by "s". And the electronic Hamiltonian is

$$\mathcal{H}_{ele}\ =\ -\frac{1}{2}\sum_i \nabla^2_{r_i}\ +\ \frac{1}{2}\sum_{i\neq j}\frac{1}{|\boldsymbol{r}_i\ -\ \boldsymbol{r}_j|}\ -\ \sum_{s,i}\frac{Z_s}{|\boldsymbol{R}_s\ -\ \boldsymbol{r}_i|}. \tag{2.49}$$

If the nuclei are fixed, i.e., $\{\boldsymbol{R}\}\ = const.$, the molecular problem is reduced to the atomic one as discussed in section 2.2. But in reality, the nuclear motions are in an interplay with the electron dynamics, complicating the molecular problem compared with the atomic case.

[1] The derivation in this section is based on section 2.2 "Molecular Schrödinger Equation" in [51].

Approximations are needed to proceed from Eq. (2.47) and gain insight on the molecular states. Even if the nuclei can not be fixed, they are more than three orders of magnitude heavier than electron, making them move much slower than the electrons. So the electrons can be approximated as responding instantaneously to the nuclear dynamics, and the electronic state $\Psi_{k,\{\boldsymbol{R}\}}(\{\boldsymbol{r}\})$ with eigen energy E^k_{ele} can be solved at each of the fixed nuclear spatial arrangements defined by $\{\boldsymbol{R}\}$:

$$\mathcal{H}_{ele}\Psi_{k,\{\boldsymbol{R}\}}(\{\boldsymbol{r}\}) \;=\; E^k_{ele}\Psi_{k,\{\boldsymbol{R}\}}(\{\boldsymbol{r}\}). \tag{2.50}$$

For a fixed nuclear arrangement $\{\boldsymbol{R}\}$, the equation above is the same in form as the one used for many-electron atoms. So the Hartree-Fock method introduced in subsection 2.2.2 can be used to get the many-electron eigen state $\Psi_{k,\{\boldsymbol{R}\}}(\{\boldsymbol{r}\})$ (implicitly containing the spin part of the wavefunction) and eigen energy E^k_{ele}.

Once the electronic states are solved at the fixed $\{\boldsymbol{R}\}$, the total molecular state $\Phi(\{\boldsymbol{R}\})$can be expressed as a linear combination of the products of the electronic state $\Psi_{k,\{\boldsymbol{R}\}}(\{\boldsymbol{r}\})$ with the corresponding nuclear state $\Theta_k(\{\boldsymbol{R}\})$:

$$\Psi(\{\boldsymbol{R}\}) \;=\; \sum_k \Theta_k(\{\boldsymbol{R}\})\Psi_{k,\{\boldsymbol{R}\}}(\{\boldsymbol{r}\}), \tag{2.51}$$

and only the nuclear state $\Theta_k(\{\boldsymbol{R}\})$, which contains the ro-vibrational information of the nuclei, remains to be solved.

Substituting $\Psi(\{\boldsymbol{R}\})$ of Eq. (2.51) into Eq. (2.47), projecting both sides to the electronic state $\Psi_{j,\{\boldsymbol{R}\}}(\{\boldsymbol{r}\})$ and using the orthonormality $\langle\Psi_j|\Psi_k\rangle \;=\; \delta_{jk}$,

$$\sum_k \langle\Psi_j| - \sum_s \frac{\nabla^2_{R_s}}{2M_s}(|\Theta_k\rangle\,|\Psi_k\rangle) \;+\; \left[\frac{1}{2}\sum_{s\neq t}\frac{Z_sZ_t}{|\boldsymbol{R}_s \;-\; \boldsymbol{R}_t|} \;+\; E^j_{ele}\right]|\Theta_j\rangle \;=\; E\,|\Theta_j\rangle\,. \tag{2.52}$$

The first term can be expanded:

$$\sum_k \langle\Psi_j| - \sum_s \frac{\nabla^2_{R_s}}{2M_s}(|\Theta_k\rangle\,|\Psi_k\rangle) \;=\; -\sum_{k,s} \frac{1}{2M_s}\langle\Psi_j|\Big[(\nabla^2_{R_s}\,|\Theta_k\rangle)\,|\Psi_k\rangle \;+ \\ |\Theta_k\rangle\,\nabla^2_{R_s}\,|\Psi_k\rangle \;+\; 2\,\nabla_{R_s}\,|\Theta_k\rangle\,\nabla_{R_s}\,|\psi_k\rangle\Big] \\ =\Big[-\sum_s \frac{\nabla^2_{R_s}}{2M_s} \;+\; \sum_k \hat{\eta}_{jk}\Big]\,|\Theta_k\rangle\,. \tag{2.53}$$

The first term in the equation above is the nuclear kinetic energy operator, and the second term is the sum over the nonadiabaticity operators:

$$\hat{\eta}_{jk} = \sum_s \Big[-\langle\Psi_j|\,\frac{\nabla^2_{R_s}}{2M_s}\,|\Psi_k\rangle \;-\; \frac{1}{M_s}\,\langle\Psi_j|\,\nabla_{R_s}\,|\Psi_k\rangle\,\nabla_{R_s}\Big], \tag{2.54}$$

which is attributable to the effect of coupling among different electronic states (for $j \neq k$) through nuclear motion.

With the insertion of Eqs. (2.53) and (2.54), Eq. (2.52) becomes

$$\Big[-\sum_s \frac{\nabla^2_{R_s}}{2M_s} \;+\; \Big[\frac{1}{2}\sum_{s\neq t}\frac{Z_s Z_t}{|\boldsymbol{R}_s \;-\; \boldsymbol{R}_t|} \;+\; E^j_{ele} \;+\; \hat{\eta}_{jj}\Big]\Big]\,|\Theta_j\rangle \;=\; E\,|\Theta_j\rangle \;-\; \sum_{k\neq j}\hat{\eta}_{jk}\,|\Theta_k\rangle \tag{2.55}$$

With the Born-Oppenheimer approximation in which the nonadiabatic coupling is neglected, the above equation takes the form of the time-independent Schrödinger equation:

$$\Big[-\sum_s \frac{\nabla^2_{R_s}}{2M_s} \;+\; \mathcal{V}_{nuc}\Big]\,|\Theta_j\rangle \;=\; E\,|\Theta_j\rangle\,, \tag{2.56}$$

where

$$\mathcal{V}_{nuc} \;=\; \frac{1}{2}\sum_{s\neq t}\frac{Z_s Z_t}{|\boldsymbol{R}_s \;-\; \boldsymbol{R}_t|} \;+\; E^j_{ele} \;+\; \hat{\eta}_{jj} \tag{2.57}$$

defines the potential energy hypersurface for the nuclei when the electronic state is $|\Psi_j\rangle$. If

the electrons are at the stationary state $|\Psi_j\rangle$, upon solving Eq. (2.56), the total molecular state becomes

$$\Phi_j(\{\boldsymbol{R}\}) \;=\; \Theta_j(\{\boldsymbol{R}\})\Psi_{j,\{\boldsymbol{R}\}}(\{\boldsymbol{r}\}). \tag{2.58}$$

However, Born-Oppenheimer approximation can not be applied when there is a strong coupling between different electronic states and the potential energy hypersurfaces of these states are getting too close to one and another. In these cases, the nonadiabatic operators for the coupled states have to be included to study the nuclear motions.

2.4 Interaction between ultra-intense x-rays and molecules

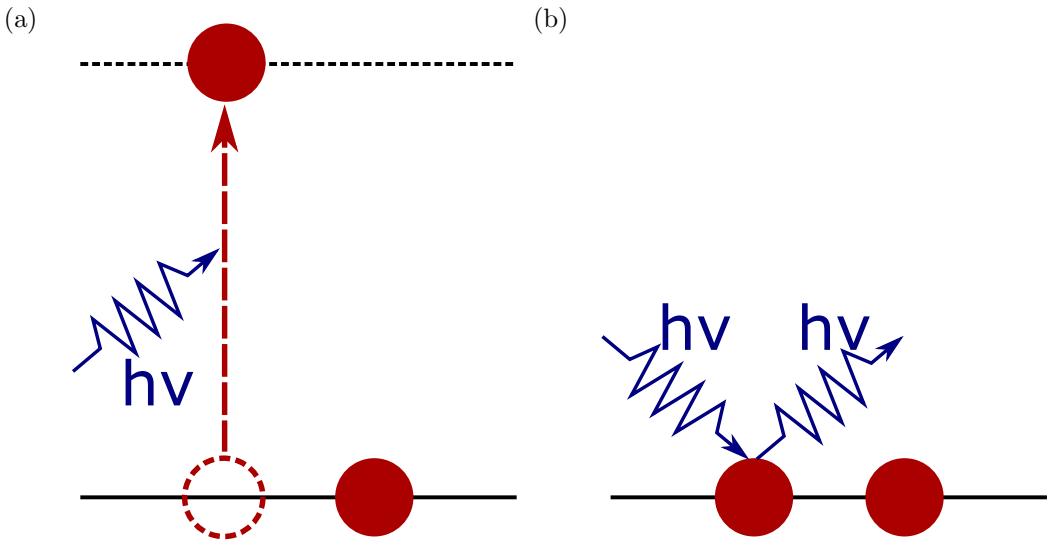

Figure 2.3: Two major electronic responses to x-rays below 10 keV. (a) Photoabsorption: an electron (dark red closed circle) transits to an excited state by absorbing a photon (dark blue). (b) Rayleigh scattering: a photon is scattered off an electron without changing either the photon energy or the electronic state.

Up to this point, only the stationary quantum states of atoms and molecules have been discussed. In the interaction of ultra-intense x-rays with molecules, the quantum states become time dependent and evolve according to the Schrödinger equation. In this section, the quantum state evolution will be first discussed, which will then be applied to the different

kinds of interactions between x-rays and molecules. The photoabsorption and Rayleigh scattering processes as two major electronic responses of molecules to x-rays below 10 keV are illustrated in Fig. 2.3. For x-rays with photon energy below 10 keV, the photoabsorption cross section is, in general, orders of magnitude larger than that of scattering. Take carbon as an example, as shown in Fig. 2.4, its cross section of photoabsorption is one to three orders of magnitude larger than that of scattering for x-rays with photon energy ranging from 1 keV to 10 keV.

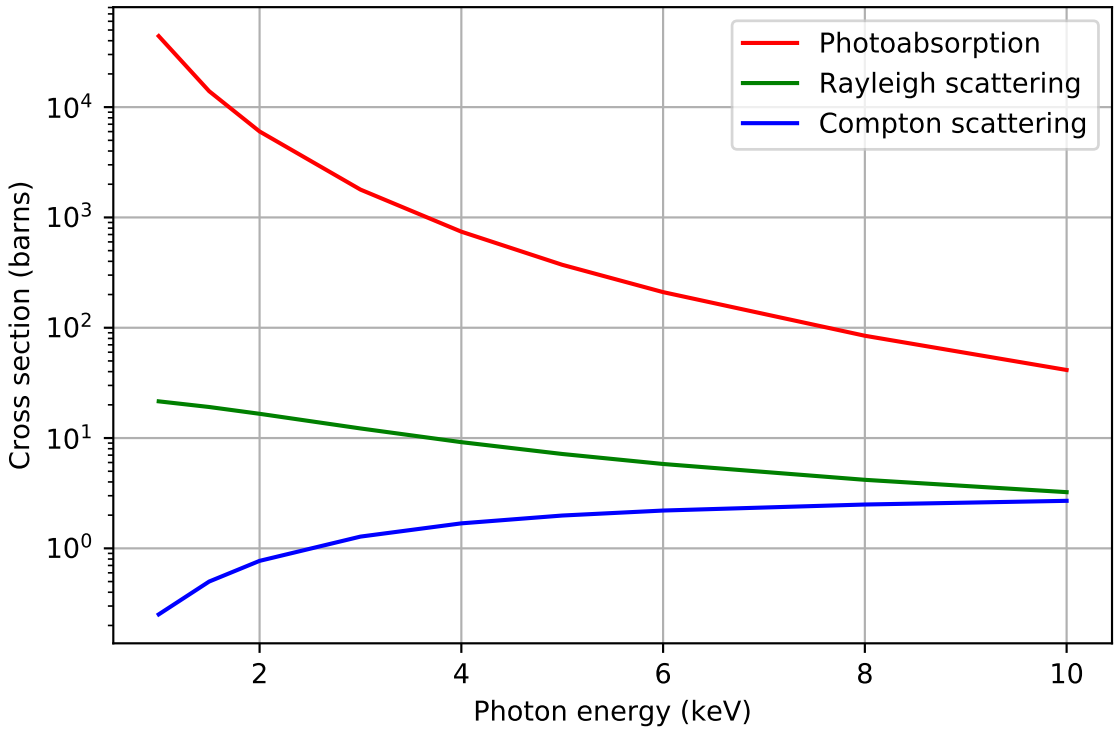

Figure 2.4: The photoabsorption, Rayleigh scattering and Compton scattering cross sections of carbon with x-ray photon energy from 1 keV to 10 keV. Photoabosrption is orders of magnitude more probable than the scattering process. The data is taken from [52].

2.4.1 Quantum state evolution

The evolution of a quantum state follows the time-dependent Schrödinger equation

$$i\frac{\partial\psi}{\partial t} = \mathcal{H}\psi \tag{2.59}$$

If the quantum system is under no external potential, the total Hamiltonian $\mathcal{H}$ is the system-intrinsic Hamiltonian $\mathcal{H}_0$, and its state ψ_0 at time t is $\psi_0(t) = U_0(t)\psi_0(t=0)$, with $U_0(t) = e^{-i\mathcal{H}_0 t}$ being the state evolution operator.

When the quantum system is under external potential $\mathcal{V}$, the total Hamiltonian $\mathcal{H}$ becomes the sum of the system-intrinsic Hamiltonian $\mathcal{H}_0$ and the external potential or interaction Hamiltonian $\mathcal{V}$, i.e., $\mathcal{H} = \mathcal{H}_0 + \mathcal{V}$. It's convenient to work in the "interaction picture" to study the response of the system to the external potential, from which follows naturally the interaction-related quantities such as the transition probability.

Interaction picture

In the "interaction picture", the quantum state $|\psi_I\rangle$ is related to the state in the "Schrödinger picture" $|\psi\rangle$ by

$$|\psi_I\rangle = U_0^\dagger |\psi\rangle , \tag{2.60}$$

and the operator $\mathcal{V}_I$ is related to the operator in the "Schrödinger picture" $\mathcal{V}$ by

$$\mathcal{O}_I = U_0^\dagger \mathcal{O} U_0. \tag{2.61}$$

Inserting $|\psi\rangle = U_0 |\psi_I\rangle$ and $\mathcal{O} = U_0 \mathcal{O}_I U_0^\dagger$ into Eq. (2.59), the equation of motion in the "interaction picture" is obtained:

$$i\frac{\partial |\psi_I\rangle}{\partial t} = \mathcal{V}_I |\psi_I\rangle , \tag{2.62}$$

which is in the same form as the Schrödinger equation (2.59), with $|\psi\rangle$ replaced by $|\psi_I\rangle$ and the total Hamiltonian $\mathcal{H}$ replaced by the external potential $\mathcal{V}_I$.

State evolution and transition

With $|\psi_I(t_0)\rangle$ as the initial state at t_0, the state $|\psi_I(t)\rangle$ at t can be solved by iterative integration starting from Eq. (2.62):

$$
\begin{aligned}
|\psi_I(t)\rangle &= \left[\mathbb{1} + (-i)\int_{t_0}^{t} \mathcal{V}_I(t')\,dt' + \right. \\
&\qquad \left. (-i)^2 \int_{t_0}^{t}\int_{t0}^{t'} \mathcal{V}_I(t')\mathcal{V}_I(t'')\,dt''dt' + \cdots\right] |\psi_I(t_0)\rangle \qquad (2.63)\\
&= \left[\mathcal{T}\sum_{n=0}^{\infty}\frac{(-i)^n}{n!}\Big[\int_{t_0}^{t}\mathcal{V}_I(t')\,dt'\Big]^n\right]|\psi_I(t_0)\rangle \qquad (2.64)\\
&= \left[\mathcal{T}e^{-i\int_{t0}^{t}\mathcal{V}_I(t')\,dt'}\right]|\psi_I(t_0)\rangle \qquad (2.65)\\
&= U_I(t,t_0)\,|\psi_I(t_0)\rangle\,, \qquad (2.66)
\end{aligned}
$$

where

$$
U_I(t,t_0) = \left[\mathcal{T}e^{-i\int_{t0}^{t}\mathcal{V}_I(t')\,dt'}\right] \qquad (2.67)
$$

is the state evolution operator from time t_0 to t in the "interaction picture", $\mathcal{T}$ is the time-ordering operator which guarantees that the potential operator $\mathcal{V}_I(t'_i)$ at t'_i acts on the state $|\psi_I(t_0)\rangle$ before $\mathcal{V}_I(t'_j)$ at t'_j if $t'_i < t'_j$. The factor $\frac{1}{n!}$ in Eq. (2.64) is for removing double counting, because when the n integrals in each term in the square bracket of Eq. (2.63) are transformed to one integral to the n^{th} power in Eq. (2.64), each of the to-be-integrated elements is counted $n!$ times more.

Let $\left|\psi_k^I\right\rangle$ (with $k = 0, 1, \ldots$) denote the eigenstates of the system in the "interaction picture". If the initial state of the system at t_0 is $\left|\psi_i^I\right\rangle$, the probability of transitioning to the state $\left|\psi_j^I\right\rangle$ at time t is, according to Eq. (2.66),

$$
P_{i\to j} = |\left\langle\psi_j^I\right| U_I(t,t_0)\left|\psi_i^I\right\rangle|^2. \qquad (2.68)
$$

Perturbation

Obtaining the state evolution operator U_I can be a formidable task since it requires the sum over infinite number of terms. It's often the case for Eq. (2.63) that the terms in the square brackets up to the first order dominate over higher-order terms, such that the sum over the first two terms is a good first-order approximation to U_I:

$$U_I^{(1)}(t, t_0) \ = \mathbb{1} \ + \ (-i) \int_{t_0}^{t} \mathcal{V}_I(t') \ dt'. \tag{2.69}$$

To the first order, the transition probability in Eq. (2.68) becomes

$$P_{i\to j}^{(1)} \ = \ |\left\langle \psi_j^I \right| U_I^{(1)}(t, t_0) \left| \psi_i^I \right\rangle|^2 \ = \ |\left\langle \psi_j^I \right| \int_{t_0}^{t} \mathcal{V}_I(t') \ dt' \left| \psi_i^I \right\rangle|^2. \tag{2.70}$$

If $P_{i\to j}^{(1)}$ is zero, the second-order probability which uses the second-order term in the square brackets of Eq. (2.63) needs to be calculated:

$$P_{i\to j}^{(2)} \ = \ |\left\langle \psi_j^I \right| \int_{t_0}^{t} \int_{t0}^{t'} \mathcal{V}_I(t')\mathcal{V}_I(t'') \ dt''dt' \left| \psi_i^I \right\rangle|^2. \tag{2.71}$$

Consider an external potential $\mathcal{V}$ ($\mathcal{V}_I$ in the "interaction picture") existing in time from $-\infty$ to ∞, which can be separated into the time-independent part $\mathcal{V}_0$ and time-dependent part $e^{-i\omega t}$, i.e., $\mathcal{V} \ = \ \mathcal{V}_0 e^{-i\omega t}$. $\mathcal{V}$ is then of the same form as the single mode electromagnetic field potential with frequency ω. Under it, the first-order transition probability can be

calculated:

$$
\begin{aligned}
P^{(1)}_{i\to j} &= |\left\langle \psi^I_j \right| \int_{-\infty}^{\infty} \mathcal{V}_I(t')\, dt' \left|\psi^I_i\right\rangle|^2 && (2.72)\\
&= |\left\langle \psi^I_j \right| \int_{-\infty}^{\infty} U_0^\dagger \mathcal{V}(t') U_0\, dt' \left|\psi^I_i\right\rangle|^2 && (2.73)\\
&= |\left\langle \psi_j \right| \int_{-\infty}^{\infty} e^{i\omega_j t'} \mathcal{V}(t') e^{-i\omega_i t}\, dt' \left|\psi_i\right\rangle|^2 && (2.74)\\
&= |\left\langle \psi_j \right| \mathcal{V}_0 \left|\psi_i\right\rangle|^2 \, |\int_{-\infty}^{\infty} e^{i(\omega_j-\omega_i-\omega)t'}\, dt'|^2 && (2.75)\\
&= \lim_{t\to\infty} 2\pi t |\left\langle \psi_j \right| \mathcal{V}_0 \left|\psi_i\right\rangle|^2 \delta(\omega_j-\omega_i-\omega) && (2.76)
\end{aligned}
$$

and the transition rate is

$$
T^{(1)}_{i\to j} = \frac{P^{(1)}_{i\to j}}{t} = 2\pi |\left\langle \psi_j \right| \mathcal{V}_0 \left|\psi_i\right\rangle|^2 \delta(\omega_j-\omega_i-\omega), \tag{2.77}
$$

where $|\psi_i\rangle\, e^{-i\omega_i t}$ and $|\psi_j\rangle\, e^{-i\omega_j t}$ are the i^{th} and j^{th} eigenstates of the system in the "Schrödinger picture", with ω_i and ω_j being the corresponding eigen energies.

Under such external potential $\mathcal{V} = \mathcal{V}_0 e^{-i\omega t}$, the second-order transition probability is

$$
\begin{aligned}
P^{(2)}_{i\to j} &= |\left\langle \psi^I_j \right| \int_{-\infty}^{\infty}\int_{-\infty}^{t'} \mathcal{V}_I(t')\mathcal{V}_I(t'')\, dt''dt' \left|\psi^I_i\right\rangle|^2 && (2.78)\\
&= \sum_k |\left\langle \psi^I_j \right| \int_{-\infty}^{\infty}\int_{-\infty}^{t'} \mathcal{V}_I(t') \left|\psi^I_k\right\rangle \left\langle \psi^I_k \right| \mathcal{V}_I(t'')\, dt''dt' \left|\psi^I_i\right\rangle|^2 && (2.79)\\
&= \sum_k |\left\langle \psi_j \right| \mathcal{V}_0 \left|\psi_k\right\rangle \left\langle \psi_k \right| \mathcal{V}_0 \left|\psi_i\right\rangle|^2 \, |\int_{-\infty}^{\infty}\int_{-\infty}^{t'} e^{i(\omega_j-\omega_k-\omega)t'} e^{i(\omega_k-\omega_i-\omega)t''}\, dt''dt'|^2 && (2.80)\\
&= \lim_{t\to\infty} \sum_k \frac{2\pi t |\left\langle \psi_j \right| \mathcal{V}_0 \left|\psi_k\right\rangle \left\langle \psi_k \right| \mathcal{V}_0 \left|\psi_i\right\rangle|^2 \delta(\omega_j-\omega_i-2\omega)}{(\omega_k-\omega_i-\omega)^2}, && (2.81)
\end{aligned}
$$

The result above can be interpreted as the system first transiting from $|\psi_i\rangle$ to an intermediate state $|\psi_k\rangle$ through the first interaction, and then from $|\psi_k\rangle$ to the final state $|\psi_j\rangle$ through the second interaction. However, as will be discussed in the subsection 2.4.5, the intermediate state has a finite life time τ_k and decays exponentially according to $e^{-\frac{\Gamma_k t}{2}}$, with $\Gamma_k = \frac{1}{\tau_k}$ being the decay rate. So for the second-order probability derivation, the scaling factor $e^{-\frac{\Gamma_k(t'-t'')}{2}}$

should be added to $\left|\psi_k^I\right\rangle\left\langle\psi_k^I\right|$ to account for its decay:

$$
\begin{aligned}
P_{i\to j}^{(2)} &= |\left\langle\psi_j^I\right| \int_{-\infty}^{\infty}\int_{-\infty}^{t'} \mathcal{V}_I(t')\mathcal{V}_I(t'')\, dt''dt' \left|\psi_i^I\right\rangle|^2 \\
&= \sum_k |\left\langle\psi_j^I\right| \int_{-\infty}^{\infty}\int_{-\infty}^{t'} \mathcal{V}_I(t')e^{-\frac{\Gamma_k(t'-t'')}{2}} \left|\psi_k^I\right\rangle\left\langle\psi_k^I\right| \mathcal{V}_I(t'')\, dt''dt' \left|\psi_i^I\right\rangle|^2 \\
&= \sum_k |\left\langle\psi_j\right| \mathcal{V}_0 \left|\psi_k\right\rangle\left\langle\psi_k\right| \mathcal{V}_0 \left|\psi_i\right\rangle|^2 \, |\int_{-\infty}^{\infty}\int_{-\infty}^{t'} e^{i(\omega_j-\omega_k-\omega+i\frac{\Gamma_k}{2})t'} e^{i(\omega_k-\omega_i-\omega-i\frac{\Gamma_k}{2})t''}\, dt''dt'|^2 \\
&= \lim_{t\to\infty}\sum_k \frac{2\pi t|\left\langle\psi_j\right| \mathcal{V}_0 \left|\psi_k\right\rangle\left\langle\psi_k\right| \mathcal{V}_0 \left|\psi_i\right\rangle|^2\delta(\omega_j-\omega_i-2\omega)}{(\omega_k-\omega_i-\omega-i\Gamma_k/2)^2},
\end{aligned}
\tag{2.82}
$$

and the transition rate is obtained by dividing the probability with the time t

$$
T_{i\to j}^{(2)} = \sum_k \frac{2\pi|\left\langle\psi_j\right| \mathcal{V}_0 \left|\psi_k\right\rangle\left\langle\psi_k\right| \mathcal{V}_0 \left|\psi_i\right\rangle|^2\delta(\omega_j-\omega_i-2\omega)}{(\omega_k-\omega_i-\omega-i\Gamma_k/2)^2}. \tag{2.83}
$$

2.4.2 Hamiltonian in the interaction between x-rays and molecules

The x-rays used in the work of this thesis mainly interact with the electrons in the molecule. In the following, this interaction will be discussed based on the independent-electron model introduced in previous sections 2.2.2 and 2.3. The Hamiltonian for a single electron in the molecule irradiated by x-rays is

$$
\begin{aligned}
\mathcal{H}_1 &= \frac{1}{2}(\hat{\boldsymbol{p}} - \alpha\hat{\boldsymbol{A}})^2 + \mathcal{V}_{mol} \\
&= (-\frac{1}{2}\bigtriangledown^2 + \mathcal{V}_{mol}) + (-i\alpha\hat{\boldsymbol{A}}\cdot\bigtriangledown + \frac{1}{2}\alpha^2\hat{\boldsymbol{A}}^2),
\end{aligned}
\tag{2.84}
$$

where $\hat{\boldsymbol{p}}$ is the momentum operator, $\hat{\boldsymbol{A}}$ is the vector potential operator given in Eq. (2.22), and $\mathcal{V}_{mol}$ is the operator accounting for the interaction with the nuclei and the other electrons in the molecule. The terms in the first bracket constitute the intrinsic Hamiltonian for obtaining the electron's stationary states as discussed in previous sections 2.2.2 and 2.3,

whereas the remaining part is the interaction Hamiltonian:

$$\mathcal{V} \;=\; -i\alpha\hat{\boldsymbol{A}}\cdot\bigtriangledown + \;\frac{1}{2}\alpha^2\hat{\boldsymbol{A}}^2 \tag{2.85}$$

As will be discussed, the two terms in $\mathcal{V}$ are responsible for different processes in the interaction between x-rays and molecules.

The subsections below will use the number states $\left|n_{\boldsymbol{k_1},\xi_1},\; n_{\boldsymbol{k_2},\xi_2},\; \ldots, n_{\boldsymbol{k_j},\xi_j},\; \ldots\right\rangle$ introduced in 2.1.2 to describe the state of photons in the x-ray field, and the vector potential operator is again given by

$$\hat{\boldsymbol{A}}(\boldsymbol{r},\; t) \;= \sum_{\boldsymbol{k},\xi}\sqrt{\frac{2\pi}{V\omega_{\boldsymbol{k}}\alpha^2}}[\hat{a}_{\boldsymbol{k},\xi}\boldsymbol{\epsilon}_{\boldsymbol{k},\xi}e^{i(\boldsymbol{k}\cdot\boldsymbol{r}\;-\;\omega_{\boldsymbol{k}}t)} \;+\; \hat{a}^{\dagger}_{\boldsymbol{k},\xi}\boldsymbol{\epsilon}^{*}_{\boldsymbol{k},\xi}e^{-i(\mathbf{k}\cdot\boldsymbol{r}\;-\;\omega_{\boldsymbol{k}}t)}]. \tag{2.86}$$

The stationary states for the single electron will be denoted by $|\psi_i\rangle\, e^{-i\omega_i t}$, with ω_i being the eigen energy and the subscript $i \;=\; 0, 1,\; \ldots$.

2.4.3 Photoabsorption

Absorption rate and cross section

Photoabsorption is the process through which an electron transits from the initial state $|\psi_i\rangle\, e^{-i\omega_i t}$ to a high-lying state $|\psi_j\rangle\, e^{-i\omega_j t}$ by absorbing photons. If one photon in the mode $(\boldsymbol{k},\xi)$ is absorbed, the only responsible term of the interaction Hamiltonian (see Eqs. (2.85) and (2.86)) is the one containing a single photon annihilation operator:

$$-i\alpha\left[\sqrt{\frac{2\pi}{V\omega_{\boldsymbol{k}}\alpha^2}}\hat{a}_{\boldsymbol{k},\xi}e^{i(\boldsymbol{k}\cdot\boldsymbol{r}\;-\;\omega_{\boldsymbol{k}}t)}\boldsymbol{\epsilon}_{\boldsymbol{k},\xi}\right]\cdot\bigtriangledown, \tag{2.87}$$

which can be expressed as $\hat{\mathcal{V}}_0 e^{-i\omega_{\boldsymbol{k}}t}$ with $\hat{\mathcal{V}}_0 \;=\; -i\alpha\left[\sqrt{\frac{2\pi}{V\omega_{\boldsymbol{k}}\alpha^2}}\hat{a}_{\boldsymbol{k},\xi}e^{i\boldsymbol{k}\cdot\boldsymbol{r}}\boldsymbol{\epsilon}_{\boldsymbol{k},\xi}\right]\cdot\bigtriangledown$ being the time-independent part. So by inserting $\mathcal{V}_0 \;= \langle\ldots, n_{\boldsymbol{k},\xi}-1,\; \ldots|\,\hat{\mathcal{V}}_0\,|\ldots, n_{\boldsymbol{k},\xi},\; \ldots\rangle$ into Eq.

(2.77), the first-order rate for this transition is:

$$
\begin{aligned}
T^{(1)}_{i\to j} &= \frac{4\pi^2}{V\omega_{\boldsymbol{k}}} |\langle\psi_j| \langle \ldots, n_{\boldsymbol{k},\xi}-1, \ldots| \hat{a}_{\boldsymbol{k},\xi} e^{i\boldsymbol{k}\cdot\boldsymbol{r}} \boldsymbol{\epsilon}_{\boldsymbol{k},\xi}\cdot\bigtriangledown |\ldots, n_{\boldsymbol{k},\xi}, \ldots\rangle |\psi_i\rangle|^2 \delta(\omega_j-\omega_i-\omega) \\
&= \frac{4\pi^2 n_{\boldsymbol{k},\xi}}{V\omega_{\boldsymbol{k}}} |\langle\psi_j| e^{i\boldsymbol{k}\cdot\boldsymbol{r}} \boldsymbol{\epsilon}_{\boldsymbol{k},\xi}\cdot\bigtriangledown |\psi_i\rangle|^2 \delta(\omega_j-\omega_i-\omega) \qquad (2.88)
\end{aligned}
$$

The photoabsorption cross section for this transition can be obtained by dividing the transition rate $T^{(1)}_{i\to j}$ with the photon flux $f_{\boldsymbol{k},\xi} = c\frac{n_{\boldsymbol{k},\xi}}{V} = \frac{n_{\boldsymbol{k},\xi}}{\alpha V}$:

$$
\sigma^{(1)}_{i\to j} = \frac{4\pi^2\alpha}{\omega_{\boldsymbol{k}}} |\langle\psi_j| e^{i\boldsymbol{k}\cdot\boldsymbol{r}} \boldsymbol{\epsilon}_{\boldsymbol{k},\xi}\cdot\bigtriangledown |\psi_i\rangle|^2 \delta(\omega_j-\omega_i-\omega) \qquad (2.89)
$$

Photoionization

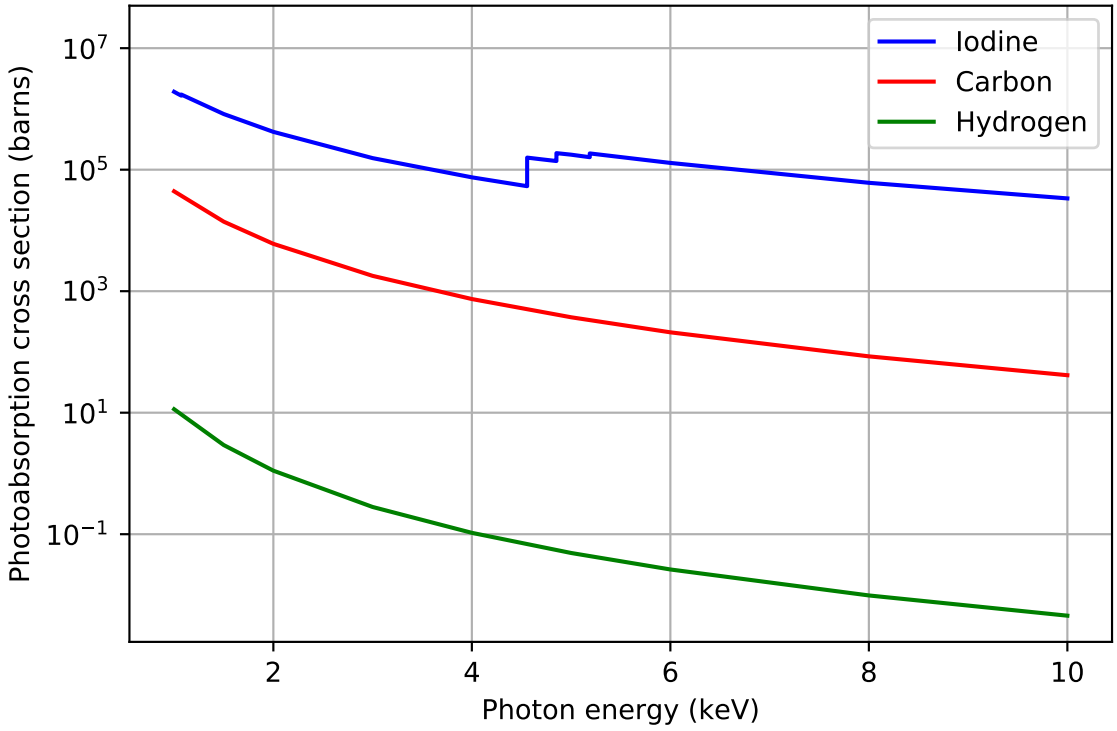

Figure 2.5: The photoabsorption cross sections of iodine, carbon and hydrogen with x-ray photon energy from 1 keV to 10 keV. The data is taken from [52].

If the state $|\psi_j\rangle$ is in the continuum, the transition corresponds to the photoionization. With the high photon energy of x-rays, this is a common process in their interaction with

matter. There are general dependencies for x-ray photoionization processes, e.g. on the element and x-ray photon energy, which can be revealed by the example of x-ray photoionizatin of hydrogenic atoms. In this case, the initial state is the ground state of hydrogenic atoms discussed in subsection 2.2.1, i.e., $\psi_i = (\frac{Z^3}{\pi})^{\frac{1}{2}} e^{-Zr}$. The final state is $\psi_j = \frac{1}{\sqrt{V}} e^{i\boldsymbol{k}_j \cdot \boldsymbol{r}}$ for electrons ejected into the continuum with momentum vector $\boldsymbol{k}_j$. From energy conservation, the final electron energy is $\omega_j = \frac{k_j^2}{2} = \omega + \omega_i = \omega - \frac{Z^2}{2}$. The differential cross section for this transitions is

$$\frac{d\sigma}{d\Omega} = \sigma_{i\to j}^{(1)} \rho_j = \frac{4\pi\alpha Z^3}{V\omega_{\boldsymbol{k}}} |e^{-i\boldsymbol{k}_j \cdot \boldsymbol{r}} e^{i\boldsymbol{k}\cdot\boldsymbol{r}} \boldsymbol{\epsilon}_{\boldsymbol{k},\xi} \cdot \bigtriangledown e^{-Zr}|^2 \rho_j, \tag{2.90}$$

where $\Omega = (\theta, \phi)$ is the solid angle denoting the direction of $\boldsymbol{k}_j$, and $\rho_j = \frac{V}{8\pi^3} k_j$ is the density of final states with energy $\frac{k_j^2}{2}$. By integrating over all solid angles, the total photoionization cross section can be found (see [53] for the integration.) to be

$$\sigma \propto \frac{Z^5}{\omega^{\frac{7}{2}}}. \tag{2.91}$$

So the photoionization cross section is proportional to the atomic number to the fifth power, i.e., Z^5, and inversely proportional to the photon energy ω to the power of $\frac{7}{2}$. This is the reason why heavy elements are strong x-ray absorbers and photoabsorption cross section in general gets smaller with larger photon energies.

Fig. 2.5 shows the photoabsorption cross sections of iodine, carbon and hydrogen with x-ray photon energy from 1 keV to 10 keV. It can be seen that the cross section of iodine is orders of magnitude larger than those of carbon and hydrogen. So when an x-ray pulse with photon energy in this range interacts with a CH_3I molecule, it would mainly interact with iodine.

Photoabsorption from ultra-intense x-rays

For the femtosecond x-ray pulses produced by free-electron lasers, containing a typical number of photons on the order of 10^{12} and focused into a typical spot size of 1 μm^2, the typical

fluence (number of photons per unit area per pulse) is $\mathcal{F} = 10^{20}\ photons/cm^2$. Considering atoms with a typical x-ray absorption cross section σ on the order of $0.1 - 1\ Mbarn$, the photoabsorption probability calculated by $\mathcal{F}\sigma$ is larger than one. This means more than one single-photon absorption described by Eqs. (2.88) and (2.89) occurs within a single x-ray pulse. If n photons are sequentially absorbed in the interaction, a question arises how likely it is for this process to happen. As will be shown in subsection 5.1.1, the average probability is not simply proportional to the photon flux f to the n^{th} power which is the case for direct n-photon absorption. Instead, the probability for such sequential n-photon absorption will be shown to be proportional to $e^{-bf}f^n$, with b the constant depending on the pulse duration and photoabsorption cross section.

After several steps of sequential ionization, the electron binding energy may become larger than the photon energy, i.e. $\omega < -\omega_i$. If the photon energy value is such that the electron can't get directly ionized but can be excited to a high-lying bound state, more electrons can be ejected through subsequent Auger decay and direct photoionization from this high-lying bound state. This effect, which is called "Resonance-Enabled X-ray Multiple Ionization" [5, 8], can greatly enhance the ionization of heavy atoms up to charge states which are otherwise unreachable.

The multiple photoabsorptions discussed above are sequential . With the x-ray intensity high enough, multiple photons can also be absorbed simultaneously in a direct process, the rate [54] of which can be described qualitatively by

$$T_{dir} = \left[\prod_{t=1}^{n-1} T^{(1)}_{it\to jt}\tau_t\right] T_{in\to jn} = \left[\prod_{t=1}^{n-1} \sigma^{(1)}_{it\to jt}\tau_t\right] \sigma^{(1)}_{in\to jn} f^n_{\boldsymbol{k},\xi} = \sigma_{dir,n} f^n_{\boldsymbol{k},\xi}, \tag{2.92}$$

where τ_t is the lifetime of the state identified by jt if the t^{th} photon is absorbed resonantly, otherwise it's the lifetime of a virtual state and of order Δ^{-1}, with Δ being the detuning of the energy $\omega + \omega_{it}$ from that of the nearest eigen state. $\sigma_{dir,n}$ is the generalized direct n-photon absorption cross section. With x-rays from free-electron lasers, direct two-photon, one-electron ionization has been observed with neon atoms at a photon energy of 1100 eV [2]. The upper limit for the two-photon absorption cross section $\sigma_{dir,2}$ of neon at 1100

eV determined in that experiment is $7 \times 10^{-54}\ cm^4 s$. Later studies [55] demonstrated the importance of the direct two-photon absorption for XFEL pulse interaction with solid targets.

2.4.4 Auger decay

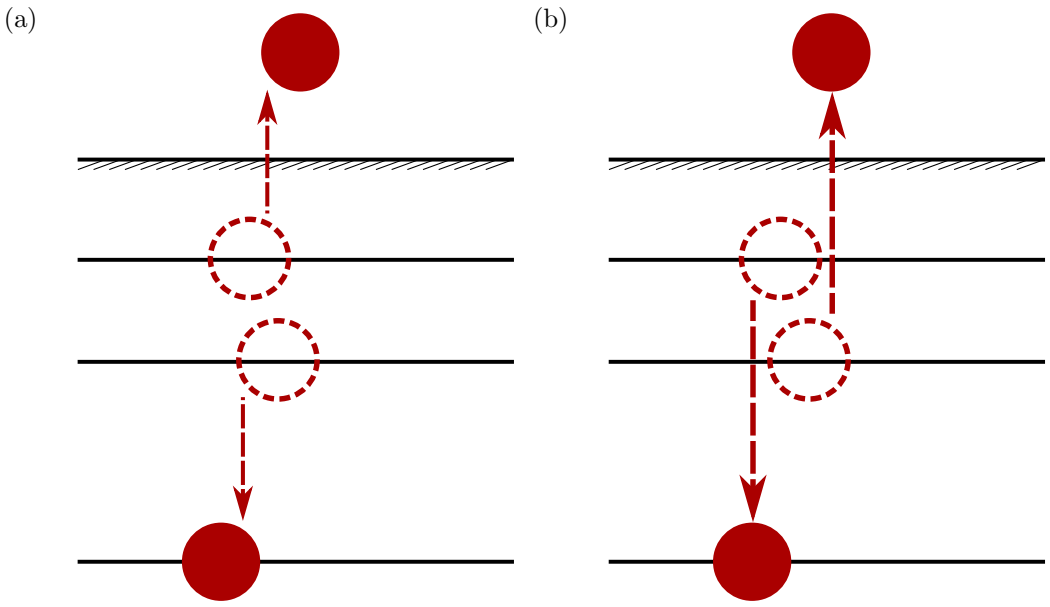

Figure 2.6: Two possible Auger processes which can lead to the same final state.

After an electron, initially at the state $|\psi_i\rangle$ corresponding to an inner shell orbital, is excited to the high-lying state $|\psi_j\rangle$, the molecule, which is now highly exicted, will decay to a less excited state, with the core hole filled either through spontaneous emission to be discussed in subsection 2.4.5 or Auger process. The Auger process is due to the Coulomb interaction between electrons. With the Coulomb interaction $\frac{1}{|\boldsymbol{r}_1 - \boldsymbol{r}_2|}$, one electron transits from the state $|\psi_{i1}\rangle$ to the final state $|\psi_{j1}\rangle$ which is the state $|\psi_i\rangle$ from which an electron was removed previously, the other electron transits from $|\psi_{i2}\rangle$ to the final state $|\psi_{j2}\rangle$ which is in the continuum and hence gets ejected. The Auger decay rate can therefore be written with the help of Eq. (2.77) as

$$T^{(1)}_{Auger'} = 2\pi |\langle\psi_{j1}(\boldsymbol{r}_1)| \langle\psi_{j2}(\boldsymbol{r}_2)| \frac{1}{|\boldsymbol{r}_1 - \boldsymbol{r}_2|} |\psi_{i1}(\boldsymbol{r}_1)\rangle |\psi_{i2}(\boldsymbol{r}_2)\rangle|^2 \delta(\omega_{j1} - \omega_{i1} + \omega_{j2} - \omega_{i2}) \tag{2.93}$$

Since the two electrons participating the Auger decay are indistinguishable, the other process, with the two electrons switching roles with respect to the above process, is also possible as illustrated in Fig. 2.6. The total Auger decay rate should therefore be obtained by coherently taking into account these two processes:

$$\begin{aligned} T^{(1)}_{Auger} &= 2\pi |\langle\psi_{j1}(\boldsymbol{r}_1)|\langle\psi_{j2}(\boldsymbol{r}_2)| \frac{1}{|\boldsymbol{r}_1 - \boldsymbol{r}_2|} |\psi_{i1}(\boldsymbol{r}_1)\rangle |\psi_{i2}(\boldsymbol{r}_2)\rangle \\ &- \langle\psi_{j2}(\boldsymbol{r}_1)|\langle\psi_{j1}(\boldsymbol{r}_2)| \frac{1}{|\boldsymbol{r}_1 - \boldsymbol{r}_2|} |\psi_{i1}(\boldsymbol{r}_1)\rangle |\psi_{i2}(\boldsymbol{r}_2)\rangle |^2 \delta(\omega_{j1} - \omega_{i1} + \omega_{j2} - \omega_{i2}) \end{aligned} \tag{2.94}$$

2.4.5 Spontaneous emission, stimulated emission and life time

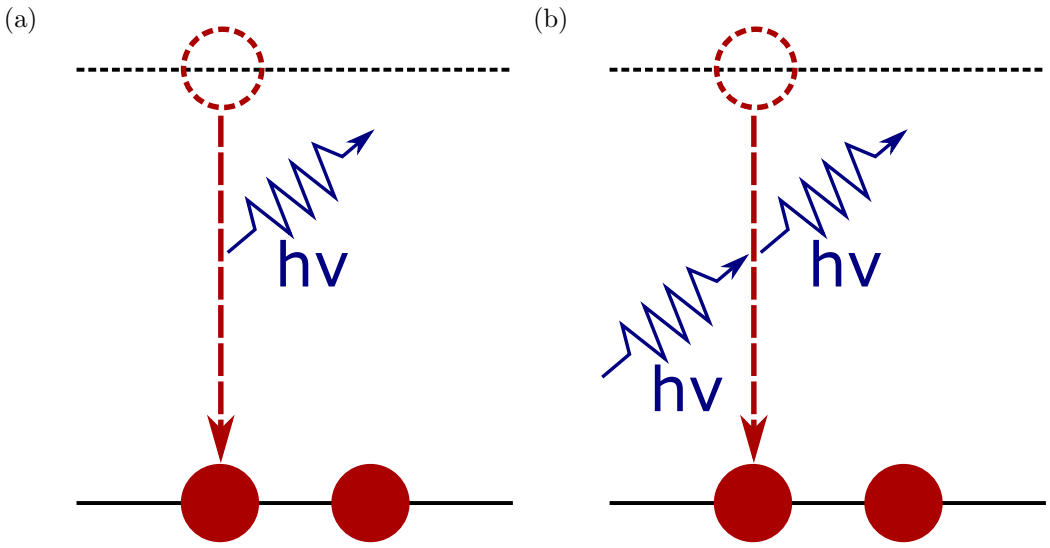

Figure 2.7: Illustration of x-ray emission processes. (a) Spontaneous emission. (b) Stimulated emission.

When the electron transits from the state $|\psi_j\rangle$ to a low-lying state $|\psi_i\rangle$, a photon in the mode $(\boldsymbol{k}, \xi)$ can be emitted. The only responsible term of the interaction Hamiltonian (see Eqs. (2.85) and (2.86)) is the one containing a single photon creation operator:

$$-i\alpha \left[\sqrt{\frac{2\pi}{V\omega_{\boldsymbol{k}}\alpha^2}} \hat{a}^\dagger_{\boldsymbol{k},\xi} e^{-i(\boldsymbol{k}\cdot\boldsymbol{r} - \omega_{\boldsymbol{k}}t)} \boldsymbol{\epsilon}^*_{\boldsymbol{k},\xi} \right] \cdot \bigtriangledown, \tag{2.95}$$

which can be expressed as $\hat{\mathcal{V}}_0' e^{-i(-\omega_{\boldsymbol{k}} t)}$ with $\hat{\mathcal{V}}_0' = -i\alpha\left[\sqrt{\frac{2\pi}{V\omega_{\boldsymbol{k}}\alpha^2}}\hat{a}^\dagger_{\boldsymbol{k},\xi} e^{-i\boldsymbol{k}\cdot\boldsymbol{r}}\boldsymbol{\epsilon}^*_{\boldsymbol{k},\xi}\right]\cdot\bigtriangledown$ being the time-independent part. So by inserting $\mathcal{V}_0 = \langle \ldots, n_{\boldsymbol{k},\xi}+1, \ldots|\,\hat{\mathcal{V}}_0'\,|\ldots, n_{\boldsymbol{k},\xi}, \ldots\rangle$ into Eq. (2.77), the first-order rate for the emission is:

$$
\begin{aligned}
T^{(1)}_{emission} &= \frac{4\pi^2}{V\omega_{\boldsymbol{k}}}|\,\langle\psi_i|\,\langle \ldots, n_{\boldsymbol{k},\xi}+1, \ldots|\,\hat{a}^\dagger_{\boldsymbol{k},\xi} e^{-i\boldsymbol{k}\cdot\boldsymbol{r}}\boldsymbol{\epsilon}^*_{\boldsymbol{k},\xi}\cdot\bigtriangledown\,|\ldots, n_{\boldsymbol{k},\xi}, \ldots\rangle\,|\psi_j\rangle\,|^2\delta(\omega_i-\omega_j+\omega) \\
&= \frac{4\pi^2(n_{\boldsymbol{k},\xi}+1)}{V\omega_{\boldsymbol{k}}}|\,\langle\psi_i|\,e^{-i\boldsymbol{k}\cdot\boldsymbol{r}}\boldsymbol{\epsilon}^*_{\boldsymbol{k},\xi}\cdot\bigtriangledown\,|\psi_j\rangle\,|^2\delta(\omega_i-\omega_j+\omega) \\
&= \frac{4\pi^2}{V\omega_{\boldsymbol{k}}}|\,\langle\psi_i|\,e^{-i\boldsymbol{k}\cdot\boldsymbol{r}}\boldsymbol{\epsilon}^*_{\boldsymbol{k},\xi}\cdot\bigtriangledown\,|\psi_j\rangle\,|^2\delta(\omega_i-\omega_j+\omega) + \\
&\quad \frac{4\pi^2 n_{\boldsymbol{k},\xi}}{V\omega_{\boldsymbol{k}}}|\,\langle\psi_i|\,e^{-i\boldsymbol{k}\cdot\boldsymbol{r}}\boldsymbol{\epsilon}^*_{\boldsymbol{k},\xi}\cdot\bigtriangledown\,|\psi_j\rangle\,|^2\delta(\omega_i-\omega_j+\omega). \qquad (2.96)
\end{aligned}
$$

The first term in Eq. (2.96) is the spontaneous emission or fluorescence rate $T^{(1)}_{spon}$. The second term, which is proportional to the number of photons $n_{\boldsymbol{k},\xi}$ in the mode $(\boldsymbol{k},\xi)$, is the stimulated emission rate $T^{(1)}_{stim}$. The two kinds of emission processes are illustrated in Fig. 2.7.

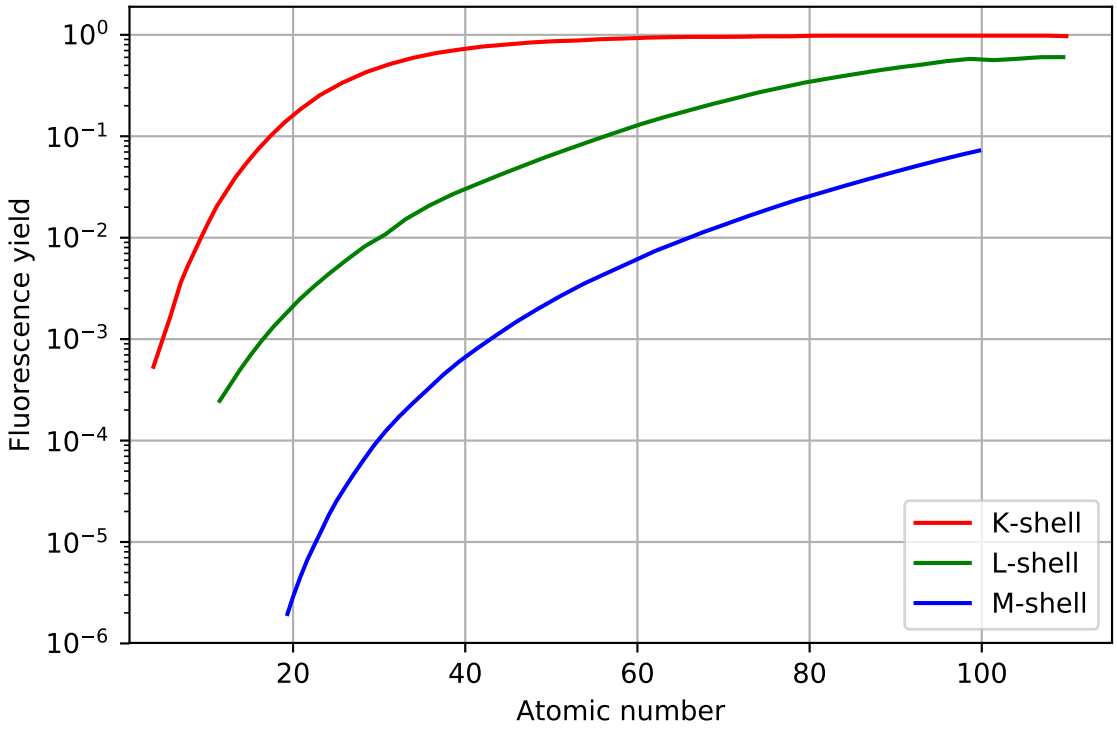

Figure 2.8: Fluorescence yield for states with core holes in K, L and M shells of atoms with different atomic numbers. The data is taken from [56].

A core-hole state can decay by fluorescence or Auger process which was discussed in subsection 2.4.4. Assuming a total decay rate Γ, this core-hole state will decay exponentially with a lifetime $\tau = \frac{1}{\Gamma}$. From Heisenberg's Uncertainty Principle, the observed energy of the excited state has an uncertainty on the order of $\frac{1}{2\tau} = \frac{\Gamma}{2}$.

The fluorescence yield Y_f is defined as the ratio between the fluorescence rate Γ_f and the total decay rate Γ:

$$Y_f = \frac{\Gamma_f}{\Gamma}. \tag{2.97}$$

It's the relative probability that a core-hole state decays radiatively. The fluorescence yield for states with core holes in K, L and M shells of atoms with different atomic numbers is plotted in Fig. 2.8. As the atom gets heavier, radiative decay increases. For light atoms with atomic number below 20, the core holes in these shells are mainly filled by Auger decay. For heavy atoms with atomic numbers above 40, the core holes in the K shell is more likely to be filled by fluorescence. But for core-holes in the L shell, the Auger process continues to dominate over fluorescence until the atomic number is above 90. Take 8.3 keV x-ray ionization of iodine (Z = 53) as an example, the x-rays mainly interact with electrons in the L shell. With a fluorescence yield of 0.08, the core holes in the L shell is mostly filled by Auger decay.

2.4.6 Scattering

Through the scattering process, the interaction between a photon in the mode $(\boldsymbol{k}, \xi)$ and an electron at state $|\psi_i\rangle$ results in either a photon in the mode $(\boldsymbol{k}', \xi')$ emitted with the electron at the same state $|\psi_i\rangle$, or a photon in the mode $(\boldsymbol{k}', \xi')$ emitted with the electron transiting to a different state $|\psi_j\rangle$. The former case is the elastic scattering and the latter inelastic. Both terms in the interaction Hamiltonian Eq. (2.85) can contribute to the scattering, with the first term $-i\alpha\hat{\boldsymbol{A}} \cdot \bigtriangledown$ through a second-order process, and the second term $\frac{1}{2}\alpha^2\hat{\boldsymbol{A}}^2$ through a first-order process. In general, for x-ray photon energy below 1 MeV, the scattering is mainly

contributed by Rayleigh scattering, in which the photons interact with bound electrons and leave electronic state unchanged. With increasing photon energy, the Compton scattering gets more and more important because the high-energy photons see the bound electrons more and more like free electrons. Rayleigh and Raman scatterings, which are more relevant for the photon energy range ($< 15\ keV$) of current XFEL facilities, will be discussed in the following subsections.

Rayleigh scattering

Rayleigh scattering is elastic, which is mainly contributed by the interaction term $\frac{1}{2}\alpha^2\hat{\boldsymbol{A}}^2$ by a first-order process. With it, a photon in the mode $(\boldsymbol{k}', \xi')$, which has the same energy as the absorbed photon, is emitted, i.e., $\omega_{\boldsymbol{k}} = \omega'_{\boldsymbol{k}}$, leaving the electron at the same state $|\psi_i\rangle$. The only contributing terms in $\frac{1}{2}\alpha^2\hat{\boldsymbol{A}}^2$ for this process (photon annihiliation in mode $(\boldsymbol{k}', \xi')$ and creation in mode $(\boldsymbol{k}, \xi)$) are

$$\begin{aligned}
&\frac{1}{2}\sqrt{\frac{4\pi^2}{V^2\omega_{\boldsymbol{k}}\omega_{\boldsymbol{k}'}}}\left[\hat{a}_{\boldsymbol{k},\xi}\hat{a}^\dagger_{\boldsymbol{k}',\xi'} + \hat{a}^\dagger_{\boldsymbol{k}',\xi'}\hat{a}_{\boldsymbol{k},\xi}\right]\left[\boldsymbol{\epsilon}_{\boldsymbol{k},\xi}\boldsymbol{\epsilon}^*_{\boldsymbol{k}',\xi'}e^{i(\boldsymbol{k}\cdot\boldsymbol{r} - \mathbf{k}'\cdot\boldsymbol{r})}\right]e^{-i(\omega_{\boldsymbol{k}} - \omega_{\boldsymbol{k}'})t} \\
&= \sqrt{\frac{4\pi^2}{V^2\omega_{\boldsymbol{k}}\omega_{\boldsymbol{k}'}}}\left[\hat{a}_{\boldsymbol{k},\xi}\hat{a}^\dagger_{\boldsymbol{k}',\xi'}\boldsymbol{\epsilon}_{\boldsymbol{k},\xi}\boldsymbol{\epsilon}^*_{\boldsymbol{k}',\xi'}e^{i(\boldsymbol{k}\cdot\boldsymbol{r} - \mathbf{k}'\cdot\boldsymbol{r})}\right]e^{-i(\omega_{\boldsymbol{k}} - \omega_{\boldsymbol{k}'})t} \\
&= \hat{\mathcal{V}}_0 e^{-i(\omega_{\boldsymbol{k}} - \omega_{\boldsymbol{k}'})t},
\end{aligned} \tag{2.98}$$

with $\hat{\mathcal{V}}_0 = \sqrt{\frac{4\pi^2}{V^2\omega_{\boldsymbol{k}}\omega_{\boldsymbol{k}'}}}\left[\hat{a}_{\boldsymbol{k},\xi}\hat{a}^\dagger_{\boldsymbol{k}',\xi'}\boldsymbol{\epsilon}_{\boldsymbol{k},\xi}\boldsymbol{\epsilon}^*_{\boldsymbol{k}',\xi'}e^{i(\boldsymbol{k}\cdot\boldsymbol{r} - \mathbf{k}'\cdot\boldsymbol{r})}\right]$ being the time-independent part. Upon substituting $\mathcal{V}_0$ in Eq. (2.77) with $\hat{\mathcal{V}}_0$ and appropriate photon number states, and replacing the energy conservation condition $\delta(\omega_i - \omega_j + \omega)$ with $\delta(\omega_{\boldsymbol{k}} - \omega_{\boldsymbol{k}'})$, the Rayleigh scattering rate can be calculated as

$$\begin{aligned}
T^{(1)}_{Rayleigh} &= \frac{8\pi^3}{V^2\omega_{\boldsymbol{k}}\omega_{\boldsymbol{k}'}}|\langle\psi_i|\langle\ldots, n_{\boldsymbol{k},\xi} - 1,\ \ldots, n_{\boldsymbol{k}',\xi'} = 1,\ \ldots|\,\hat{a}_{\boldsymbol{k},\xi}\hat{a}^\dagger_{\boldsymbol{k}',\xi'}\boldsymbol{\epsilon}_{\boldsymbol{k},\xi}\cdot\boldsymbol{\epsilon}^*_{\boldsymbol{k}',\xi'} \\
&\quad e^{i(\boldsymbol{k}\cdot\boldsymbol{r} - \mathbf{k}'\cdot\boldsymbol{r})}\,|\ldots, n_{\boldsymbol{k},\xi},\ \ldots, n_{\boldsymbol{k}',\xi'} = 0,\ \ldots\rangle\,|\psi_i\rangle\,|^2\delta(\omega_{\boldsymbol{k}} - \omega_{\boldsymbol{k}'}) \\
&= \frac{8\pi^3 n_{\boldsymbol{k},\xi}|\boldsymbol{\epsilon}_{\boldsymbol{k},\xi}\cdot\boldsymbol{\epsilon}^*_{\boldsymbol{k}',\xi'}|^2}{V^2\omega_{\boldsymbol{k}}\omega_{\boldsymbol{k}'}}|\langle\psi_i|\,e^{i\boldsymbol{q}\cdot\boldsymbol{r}}\,|\psi_i\rangle\,|^2\delta(\omega_{\boldsymbol{k}} - \omega_{\boldsymbol{k}'}),
\end{aligned} \tag{2.99}$$

where $\boldsymbol{q} = \boldsymbol{k} - \boldsymbol{k'}$ is the photon momentum transfer.

Dividing $T^{(1)}_{Rayleigh}$ by the photon flux $f_{\boldsymbol{k'},\xi'} = \frac{n_{\boldsymbol{k},\xi}}{\alpha V}$ and multiplying by the density of states of the emitted photon $\rho_{\boldsymbol{k'},\xi'} = \alpha\frac{V}{8\pi^3}k'^2$, the Rayleigh scattering differential cross section is obtained:

$$\frac{d\sigma^{(1)}_{Rayleigh}}{d\Omega} = \alpha^4|\boldsymbol{\epsilon}_{\boldsymbol{k},\xi}\cdot\boldsymbol{\epsilon}^*_{\boldsymbol{k'},\xi'}|^2|\left\langle\psi_i\right|e^{i\boldsymbol{q}\cdot\boldsymbol{r}}\left|\psi_i\right\rangle|^2\delta(\omega_{\boldsymbol{k}} - \omega_{\boldsymbol{k'}}) \tag{2.100}$$

if $|\left\langle\psi_i\right|e^{i\boldsymbol{q}\cdot\boldsymbol{r}}\left|\psi_i\right\rangle|^2 = 1$, the differential cross section becomes that of Thomson scattering: $\alpha^4|\boldsymbol{\epsilon}_{\boldsymbol{k},\xi}\cdot\boldsymbol{\epsilon}^*_{\boldsymbol{k'},\xi'}|^2\delta(\omega_{\boldsymbol{k}} - \omega_{\boldsymbol{k'}})$.

Now consider a sample with many electrons occupying the same state $|\psi_i\rangle$ which undergo the same Rayleigh scattering process coherently, the differential cross section becomes

$$\frac{d\sigma^{(1)}_{Rayleigh'}}{d\Omega} = \alpha^4|\boldsymbol{\epsilon}_{\boldsymbol{k},\xi}\cdot\boldsymbol{\epsilon}^*_{\boldsymbol{k'},\xi'}|^2|\sum_s\left\langle\psi_i\right|e^{i\boldsymbol{q}\cdot\boldsymbol{r}_s}\left|\psi_i\right\rangle|^2\delta(\omega_{\boldsymbol{k}} - \omega_{\boldsymbol{k'}}) \tag{2.101}$$

$$= \alpha^4|\boldsymbol{\epsilon}_{\boldsymbol{k},\xi}\cdot\boldsymbol{\epsilon}^*_{\boldsymbol{k'},\xi'}|^2|\left\langle\psi_i\right|\sum_s e^{i\boldsymbol{q}\cdot\boldsymbol{r}_s}\left|\psi_i\right\rangle|^2\delta(\omega_{\boldsymbol{k}} - \omega_{\boldsymbol{k'}}) \tag{2.102}$$

$$= \alpha^4|\boldsymbol{\epsilon}_{\boldsymbol{k},\xi}\cdot\boldsymbol{\epsilon}^*_{\boldsymbol{k'},\xi'}|^2|f(\boldsymbol{q})|^2\delta(\omega_{\boldsymbol{k}} - \omega_{\boldsymbol{k'}}), \tag{2.103}$$

where the form factor $f(\boldsymbol{q})$ can be rewritten as

$$f(\boldsymbol{q}) = \left\langle\psi_i\right|\sum_s e^{i\boldsymbol{q}\cdot\boldsymbol{r}_s}\left|\psi_i\right\rangle \tag{2.104}$$

$$= \left\langle\psi_i\right|\int e^{i\boldsymbol{q}\cdot\boldsymbol{r}}\rho(\boldsymbol{r})\ d^3r\left|\psi_i\right\rangle \tag{2.105}$$

$$= \int e^{i\boldsymbol{q}\cdot\boldsymbol{r}}\rho_{avg}(\boldsymbol{r})\ d^3r, \tag{2.106}$$

where $\rho(\boldsymbol{r}) = \sum_s\delta(\boldsymbol{r} - \boldsymbol{r}_s)$, and $\rho_{avg}(\boldsymbol{r})$ is the average electron density. So the form factor $f(\boldsymbol{q})$ is the Fourier Transform of the average electron density ρ_{avg}. By detecting the scattered photon pattern (i.e., photon signals with different momentum transfers), the form factor $f(\boldsymbol{q})$ can be obtained. The form factor can then be used to retrieve the average electron density which in turn reflects the atomic structure of the sample. This is the underlying principle

for coherent imaging applications at XFEL facilities.

Raman scattering

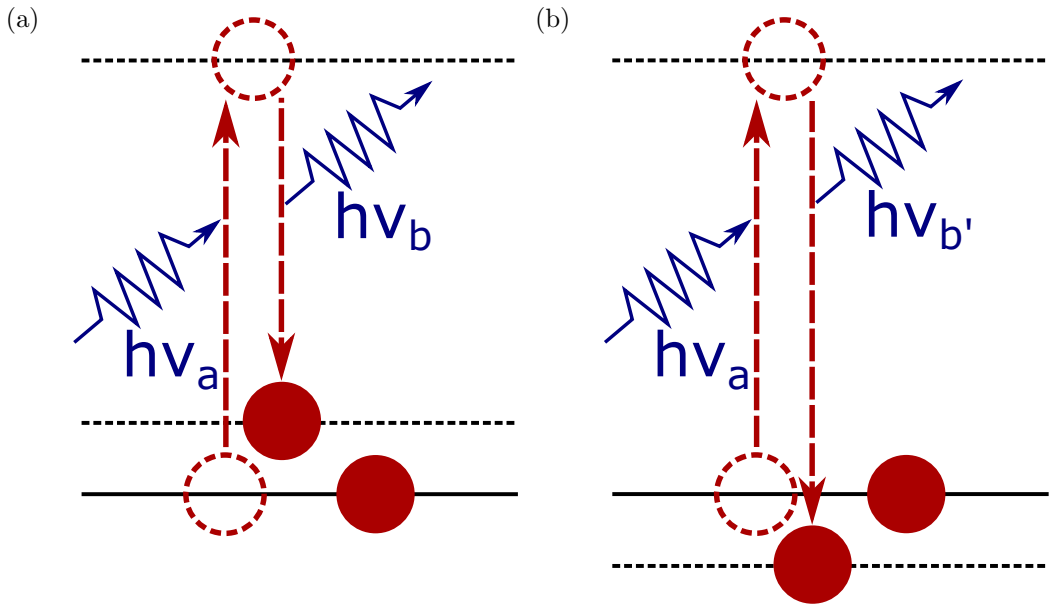

Figure 2.9: Two kinds of Raman scattering processes. (a) Stokes Raman scattering. (b)Anti-Stokes Raman scattering.

Raman scattering is a second-order inelastic process due to the interaction term $-i\alpha\hat{\boldsymbol{A}}\cdot\bigtriangledown$. The first photon in the mode $(\boldsymbol{k},\xi)$ excites the electron at the state $|\psi_i\rangle$ to a high-lying intermediate state $|\psi_k\rangle$ with the "absorption" term $-i\alpha\left[\sqrt{\frac{2\pi}{V\omega_{\boldsymbol{k}}\alpha^2}}\hat{a}_{\boldsymbol{k},\xi}e^{i(\boldsymbol{k}\cdot\boldsymbol{r}\ -\ \omega_{\boldsymbol{k}}t)}\boldsymbol{\epsilon}_{\boldsymbol{k},\xi}\right]\cdot\bigtriangledown$, which then transits to a low-lying state $|\psi_j\rangle$ accompanied by a photon emitted in the mode $(\boldsymbol{k}',\xi')$ through the "emission" term $-i\alpha\left[\sqrt{\frac{2\pi}{V\omega_{\boldsymbol{k}}\alpha^2}}\hat{a}^{\dagger}_{\boldsymbol{k},\xi}e^{-i(\boldsymbol{k}\cdot\boldsymbol{r}\ -\ \omega_{\boldsymbol{k}}t)}\boldsymbol{\epsilon}^{*}_{\boldsymbol{k},\xi}\right]\cdot\bigtriangledown$. As discussed in subsections 2.4.3 and 2.4.5, the "absorption" and "emission" terms can respectively be expressed as $\hat{\mathcal{V}}_0e^{-i(\omega_{\boldsymbol{k}}t)}$ and $\hat{\mathcal{V}}'_0e^{-i(-\omega_{\boldsymbol{k}}t)}$ with $\hat{\mathcal{V}}_0$ and $\hat{\mathcal{V}}'_0$ being the time-independent parts. So the second-order scattering rate can be derived similarly as the derivation of the second-order transition rate $T^{(2)}_{i\to j}$ in Eq. (2.83), and the result can also be directly obtained by replacing the two $\mathcal{V}_0$'s in Eq. (2.83) with $\hat{\mathcal{V}}_0$, $\hat{\mathcal{V}}'_0$ and appropriate photon number states, and replacing

the energy conservation condition $\delta(\omega_j - \omega_i - 2\omega)$ with $\delta(\omega_j - \omega_i - \omega_{\boldsymbol{k}} + \omega_{\boldsymbol{k}'})$:

$$
\begin{aligned}
T^{(2)}_{Raman} &= \sum_k \frac{\delta(\omega_j - \omega_i - \omega_{\boldsymbol{k}} + \omega_{\boldsymbol{k}'})}{(\omega_k - \omega_i - \omega - i\Gamma_k/2)^2} 2\pi \\
&\quad |\left\langle \psi_j \right| \left\langle \ldots, n_{\boldsymbol{k},\xi} - 1, \ \ldots, n_{\boldsymbol{k}',\xi'} + 1, \ \ldots \right| \hat{\mathcal{V}}'_0 \left| \ldots, n_{\boldsymbol{k},\xi} - 1, \ \ldots, n_{\boldsymbol{k}',\xi'}, \ \ldots \right\rangle \left| \psi_k \right\rangle \\
&\quad \left\langle \psi_k \right| \left\langle \ldots, n_{\boldsymbol{k},\xi} - 1, \ \ldots, n_{\boldsymbol{k}',\xi'}, \ \ldots \right| \hat{\mathcal{V}}_0 \left| \ldots, n_{\boldsymbol{k},\xi}, \ \ldots, n_{\boldsymbol{k}',\xi'}, \ \ldots \right\rangle \left| \psi_i \right\rangle |^2 \\
&= \sum_k \frac{8\pi^3 n_{\boldsymbol{k},\xi}(n_{\boldsymbol{k}',\xi'} + 1)}{V^2 \omega_{\boldsymbol{k}} \omega_{\boldsymbol{k}'}} \\
&\quad \frac{|\left\langle \psi_j \right| e^{i\boldsymbol{k}\cdot\boldsymbol{r}} \boldsymbol{\epsilon}_{\boldsymbol{k},\xi} \cdot \bigtriangledown \left| \psi_k \right\rangle \left\langle \psi_k \right| e^{-i\boldsymbol{k}'\cdot\boldsymbol{r}} \boldsymbol{\epsilon}^*_{\boldsymbol{k}',\xi'} \cdot \bigtriangledown \left| \psi_j \right\rangle |^2}{(\omega_k - \omega_i - \omega - i\Gamma_k/2)^2} \delta(\omega_j - \omega_i - \omega_{\boldsymbol{k}} + \omega_{\boldsymbol{k}'}).
\end{aligned}
\tag{2.107}
$$

The energy conservation condition $\delta(\omega_j - \omega_i - \omega_{\boldsymbol{k}} + \omega_{\boldsymbol{k}'})$ can be satisfied in two ways. One possibility is that the final state energy ω_j is larger than that of the initial sate ω_i, with the energy of the absorbed photon $\omega_{\boldsymbol{k}}$ larger than that of the emitted photon $\omega_{\boldsymbol{k}'}$, which corresponds to the Stokes Raman scattering. The other is that the final state energy ω_j is smaller than that of the initial sate ω_i, with the energy of the absorbed photon $\omega_{\boldsymbol{k}}$ smaller than that of the emitted photon $\omega_{\boldsymbol{k}'}$, which corresponds to the anti-Stokes Raman scattering. These two kinds of Raman scattering processes are illustrated in Fig. 2.9.

From Eq. (2.107), the Raman scattering rate is proportional to the photon number in the mode $(\boldsymbol{k}', \xi')$ plus one: $(n_{\boldsymbol{k}',\xi'} + 1)$. Similar to the division of the emission into spontaneous and stimulated emissions in subsection 2.4.5, $T^{(2)}_{Raman}$ can also be divided into the spontaneous Raman scattering rate which is independent of the photon number in the mode $(\boldsymbol{k}', \xi')$, and the stimulated Raman scattering rate which is proportional to the photon number $n_{\boldsymbol{k}',\xi'}$ in the mode $(\boldsymbol{k}', \xi')$.

Visible-light-stimulated Raman scattering has been a powerful nonlinear technique for studying nuclear motion in molecules, in which the initial and final states are respectively the ground and vibrationally excited states on the same potential energy surface (or the same electronic state), and the intermediate state is a high-lying excited electronic state.

As a nonlinear process which requires high field intensity, the x-ray-stimulated Raman

scattering by atoms was only observed six years ago after the LCLS was turned on to produce ultra-intense x-rays [3]. In analogy to the application of the femtosecond stimulated Raman scattering with visible light to study nuclear motion, the stimulated Raman scattering with intense attosecond x-ray pulses is a promising method for investigating electronic dynamics [57]. The initial and final states are now respectively the ground state and the excited electronic state (or a superposition of excited electronic states allowed by the x-ray bandwidth), with the intermediate state being the core-excited state. The excited electronic states populated by x-ray-stimulated Raman scattering have been demonstrated in a recent experiment [58] at the LCLS with NO molecules and intense attosecond x-rays.

2.4.7 Charge rearrangement

X-rays typically interact with a specific element in the molecule, which has the largest absorption cross section compared to the other elements. With the strong ionization at that specific site, a charge imbalance in the molecule is created, which can drive electron transfer from the non-ionized partner to the ionized site. So with the exception of possible inter-atomic decay processes (see e.g. [59–63]), the charge rearrangement discussed here is essentially the same as the charge capture process studied in ion and atom collision physics, with the difference being that the charge capture here is complicated with other processes such as sequential photoionizations, decays and fragmentation. It should be distinguished from the charge migration process, which is due to electron motion in a superposition state and has been predicted [64] to happen in the interaction between x-rays and molecules. The following subsections will discuss the electron transfer process in a simple molecular model consisting of an electron donor (D) and an acceptor (A), with both the quantum mechanical [51] and classical approaches [65, 66].

Hamiltonian for electron transfer

In a charge transfer process, an electron is relocated from the donor site to the acceptor site, both corresponding to specific elements within the molecule. The electron can be described

by a wavefunction extending over both the donor and acceptor sites, but for the purpose of electron transfer modeling, two sets of eigen states $|\psi_{Dm}\rangle$ and $|\psi_{An}\rangle$ are used, depending on whether the electron is at the donor or acceptor site. And they can be determined by the time-independent Schrödinger equation:

$$(-\frac{1}{2}\bigtriangledown^2 + \mathcal{V}_S)\,|\psi_{Sm}\rangle = E_{Sm}\,|\psi_{Sm}\rangle\,, \tag{2.108}$$

where $\mathcal{V}_S$ is the potential energy operator when the electron is at the donor ($S = D$) or acceptor ($S = A$) site. For simplicity, in the following discussion, the electron is assumed to be in either the donor-site ground states $|\psi_{D0}\rangle$ or the acceptor-site ground state $|\psi_{A0}\rangle$. Further it is assumed that the overlap integral $\langle\psi_{D0}|\psi_{A0}\rangle$ is negligibly small, so the two states are orthogonal. The electron Hamiltonian in the space spanned by these two ground states then becomes

$$\mathcal{H}_{ET,ele} = E'_{D0}\,|\psi_{D0}\rangle\,\langle\psi_{D0}| + E'_{A_0}\,|\psi_{A0}\rangle\,\langle\psi_{A0}| + V_{DA}\,|\psi_{D0}\rangle\,\langle\psi_{A0}| + V_{AD}\,|\psi_{A0}\rangle\,\langle\psi_{D0}|\,, \tag{2.109}$$

where $E'_{S0} = E_{S0} + \langle\psi_{S0}|\,\mathcal{V}_T\,|\psi_{S0}\rangle$, with $S = D$ *or* A and $\langle\psi_{S0}|\,\mathcal{V}_T\,|\psi_{S0}\rangle$ being the correction to the energy E_{S0} due to the presence of the neighbor potential $\mathcal{V}_T$. $V_{ST} = \frac{1}{2}\langle\psi_{S0}|\,(\mathcal{V}_S + \mathcal{V}_T)\,|\psi_{T0}\rangle$ is the interstate coupling.

So far the electron-transfer Hamiltonian has been considered with a fixed spatial arrangement of the nuclei, i.e., with the distance R_{DA} between the donor and acceptor fixed. However, the nuclear motion also plays a role in the charge transfer process. So the Hamiltonian in Eq. (2.110) must be parameterized by R_{DA}, with the nuclear Hamiltonian added. And the total Hamiltonian is

$$\begin{aligned}\mathcal{H}_{ET} = {} & \Big[\mathcal{K}_{nuc} + \mathcal{V}_{nuc,D0}(R_{DA})\Big]\,|\psi_{D0}\rangle\,\langle\psi_{D0}| + \Big[\mathcal{K}_{nuc} + \mathcal{V}_{nuc,A0}(R_{DA})\Big]\,|\psi_{A0}\rangle\,\langle\psi_{A0}| \\ & + V_{DA}(R_{DA})\,|\psi_{D0}\rangle\,\langle\psi_{A0}| + V_{AD}(R_{DA})\,|\psi_{A0}\rangle\,\langle\psi_{D0}|\,,\end{aligned} \tag{2.110}$$

where $\mathcal{K}_{nuc} = -\sum_S \frac{\nabla_S^2}{2M_s}$ is the nulcear kinetic energy operator as introduced in section 2.3, and $\mathcal{V}_{nuc,S0}(R_{DA}) = \frac{1}{2}\sum_{S\neq T}\frac{Z_S Z_T}{|\boldsymbol{R}_S - \boldsymbol{R}_T|} + E'_{S0}(R_{DA}) + \hat{\eta}_{SS}$ is the potential energy curve defined in Eq. (2.57).

Qualitative discussion of the charge-transfer dependence on the donor-acceptor distance

$V_{AD}(R_{DA})\,|\psi_{A0}\rangle\,\langle\psi_{D0}|$ in Eq. (2.110) is the major term responsible for electron transfer from the donor to acceptor. The electron transfer probability can be calculated approximately with Eq. (2.68)

$$P_{ET} = |\,\langle\psi_{A0}|\,U_I(t,t_0)\,|\psi_{D0}\rangle\,|^2, \tag{2.111}$$

with the state evolution operator given by (according to Eq. (2.67))

$$U_I(t,t_0) = \left[\mathcal{T}e^{-i\int_{t0}^{t}\; U_0^\dagger\left[V_{AD}(R_{DA})|\psi_{A0}\rangle\langle\psi_{D0}|\right]U_0\; dt'}\right], \tag{2.112}$$

where $U_0 = e^{-i\mathcal{H}_0 t}$ is the stationary state evolution operator, such that $U_0\,|\psi_{D0}\rangle = e^{-iE_{D0}t}\,|\psi_{D0}\rangle$ and $U_0\,|\psi_{A0}\rangle = e^{-iE_{A0}t}\,|\psi_{A0}\rangle$.

Since the interstate coupling $V_{AD} = \frac{1}{2}\,\langle\psi_{A0}|\,(\mathcal{V}_A + \mathcal{V}_D)\,|\psi_{D0}\rangle$ is determined by the overlap of the exponential tail of the the two wave functions $|\psi_{A0}\rangle$ and $|\psi_{D0}\rangle$, it's expected to decrease exponentially with internulcear distance R_{DA}, i.e.,

$$V_{AD} \propto e^{-\alpha R_{DA}}, \tag{2.113}$$

with α being a constant. From Eqs. (2.111-2.113), the electron transfer probability P_{ET} also decreases rapidly with internulcear distance R_{DA}. This dependence is confirmed in the experimental observations to be discussed in subsection 5.4.1.

Landau-Zener model

Assuming the electon is initially at the state $|\psi_{D0}\rangle$, so the nuclei are moving on the potential energy curve $\mathcal{V}_{nuc,D0}(R_{DA})$ at the donor side. At the distance $R_{DA} = R^x_{DA}$, $\mathcal{V}_{nuc,D0}(R_{DA})$ has a crossing point with the acceptor-side potential energy curve $\mathcal{V}_{nuc,D0}(R_{DA})$, i.e., $\mathcal{V}_{nuc,D0}(R^x_{DA}) = \mathcal{V}_{nuc,A0}(R^x_{DA})$. At this crossing region when the two ground states $|\psi_{D0}\rangle$ and $|\psi_{A0}\rangle$ are almost degenerate, there is a relatively high probability for the electron to transfer from the donor side to the acceptor side, i.e., transiting from the state $|\psi_{D0}\rangle$ to $|\psi_{A0}\rangle$. This probability will be calculated with the Landau-Zener method[67, 68].

At the crossing region, the two potential energy curves can be approximated by their slopes at the crossing point. The electron transfer Hamiltonian in Eq. (2.110) at the crossing region becomes

$$\begin{aligned}\mathcal{H}_{ET} &= \left[\mathcal{K}_{nuc} + \mathcal{V}_{nuc,D0}(R^x_{DA}) - vtF^x_{D0}\right]|\psi_{D0}\rangle\langle\psi_{D0}| \\ &+ \left[\mathcal{K}_{nuc} + \mathcal{V}_{nuc,A0}(R^x_{DA}) - vtF^x_{A0}\right]|\psi_{A0}\rangle\langle\psi_{A0}| \\ &+ V_{DA}|\psi_{D0}\rangle\langle\psi_{A0}| + V_{AD}|\psi_{A0}\rangle\langle\psi_{D0}|, \end{aligned} \tag{2.114}$$

where t is time and $v = \frac{dR_{DA}}{dt}$ is the relative velocity of the donor and acceptor at the crossing point. F^x_{D0} and F^x_{A0} are the negative of the slope values at $R_{DA} = R^x_{DA}$ of the donor- and acceptor- side potential energy curves, respectively.

This Hamiltonian can be separated into the part which has $|\psi_{D0}\rangle$ and $|\psi_{A0}\rangle$ as the eigen states and the interaction part $\mathcal{V}_{int} = \big[-vtF^x_{D0}|\psi_{D0}\rangle\langle\psi_{D0}| - vtF^x_{A0}|\psi_{A0}\rangle\langle\psi_{A0}| + V_{DA}|\psi_{D0}\rangle\langle\psi_{A0}| + V_{AD}|\psi_{A0}\rangle\langle\psi_{D0}|\big]$ which is responsible for the charge transfer.

And the probability for the electron to transfer from the donor to acceptor can be calculated with Eq. (2.68):

$$\begin{aligned}P_{ET} &= |\langle\psi_{A0}|U(-\infty,\infty)|\psi_{D0}\rangle|^2 \\ &= 1 - |\langle\psi_{D0}|U(-\infty,\infty)|\psi_{D0}\rangle|^2, \end{aligned} \tag{2.115}$$

with $U(-\infty,\infty) = \left[\mathcal{T} e^{-i\int_{-\infty}^{\infty} U_0^{\dagger}\mathcal{V}_{int}(t')U_0\ dt'}\right]$ being the time evolution operator introduced in Eq. (2.67).

It can be shown (see e.g. [51]) that the result of Eq. (2.115) is

$$P_{ET} = 1 - e^{-\frac{2\pi}{v}\frac{|V_{DA}|^2}{|F_{D0} - F_{A0}|}}, \tag{2.116}$$

This model has been applied to calculating the charge transfer cross sections in ion and atom collisions [69, 70].

Classical "over-the-barrier" model

The classical "over-the-barrier" model [65, 66] is a simple but effective model initially proposed in 1980s for predicting the charge transfer cross sections in ion-atom collisions. In this model, the to-be-transferred electron is in the potential defined by its Coulomb interaction with the remaining part of the molecule:

$$V(r) = -\frac{p+1}{r} - \frac{q}{R_{DA}-r}, \tag{2.117}$$

where the donor and acceptor are assumed as point charges with initial charge number p and q, and r is the distance from the electron to the donor. The donor charge p is added by 1 in Eq. (2.117) to account for the addition of one charge by the to-be-transferred electron. $V(r)$ is composed of two coulomb potential wells centered at the donor and acceptor, with a potential barrier in between. At some distance $r = r_{max}$ within the barrier region, the barrier reaches a maximum. This distance can be found by setting the slope of the potential to be 0:

$$\frac{dV(r)}{dr}|_{r\,=\,r_{max}} = \frac{p+1}{r_{max}^2} - \frac{q}{(R-r_{max})^2} = 0. \tag{2.118}$$

From the above equation, $r_{max} = \frac{\sqrt{p+1}}{\sqrt{p+1}+\sqrt{q}}R$. By inserting $r = r_{max}$ into $V(r)$, the maximum value of the barrier is found:

$$V(r_{max}) = -\frac{p + 1 + q + 2\sqrt{q(p+1)}}{R}. \tag{2.119}$$

For the electron to be transferred from the donor to the acceptor, its initial kinetic energy at the donor $-E_{binding} - \frac{q}{R_{DA}}$ ($E_{binding}$ is the binding energy of the to-be-transferred electron in the donor, $-\frac{q}{R_{DA}}$ is added to account for the presence of the acceptor.) must be larger than the maximum of the barrier $V(r_{max})$, i.e.,

$$-E_{binding} - \frac{q}{R_{DA}} > -\frac{p + 1 + q + 2\sqrt{q(p+1)}}{R_{DA}}, \tag{2.120}$$

from which the critical distance $R_{DA,crit}$ beyond which charge transfer is classically forbidden can be determined:

$$R_{DA,crit} = \frac{p + 1 + 2\sqrt{q(p+1)}}{E_{binding}}. \tag{2.121}$$

This formula has recently been successfully applied to predicting the critical distances of charge transfer processes in the interaction between molecules and free-electron laser pulses [16, 17, 63, 71].

2.4.8 Dissociation and Coulomb explosion

With each photoabsorption and decay step, the molecule transits to a different electronic state, which corresponds to a different potential energy hypersurface for the nuclei to move upon. As an example, in Fig. 2.10 a diatomic molecule, initially in the ground state, is core-ionized. After Auger decay, the molecule becomes a dication populating a dissociative state. Along the dissociative potential energy curve, the two atomic parts of the molecular ion fly apart until they become isolated atomic ions. The energy accumulated by the two atomic parts during this dissociation process is the kinetic energy release, which can be measured

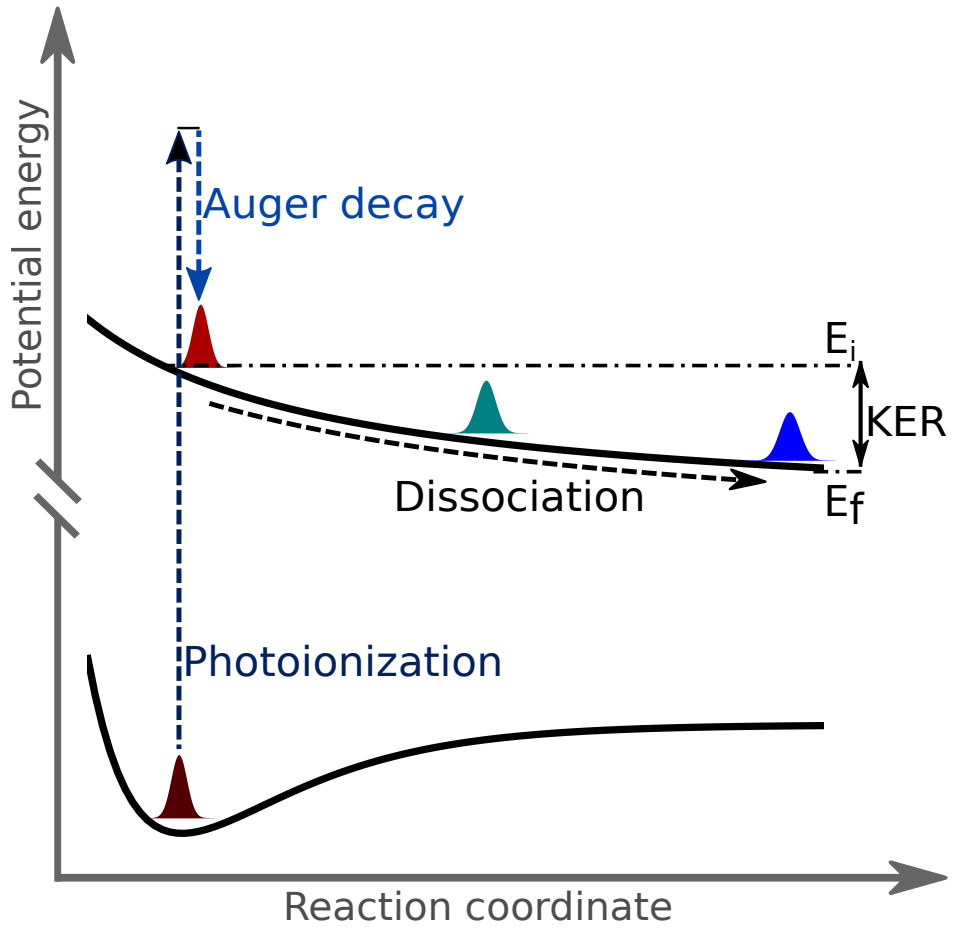

Figure 2.10: Illustration of Kinetic Energy Release from a core-ionized diatomic molecule. E_i is the initial potential when the molecule populates the dissociative state. E_f is the asymptotic potential of the dissociative state at infinitely large internuclear distances. Kinetic energy release is determined by $KER = E_i - E_f$. Strictly speaking, this is only the kinetic energy release gained from the dissociation after Auger decay. Some energy can also be gained or lost during or before the Auger decay process, but it's a much smaller contribution.

in the experiment.

With the ultra-intense XFEL pulses, a molecule can be heavily charged by the sequential photoionization and decay process within a very short time defined by either the ultrashort pulse duration or the ultrafast Auger decay life time (the longer of the two). So the molecule is charged up before the nuclei can have any significant movements, and the potential defined by the Coulomb repulsion between ion fragments becomes a good approximation to the real potential energy hypersurfaces the nuclei move upon. This is the reason why the momentum

distribution of final fragments reflects the initial molecular geometry, which is the underlying principle for the "Coulomb Explosion Imaging" method, as will be discussed in Chapter 6.

2.4.9 Ab initio model calculations of ultra-intense x-ray interaction with atoms and molecules

When an atom or a molecule is exposed to an ultra-intense XFEL pulse, every step of the sequential x-ray absorption and decay processes causes a change in the electronic configurations. Such changes among electronic configurations can be modeled with a set of rate equations [72], each of which describes the transition to a particular configuration from all other possible configurations. Such equations can be solved with a numerical integration procedure. For each integration over an infinitesimal time interval at a particular instant, given the x-ray photon flux and spin orbitals optimized for the relevant electronic configurations by the Hartree-Fock-Slater method, the rates of transitions through photoabsorption, emission and Auger decay can be calculated with the formulas derived in previous sections. With these calculated rates, the integration for that instant can be performed, which updates the population of the involved electronic configurations. This procedure is repeated many times until the x-ray pulse is gone and the electronic structure is stabilized via the decay processes.

For heavy atoms, billions of electronic configurations (and hence rate equations) can get involved during the interaction, making the rate-equation-solving approach become unrealistic with the current computing power. This problem can be solved with the Monte Carlo method [73]. During the simulation of each interaction trajectory, the transition from one configuration to the next is determined through the Monte Carlo approach based on the spin orbitals and transitions rates calculated on the fly. By repeating and averaging over many trajectory calculations, a converged solution can be found, which approaches the one from solving rate equations. Such methods have been implemented in x-ray ionization of both atoms [73, 74] and molecules [75, 76], and good matches with experimental data (see e.g. [5, 8, 43, 77]) were achieved.

Chapter 3

Experimental techniques

The experimental techniques for the study of molecular response to ultra-intense x-rays will be presented in this chapter. The ultra-intense x-ray pulses are produced by free-electron lasers. The generation and characterization of such pulses will be discussed in the first section. In a typical ion and electron momentum imaging experiment, the x-rays are focused by a pair of Kirkpatrick–Baez mirrors to the center of the imaging setup, where they interact with cold and localized atomic or molecular targets. The electron and ion fragments from the interaction are then guided by the electromagnetic filed of the spectrometer to the time- and position- sensitive detectors, allowing reconstruction of the 3D momenta of these interaction products, which in turn can reveal the information of atomic and molecular responses to ultra-intense x-rays. The supersonic gas jets, spectrometers and detectors, which are the key components of an imaging setup, will be discussed in the second section.

3.1 X-ray free-electron laser

The free-electron laser was proposed by John Madey [79] and demonstrated [80] by his group at Stanford in the 1970s. Through the resonant interaction between an ultrashort bunch of relativistic electrons and their radiation, a free-electron laser can produce an intense beam of electromagnetic radiation, which shares similar properties as those from conventional lasers

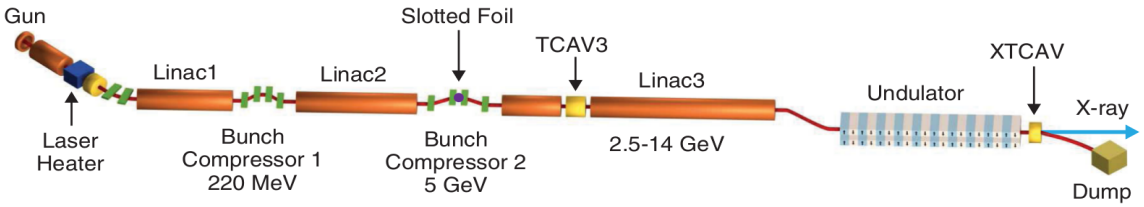

Figure 3.1: Layout of the Linac Coherent Light Source, the first x-ray free-electron laser. Adapted from [78]. Slotted foil can be used for ultrashort pulse generation. TCAV3 and XTCAV are setups for electron bunch characterizations. XTCAV will be discussed in subsection 3.1.2.

in terms of brightness, bandwidth and transverse coherence. Due to the lack of suitable x-ray optics, the x-ray free-electron laser has to achieve its gain without a cavity in which the beam can propagate back and forth until saturation. The gain is instead realized by sending high-brightness electron beam from the linear accelerators to a long undulator, in which the x-ray power grows exponentially in power by pumping energy from the electron beam through the so-called self-amplified sponteneous emission (SASE) process.

The layout of the first x-ray free-electron laser, the Linac Coherent Light Source, is illustrated in Fig. 3.1. The electron bunch (tens of pC to nC) is sent from the injector to 3 stages of linear accelerators (Linac) separated by two compressors, through which the bunch acquires a high peak current ($\geqslant 1kA$) with confined energy and angular spread. The accelerated electrons (with energy on the order of 10 GeV) are then guided to the undulator in which x-rays are produced through the free-electron laser interaction to be discussed in the following subsection.

3.1.1 Basics of operation

X-rays are produced in the undulator through the resonant interaction between electrons and their radiated x-rays. This interaction consists of three interdependent processes including electron energy modulation, microbunching and coherent x-ray emission.

Undulator radiation

In the periodic undulator magnetic field, an electron performs periodic motion under the Lorentz force, with the periodicity determined by the undulator period λ_U. In the far field (e.g. in the experimental hall), the light is the superposition of x-rays emitted by electrons at every point along their trajectories in the undulator. In analogy to light passing trough a diffraction grating, the superposition of the x-rays emitted by an electron at different locations in the undulator consists of only one major component, which is at the fundamental undulator frequency ω_r, due to the constructive interference, and the components at other frequencies are negligible due to the destructive interference.

The fundamental undulator frequency ω_r can be found by considering the relative longitudinal location of an electron and the wavefront of its radiation. After radiating light at some location in the undulator and traveling over one undulator period from that location, the electron lags behind the wavefront of its previous radiation by

$$\triangle \;=\; \frac{c\lambda_U}{v_z} \;-\; \lambda_U, \tag{3.1}$$

where the first and second terms are the distances traveled by the wavefront and electron, respectively. v_z is the electron longitudinal velocity. At the current location, the electron continues to emit light. Constructive interference between currently and previously emitted light occurs if the wavelength λ_r equals $\triangle$, i.e.,

$$\lambda_r \;=\; \frac{c\lambda_U}{v_z} \;-\; \lambda_U, \tag{3.2}$$

which corresponds to the fundamental undulator frequency $\omega_r \;=\; \frac{2\pi c}{\lambda_r}$.

From the relativistic energy-momentum relation

$$E_{ele}^2 \;=\; (pc)^2 \;+\; (mc^2)^2 \tag{3.3}$$

(m is the electron rest mass, $p \;=\; \gamma m\sqrt{v_z^2 \;+\; v_\perp^2}$ is the magnitude of the electron momentum,

$\gamma = \frac{1}{\sqrt{1-\frac{v^2}{c^2}}}$ is the Lorentz factor with v being the electron velocity, and $v_\perp$ is the electron transverse velocity), the longitudinal velocity is given by

$$v_z = c\sqrt{1 - \frac{1}{\gamma^2} - \frac{v_\perp^2}{c^2}}. \tag{3.4}$$

With the equation above and the relation

$$\frac{1}{\gamma^2} - \frac{v_\perp^2}{c^2} = 1 - \frac{v^2 + v_\perp^2}{c^2} \ll 1, \tag{3.5}$$

$\frac{c}{v_z} \approx 1 + \frac{1}{2\gamma^2} + \frac{v_\perp^2}{2c^2}$ and the fundamental undulator wavelength in Eq. 3.2 can be approximated as

$$\lambda_r = \frac{c\lambda_U}{v_z} - \lambda_U \approx \lambda_U(1 + \frac{1}{2\gamma^2} + \frac{v_\perp^2}{2c^2}) - \lambda_U = \lambda_U(\frac{1}{2\gamma^2} + \frac{v_\perp^2}{2c^2}). \tag{3.6}$$

For planar undulator, the transverse velocity is given by (see e.g. [81] for a derivation)

$$v_\perp = \frac{cKcos(\frac{2\pi z}{\lambda_U})}{\gamma}, \tag{3.7}$$

where $K = \frac{2\pi eB_0}{mc^2\lambda_U}$ is the undulator parameter, with B_0 being the magnetic field on axis.

By inserting $v_\perp$ into Eq. (3.6) and taking the average over one undulator period, the fundamental undulator wavelength for a planar undulator is obtained

$$\lambda_r = \lambda_U \frac{1 + \frac{K^2}{2}}{2\gamma^2}. \tag{3.8}$$

From Eq. (3.8), the photon energy $E_r = \hbar\frac{2\pi c}{\lambda_r}$ is proportional to the squared electron energy $E_{ele}^2 = (\gamma mc^2)^2$, and hence the squared electron beam energy E_{ebeam}^2, i.e., $E_r = aE_{ebeam}^2$. This relation can be used in the calibration of photon energy. For a typical calibration in atomic and molecular experiments, a set of runs with different electron beam energy settings is carried out, with a corresponding photon energy measured (e.g. by mea-

suring the photoelectron energy) for each setting. The calibration can then be performed by finding the proportionality constant a through a linear fitting of these (E_r, E^2_{ebeam}) data points.

Energy modulation, electron microbunching and coherent x-ray emission

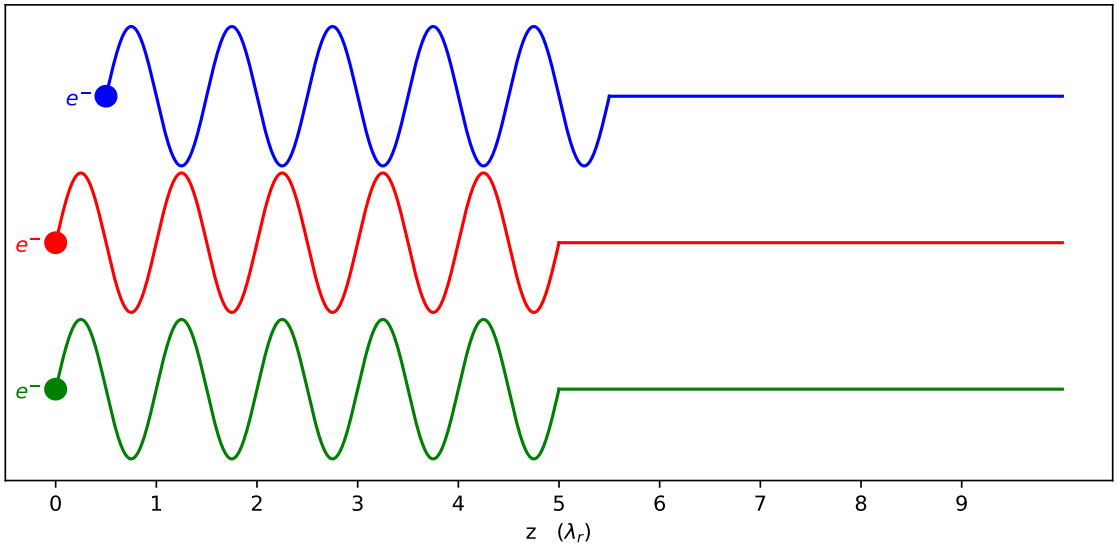

Figure 3.2: Wave trains radiated by 3 electrons from an undulator with 5 periods. The wave trains in red and green are in phase, which are out of phase with the one in blue due to the electron location difference in $\boldsymbol{z}$.

For each undulator period traveled by the electron, the wavefront of its emitted light slips ahead by one wavelength λ_r. At the exit of the undulator with N_u periods, the emitted light becomes a wave train with N_u cycles, as shown in Fig. 3.2 where wave trains of 5 cycles, emitted by 3 representative electrons after exiting an undulator with 5 periods, are plotted. $N_u\lambda_r$, which is the total length the wavefront slips ahead of the corresponding electron at the undulator exit, is called the slippage length. Such wave train is emitted by every electron in the bunch. With the electron bunch length typically larger than the x-ray wavelength and electrons randomly distributed within the bunch, the emitted wave trains also have a random phase relation among each other, resulting in the total radiation intensity I_{total} only proportional to the number N_{ele} of electrons in the bunch, i.e., $I_{total} = N_{ele}I_{ele}$, with I_{ele} being the radiation intensity from a single electron. This is the case for the synchrotron

radiation. As one key difference between free-electron lasers and synchrotrons, the electrons in free-electron lasers are spatially arranged within the bunch in such a way that they radiate in phase between each other, resulting in the total radiation intensity approaching the limit $I_{total} = N_{ele}^2 I_{ele}$. It is a huge gain from $I_{total} = N_{ele} I_{ele}$ of incoherent emission to $I_{total} = N_{ele}^2 I_{ele}$ of coherent emission, given that the typical number of electrons in a bunch of an XFEL is on the order of 10^7.

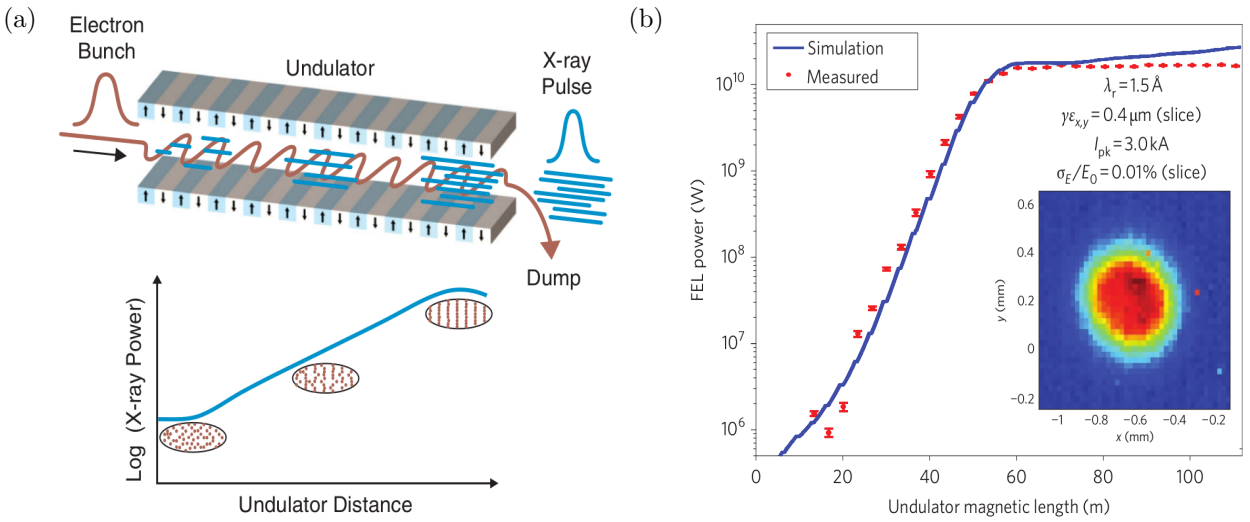

Figure 3.3: (a) Top figure is an illustration of the x-ray generation from an electron bunch traveling in an undulator. Bottom figure shows the corresponding x-ray power exponential growth as a function of undulator distance, accompanied with more and more microbunching. Adapted from [78]. (b) Free-electron laser power as a function of undulator length, measured at the first lasing of the LCLS. The gain length was determined to be 3.5 m. Adapted from [82].

The spatial arrangement for the electrons to radiate in phase is achieved through the resonant interaction between electrons and their radiation. The electric field is in the transverse direction and along the electron wiggling direction. At some instant in the undulator, some electrons have wiggling directions parallel to the electric field and lose energy (γ is smaller), while other electrons have wiggling directions anti-parallel to the electric field and gain energy (γ is larger). The energy of electrons are modulated on the scale of the wavelength λ_r.

From Eqs. (3.4) and (3.5), the longitudinal velocity is given by

$$v_z \approx c(1 - \frac{1}{2\gamma^2} - \frac{v_\perp^2}{2c^2}) = c(1 - \frac{1 + \frac{K^2}{2}}{2\gamma^2}). \tag{3.9}$$

From the equation above, the longitudinal velocity gets larger with larger γ, which can happen when an electron gains energy in the transverse direction. With the electrons gaining energy traveling faster in the longitudinal direction and those losing energy slower, higher-energy electrons catch up to lower-energy electrons, leading to the formation of microbunches of electrons at multiples of the wavelength λ_r. The michrobunched electrons start to radiate in phase, producing light with larger intensity. The more intense light then causes more energy modulation of electrons and more microbunching, which in turn results in even more intense light being radiated. Such emission process is called the self-amplified spontaneous emission. As illustrated in Fig. 3.3a, this resonant interaction leads to an exponential growth of the x-ray power, which is accompanied by more and more microbunching, with the peak power [78] given by

$$P(z) \propto e^{\frac{z}{L_g}}, \tag{3.10}$$

where $L_g \approx \frac{\lambda_U}{4\pi\sqrt{3}\rho}$. $\rho = \left[\frac{1}{64\pi^2}\frac{I_p}{I_A}\frac{K^2[J_0(\xi) - J_1(xi)]^2\lambda_U^2}{\gamma^3\sigma_x^2}\right]^{\frac{1}{3}}$ is the FEL Pierce parameter [78, 83], I_p is the electron peak current, $I_A \approx 17kA$ is the Alfvén current, $J_0(\xi)$ and $J_1(\xi)$ are the Bessel functions of orders zero and one, with $\xi = \frac{K^2}{4 + 2K^2}$ for a planar undulator, and σ_x is the rms transverse size of the electron beam. The peak power at saturation is approximately given by $P_{saturation} = \frac{\rho\gamma mc^2 I_p}{e}$ [78]. With the FEL Pierce parameter on the order of 10^{-3}, typical electron energy γmc^2 about 10 GeV, typical peak current I_p around 3 kA, the saturation peak power $P_{saturation}$ is on the order of 30 GW. With the typical focal spot area $\sim$ 1 μm^2, this gives an peak intensity of 3×10^{18} W/cm^2. Fig. 3.3, which is obtained during the start-up operation of the Linac Coherent Light Source [82], shows the exponential x-ray power growth with the undulator length, and the transverse beam profile imaged by an intercepting yttrium aluminum garnet (YAG) screen.

SASE and seeded operations

The FEL interaction can either starts with the radiation from first few undulator sections, with the exponential x-ray power growth happening in the remaining undulator sections, or with an externally seeded radiation right from the beginning of the undulator. A FEL with the former operation mode is called a SASE FEL, and the latter seeded FEL. For SASE FELs, due to the interaction start-up from spontaneous emission of electron beam shot noise, the produced x-rays have limited temporal coherence. With the electron bunch length longer than the radiation coherence length $L_{coh} \approx \frac{\lambda_r}{2\sqrt{\pi}\rho}$, a typical x-ray pulse consists of tens to hundreds of coherent spikes ($\sim 1\ fs$) with no fixed phase relation with one and another [78]. These independent coherent spikes are sources of x-ray intensity fluctuations.

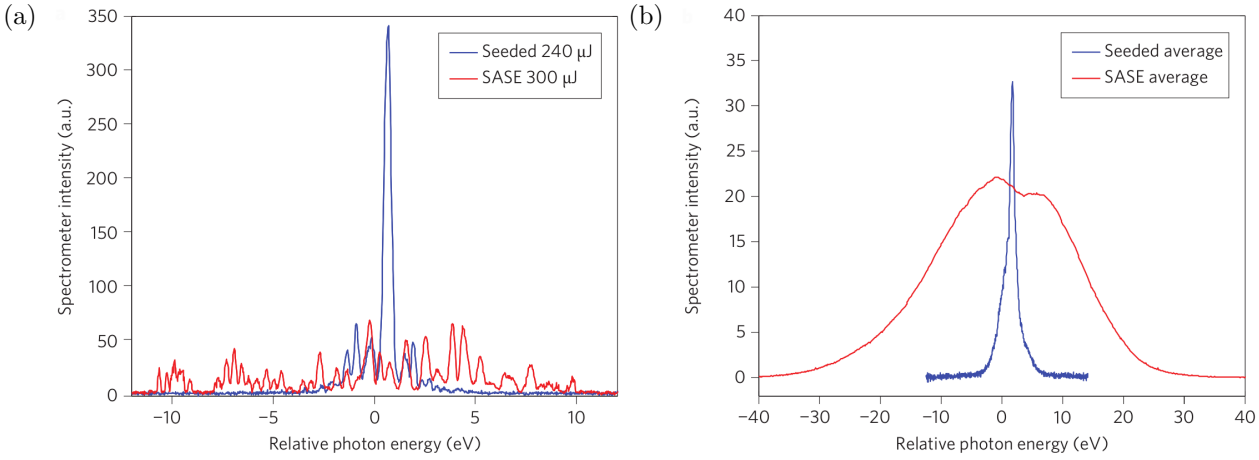

Figure 3.4: Comparison of measured SASE and seeded x-ray (photon energy 8.3 keV) spectra. Adapted from [84]. (a) Single-shot spectra. (b) Averaged spectra. For the single-shot spectra, the SASE FWHM bandwidth is $\sim 20\ eV$, whereas the seeded bandwidth is $\sim 0.4\ eV$.

The temporal coherence can be improved with a seeded FEL. Even if external seeding is possible for x-ray free electron lasers through techniques such as high-gain harmonics generation [85] and echo-enabled harmonic generation [86], it is still difficult because of the lack of appropriate external x-ray sources. To circumvent this issue, the self-seeding scheme [84, 87, 88] is implemented at the LCLS, in which x-rays from the first half of the undulator, after passing through a diamond-based monochromator, serve as the seed for the FEL interaction in the second half of the undulator. Through self-seeding, production

of near Fourier-transform-limited x-ray pulses at angstrom wavelengths was demonstrated, with a relative bandwidth reduction of a factor of 40-50 with respect to SASE operation, as shown in Fig. 3.4.

Recent developments

Over the last decade, new FEL capabilities have become available. They include, for example, x-rays with the circular polarization [89], two-color x-rays [90, 91] for x-ray-pump and x-ray-probe experiments and ultrashort x-ray pulse generation ($\sim 5\ fs$) through the low-charge mode operation [92] or the use of emittance-spoiling slotted foil [93]. And very recently, the lower limit of ultrashort XFEL pulse was pushed down to hundreds of attoseconds, through single-spike pulse generation with nonlinear bunch compression in the hard x-ray range [94], and through the enhanced self-amplified spontaneous emission (ESASE) scheme [95–97] in the soft x-ray range.

Currently available x-ray pulse parameters can be found in [98] for the LCLS with different operation modes, and [99, 100] for the EuXFEL.

3.1.2 Pulse characterization

X-ray pulse parameters are required for both performing the experiment and interpreting the experimental data. For the experiments in this thesis, the key parameters are photon energy, pulse energy, pulse length and pulse intensity in the interaction region. As discussed in 3.1.1, the photon energy E_r can be calculated from electron beam energy E_{ebeam}^2 through the relation $E_r = aE_{ebeam}^2$, with the proportionality constant a defined by the undulator parameters and able to be determined through calibration procedures, e.g. by electron beam energy scan in photoionization measurements. The pulse energy can be measured shot-by-shot with gas monitor detectors, based on the near-ultraviolet luminescence of x-ray-irradiated N_2 molecules [101].

The average x-ray pulse length has been shown to be about 70% of the electron bunch length [102–104]. Shot-by-shot x-ray pulse profile can be retrieved through techniques which

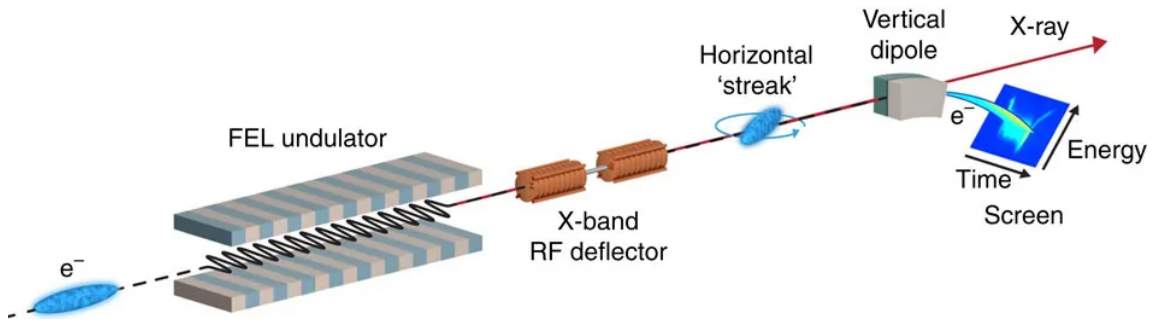

Figure 3.5: Layout of the XTCAV setup for characterizing x-ray pulse power profiles at the LCLS. Adapted from [102].

either measure the electron bunch phase (time-energy) space distribution [102, 105] or directly apply the streaking method [106–109] to the x-ray pulse. The former technique has been implemented at the LCLS as the XTCAV [102, 110] (X-band Transverse deflecting mode CAVity) setup in Fig. 3.5, which is located downstream of the FEL undulator (hence non-invasive) and provides the LCLS experiments with shot-by-shot electron phase space distributions used for reconstruction of x-ray pulse power profiles. After exiting the undulator, the electron bunch is sent to the X-band RF (Radio-Frequency) Deflector which generates horizontally polarized electromagnetic waves at 11.4 GHz. The electron bunch (thousands of times shorter than the RF wavelength) arrival time is set so that its center overlaps with the RF wave's zero-crossing point, with its electrons traveling before and behind the center experiencing opposite electromagnetic forces which are approximately linearly proportional to the electron displacement relative to the bunch center. Under such forces, the front- and back-end electrons are deflected horizontally to opposite directions, with the deflection amount linearly proportional to the electron's original distance to the bunch center, which maps electron distribution along the longitudinal (time) axis to the horizontal direction. The horizontally deflected electron bunch is then sent through a static bending magnet. The Lorenz force bend vertically the high-energy electron trajectories less than those of low-energy ones, effectively mapping the electron energy distribution to the vertical axis. The electron phase space distribution as the result of the horizontal (time) and vertical (energy) deflections is then imaged by a fluorescent screen. From the phase space image, the average energy of electrons $< E(t) >$, electron beam current $I(t)$ and rms slice energy spread $\sigma_E(t)$

can be directly obtained.

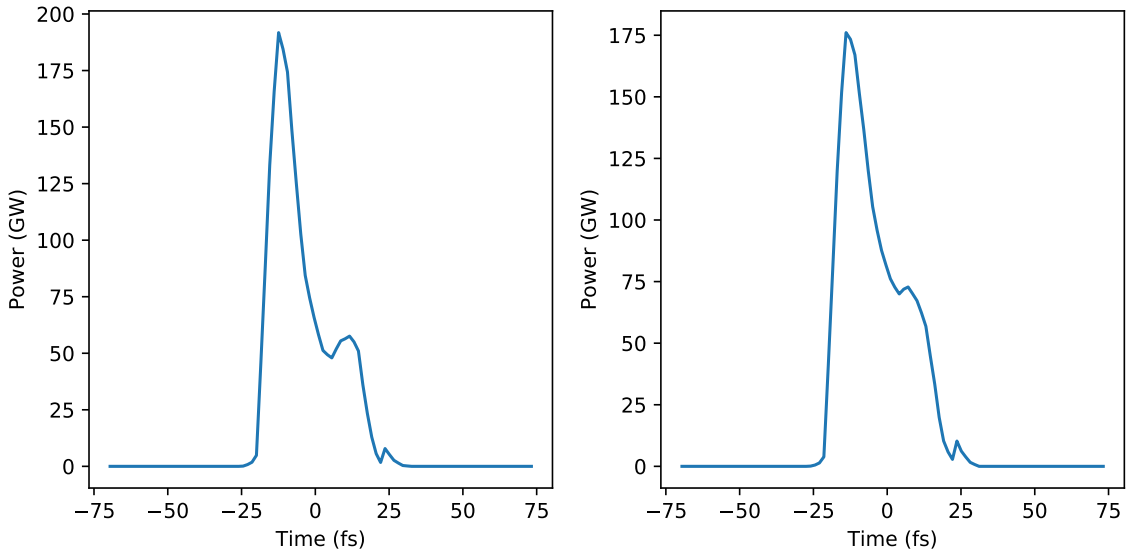

Figure 3.6: Two representative 8.3 keV x-ray pulse power profiles measured at the LCLS.

For a successful x-ray pulse characterization using XTCAV, a dark run with no electrons being imaged, a lasing-off run with electrons being imaged and a lasing-on (when taking experimental data) run are required. The dark run is for getting the camera's backgroud image pixel values, which will be subtracted from both the lasing-off and -on electron images. From energy conservation, the electron energy loss with lasing on, which can be obtained by comparing lasing-on electron image with that of lasing-off, correspond to the energy of the x-ray pulse. The x-ray pulse power profile can be calculated by

$$P(t) \;=\; [< E_{FEL\ off}(t) > \;-\; < E_{FEL\ on}(t) >] \;\times\; I(t), \tag{3.11}$$

where $< E_{FEL\ off}(t) >$ and $< E_{FEL\ on}(t) >$ are respectively the average energy of electrons when lasing is on and off. From FEL thoery [111], the x-ray power can also be calculated from the energy spread $\sigma_E(t)$ with

$$P(t) \;=\; [\sigma^2_{E,FEL\ on}(t) \;-\; \sigma^2_{E,FEL\ off}(t)] \;\times\; I^{2/3}(t), \tag{3.12}$$

with "$FEL\ on$" and "$FEL\ off$" again representing lasing on and off.

Two typical 8.3 keV x-ray pulse power profiles reconstructed with this method are shown in Fig. 3.6. Note that the generally expected spikes within the SASE pulse are not resolved. This can be attributed to the fact that the displayed x-ray pulses are obtained after FEL saturation and the XTCAV method's resolving power is downgraded for pulses after saturation than before saturation[110]. But the reconstructed pulse profiles can still represent the pulse envelopes.

Given the pulse energy and duration measurement, in order to get the pulse intensity or photon flux in the interaction region, the photon density distribution in the focal volume is still needed. It can be obtained by first assuming a distribution function with adjustable parameters, and then finding these parameters by fitting the experimental charge state distribution of atomic ions. For a characterization of photon density distribution with such method, see e.g. [112].

3.2 Ion and electron momentum imaging setup

The reconstruction of ion and electron momentum gained from the interaction is an initial value problem, which requires the initial particle velocity to be solved given its afterwards trajectory in an electromagnetic field. Several challenges exist in setting up this problem in an experiment:

(1) Thermal velocity. Molecules have thermal velocity which contributes to the initial momentum. To make the initial momentum as close in value as possible to the momentum gained from interaction, the molecules have to be cooled down such that the thermal velocity is negligibly small. This can be achieved by employing a supersonic gas jet as the target.

(2) Initial location. The interaction region in a photoionization experiment is defined by the intersection between the laser beam in the Raleigh range and the target distribution. Due to the finite interaction region, there is, instead of a single location, a variety of initial particle locations, which can degrade the accuracy of the calculated initial momenta. This problem can be solved by making the target very well confined with a supersonic gas jet, tightly focusing of the laser beam, or controlling the charged particle trajectory by electric

field in such a way that in the detection region the particle location becomes independent of its initial position.

(3) Control over ion and electron trajectories. Particle trajectories have to be controlled so that particles can arrive at detectors, and in the meantime should make the initial value problem feasible to be solved. Various electomagnetic field configurations can be applied to implement such control, with the use of ion and electron spectrometers.

(4) Trajectory measurement. The particle trajectory can be measured by the detectors which record the particle time of arrival and hit position on the detector. More than one types of detectors can be used for such purpose.

3.2.1 Supersonic gas jet

The supersonic gas jet device includes a nozzle (with diameter $d \sim 10\ \mu m$), which is followed in the gas flow direction by skimmers and apertures or slits, with differential pumping stages reducing the gas load along the flow path until the gas reaches the interaction chamber, after which the gas is dumped through the catcher chamber. With the nozzle connected at one side to a gas bottle with typical pressure ranging from one to several tens of bars, and at the other side with pressure orders of magnitude lower, the high-pressure gas expands through the nozzle to the low-pressure region, reaching a gas flow speed larger than that of sound, hence the name supersonic gas jet. The process can be modeled by an adiabatic expansion of ideal gas. By such expansion, the gas enthalpy consisting of compression and internal energies is converted to directional kinetic energy:

$$k_B T_0 \ + \frac{f k_B T_0}{2} \ = \frac{1}{2} m V_{jet}^2, \tag{3.13}$$

where k_B is Bolzmann constant ,T_0 is the initial gas temperature before the expansion, m is the mass of the atom or molecule and f is its number of degrees of freedom. The jet velocity

V_{jet} is therefore

$$V_{jet} = \sqrt{\frac{(2+f)k_B T_0}{m}} = \sqrt{\frac{2k_B}{m}\frac{\gamma}{\gamma - 1}T_0}, \tag{3.14}$$

where $\gamma = 1 + \frac{2}{f}$ is the heat capacity ratio. This jet velocity is achieved in the ideal case if after expansion the gas temperature T is zero. In reality, T is nonzero and its achievable value is determined by the ratio S between the jet speed V_{jet} and the speed $V_{thermal} = \sqrt{\frac{2k_B T}{m}}$ due to thermal motion,

$$S = \frac{V_{jet}}{V_{thermal}} = \sqrt{\frac{\gamma}{\gamma - 1}\frac{T_0}{T}}, \tag{3.15}$$

which in turn depends on the nozzle diameter d, initial temperature T_0 and the pressure P_0 before expansion [113]. Given the speed ratio S and the initial temperature T_0 ,the jet temperature can be calculated as

$$T = \frac{\gamma}{\gamma - 1}\frac{T_0}{S^2}. \tag{3.16}$$

Since the pressure in the region beyond the nozzle is not zero, the expansion further away from the nozzle is less free due to larger influence of the residual gas. Because the inner part of the jet close to the nozzle is not affected by the residual gas and hence experiences a free expansion, it has a cooler temperature and can be picked out by a skimmer mounted after the nozzle at a distance before the free expansion breaks down. Downstream along the gas flow, more skimmers, apertures and slits can be mounted, to both collimate the beam and keep only its cooler inner part. At the interaction region, a gas jet, with temperature as low as tens of mK, diameter about 1 mm, and taget density typically in the range of $10^9 - 10^{11}$ $particles/cm^3$, can be achieved.

In addition to the supersonic gas jet, there are other methods for target preparation, such as effusive gas jet, which is of much higher temperature, but has a higher target density suited for interaction with weak light pulses, and magneto-optical traps [114, 115] which can

cool the targets down to a even lower temperature ($\sim 100\ \mu K$) than the supersonic gas jet.

3.2.2 Spectrometer

Electromagnetic field generated by a spectrometer is needed in order to guide the particles in a predictable fashion towards the detector. Different field configurations have been implemented and can be chosen according to particle species and the experimental requirements such as acceptance and resolution. Two most popular ones are the homogeneous field and velocity map imaging configurations.

Homogeneous field configuration

Homogeneous field configuration is the one commonly used in the so-called REMI (reaction microscope) or COLTRIMS (COLd Target Recoil Ion Momentum Spectroscopy) setup [116, 117] as sketched in Fig. 3.7. These instruments can be used for the so-called kinematically complete measurements of the reaction products. In a typical COLTRIMS setup, the spectrometer consists of a series of equally spaced ring-shaped electrodes, with each electrode connected with its neighbors by resistors of the same resistance. By applying a higher voltage to the electrode at one end of the spectrometer and lower voltage to the electrode at the other, there is a constant voltage drop with distance from the higher to the lower voltage end, and a homogeneous electric field is thus created.

In some spectrometers, this homogeneous region is followed by a field-free drift region. With the combination of the two regions, the "time focusing" condition can be fulfilled such that particles of the same species, with the same initial velocity but different initial locations along the spectrometer axis, are guaranteed to have the same flight time.

The voltage and spectrometer length settings can be adjusted so that all the reaction products are detected both with the 4π angle acceptance and optimal resolution. In general, faster fragments can be detected by increasing the voltage or shortening the spectrometer length, but at the sacrifice of worsening the resolution.

Ions are the electric field to the detector at one end of the detector. Electrons can be

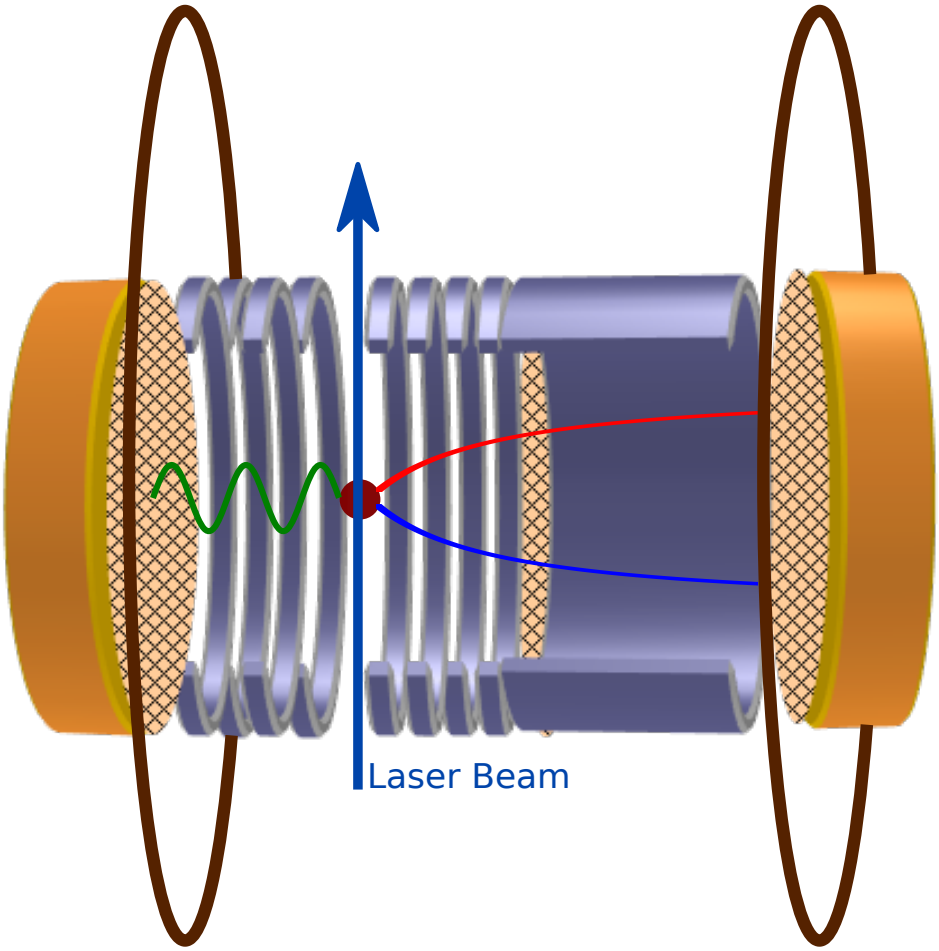

Figure 3.7: Sketch of a COLTRIMS setup, with ion (red and blue trajectories) and electron (green helical trajectory) fragments guided by a homogeneous electric field generated by the spectrometer. A pair of Helmholtz coils (dark brown) is used to produce a homogeneous magnetic field along the spectrometer axis and increase the detector acceptance of electrons by bending their motions with the Lorentz force.

directed to the detector at the other end, with the same electric field as the one for ions. But due to the much smaller electron mass and hence larger initial velocity, the 4π angle collection efficiency is hard to be achieved solely by the electric field. To circumvent this issue, a homogeneous magnetic field generated by a pair of Helmholtz coils and with direction parallel to the existing electric field can be added. This magnetic field, together with the electric field, forces the electron into a spiral motion towards the detector. So those electrons, which have high speed perpendicular to the spectrometer axis and would otherwise not be detected just with the electric field, can now be confined by the magnetic field within a

cylinder with radius smaller than that of the detector and are guaranteed to arrive at the detector. Because radius of the spiral motion is proportional to the velocity perpendicular to the spectrometer axis and inversely proportional to the magnetic field strength, acceptance of higher-energy electrons can be improved by increasing the magnetic field strength.

The initial momentum of particles flying in such configuration can be easily reconstructed by solving the equation of motion according to Newton's second law, as will be discussed in section 4.5.1.

Velocity map imaging configuration

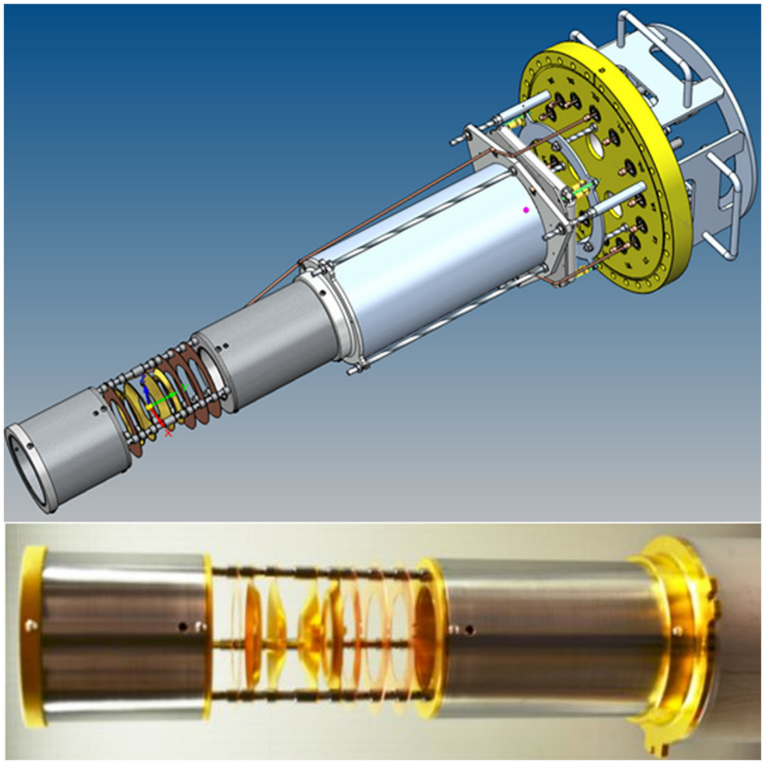

Figure 3.8: Double-sided velocity map imaging spectrometer in the AMO hutch of the LCLS. Adapted from [118].

In contrast to the homogeneous field configuration, in the velocity map imaging (VMI) configuration as typically used in a double-sided VMI spectrometer shown in Fig. 3.8, the electric field acts as a "lens", which guides the particles with the same initial velocity originating from different positions of the interaction region to the same spot on the detector.

So each point on the detector image corresponds to particles with a certain initial velocity, explaining the name "velocity map imaging".

The original design [119] of velocity map imaging spectrometer consists of a repeller, an open extractor and a ground electrode. With later designs (see e.g. [118, 120]), more electrodes are added to achieve better focusing performance. And to detect ion and electrons in coincidence, the spectrometers become double sided, with the ion repeller working at the same time as electron extractor and vice versa.

The voltage settings can be optimized such that the fragments with zero kinetic energy (such as parent ions) are focused to a detector spot as tiny as possible. This optimization can be performed either with SIMION [121] simulation or in a real experiment by looking at detector images. For example, with the original design, by setting the extractor voltage to be 70% of the repeller voltage, the ions are focused to a dot with diameter only limited by the detection system.

When VMI configuration is used, it's important to keep at least one symmetry axis of the interaction in the detector plane, to allow for the 3D momentum reconstruction from the 2D velocity map with Abel inversion or deconvolution procedures (see subsection 4.5.2).

If the arrival time and position are recorded separately for each particle, the momentum can also be calculated for each individual particle with an empirical formula (see subsection 4.5.2) which can be constructed with the help of SIMION simulations.

Discussion

While spectrometers are in general designed to produce either a homogeneous field or a VMI configuration, both configurations can be formed with appropriate voltage settings by a single spectrometer as long as it has enough number of properly positioned electrodes [118]. The electric field of the homogeneous field configuration typically ranges from a few volts to hundreds of volts per centimeter, whereas it's up to thousands of volts per centimeter for the VMI configuration. With the much higher electric field strength of the VMI configuration, electrons can be projected to the detector without the confinement of magnetic field. But

due to the much higher field strength, the ion flight time resolution is worse.

3.2.3 Ion and electron detectors

Detectors are needed to record the particle arrival times and positions at the detector plane. Microchannel plate with delay line anode and microchannel plate with phosphor screen are two types of such detectors, with each more applicable than the other depending on the experimental conditions.

Microchannel palte

The microchannel plate (MCP) (see e.g. [122]) contains, in a "honeycomb" structure, millions of micron-diameter glass capillaries (channels), each of which acts as an independent secondary electron multiplier. Upon particle impact on the channel wall, electrons are emitted. They are then accelerated by the static electric field (generated by the voltage applied on the front and rear sides of the MCP) until hitting the channel wall and resulting in more secondary electrons emitted. This impact-emission-acceleration process is repeated in a cascade fashion many times before thousands of electrons emerge from the rear side of that channel. To avoid particles passing through channels without hitting the wall, channels are arranged in a bias angle (10 degrees) with respect to the axis perpendicular to the plate surface. Higher amplification can be achieved by stacking two or more plates together with their channel axis in a zig-zag arrangement.

The MCP-amplified signal contains the time and position information of the incident particle. A single metal anode can be used to read out the arrival time signal, which is then amplified by an amplifier before being sent to the constant fraction discriminator to be discussed in section 4.1. The position information can be obtained by adding to the back of MCP, either a delay line anode or a phosphor screen coupled with a camera. These two types of detectors will be discussed in the next two subsections.

Microchannel plate detector with delay-line anode

A delay-line anode consists of two or three wires wound helically around an insulator holder, with each wire having a different winding direction. Every wire is accompanied by a parallel reference wire and the signals from both wires are sent to a differential amplifier for noise cancellation and signal amplification. Higher (20-50V) voltage is applied to signal wires than their reference partners to ensure it's mainly the signal wires collecting the electron cloud from the MCP. The picked-up electron cloud signal then propagates along the wire. Its arrival times t_1 and t_2 at the two ends of the wire are recorded, and the position information is encoded in the difference of these two arrival times.

With the distance D_{1mm} (mm) along which the signal needs to travel in the wire to achieve a 1mm movement in the wire helical propagation direction and the signal group velocity V_{group} (close to the speed of the light), the incident particle hit position along this wire helical propagation direction is given by

$$Pos = \frac{V_{group}}{2D_{1mm}}(t_1 \ - \ t_2) \ + \ O, \tag{3.17}$$

where O is an arbitrary offset.

QUAD delay-line anode has two signal wires propagating along two perpendicular directions x and y. The incident particle hit position (X_{Pos}, Y_{Pos}) is obtained by

$$\begin{cases} X_{Pos} \ = \ \dfrac{V^x_{group}}{2D^x_{1mm}}(t^x_1 \ - \ t^x_2) \ + \ O_x & (3.18) \\ Y_{Pos} \ = \ \dfrac{V^y_{group}}{2D^y_{1mm}}(t^y_1 \ - \ t^y_2) \ + \ O_y, & (3.19) \end{cases}$$

where V^i_{group}, D^i_{1mm}, t^i_1, t^i_2 and O_i, with i being x or y, have the same meaning as the corresponding variables in Eq. (3.17), except they are now for a particular direction specified by i.

HEX delay-line anode has three signal wires with their propagation directions u, v and$w$ oriented 60 degrees between one and another in a plane as shown in Fig. 3.9. The particle

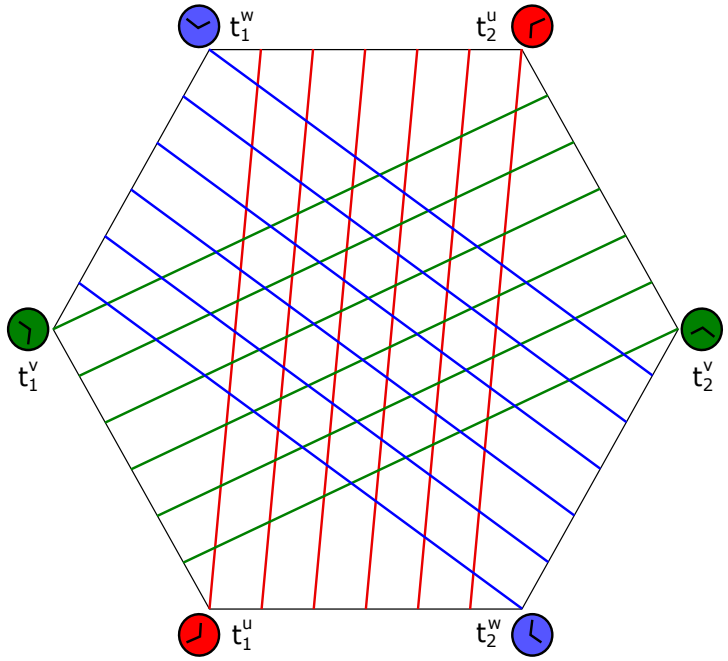

Figure 3.9: A sketch of the delay lines in a HEX delay-line detector.

hit position along each direction can be similarly calculated by

$$\begin{cases} U_{Pos} = \dfrac{V^u_{group}}{2D^u_{1mm}}(t^u_1 - t^u_2) + O_u & (3.20) \\ V_{Pos} = \dfrac{V^v_{group}}{2D^v_{1mm}}(t^v_1 - t^v_2) + O_v & (3.21) \\ W_{Pos} = \dfrac{V^w_{group}}{2D^w_{1mm}}(t^w_1 - t^w_2) + O_w, & (3.22) \end{cases}$$

with the variables having the same meanings as the corresponding ones in Eq. (3.20), except that they are now for a particular direction specified in the super- or subscript by u, v or w.

From the geometrical relations between the directions u, v, w and x,y, the particle hit position in (X_{Pos}, Y_{Pos}) can be expressed as a linear combination of the positions along any two of the u, v and w directions:

$$\begin{cases} X^{uv}_{Pos} = U_{Pos} + O^{uv}_x & (3.23) \\ Y^{uv}_{Pos} = \dfrac{U_{Pos} - 2V_{Pos}}{\sqrt{3}} + O^{uv}_y, & (3.24) \end{cases}$$

$$\begin{cases} X_{Pos}^{uw} = U_{Pos} + O_x^{uw} & (3.25) \\ Y_{Pos}^{uw} = \dfrac{2W_{Pos} - U_{Pos}}{\sqrt{3}} + O_y^{uw}, & (3.26) \end{cases}$$

or

$$\begin{cases} X_{Pos}^{vw} = V_{Pos} + W_{Pos} + O_x^{vw} & (3.27) \\ Y_{Pos}^{vw} = \dfrac{W_{Pos} - V_{Pos}}{\sqrt{3}} + O_y^{vw}, & (3.28) \end{cases}$$

with O_i^{jk} being arbitrary offsets for hit position along i direction determined by the positions along j and k directions.

Microchannel plate detector with phosphor screen

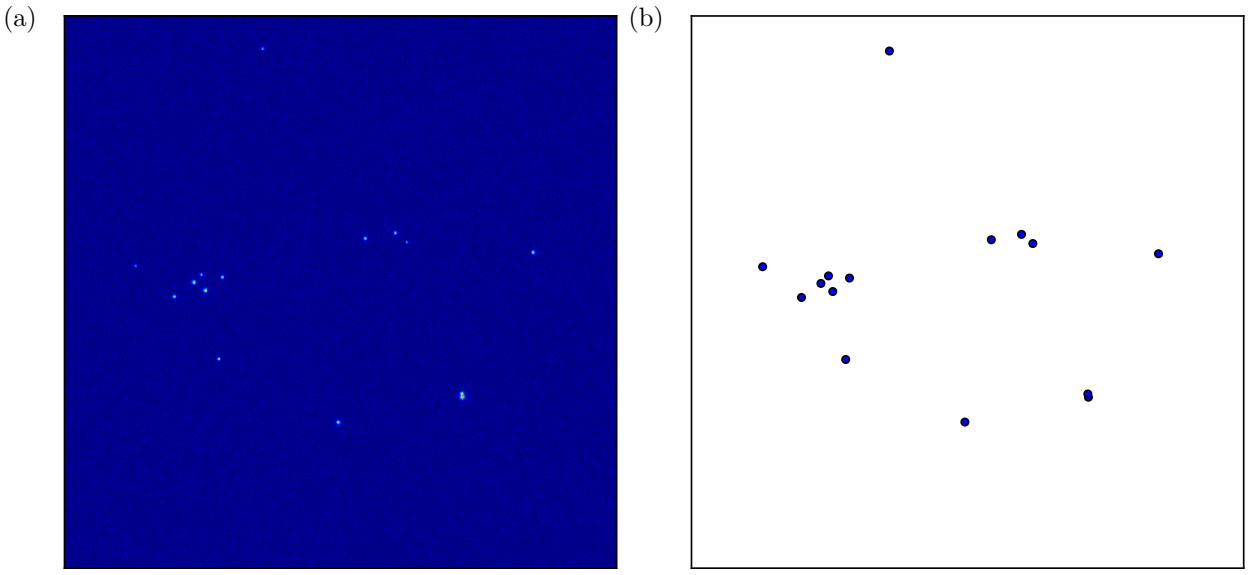

Figure 3.10: (a)Phosphor screen image of electron hits taken by a CCD for a single interaction event. (b) Electron hits identified by a peak-finding algorithm.

When the electron cloud emerged from the MCP back hits the phosphor screen, photons are emitted from the impact position and can be captured by a charge-coupled device (CCD) camera, through which the particle hit positions on the MCP can be recorded. Fig. 3.10a is the phosphor screen image taken by a CCD for a single interaction event, with the electron hits displayed as the bright spots in the blue background. These electron hits picked out with peak-finding algorithms (see e.g. [123]) are shown in Fig. 3.10b.

Discussion

Microchannel plate detector with delay-line anode is commonly used in COLTRIMIS setups, and microchannel plate detector with phosphor screen is commonly used in VMI spectrometers. Even though such combinations are not hard requirements, they have their underlying reasons.

COLTRIMS setup is typically used for the electron and ion coincidence experiment in which the reaction rate is much lower than one, and if there is a reaction, only few particles are produced and detected by the detector. For this case, microchannel plate detector with delay-line anode should be the choice rather than with phosphor screen. The delay-line anode has a much faster readout time (below one microsecond) which is limited by the signal traveling time along the wire, whereas that of phosphor screen with CCD is on the order of millisecond. To avoid cross talk between adjacent interaction events, the laser repetition rate has to be smaller than 1 MHz when using a microchannel plate detector with delay-line anode (the time of flight range of all fragments (up to several microseconds) is more of a limitation than the readout time, and can limit the repetition rate to hundreds of kHz). With phosphor screen, the repetition rate should be smaller than 1 kHz to avoid such cross talk. For coincidence experiments with low reaction rate per laser shot, to accumulate statistics more efficiently, a laser repetition rate higher than 1 kHz is definitely more desirable and delay-line anode should therefore be used. With this in mind, the electron and ion coincidence measurement apparatuses at current and future MHz XFEL facilities such as the EuXFEL and LCLS-II are equipped with delay line detectors. In fact, the delay line detector is one of only a few detectors capable of utilizing the high repetition rates of the MHz facilities.

However, when the reaction rate is higher and up to hundreds of particles are produced per laser shot, delay-line detectors can not resolve such large amount of particles anymore due to the dead time. In this case, microchannel plate detector with phosphor screen comes to the rescue. In general, for these experiments, which produce many particles per laser shot and do not need to resolve each interaction event, microchannel plate detector with phosphor screen is a better choice. In an electron and ion imaging experiment, if it's the

case that delay-line detector is a better choice for ion detection, whereas microchannel plate detector with phosphor screen is better for the detection of electrons, a combination of these two types of detectors can be used in a single experimental setup.

Chapter 4

Data analysis

The raw data to be analyzed in an ion and electron momentum imaging experiment consist of a sequence of data listed event by event, with each event defined by one laser shot. And the event data is constituted by the output (signal trace, camera image, etc.) from the ion and electron imaging detectors, as well as the machine data such as pulse energy and photon energy. This chapter will focus on the analysis of the output from ion and electron detectors, especially the HEX delay-line detector. In the experiments of this thesis, each of the outputs from the anodes of MCP and delay line are amplified and then sent to a digitizer, from which the entire digitized trace is used for further software analysis. (It should be noted that in many experiments employing delay-line detectors, each of the anode outputs (after amplification) is sent to a hardware Constant Fraction Discriminator for identifying signals which are then digitized. And only the identified signal arrival times are recorded instead of the full waveforms analyzed in this work.) The analysis starting with the digitized full waveforms can be divided into four steps: signal arrival time identification, hit reconstruction, calibration and physical quantities calculation.

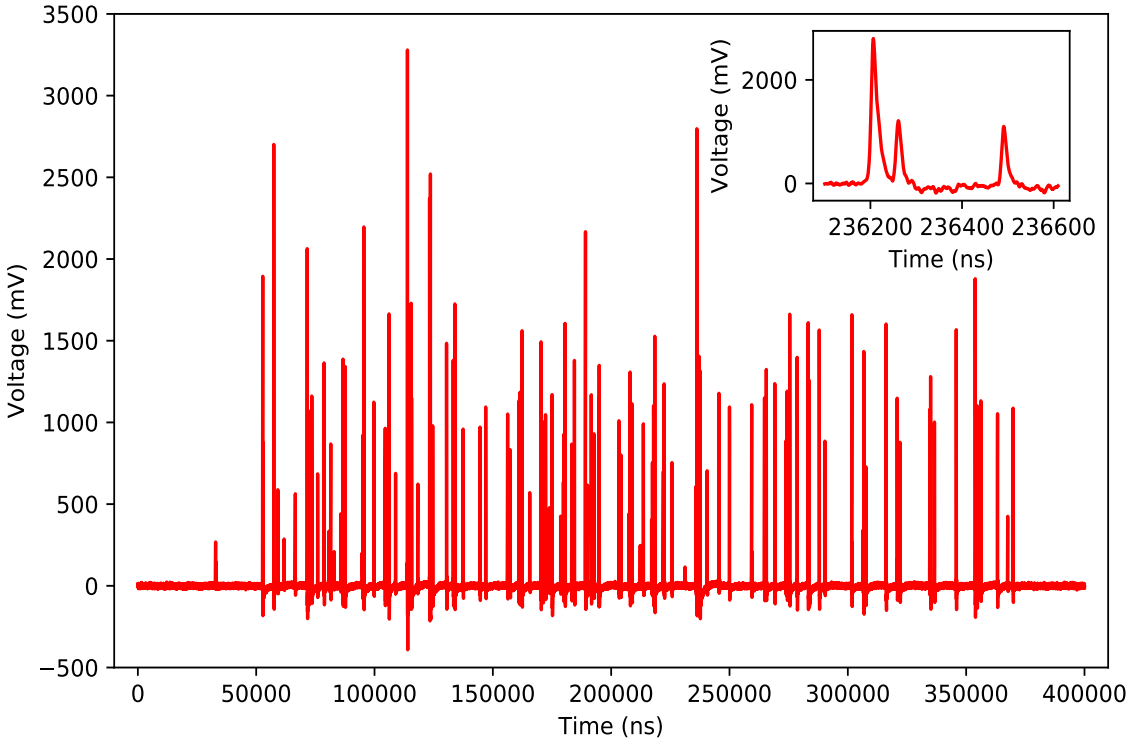

Figure 4.1: A typical waveform from a delay-line detector. The inset is the zoomed-in waveform within a narrow time range.

4.1 Signal arrival time identification

Shown in Fig. 4.1 is a typical waveform recorded in an experiment. The easiest way to pick out signals from such waveform is by identifying the peaks and use the times corresponding to peak maxima as the signal arrival times. But for different signals, the maximum doesn't appear at the same relative time point within the peak, which degrades the temporal resolution of this approach. In addition, when multiple signals arrive very close in time, as is often the case in the detection of fragments from polyatomic molecules, it can happen that a signal is overlapping with its neighbors, does not appear as a well-separated peak and hence cannot be identified. Another method, which is very robust for signal detection, relies on taking the time point when the trace rises above a constant threshold as the signal arrival time. But it also has rather poor performance in terms of time resolution because the time thus identified can move around within the rise time (10 ns) when the signal height changes. A third method is the "Center of Mass" method, which takes the center of mass of the peak

as the signal arrival time, has better resolution, but it can't deal with multiple coincident ions when they come close in time. The "Constant Fraction Discrimination" (CFD) method, which can effectively mitigate the issues of the methods discussed above, is applied for the identification of signal arrival times for the work in this thesis.

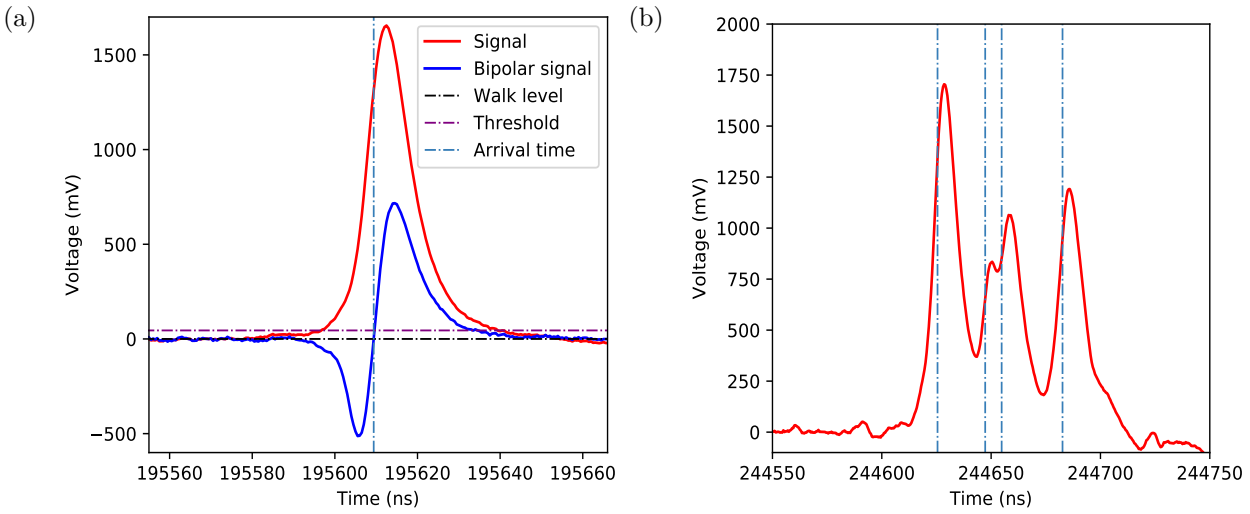

Figure 4.2: Peak identification with the "Constant Fraction Discrimination" method. (a) Peak identification. (b) Identification of multiple overlapping peaks.

To apply "Constant Fraction Discrimination" algorithm to a singal trace of positive polarity, one copy of the trace is delayed, the other copy is inverted, attenuated by a constant fraction, and then added to the first copy to get a bipolar signal. Then the signal arrival time is identified to be when the bipolar signal crosses a preset walk level on the rising edge, with the condition that the original signal at this crossing point is above a preset threshold. An example of the arrival time identification by CFD is displayed in Fig. 4.2a. Fig. 4.2b shows the capability of CFD to identify multiple overlapping signals. Several parameters need to be determined before using CFD, including signal polarity, time delay, constant fraction, walk level and threshold. A good parameter setting can make the signal detection both sensitive and precise.

Obtaining the statistical characteristics of the signal traces, including signal baseline, noise level, peak height and rise time as shown in Fig. 4.3, is the first step to set optimal CFD parameters. The threshold should be set just above the noise level in order to avoid

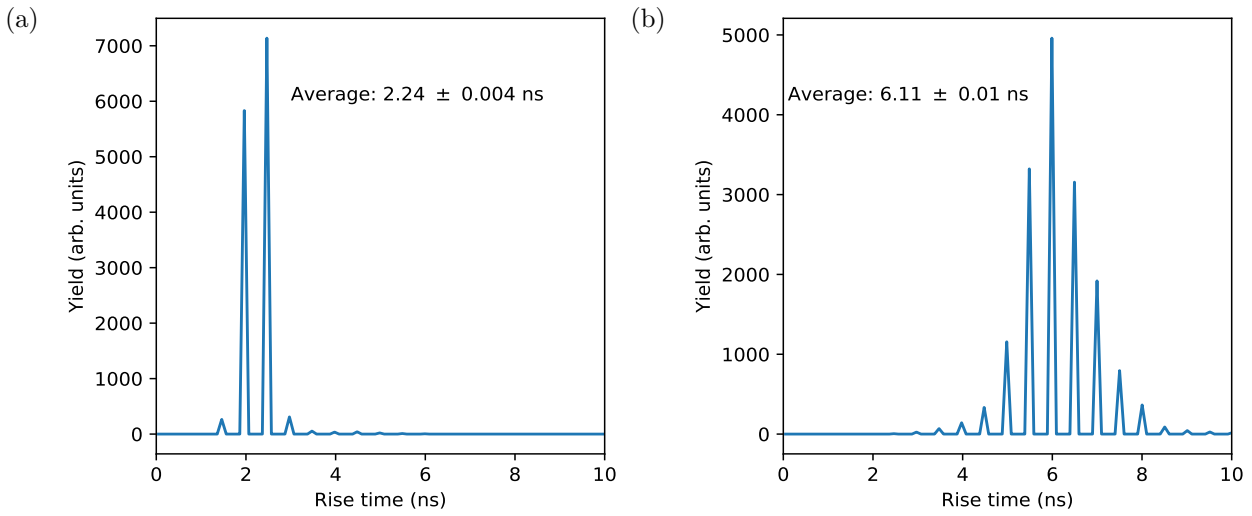

Figure 4.3: (a) Rise time of signals from a MCP anode. (b) Rise time of signals from a wire end of a delay-line anode. The rise time for a signal is determined as the time it takes from reaching 10% to 90% of the signal maximum. The entries in these two histograms are rise times of many different signals, from the anode of a MCP and a wire end of a delay-line anode, respectively.

missing small signals. The walk level should be just above the signal base line. Time delay D and constant fraction F are related and both depend on the signal rise time RT. With good settings for D and F, the identified signal arrival time should be when the bipolar signal has maximum slope. A rule of thumb for tuning D and F is $D = RT(1 - F)$ [124].

The parameter settings need to be determined separately for each of the waveform channels. For a HEX (QUAD) delay-line detector, there are seven (five) channels, one for MCP and the other six (four) for delay-line anode. By applying the CFD procedure to each waveform, the identified signal arrival times from each of the seven (five) channels, including t_{mcp}, t_1^u, t_2^u, t_1^v, t_2^v, t_1^w and t_2^w (t_{mcp}, t_1^x, t_2^x, t_1^y and t_2^y) are either saved for later analysis or directly sent to the hit reconstruction routine discussed in the the next section. (u, v and w (x and y) specify different layers of the HEX (QUAD) delay-line anode.)

4.2 Hit reconstruction

For each event, starting with the signal arrival times found out by the CFD, the hit reconstruction routine reconstructs the position and time of the particles when they hit the

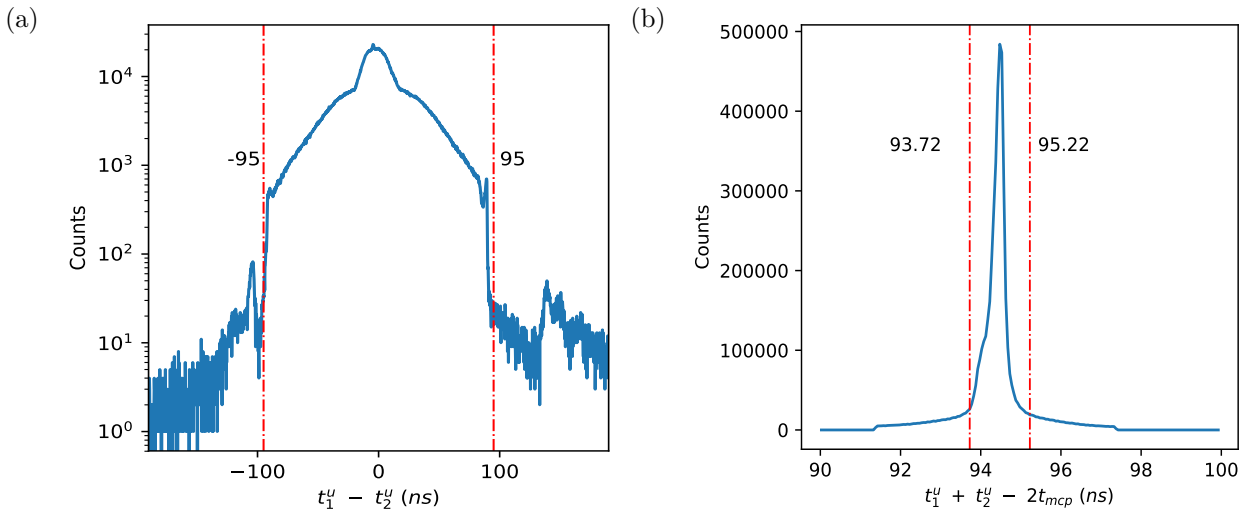

Figure 4.4: (a) Time difference of signal arrival times at the two ends of the u layer. (b)Time sum of signal arrival times at the two ends of the u layer, with respect to the signal arrival time at the MCP.

detector. Multiple particles can hit the detector with each event, creating multiple signals in each channel. The particle number to the power of 7 is the number of possible combinations of the signal arrival times from the 7 channels. Two physical constraints of the detector can be used to reduce this number to a smaller value. One is that after a particle hits the MCP, the electron cloud from the MCP is then picked up by the delay line on which the signal has a maximum run time determined by the wire length. The anode signals from the delay line, corresponding to this MCP signal, can therefore be searched within a much narrower time window. The maximum run time can be found by histograming the differences of the signal arrival times at the two ends of the wire. In Fig. 4.4a, the "$t_1^u - t_2^u$" histogram shows the distribution is almost symmetric with respect to $t_1^u - t_2^u = 0$, and has sharp edges at -95 ns and 95 ns. Within these two edges are contained the majority of counts. The symmetry is because the two ends of the wire are equivalent and the laser focal spot corresponds to the detector center. 95 ns is the maximum run time of signals along the wire. This gives the time difference condition

$$|t_1^u - t_2^u| < 95\ ns. \tag{4.1}$$

The other constraint is that after the electron cloud gets picked up by the delay line wire, two signals propagate in opposite directions. Upon arrival at the wire ends, the sum of the distance traveled by the two signals equals the wire length. The sum of the arrival times at the two wire ends, with respect to the arrival time on MCP, $t_1^u + t_2^u - t_{mcp}$ should therefore be narrowly distributed around a constant value. An example of the time sum "$t_1^u + t_2^u - t_{mcp}$" distribution is shown in Fig. 4.4b. The distribution is mainly confined in the time range from 93.72 ns to 95.22 ns. This gives the time sum condition

$$93.72\ ns < t_1^u + t_2^u - t_{mcp} < 95.22\ ns. \tag{4.2}$$

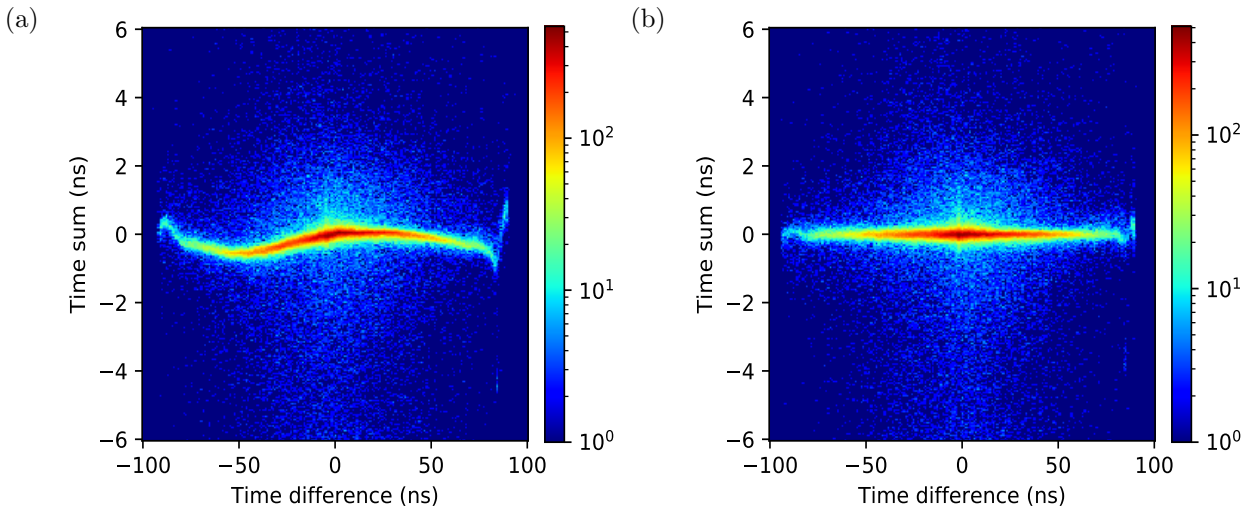

Figure 4.5: Time sum of signal arrival times at the two ends of a delay-line layer for different hit positions, without and with the non-linearity correction. (a)Without the non-linearity correction. (b) With the non-linearity correction.

With the time difference condition Eq. (4.1) and time sum condition Eq. (4.2), the time window to search anode (U) signals for a given MCP signal is

$$\frac{t_{mcp} - (95 - 93.72)\ ns}{2} < t_i^u < \frac{t_{mcp} + (95 + 95.22)\ ns}{2}, \tag{4.3}$$

with $i = 1, 2$.

For a given MCP signal with arrival time t_{mcp}, if the wire ends arrival times t_1^u and t_2^u

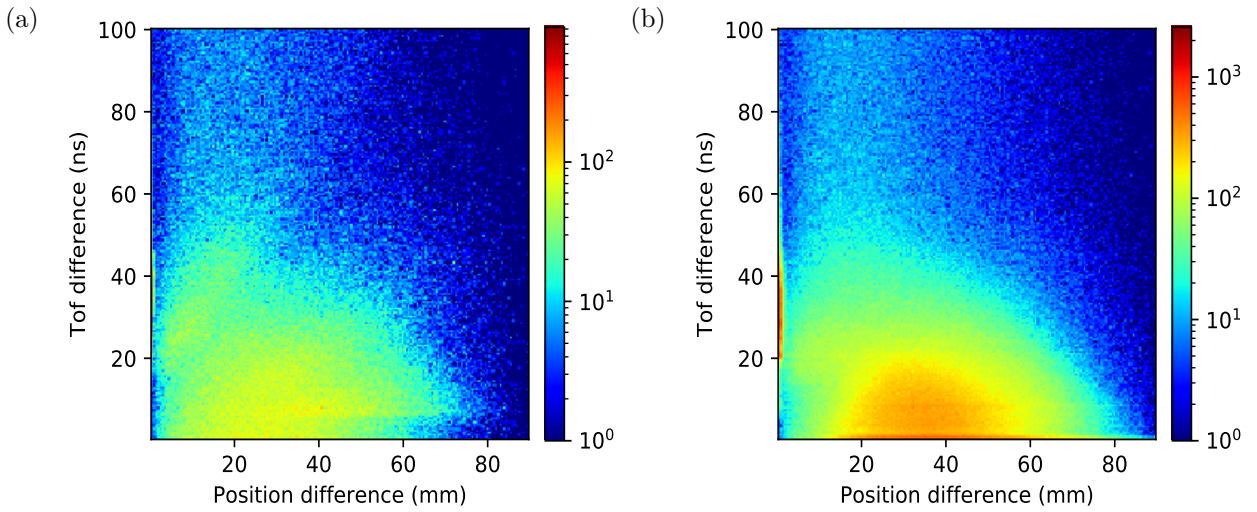

Figure 4.6: Time of flight difference with position difference for two consecutively arriving particles. (a) Without recovering missing signals. (b)With recovering signals.

are not only within the time window defined by Eq. (4.3), but also satisfy the time sum condition in Eq. (4.2), the three arrival times t_{mcp}, t_1^u and t_2^u are then from the same hit and can be used for hit reconstruction. Similar procedures are applied to find the other arrival times t_1^v, t_2^v, t_1^w and t_2^w for v and w layers. Once the arrival times t_{mcp}, t_1^u, t_2^u, t_1^v, t_2^v, t_1^w and t_2^w of all the channels for a single hit are picked out, the hit arrival time and impact position on the detector can be calculated according to the formulas in the delay-line detector section 3.2.3.

It can happen that not all signals from the 7 channels are successfully detected for each hit, due to, for example, the detector dead time. This issue can be mitigated by recovering the missing signals with the detected ones according to the time sum condition in Eq. (4.2). However, this condition can not be directly applied because it has a wide range of possible time sum values and can't give a definite missing signal arrival time. The finite width of the time sum distribution in Fig. 4.4b is mainly due to the non-linearity of delay-line wires, which is illustrated in Fig. 4.5a where the time sum values (shifted so that the peak position is at zero) can be seen to depend on the hit impact positions on the wire. This non-linearity can be corrected with a calibration table containing the offsets of time sum values from the time sum peak value for all possible hit impact positions. After non-linearity correction as

shown in Fig. 4.5b, the time sum distribution gets narrower and is more suited for recovering missing signals. Such signal-recovering procedures are implemented in the hit reconstruction routine by Achim Czasch from Roentdek company. Using this routine, a considerable amount of otherwise missed hits due to signal detection failures can be reconstructed. Fig. 4.6b are the histograms of time of flight difference and position difference between two consecutively arriving particles. The left histogram is plotted without using the missing-signal recovering routine, the bottom left region of which is empty due to detector dead time. This region almost gets filled up in the right histogram which is plotted after using the missing-signal recovering routine. So the signal recovering effectively pushes the dead time to less than 1 ns.

4.3 Calibration

Before calculating physical quantities, the time-to-position conversion factors $f_i = \frac{V^i_{group}}{2D^i_{1mm}}$ ($i = u,\ v\ and\ w$) introduced in the delay-line detector section 3.2.3, start time of the interaction and jet velocity need to be calibrated. Thanks to the self-calibratable property of ion and electron momentum imaging setup, these calibrations can be achieved with the same data used later for calculating physical quantities.

4.3.1 Time to position conversion factors

Precise time-to-position conversion factors are necessary to make accurate momentum and energy calculations. Their calibration can be achieved in two steps. The first step is to calculate the conversion factors using the time difference histograms Fig. 4.7. From these histograms, the time difference distribution edges t^i_{max} ($i = u,\ v\ and\ w$) as shown by the red dashed lines, can be obtained, which are the maximum run time along the u, v and w directions. With the detector size L, the conversion factors are given by $f'_i = \frac{L}{t^i_{max}}$.

The detector size L can't be accurately known beforehand and can only be roughly estimated. So the conversion factors f_i are only accurate relative to one and another, but

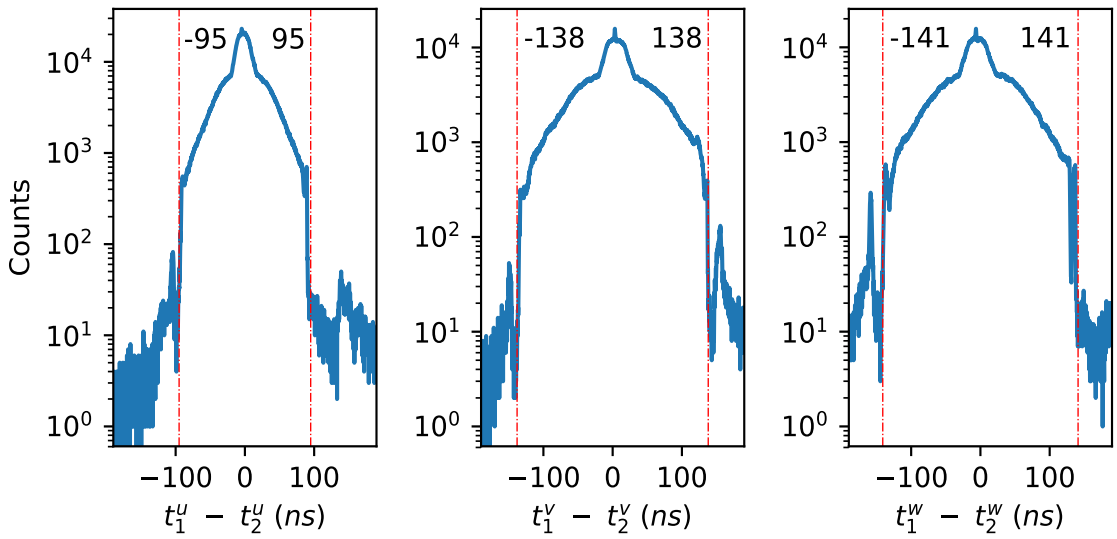

Figure 4.7: Time difference of signals from u, v and w layers.

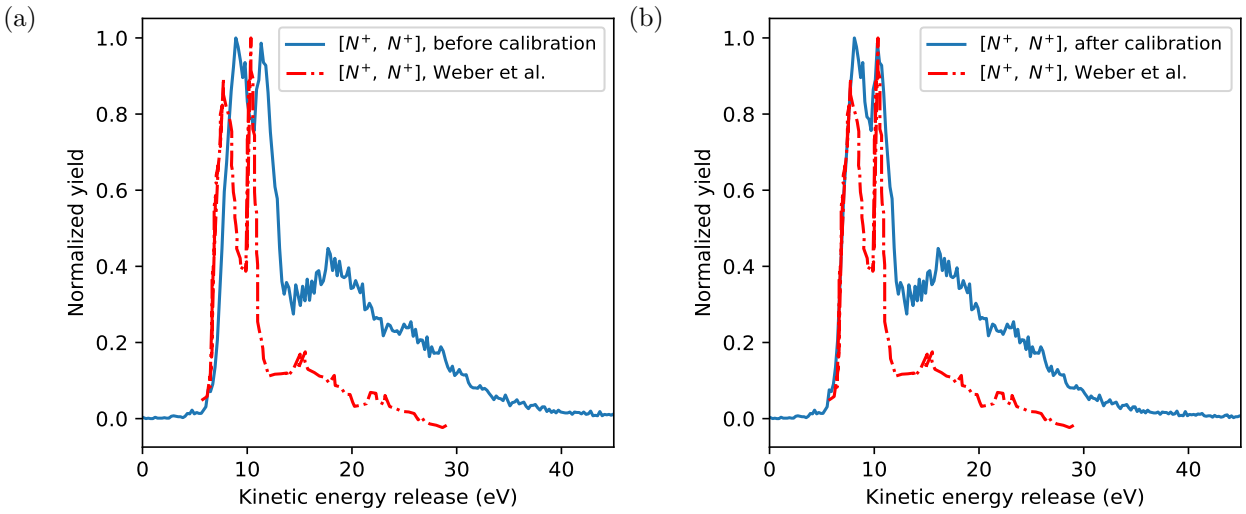

Figure 4.8: Kinetic energy release of $[N^+,\ N^+]$ coincidence channel. (a) Before calibration. (b)After calibration. $[N^+,\ N^+]$ KER data shown in red is taken from [125].

due to the uncertainty of the effective detector size L, a common scaling factor is still needed. This calls for the second step. One method to get the common scaling factor is by comparison of the uncalibrated energy spectrum calculated with the conversion factors f_i', with an already calibrated energy spectrum, as shown in Fig. 4.8a. If an energy scaling factor c_{eng} is needed to match the uncalibrated spectrum with the calibrated one, the common scale factor for the conversion factors f_i' is then $\sqrt{c_{eng}}$. So the final time-to-position conversion

factors are $f_i = \sqrt{c_{eng}} f_i'$. The energy spectrum calculated with f_i should now match the calibrated one, as shown in Fig. 4.8b.

4.3.2 Interaction start time, location and jet velocity

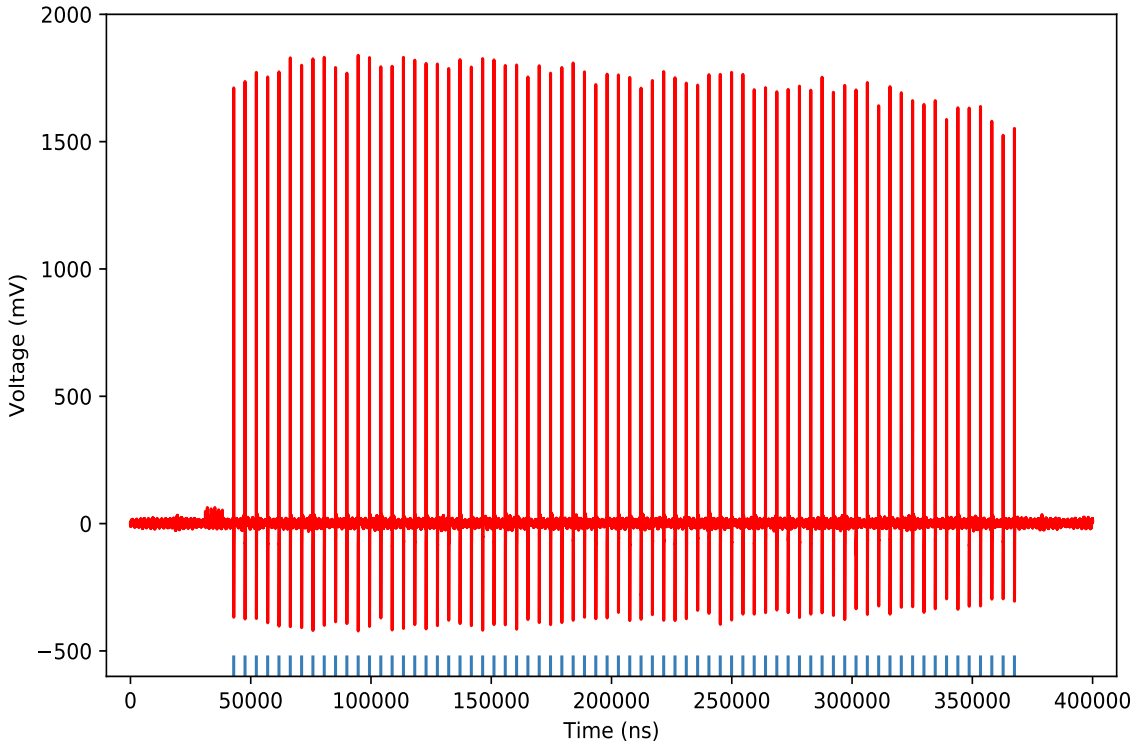

Figure 4.9: A waveform (red) from the x-ray-pulse-sensing metal plate installed at the SQS endstation of the EuXFEL. The blue lines are identified x-ray pulse arrival times.

The data acquisition is triggered for each interaction event. At the LCLS, the trigger time is set according to the master clock to make sure, for each event, the data acquisition is started at a fixed relative time before the arrival of the x-ray pulse. At the EuXFEL, the machine operates in burst mode. Separate pulse trains are generated ten times per second. In each train, there are equally spaced pulses with repetition rate up to 4.5 MHz. The data acquisition is triggered for each train, rather than for each of the pulses inside the train. One round of data acquisition is one train and hence for all the interaction events identified by the pulses within that train. At the SQS endstation of the EuXFEL, a metal plate is installed downstream of the interaction chamber to detect the arrival of each pulse within

the train and hence can also work as a trigger for each interaction event. Even if the data acquisition is triggered train-by-train, instead of on an event-by-event basis, the signal arrival times from this metal plate, displayed as blue lines in Fig. 4.9, can still be used to separate individual interaction events in each train.

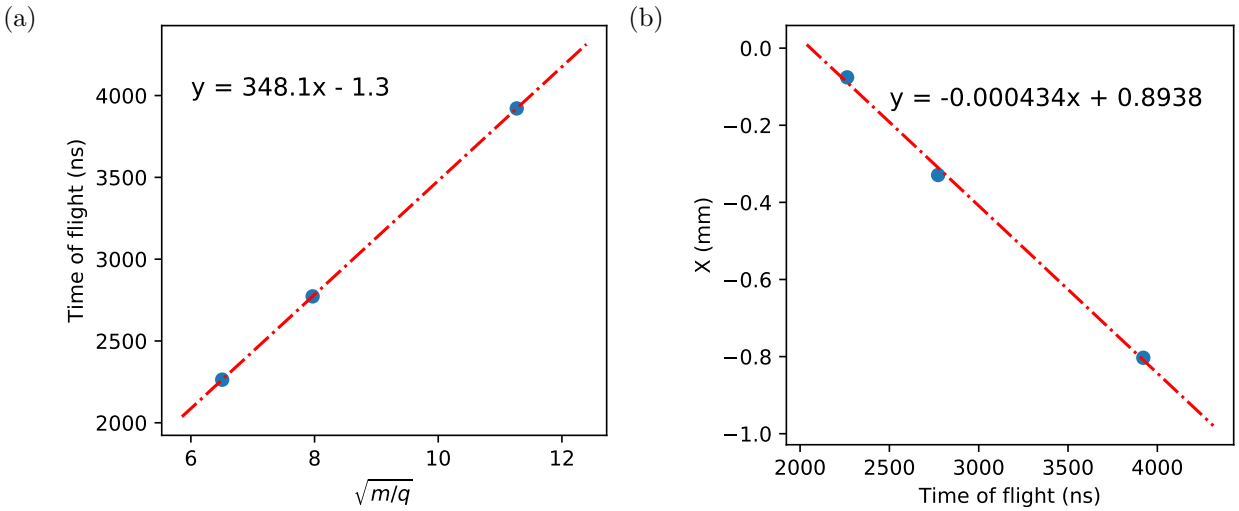

Figure 4.10: (a) Interaction start time calibration. (b)Jet velocity and interaction location calibration.

Since the metal plate is about half a meter behind the interaction region, the signals from it are delayed by about 1 ns from the start time of the interaction. At the LCLS, the trigger time is not guaranteed to be the same as the interaction start time either. Therefore, calibration of start time from existing data is needed. The time of flight of an electric-field-accelerated particle (of mass m and charge q) satisfies the relation $t = a\sqrt{\frac{m}{q}} + t_{offset}$ (see Appendix B for the derivation), with t_{offset} being the difference between the trigger time and interaction start time, and a is determined by spectrometer length and voltage settings. In Fig. 4.10a, t_{offset} is found by fitting a line to the data points $(T,\ \sqrt{m/q})$ of 3 different kinds of particles, with T and m/q being respectively the center time of flight and mass to charge ratio of each particle. This offset value $t_{offset}\ = 1.3ns$, as is found by the fitting, should be subtracted from the raw time of flight values before calculating the momenta of particles.

The gas target is cooled down by supersonic expansion, through which the gas acquires

a high directional velocity. Neglecting the velocity from the already-reduced thermal fluctuations, this jet velocity contributes to the initial velocity of all the fragments and should be found out to separate it from the velocity due to the interaction. If the electric field direction is only along the spectrometer axis as is often the case in ion and electron momentum imaging experiments, the center of fragment distributions on the detector is then mainly determined by the jet velocity. As shown in Fig. 4.10b, the jet velocity can be determined as the slope of the fitted line to the data points $(X,\ T)$, where X is the distance of the fragment impact position from the detector center, and T is the fragment time of flight. The jet velocity in the case of Fig. 4.10b (with CH_3I molecules) is about 0.000434 $mm/ns\ =\ 434\ m/s$.

4.4 Identification of ion species

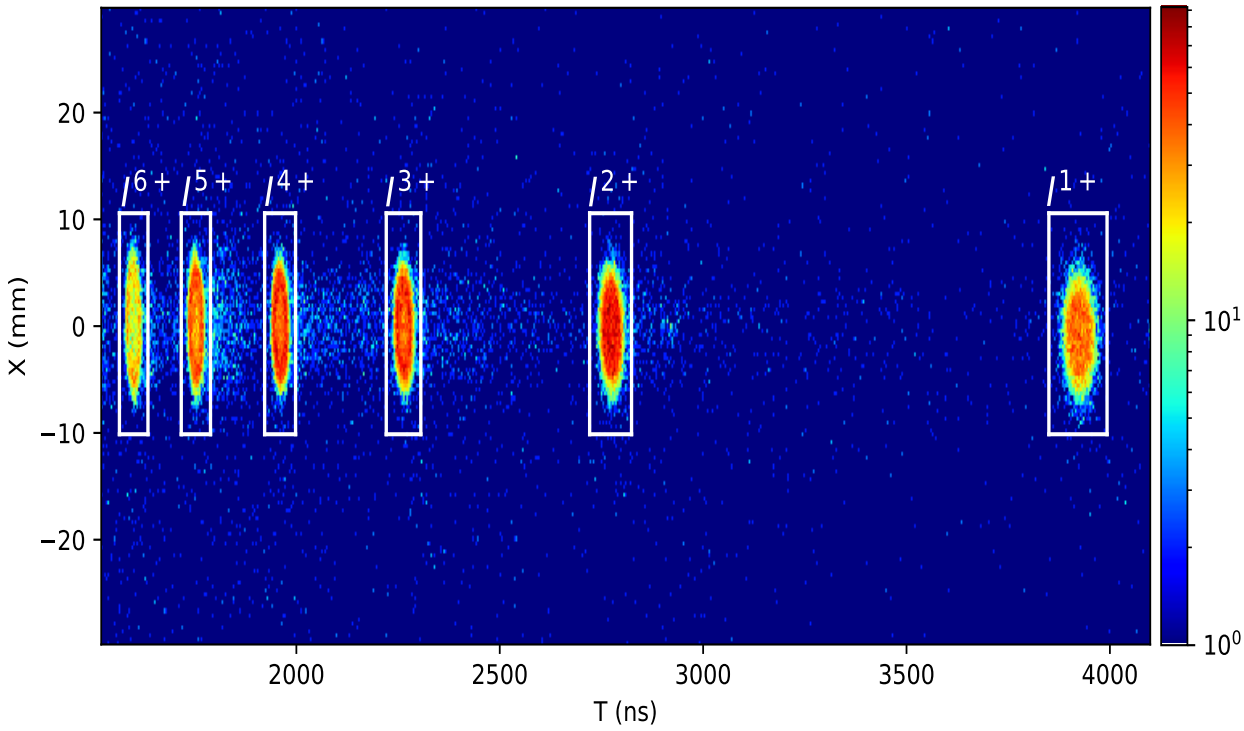

Figure 4.11: X-T histogram of low-charged iodine ions from XFEL pulse ionization of CH_3I molecules with x and t conditions shown as white rectangles.

Ion species can be identified by their times of flight T, the square of which have a linear

relation (Eq. (B.2)) with their characteristic mass to charge ratios. In addition, ion impact positions can also be used to help identify ion species. Heavier ions are detected in a more localized region on the detector than light ions. Parent ions or ions from atomic ionization impact the detector in a even more confined region. So the time and position conditions on T, X and Y, as shown in Fig. 4.11 can be applied to judging whether a particle belongs to a certain ion species.

4.5 Momentum calculation

Charged particles fly to the detector following Newton's Second Law. Given the spectrometer configuration, their initial momenta gained from the reaction can be calculated from the times of flight (t) and hit positions (x,y). Different calculation methods can be used, depending on the spectrometer field geometries and whether the particle is an ion or electron. Once the momentum ($P_x,\ P_y,\ P_z$) is determined for a particle of mass m, its kinetic energy E can be readily obtained by

$$E = \frac{P_x^2 + P_y^2 + P_z^2}{2m}. \tag{4.4}$$

4.5.1 Homogeneous field geometry

Ion momentum

In a homogeneous electric field with direction along the spectrometer axis, a charged particle moves with constant velocity in **x** and **y** directions (parallel to the detector plane) and with constant acceleration in **z** direction (along the spectrometer axis). Its momentum is

calculated by

$$P_x = \frac{m(x - x_0)}{(t - t_0)}, \tag{4.5}$$

$$P_y = \frac{m(y - y_0)}{(t - t_0)} - mV_{jet}, \tag{4.6}$$

$$P_z = \frac{l}{(t - t_0)} - \frac{1}{2}\frac{qU}{ml}(t - t_0), \tag{4.7}$$

where q is the charge of the particle. (x_0, y_0), t_0 and V_{jet} are the interaction location projected to the detector plane, interaction start time, and jet velocity, obtained from the calibration procedures discussed in section 4.3.2. U and l are respectively the electric potential difference and length across the spectrometer.

In some setups, the spectrometer has one more drift region after the acceleration region. The momenta in **x** and **y** are still given by Eqs. (4.5) and (4.6). P_z can be calculated by solving the coupled equation

$$\begin{cases} \frac{P_z}{m}t_1 + \frac{1}{2}\frac{qU}{ml}t_1^2 + d = l, & (4.8) \\ t_1 + \frac{d}{\frac{P_z}{m} + \frac{qU}{ml}t_1} = t - t_0, & (4.9) \end{cases}$$

where t_1 is the flying time in the acceleration region and d is the length of the drift region.

If the particle momentum gained from the electric field is large with respect to that from the reaction, P_z can be calculated with a simple approximate formula (see derivation in Appendix A)

$$P_z = (8.04 \times 10^{-3}\frac{cm\ a.u.}{eV\ ns}) \cdot \frac{qU}{l}(t_a - t_{a0}), \tag{4.10}$$

where t_a is the time of flight of a particle belonging to species a, and t_{a0} is the center time of flight of species a, which is also the time of flight of those ions which have zero P_z momentum. If the ion initially flies away from the detector, its time of flight would be larger than t_{a0}.

On the hand, if the ion flies towards the detector, its time of flight would be smaller than t_{a0}. And the larger is $|P_z|$, the larger is the absolute difference between t_a and t_{a0}. There is a linear relationship between this time flight difference and P_z as described by Eq. (4.10). This is the underlying reason why Coulomb-exploded fragments have broad time of flight peaks, whereas those of the parent ions are sharp. Calculation with Eq. (4.10) does not require the values of spectrometer dimensions, which can be an advantage when they are not precisely known. In those experiments where the ion momentum distributions are angularly isotropic, the need of a prior knowledge of voltage U is eliminated, because the proportionality constant in Eq. (4.10) can be calculated such that the width of P_z distribution is equal to those of P_x and P_y distributions. As an example, the 2D momentum (calculated with this method) distributions of I^+ ions, produced from XFEL pulse interaction with CH_3I molecules, are plotted in Fig. 4.12.

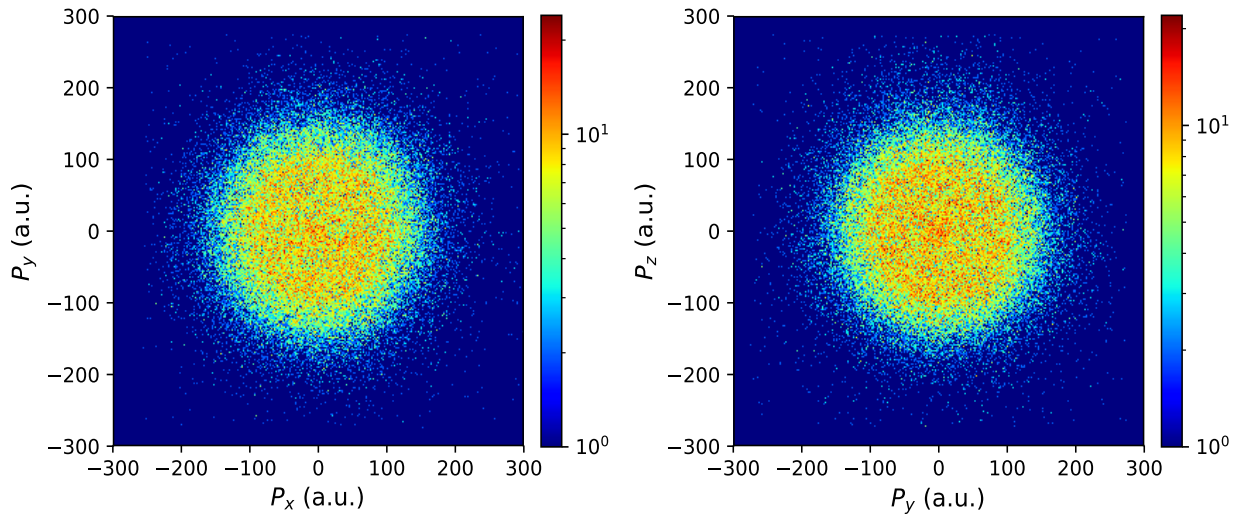

Figure 4.12: 2-D momentum histograms of I^+ ions produced from XFEL pulse interaction with CH_3I molecules, calculated by Eq. (4.10).

Numerical methods can also be applied to the calculation of P_z, especially when there are more than two regions with different electric field strengths and simple analytical formula does not exist. One such approach applies the iterative procedure:

(1) Make a guess on P_z.

(2) Calculate the times for the ion to fly through each region and sum up the times to get

the total time of flight $t(P_z)$.

(3) Calculate the time of flight difference between calculation and experiment $t(P_z) - t_{exp}$. If the difference is small than a preset tolerance, take the current P_z value and stop. Otherwise, continue to step **(4)**.

(4) Make the next best guess on P_z, based on the difference $t(P_z) - t_{exp}$. For example, according to Newton-Raphson method, the next guess is $P_z = P_z - \frac{t(P_z) - t_{exp}}{t'}$, where $t' = \frac{t(P_z) - t(P_z + dP_z)}{dP_z}$ is the approximate slope of the function $t(P_z)$ at P_z, with dP_z being the small momentum increment. Move on to step **(2)** with the new guess.

Electron momentum

In a typical COLTRIMS setup, electrons are accelerated by a homogeneous electric field, under the influence of a homogeneous magnetic field with the direction parallel to the spectrometer axis. With such field configuration, the electrons fly in spiral trajectories from the interaction region to the detector.

Since the magnetic force is perpendicular to magnetic field and hence parallel to the detector plane, it does not change electron motion along the spectrometer axis. The longitudinal momentum P_z can be determined by Eq. (4.7) after substituting the equation variables for ions with those of electrons.

With the electron transverse momentum magnitude $P_{transverse}$ staying unchanged by the electromagnetic field, the circular transverse motion due to the magnetic field with flux density B has a constant radius

$$R = \frac{P_{transverse}}{qB} \tag{4.11}$$

and frequency

$$\omega = \frac{qB}{m_e}, \tag{4.12}$$

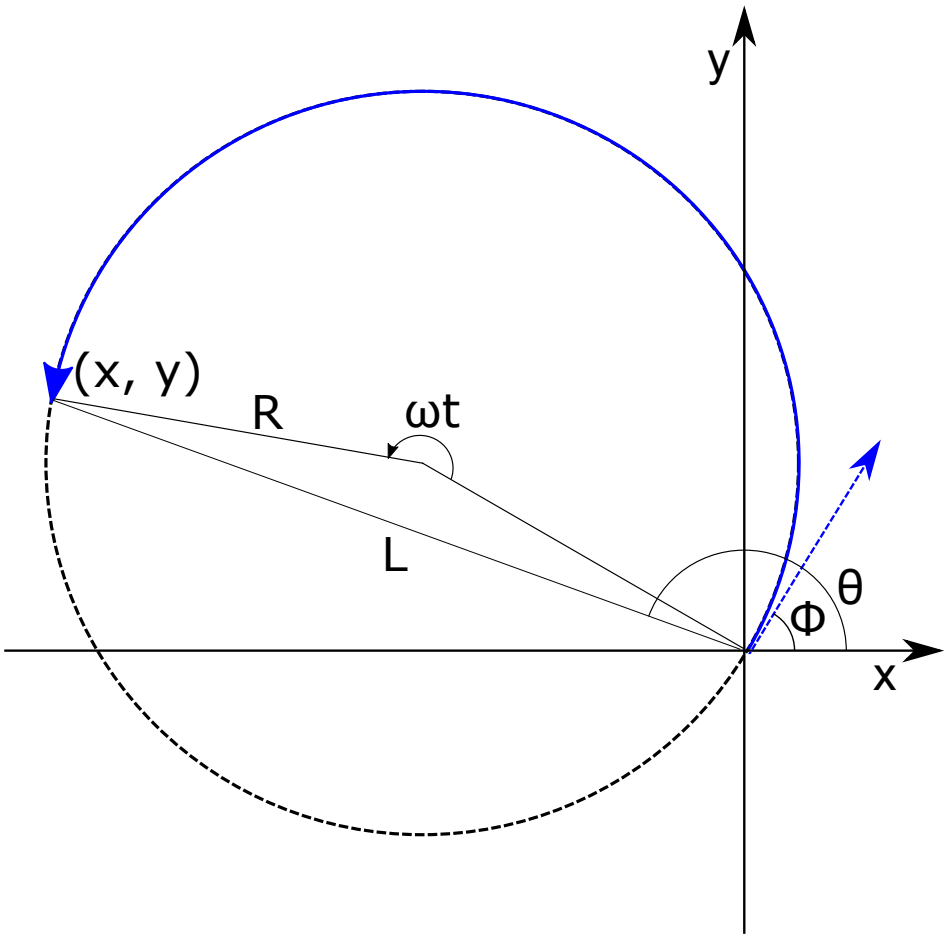

Figure 4.13: Detector-plane projection of the trajectory of an electron ejected at angle ϕ with flying time t. This illustration is a modification based on the corresponding picture in [126].

with q and m_e the electron charge and mass.

The projection of such motion to the detector plane is illustrated in Fig. 4.13 for an electron ejected at angle ϕ until it hits the detector at flight time t. The radius R can be determined geometrically from t and hit position (x, y) as

$$R = \frac{L}{2|sin(\omega t/2)|} = \frac{\sqrt{x^2 + y^2}}{2|sin(\omega t/2)|}, \tag{4.13}$$

where L is the distance from the detector hit position (x, y) to the initial detector-plane location (corresponding to the origin in Fig. 4.13) of the electron.

From Equations (4.11) - (4.13), the transverse momentum magnitude is given by

$$P_{transverse} = qB\frac{\sqrt{x^2 + y^2}}{2|sin(\omega t/2)|}, \tag{4.14}$$

and from Fig. 4.13, the ejection angle ϕ is obtained by

$$\phi = \theta - \frac{\omega t}{2}. \tag{4.15}$$

For those electrons with more than one round of circular motions, ωt in Eq. (4.13) and (4.14) should be replaced by $\omega t - 2N\pi$, with N being the number of rounds the electron has completed.

If an electron has traveled through exactly an integer number of turns before arriving at the detector, its hit position would be at its initial detector-plane location. This happens when electron time of flight is a multiple of the cyclotron period

$$T = \frac{2\pi}{\omega}. \tag{4.16}$$

Such electrons make periodic appearances as nodes ($L = 0$) in the "L - t" plot. The time difference between adjacent nodes is therefore the cyclotron period, which can be further utilized to determine the cyclotron frequency and magnetic field strength according to Eqs. (4.12) and (4.16).

4.5.2 Inhomogeneous field geometry

If the spectrometer field is inhomogeneous as shown in Fig. 4.14, simple analytical formulas typically do not exist to calculate the electron and ion momenta from their times of flight t and detector impact positions (x, y). In such cases, if a formula relating momenta to (t, x, y) is still required to determine the momenta on a particle-by-particle basis, the "Fitting" method can be applied, which yields an empirical formula by fitting the data points from SIMION [121] simulations. If only the momentum distribution is required and

the detector image which contains the axis with cylindrical symmetry can be assumed to be a projection of the Newton sphere (the spatial distribution of particles moving with their initial momenta), as is the case in velocity map imaging of charged particles, the initial 3D momentum distribution can be obtained with inversion or deconvolution methods.

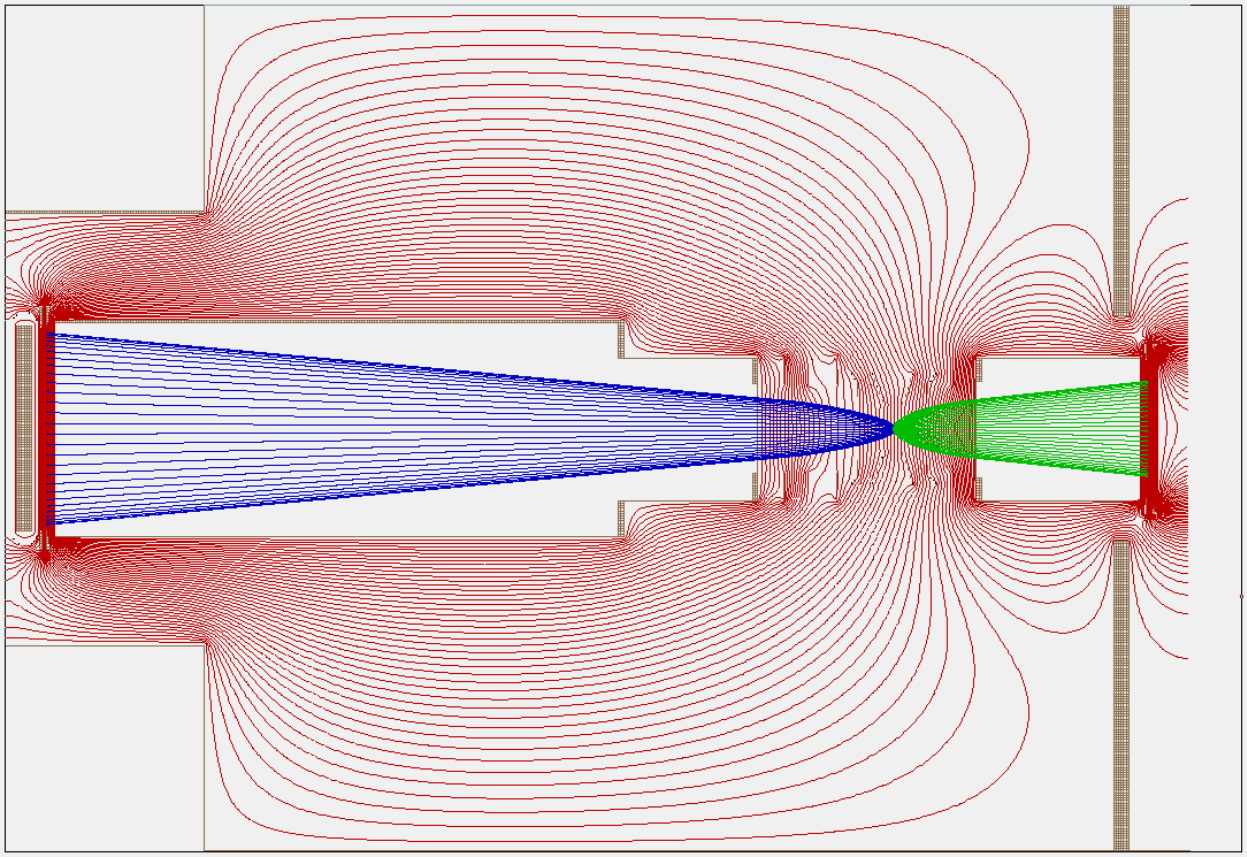

Figure 4.14: Ion (blue) and electron (green) trajectories in the field (red) of the double-sided velocity map imaging spectrometer shown in Fig. 3.8.

"Fitting" method

With the spectrometer configuration and voltage settings and given the mass, charge, and initial momentum (P_x, P_y, P_z) of a particle, the particle trajectory in the spectrometer can be simulated with the SIMION software as illustrated in Fig. 4.14, from which the corresponding time of flight t and detector impact position (x, y) can be obtained. By simulating the trajectories of particles with different representative momenta, a data set consisting of the

data points (P_x, P_y, P_z, x, y, t) can be obtained. By choosing an appropriate function form

$$\boldsymbol{\mathcal{P}} : (x,\ y,\ t)\ \rightarrow\ (P_x,\ P_y,\ P_z) \tag{4.17}$$

with adjustable parameters and fit it to this data set, the fitted function (P_x, P_y, P_z) = $\boldsymbol{\mathcal{P}}$(x, y, t) is the empirical formula for momentum calculations.

If the spectrometer field configuration is such that the particle motions in $\boldsymbol{x}$, $\boldsymbol{y}$ and $\boldsymbol{z}$ directions can be assumed to be decoupled from one and another (which can be checked by plotting the momentum dependence of one direction on the position or time of the other two dimensions, e.g. P_x vs. (y, t).), three independent functions with adjustable parameters

$$\begin{cases} \mathcal{P}_x : x\ \rightarrow\ P_x, & (4.18) \\ \mathcal{P}_y : y\ \rightarrow\ P_y, & (4.19) \\ \mathcal{P}_t : t\ \rightarrow\ P_z & (4.20) \end{cases}$$

can be used as the fitting functions, and after determining the fitting parameters, they can be used to compute the momentum (P_x, P_y, P_z) with (t, x, y). For a fitting example with $\mathcal{P}_x$, $\mathcal{P}_y$ and $\mathcal{P}_z$ as polynomial functions, see e.g. [127].

Abel inversion and deconvolution methods

The initial 3D momentum distribution can be obtained from the Newton sphere $N(x,\ y,\ z)$ which is the spatial distribution of particles moving with their initial momenta. In a velocity map imaging setup, with the initial energy of the particle much smaller than the energy it gained from the spectrometer field, the detector image $D(x,\ y)$ is a projection of such a Newton sphere. If an axis (assuming it's along $\boldsymbol{x}$) containing cylindrical symmetry of the interaction, such as the light polarization axis in a photoionization experiment, is parallel to the detector, the detector image in theory contains all the information of the Newton sphere. Different inversion methods have been developed over the last two decades to retrieve the Newton sphere from its 2D projection image.

Mathematically, this projection can be expressed as an Abel integral,

$$D(x,\ y)\ =\ \int_{-\infty}^{\infty} N(x,\ y,\ z)\ dz\ =\ 2\int_{|y|}^{\infty} \frac{rN(r,\ x)}{\sqrt{r^2\ -\ y^2}}\ dr, \tag{4.21}$$

where $r\ =\ \sqrt{y^2\ +\ z^2}$ and $N(r,\ x)$ is used in place of $N(x,\ y,\ z)$ thanks to the cylindrical symmetry. In principle, the Newton sphere can be obtained from its projection through the inverse Abel transform

$$N(r,\ x)\ =\ -\frac{1}{\pi}\int_{r}^{\infty} \frac{dD(x,\ y)/dy}{\sqrt{y^2\ -\ r^2}}\ dy. \tag{4.22}$$

The inverse Abel transform can be calculated with the Fourier-Hankel method [128]. But it doesn't perform well with noisy detector images. A better performing method, the basis set expansion (Basex) Abel transform method [129], expands the projection $D(x,\ y)$ in a basis set of functions which are projections of well-behaved functions, and then reconstructs the Newton sphere $N(x,\ y,\ z)$ as a linear combination of these well-behaved functions with the same coefficients as used for the previous expansion of the projection. The pBasex method [130], a variant of the BASEX method, uses polar basis functions instead of Cartesian basis set used in the BASEX method, and has a even better performance. Whereas the BASEX method accumulates the noise towards the center line, the pBasex method accumulates the noise to the center spot which typically can be neglected. Another method is the so-called "onion-peeling" method [131, 132], which starts by subtracting from the detector image the projection contributions of the particles distributed at the largest radius of the Newton sphere, and then repeats the subtraction with projection contributions of particles distributed at smaller and smaller radius of the Newton sphere, until the radius becomes zero. The Newton sphere can then be obtained with the "onion-peeled" detector image which is a symmetry-axis-containing slice of the Newton sphere. This method is fast but also has the disadvantage of noise accumulation towards the center line of the image. The issue is mitigated by its variant, the polar "onion-peeling" method [133], which works with polar coordinates instead of Cartesian coordinates as used in the "onion-peeling" method.

An improvement in calculation speed of the polar "onion-peeling" method is achieved with a method [134] which generates the 2D projections by fitting the experimental data with a polar basis set, instead of by simulation as in the original method. Another popular method is the "iterative" method [135] based on the similarities between the radial and angular distributions between the 2D detector image and the 3D Newton sphere. It has no center-line noise either, but can be slow to reach convergence with the iterative procedure.

4.6 Coincidence analysis

Photoelectrons, Auger electrons, photoions and photons can be produced from a single event of interaction between a molecule and an ultra-intense X-ray pulse. All four kinds of particles carry complementary information about the transient structure and dynamics unfolded during the interaction. Coincidence detection and analysis of these products is a powerful method for combining such multidimensional information in order to get a more complete picture about the interaction, and is one of the key instrument development focuses at current and future high-repetition-rate XFEL facilities. Ion-photon coincidence detection has been implemented at the LCLS, which has helped in one experiment [5] to identify a new ultra-efficient ionization mechanism. Ion-ion and ion-electron coincidence measurements are discussed in the following sections.

4.6.1 Ion-ion coincidence

Coincidence channel identification

For molecules breaking up into two or three ion fragments, the coincidence channels can be identified from the correlation maps of the ion time of flight. In these maps, the x axis shows the time of flight of the first detected ion, and the y axis is, in the two-fragment case, the time of flight of the second ion, and in the three-fragment case, the time of flight sum of the remaining two relatively slow ions. Such maps in the cases of two and three fragments are called Photoion-Photoion Coincidence Map (PiPiCo) and Triple Photoions Coincidence

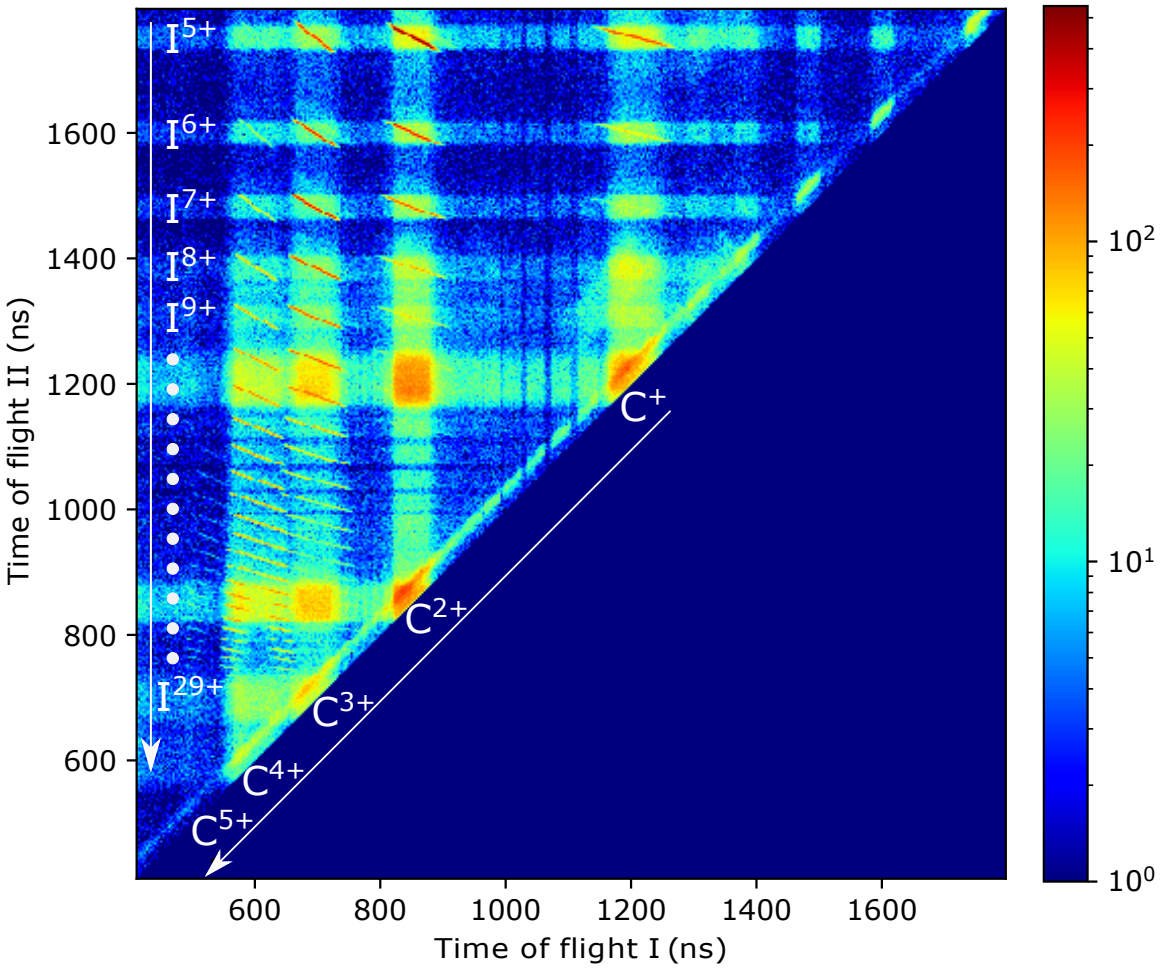

Figure 4.15: Photoion-Photoion Coincidence (PiPiCo) Map of fragments from XFEL pulse ionization of CH_3I molecules.

Map (TriPiCo), respectively. Shown in Fig. 4.15 is an example PiPiCo plot of fragments from XFEL pulse ionization of CH_3I molecules. About 65 [C^{m+}, I^{n+}] channels appear as diagonal stripes which can be identified by their expected times of flight.

In an ideal coincidence experiment, at most one interaction event per laser shot is allowed, which guarantees that the detected ions are from the same molecule. But in reality, there is always a possibility that more than one interaction events occur within one laser shot, creating false coincidences which appear as background in the PiPiCo map.

One way to isolate real coincidences from false ones is to gate on the stripes in Fig. 4.15. A better way is to gate on momentum sums because all three dimensions can be used to

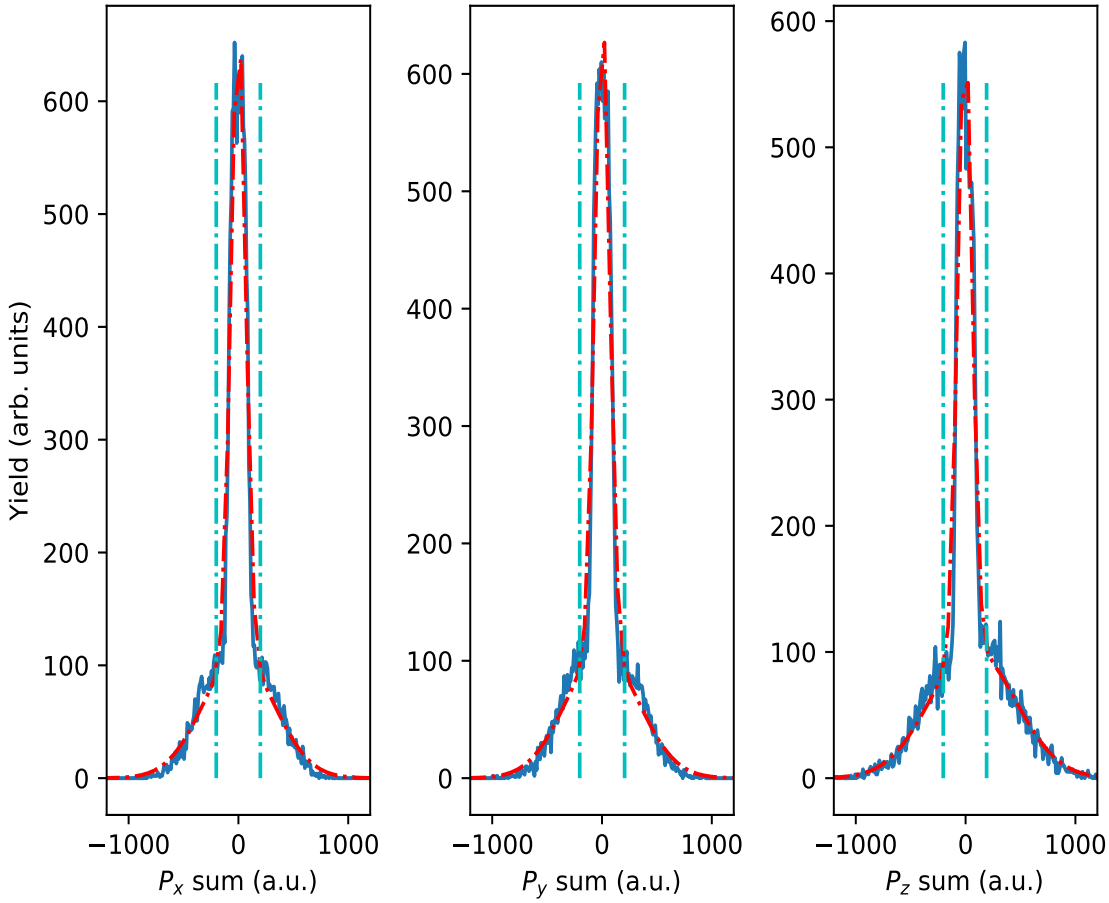

Figure 4.16: Momentum sums in $\boldsymbol{x}$, $\boldsymbol{y}$ and $\boldsymbol{z}$ directions of C^{2+} and I^{6+} ions from XFEL pulse ionization of CH_3I molecules. Gaussian fits are in red and the cyan dashed lines are the gate boundaries defined as the locations which are 3 standard deviations (of the Gaussian fitted to the peak) away from the peak center.

make a cleaner isolation. If there is a coincidence channel consisting of two ions such as C^{2+} and I^{6+}, each of the momentum sums in Fig. 4.16 shows a prominent peak on top of a broad shoulder, which corresponds to the real and false coincidences respectively. By gating on the peaks in the three momentum sums, [C^{2+}, I^{6+}] coincidence data can be separated for further analysis. To avoid the arbitrariness of judgment by naked eyes and increase the efficiency, the gates can be identified by fitting two Gaussians (one for the peak and the other for the shoulder, with the sum of the two plotted as red dashed lines in Fig. 4.16.) to the momentum sum. The location at 3 standard deviations (of the Gaussian fitted to the peak) away from the peak center can then be taken as the gate boundaries.

In cases where a molecule breaks up in more than two charged fragments, a similar momentum sum gating can be performed to get the real coincidence.

Kinetic energy release

Kinetic energy release is the total kinetic energy of all fragments in their center of mass frame. As shown in Fig. 2.10, it is the energy gained by the nuclei when moving on top of the potential energy surfaces (curves for diatomic molecules), in analogy to a ball on a surface changing its kinetic energy when moving to a location with a different gravitational potential. It therefore contains the information about nuclear motion and the characteristics of the potential energy surfaces the nuclei move upon, and can help to identify the electronic states populated during the interaction between x-rays and molecules.

Newton diagram and Dalitz plot

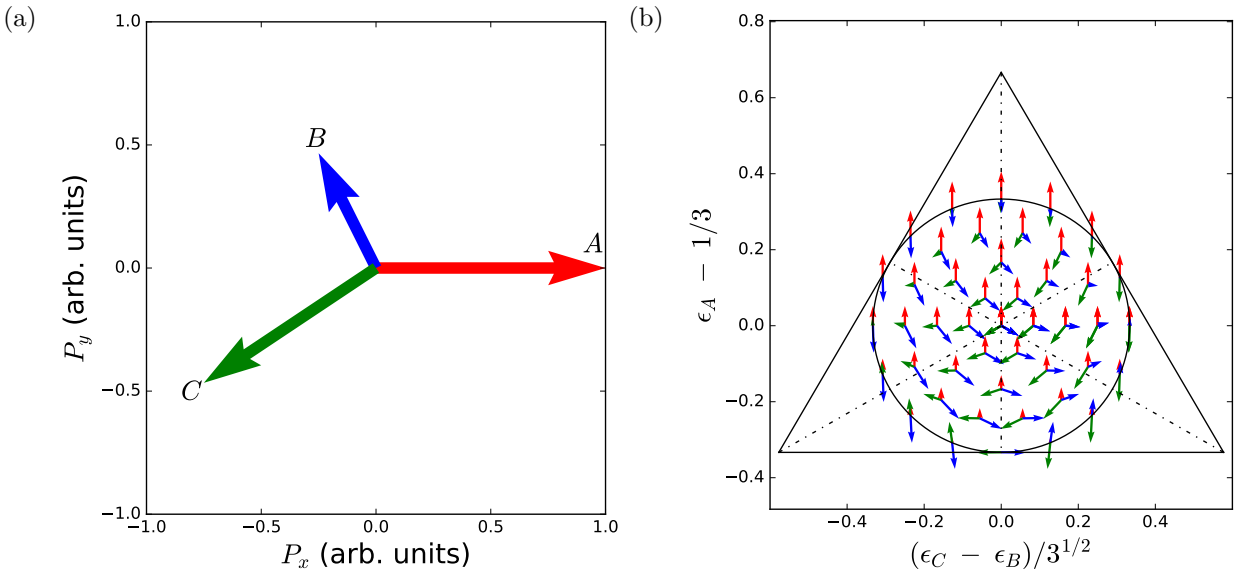

Figure 4.17: (a) Newton diagram showing the relative momentum vectors of fragments. (b) Dalitz plot, with the corresponding relative momentum vectors plotted for different graph locations.

Newton diagram [136, 137] and Dalitz plot [137, 138] as illustrated in Fig. 4.17 are used for mapping the momentum correlations and energy sharing among the coincident fragments.

In the Newton diagram, the momentum vector of fragment A is fixed at $P_x = 1$, and the relative momentum vectors of the other two fragments B and C with respect to A are then plotted.

Dalitz plot was first proposed by Dalitz to study $\tau - meson$ decay . Its coordinate system is defined, for the breakup into the three fragments A, B and C, by $x = (\epsilon_C - \epsilon_B)/3^{1/2}$ and $y = \epsilon_A - 1/3$, where $\epsilon_i = \frac{P_i^2}{\sum_i P_i^2}$ is the reduced energy and P_i is the momentum of fragment i with i = A, B, or C. For any data point within the triangle in Fig. 4.17b, its distances to the 3 sides (bottom, right and left) equal to the three corresponding reduced energies (ϵ_A, ϵ_B, and ϵ_C). With momentum conservation, the data points are constrained within the inscribed circle of the triangle. Each data point represents a single relative momentum vector configuration as shown in Fig. 4.17b.

4.6.2 Ion-electron coincidence

Photoelectrons or Auger electrons can also be detected in coincidence with the ion fragments, which can provide otherwise not available dynamical information. If the axial recoil approximation, which assumes that the Auger decay and fragmentation are fast compared with the rotation time scale of the intermediate molecular ion, is valid, electron angular distributions in the molecular frame can be reconstructed from the momentum vectors of the coincident electrons and ions.

In XFEL pulse interaction with molecules, the energy and angular distribution of photoelectrons reflect the character of core electronic structures, and that of Auger electrons can help distinguish which decayed state is populated from the core-hole state. Coincident measurement of such electron data in combination with ions can be a powerful approach for tackling such problems as how the nuclear motion affects the electronic states and vice versa.

Chapter 5

Molecular response to ultra-intense x-rays

With their high photon energy, x-ray pulses mainly interact with the inner-shell electrons of particular elements in the molecule. If the photon energy is high enough, an electron can be ejected into the continuum, leaving the molecular ion in a highly excited core-hole state. The core hole is then quickly refilled with electrons from other shells through Auger decay or fluorescence. Such photoionization-decay process can be repeated multiple times within a single ultra-intense x-ray pulse, accompanied in the meantime with other induced processes including intramolecular charge rearrangement and nuclear dynamics [13, 18, 19]. What makes this interaction more interesting is that the induced charge rearrangement and nuclear dynamics can in turn affect the photoionization and decay processes. In this chapter, the interplay between these processes will be revealed, through its dependence on x-ray pulse parameters including pulse energy, duration and photon energy, with two experimental data sets on the interaction between iodomethane (CH_3I) molecules and ultra-intense x-rays: one measured at the LCLS with x-ray photon energy at 8.3 keV and the other at the EuXFEL with x-ray photon energies at 1.2 keV, 1.5 keV and 2 keV. A simple ionization model will be built up to help interpret the experimental data. Some of the paragraphs and figures are adapted from [43–45].

5.1 Ionization

5.1.1 Sequential multiphoton ionization

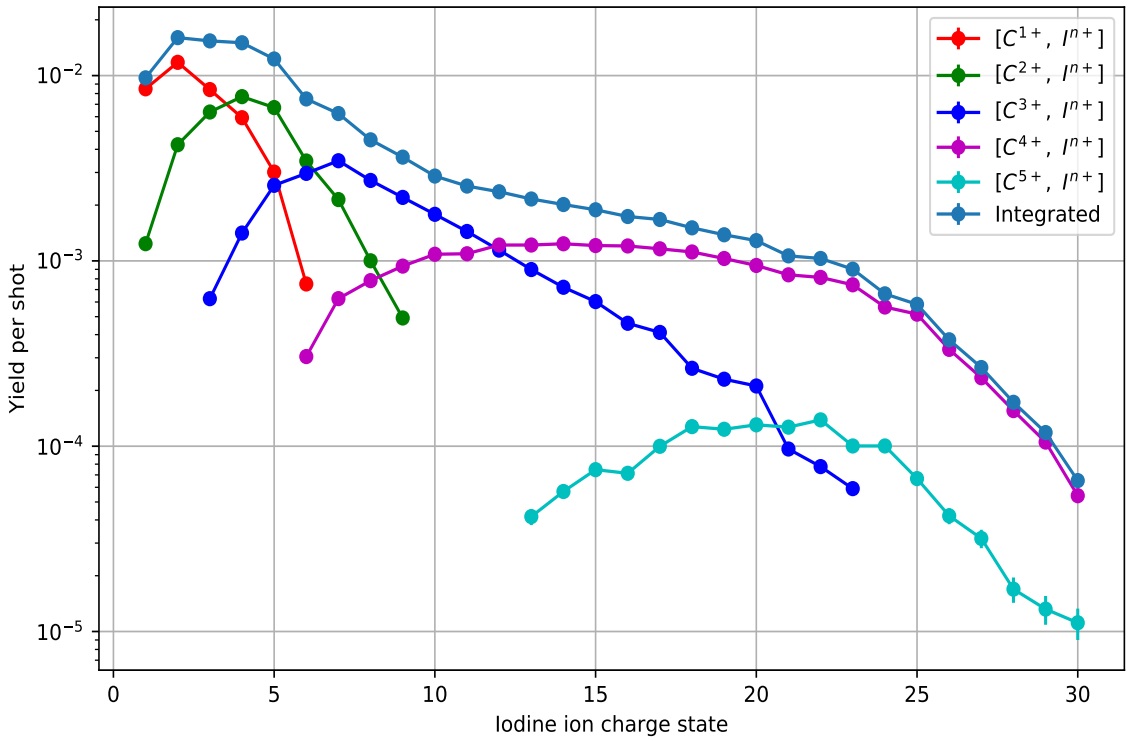

Figure 5.1: Yield per shot of products from the interaction between CH_3I molecules and 2 keV x-rays with pulse energy 1 mJ (as measured upstream of the experimental hutch) and duration 25 fs.

Since for photon energy within the range 1 keV to 10 keV, the photoabsorption cross section of iodine is about two to three orders of magnitude larger than that of carbon and hydrogen as shown in Fig. 2.5, when a molecule such as CH_3I is irradiated by ultra-intense x-rays, the sequential multiphoton ionization is localized at the iodine site. Different interaction products can be produced as the result of ionization, decay and charge rearrangement processes. Fig. 5.1 shows the per-shot yield of carbon and iodine ion pairs $[C^{m+},\ I^{n+}]$ detected in coincidence after the interaction between CH_3I molecules and 2 keV x-rays (For this experiment at the EuXFEL, the machine was operated with the effective repetition rate of $\sim$ 500 Hz, i.e., 10 trains per second each containing $\sim$ 50 pulses. The average pulse energy

is 1 mJ as measured upstream of the experimental hutch, and the estimated pulse duration is 25 fs). The carbon ion charge states range from C^{1+} to C^{5+} (C^{1+}, C^{2+}, C^{3+} and C^{4+} are mainly produced with charge rearrangement from iodine, and C^{5+} is mostly produced with x-ray ionization of C^{4+}), and the iodine ion charge states range from I^{1+} to I^{30+}. The iodine ion partner of higher-charged carbons ions tend to be also higher-charged. The dark blue curve shows the total iodine ion charge state distribution from the interaction, integrated over all carbon charge states. In general, it's expected that more photoabsorptions are needed to reach higher iodine ion charge states.

With fixed x-ray pulse parameters, there is an associated probability to get to a certain ion charge state requiring the absorption of n photons. As mentioned in section 2.4.3, such probability is not simply proportional to the photon flux to the n^{th} power, because the n absorptions are sequential rather than direct, with each absorption step starting mostly from the ground state of the remaining molecule. Since sequential multiphoton ionization is very common in XFEL pulse interaction with atoms and molecules, it's useful to build a simple model to describe this process.

Consider an arbitrary final interaction product requiring a sequence of n photoionizations from a Gaussian XFEL pulse with photon flux $F(t) = fe^{-4ln2(\frac{t}{\tau})^2}$, where f is the peak photon flux and τ is the pulse duration (full width at half maximum). And further assume an average photoabsorption cross section σ for each ionization step, which is reasonable because the x-rays mostly ionize the electrons in a particular shell of a particular element with the resulting holes refilled by decay processes. The differential probability for the sequence of n ionizations to occur at times $t_1,\ t_2,\ \ldots,\ t_n$ is

$$\begin{aligned}
\frac{dP}{dt_1 dt_2 \cdots dt_n} &= e^{-\int_{-\infty}^{t_1} F(t)\sigma dt} F(t_1)\sigma e^{-\int_{t_1}^{t_2} F(t)\sigma dt} F(t_2)\sigma \cdots e^{-\int_{t_{n-1}}^{t_n} F(t)\sigma dt} F(t_n)\sigma e^{-\int_{t_n}^{\infty} F(t)\sigma dt} \\
&= \sigma^n F(t_1)F(t_2)\cdots F(t_n) e^{-\int_{-\infty}^{\infty} F(t)\sigma dt} \\
&= e^{-\sqrt{\frac{\pi}{4ln2}}\sigma\tau f} \sigma^n F(t_1)F(t_2)\cdots F(t_n) \qquad (5.1)
\end{aligned}$$

The differential probability for the sequence of n ionizations to occur at time intervals

$\triangle t_{2,1},\ \triangle t_{3,1},\ \ldots,\ \triangle t_{n,1}$ (with $\triangle t_{n,1} = (t_n - t_1),\ i = 2,\ 3,\ \ldots,\ n$) is

$$\begin{aligned}
\frac{dP}{d\triangle t_{2,1} d\triangle t_{3,1} \cdots d\triangle t_{n,1}} &= \int_{-\infty}^{\infty}\int_{t_1}^{\infty}\cdots\int_{t_{n-1}}^{\infty} \frac{dP}{dt_1 dt_2 \cdots dt_n}\delta[\triangle t_{2,1} - (t_2 - t_1)] \\
&\quad \delta[\triangle t_{3,2} - (t_3 - t_2)]\cdots\delta[\triangle t_{n,n-1} - (t_n - t_{n-1})]dt_n \cdots dt_2 dt_1 \\
&= e^{-\sqrt{\frac{\pi}{4ln2}}\sigma\tau f}\sigma^n \int_{-\infty}^{\infty}\int_{t_1}^{\infty}\cdots\int_{t_{n-1}}^{\infty} F(t_1)\delta[\triangle t_{2,1} - (t_2 - t_1)]F(t_2) \\
&\quad \delta[\triangle t_{3,2} - (t_3 - t_2)]\cdots F(t_{n-1})\delta[\triangle t_{n,n-1} - (t_n - t_{n-1})]F(t_n) \\
&\quad dt_n \cdots dt_2 dt_1 \\
&= e^{-\sqrt{\frac{\pi}{4ln2}}\sigma\tau f}\sigma^n f^n \int_{-\infty}^{\infty} e^{\left[-\frac{-4ln2}{\tau^2}[t_1^2 + (t_1 + \triangle t_{2,1})^2 + \cdots + \right.} \\
&\quad \left.(t_1 + (\triangle t_{2,1} + \triangle t_{3,2} + \cdots + \triangle t_{n,n-1}))^2]\right] dt_1 \\
&= e^{-\sqrt{\frac{\pi}{4ln2}}\sigma\tau f}\sigma^n f^n e^{4ln2\frac{A^2 - nB}{n\tau^2}}, \qquad (5.2)
\end{aligned}$$

where $A = \triangle t_{2,1} + \triangle t_{3,1} + \cdots + \triangle t_{n,1}$ and $B = \triangle t_{2,1}^2 + \triangle t_{3,1}^2 + \cdots + \triangle t_{n,1}^2$, with $\triangle t_{2,1} \leq \triangle t_{3,1} \leq \cdots \leq \triangle t_{n,1}$.

By integrating Eq. (5.2) over all possible time intervals , the probability P_n to get to a certain interaction product requiring n-photon absorptions can be obtained:

$$P_n = ae^{-bf}f^n, \qquad (5.3)$$

where a is a constant depending on the photon number n and pulse duration τ. And $b = \sqrt{\frac{\pi}{4ln2}}\sigma\tau$.

It's convenient to rewrite the equation above in terms of per-shot ion yield Y_n which is related to P_n by $Y_n = NP_n$, with N being the number targets in the interaction volume, and pulse energy E_{pls}, which is the quantity measured in the experiment and related to the photon flux f by $E_{pls} = \frac{\tau A E_{pho}}{c_t}f$, with E_{pho} being the photon energy, A being the effective x-ray focal area, and c_t the beamline transmission coefficient:

$$Y_n = ce^{-dE_{pls}}E_{pls}^n, \qquad (5.4)$$

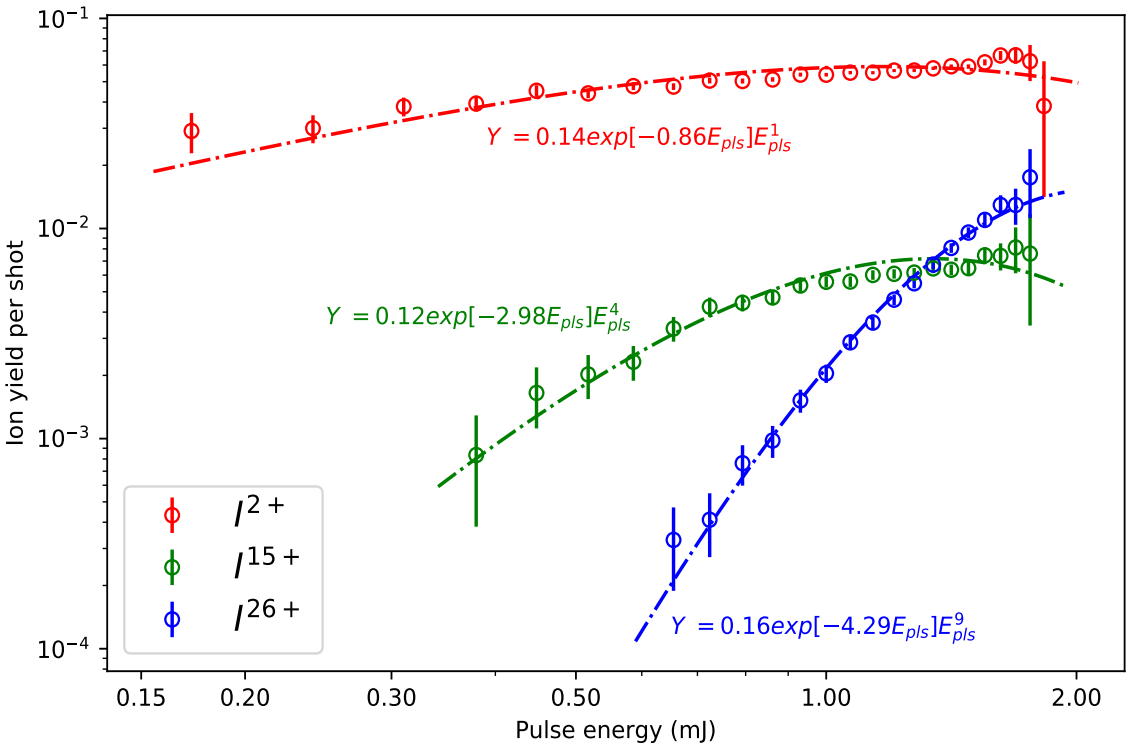

Figure 5.2: Yield of I^{2+}, I^{15+} and I^{26+} as a function of pulse energy (as measured upstream of the experimental hutch), from the interaction between CH_3I molecules and x-rays with 2 keV photon energy. These data are "non-coincident", i.e., integrated over all carbon ion charge states. Dashed lines are fittings with Eq. (5.4), with the fitted functions also displayed in the figure.

where c is the constant depending on n, τ, N, c_t and A. And $d = \frac{\sqrt{\frac{\pi}{4ln2}}\sigma c_t}{AE_{pho}}$. Eq. (5.4) can be used to describe the ion yield dependence on x-ray pulse energy. In Fig. 5.2, the per-shot yield of three representative ions I^{2+}, I^{15+} and I^{26+}, from the interaction between CH_3I molecules and x-rays with 2 keV photon energy, are plotted as a function of pulse energy as measured upstream of the experimental hutch. One photoabsorption is enough to reach I^{2+}. The number of photoabsorptions required to reach the other two charge states can be estimated with energy conservation. Take the production of I^{26+} as an example. The total energy of the neutral molecule CH_3I is approximately the sum of the energy of its atoms, which is -198.369 keV. When I^{26+} is produced, its coincident carbon partner most likely has 4 charges as shown in Fig. 5.1, and all three hydrogen fragments are also charged as will be shown in the next chapter. The total energy of all the fragments [I^{26+}, C^{4+}, 3 $\times$ H^{+}]

is -187.646 keV. The average energy of photoelectrons ionized for the production of I^{26+} is 0.599 keV. (These energy calculations were made with the Hartree-Fock method through Cowan's atomic code [139, 140].) From energy conservation, the total energy of absorbed photons subtracted by the total energy of photoelectrons, which is ($n \times 2 - n \times 0.599$) keV, should be equal to or larger (to account for radiative decay processes) than the energy change in the molecular system, which is (198.369 − 187.646) keV. The minimum of n satisfying this requirement is 8. $n = 9$ is used to account for possible radiative decays and the fact that the total energy of the neutral molecule is smaller than that estimated with the independent-atom model. (A more precise estimate of the number of photons needed to reach a particular charge state requires a detailed knowledge of the average decay pathways involved.) With n determined to be 1, 4 and 9 for I^{2+}, I^{15+} and I^{26+}, respectively, Eq. (5.4) is used to fit the experimental data. The resulting function for each charge state is displayed in Fig. 5.2. The fitting values for d contain information about the x-ray transmission, focal area and photoabsorption cross section. With x-rays at 2 keV, the photoabsorption cross section σ for the molecule is approximately that of iodine, which is about 0.4 Mbarn [52]. With the values of σ, a typical beamline transmission coefficient c_t of 0.8, and the fitting values of d for I^{2+}, I^{15+} and I^{26+}, the calculated effective focal areas are respectively about 124 μm^2, 36 μm^2 and 25 μm^2. These values are larger than the expected focal area ~ 1 μm^2, because with the applied fomula $E_{pls} = \frac{\tau A E_{pho}}{c_t} f$, the effective focal area A is the average beam area in the whole interaction region, which is larger than the focal area at the beam center. The observation that higher-charged ions have smaller effective focal areas can be attributed to the fact that such ions require higher x-ray intensity and hence are produced in a more confined region around the x-ray focus. If the beamline transmission and effective focal area are known, the fitting value for d can also be used to calculate the photoabsorption cross section.

According to Eq. (5.4), in the low pulse energy range (E_{pls} is close to zero), the yield of a particular charge state requiring n photoabsorptions follows the "power law", i.e., $Y_n \propto E_{pls}^n$. When pulse energy gets higher, the exponential factor $e^{-dE_{pls}}$ becomes non-negligible, ion yield starts to saturates and eventually decreases with increasing pulse energy. It can be

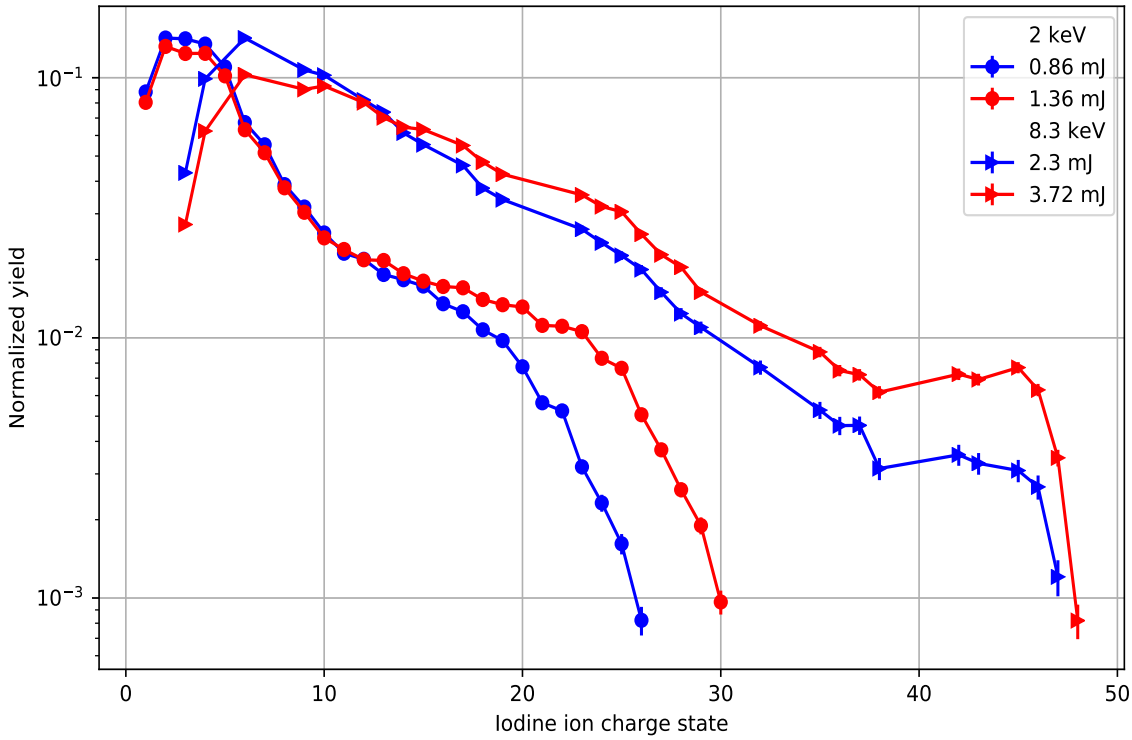

Figure 5.3: Iodine ion charge state distributions for 2 keV x-ray (with pulse duration 25 fs, pulse energy 0.86 mJ and 1.36 mJ), and 8.3 keV x-ray (with pulse duration 30 fs, pulse energy 2.3 mJ and 3.72 mJ) ionization of CH_3I molecules. The pulse energy values are measured by the gas monitor detectors upstream of the experimental hutch.

imagined that if the pulse energy continues to increase, at some point all other ion charge states are depleted, except these energetically achievable highest charge states which can not be further ionized and are left as the final interaction products. In the work of this thesis, the depletion mainly occurs for low charge states which requires one photoabsorption. For high charge states, its yield follows the power law or enters the saturation regime with increasing pulse energy. This explains the observation in Fig. 5.3 that more yield of high charge states are produced with larger pulse energy, with the low charge states yield getting relatively less.

This simple model of sequential multiphoton ionization applies to ultra-intense x-ray ionization of both atoms and molecules. The average photoabsorption cross section σ used in this model is the average of photoabsorption cross sections for all the ionization steps during the interaction. Such photoabsorption cross sections are discussed in the sense of stable electronic structures. It's in general applicable to the sequential absorptions, with each step

starting mostly from the ground state of the remaining molecule. With XFEL pulses, it's possible that the next photoabsorption happens when the system is still undergoing the dynamical processes induced by the last photoabsorption. So the cross section for the sequential photoabsorptions is time-dependent and influenced by the ionization-induced dynamics. For example, it's possible that, at some time point within the very intense XFEL pulse, the next photoabsorption will be less likely to occur if the core hole created by the previous ionization has not been refilled even though the next photon is ready for absorption. This effect, which is called "intensity-induced transparency" [1] or "frustrated absorption" [141] makes the photoabsorption cross section effectively lower. An experimental consequence is that with the same pulse energy, the shorter pulses produce less higher-charged states than longer ones, because shorter pulses are more intense and the amount of their photons wasted by the effect of "intensity-induced transparency" is larger.

With molecules, the ionization can also induce nuclear motions and charge rearrangement, which can in turn change the cross section for the next photoabsorption. With more photoabsorptions and increasing chare states, the binding energy of inner shell electrons gets larger. At some charge state, the electron binding energy becomes larger than the photon energy. This is typically the highest charge state reachable because further ionization is energetically forbidden. However, with appropriate photon energies, if the high charge states are reached within the pulse duration, it's possible that these electrons can be resonantly excited to high-lying orbitals, which can result in more electrons ejected through Auger decay. How ultra-intense x-ray ionization of molecules is affected by charge rearrangement and resonances will be discussed in the next two subsections.

5.1.2 Charge-rearrangement-enhanced ionization

According to the independent-atom model, the distribution of the total charge of all ionic fragments, from ionization of molecules by XFEL pulses, is expected to be the same as the one obtained from the ionization of corresponding isolated atoms. For CH_3I molecules ionized by 8.3 keV x-rays (with pulse duration 30 fs, pulse energy in the interaction region

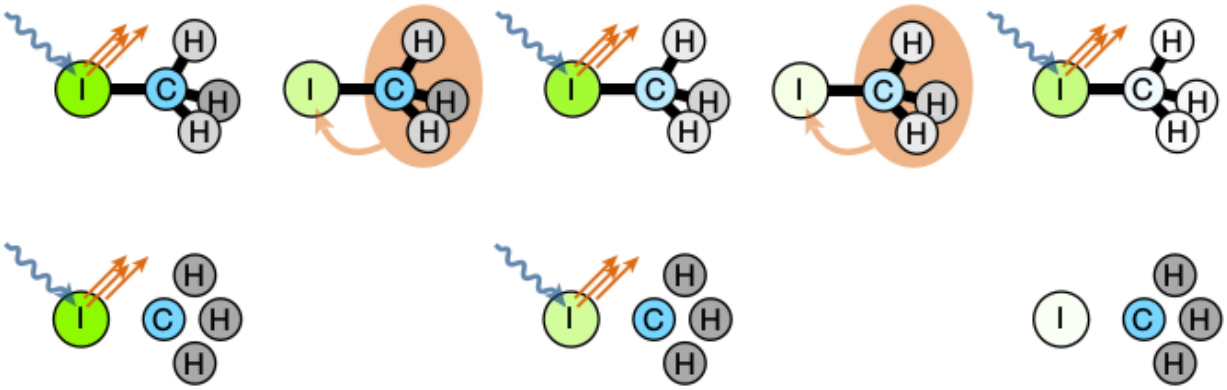

Figure 5.4: Illustration of the mechanism of "Charge-Rearrangement-Enhanced X-ray Ionization of Molecules". In the molecule (upper row), the repeated ionization (blue and orange arrows) of the iodine atom drives electrons from the methyl group to the iodine (orange shading), such that there are more electrons available for ionization compared to independent atoms (lower row). The darkness of the shading of the atoms indicates the number of electrons that remain in the atoms. Adapted from [43].

1.1 mJ and focal area $\sim 0.01\ \mu m^2$), given that the iodine photoabsorption cross section is two to three orders of magnitude larger than that of the methyl group, the ionization almost exclusively occurs at the iodine site, with carbon and hydrogen obtaining charges through charge rearrangement. So with the independent-atom model, the distribution of the total charge of all ionic fragments is expected to be the same as the charge state distribution from the ionization of isolated iodine atoms with the same x-ray pulses.

In the experiment, isolated xenon atoms were used as substitute targets for iodine because the two have similar electronic structures with an atomic number difference of 1. The iodine ion charge state distribution from ionization of CH_3I molecules is plotted in Fig. 5.5 with that of xenon ions produced from ionization of xenon atoms under the same x-ray conditions. The highest iodine ion charge state is around I^{47+}, about the same as that of xenon. Since iodine ions with more than 25 charges are detected exlusively with C^{4+} (see Fig. 5.6), and assuming one charge for each hydrogen, the maximally achieved total charge of the molecule is 54 ($I^{47+} + C^{4+} + 3 \times H^+$), which is much larger than 47 which is the highest charge number of xenon ions.

Such observation, that a higher charge state is reached by the molecule than its atomic counterpart, is due to the effect of "Charge-Rearrangement-Enhanced X-ray Ionization of

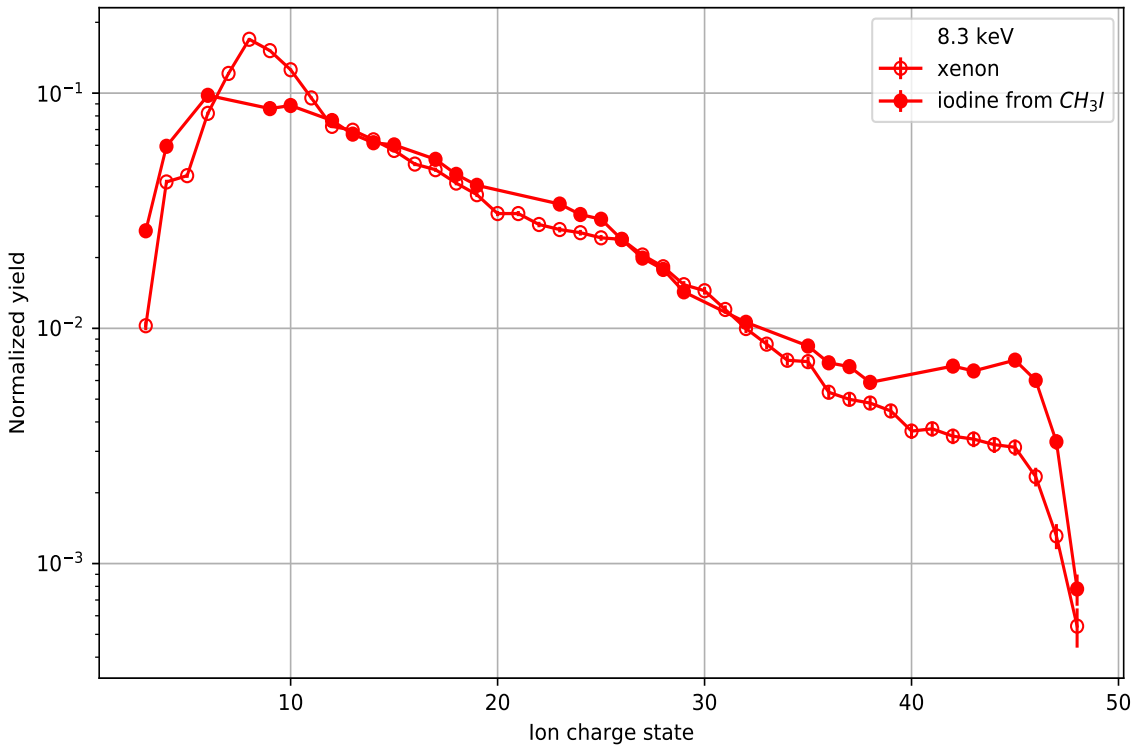

Figure 5.5: Ion charge state distributions from 8.3 keV x-ray ionization of xenon atoms and CH_3I molecules. The iodine data for CH_3I are non-coincident (i.e., integrated over all carbon ion charge states). The x-ray pulse duration is 30 fs and pulse energy is 1.1 mJ in the interaction region.

Molecules" (CREXIM) [43], which is not contained in the independent-atom model. The essence of the CREXIM effect is that the electrons, initially localized at the elements which are not interacting with x-rays, are transferred to the x-ray absorbing-site and participate in the photoionization and decay processes, resulting in more electrons ejected from the molecule. This effect plays a noticeable role when the x-ray intensity is so high (as is the case for the current experiment) that the total charge of the molecule is limited by the number of electrons available for the ionization and decay processes.

As will be shown in section 5.4.2, the charge rearrangement can not only enhance the ionization of molecules as compared to the independent-atom model, but also enhance the ionization of the x-ray-absorbing atom as compared to when it is not in the molecular environment. We call the latter effect "Extended Charge-Rearrangement-Enhanced X-ray Ionization of Molecules".

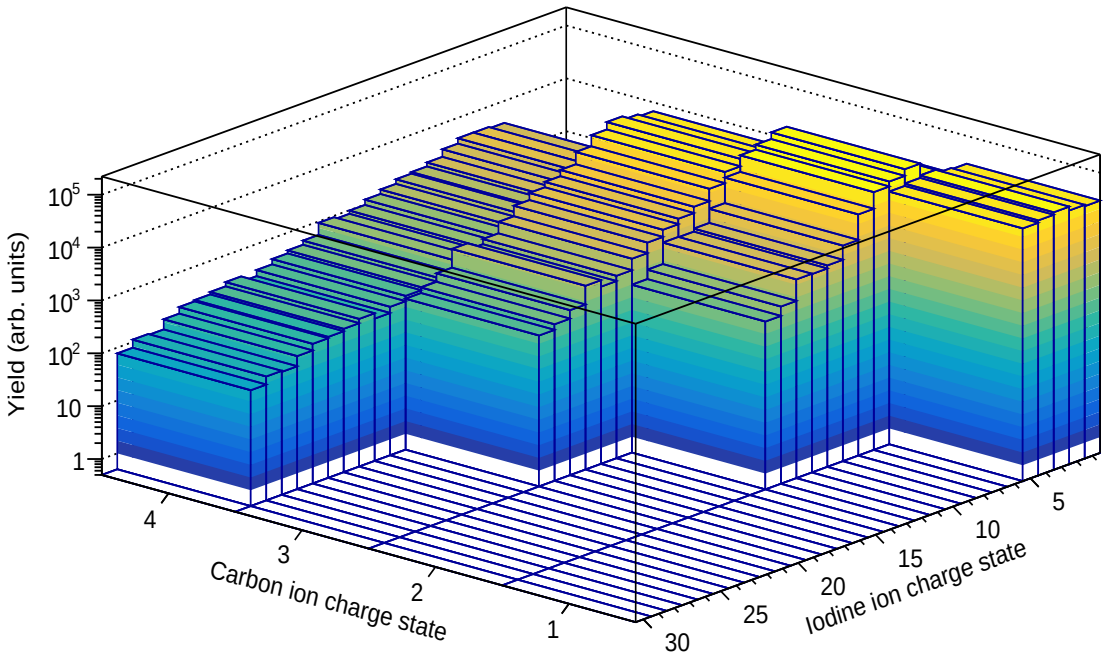

Figure 5.6: Yield of carbon and iodine ion pairs detected in coincidence from 8.3 keV x-ray ionization of CH_3I molecules. The x-ray pulse duration is 30 fs and pulse energy is 0.4 mJ in the interaction region.

5.1.3 Resonance-enhanced ionization

In the last two subsections, the photon energy is in the range such that the sequential photoionizations can continue until at some charge state the photon energy is below the increasing inner-shell electron binding energies. For example, with x-rays at 2 keV, the highest charge state ($\sim$ 32+) in the top plot of Fig. 5.7 is reached when the binding energy of the remaining 3d electrons becomes larger than 2 keV, as shown in Fig. 5.8. However, if the charge state for which the photon energy is below the ionization threshold is reached relatively early within the XFEL pulse, and the x-ray can resonantly excites the inner-shell electrons to high-lying orbitals, even higher charge states can be reached by the so-called "Resonance-Enabled X-ray Multiple Ionization" (REXMI). This phenomenon was first reported for 1.5 keV x-ray interaction with xenon atoms [5]. Here, the first observation of REXMI in the molecular case for the interaction between CH_3I molecules and x-rays at

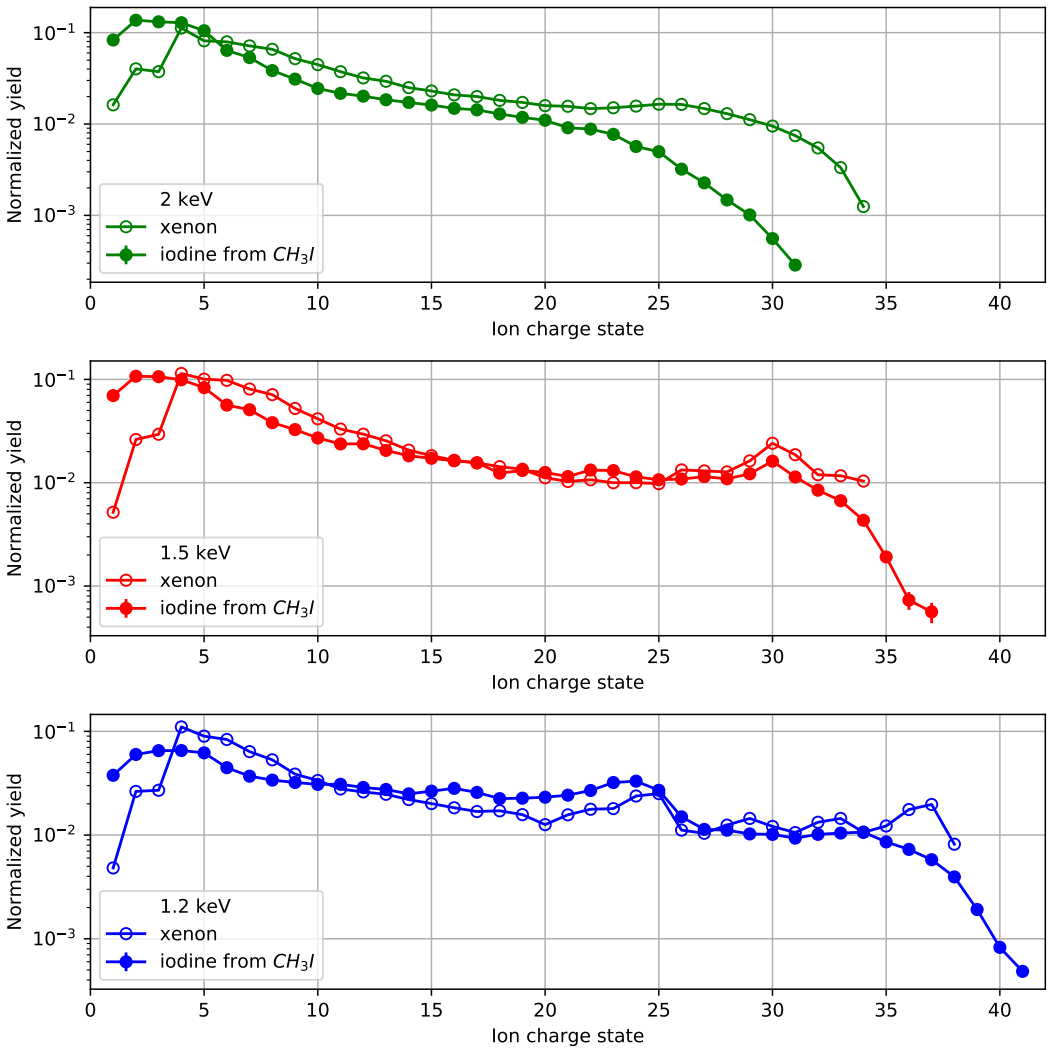

Figure 5.7: Ion charge state distributions from soft x-ray ionization of xenon atoms and CH_3I molecules. The iodine data for CH_3I are non-coincident (i.e., integrated over all carbon ion charge states). For x-rays with photon energies 2 keV, 1.5 keV and 1.2 keV, the pulse duration is 25 fs, and the pulse energies are 1.1 mJ, 1.9 mJ and 3 mJ, respectively. Pulse energy is measured by the gas monitor detector upstream of the experimental hutch.

1.2 keV and 1.5 keV is reported. Xenon, which has a similar electronic structure and hence resonance enhancement as those of iodine, is used a reference. The charge state distributions for both xenon ions and iodine ions from CH_3I are shown together in Fig. 5.7.

At 1.2 keV, the photons mainly interact with the M (n=3) shell electrons. The REXMI at 1.2 keV is illustrated in Fig. 5.8 based on the calculated energy levels of iodine ions at different charge states. When iodine is ionized to I^{8+}, I^{14+} and I^{21+}, the photon energy

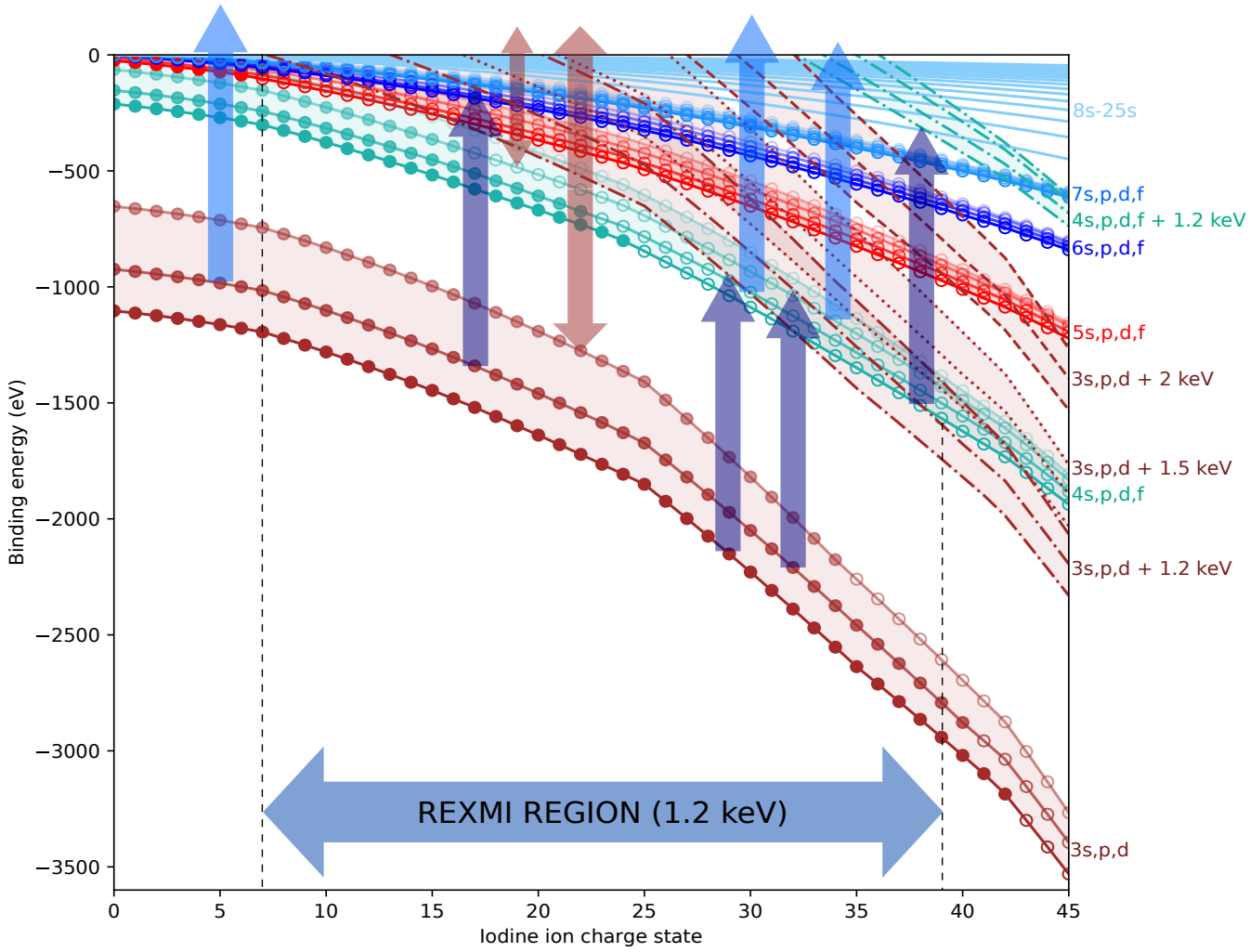

Figure 5.8: Iodine ion energy levels at different charge states and illustration of the "Resonance-Enabled X-ray Multiple Ionization" mechanism for x-rays at 1.2 keV. The energy levels are calculated by Hartree-Fock method with relativistic effect included through Cowan's atomic code [139, 140]. The light blue arrow represents photoionization, the dark blue arrow represents resonant excitation, and the brown arrows represent the Auger process.

becomes lower than the ionization thresholds of 3s, 3p and 3d electrons, respectively. Starting from these charge states, the electrons from the corresponding orbitals can be resonantly excited to densely-packed Rydberg states shown in light-sky blue and high-lying unoccupied orbitals with principal quantum numbers n = 7, 6, 5. These resonantly-excited electrons can initiate Auger decay processes ejecting more electrons out of the molecule. The electrons de-excited to the n=4 shell can be further ejected by photoionization. The resonance excitation

region ends at about I^{39+}, above which the 3p electrons cannot be energetically photo-excited to the 4s orbital, which explains the extremely low yield of the two highest charge states I^{40+} and I^{41+} in the experiment. Note that the contribution of the excitation from 3d to 4f or 4p orbital is expected to be much smaller than those excitation from 3p to 4s or 4d orbital, because no 3d electrons are left in the ground state configuration (as shown by the hollow circle) when the 3d to 4f becomes energetically possible at I^{37+}. Only the excited state configuration having electrons in the 3d orbital or decay processes filling electrons into 3d holes can make the transition from 3d to 4f or 4p orbital happen, which is less probable. The electron energy level change as a function of charge state is reflected in the structures of xenon and iodine charge state distributions. For example, the yield decrease at around I^{25+} is because at I^{24+}, 3p electrons can not be excited to 5d orbital anymore and at I^{26+} they start not to be excited to 5s orbital.

At 1.5 keV, the photons also mainly interact with the M (n=3) shell electrons. The resonance enhancement can be explained similarly as that for 1.2 keV, except that the degree of enhancement at different charge states changes because the photon energy is changed. The resonant excitation from n = 3 to n = 4, which is possible at 1.2 keV, doesn't contribute with 1.5 keV x-rays anymore, because such excitation only becomes possible at very high charge states (I^{41+}) which can't be reached by previous electron ejections. With previous ejections, the highest charge state reachable is I^{37+} at which the resonant excitation from 3d to 5p is not possible anymore. I^{37+} is also the highest charge state observed in the experiment.

Despite the general resemblance between iodine ion charge state distributions and those of xenon in Fig. 5.7, yield differences can still be discerned at some particular charge states due to the molecular effects as shown by Fig. 5.9. At 1.5 keV, the iodine ion charge state distribution shows broad peak at around I^{23+}, which is not present for that of xenon. This peak is at the states about 7 charges lower than the peak at around I^{30+} which appears in both distributions. A similar observation can be made for 1.2 keV. The iodine ion charge state distribution shows broad peak at around I^{16+}, which is again not present for that of xenon. Again, this peak is at the states about 7 charges lower than the peak at around I^{23+} which appears in both iodine and xenon ion charge state distributions. These findings can be

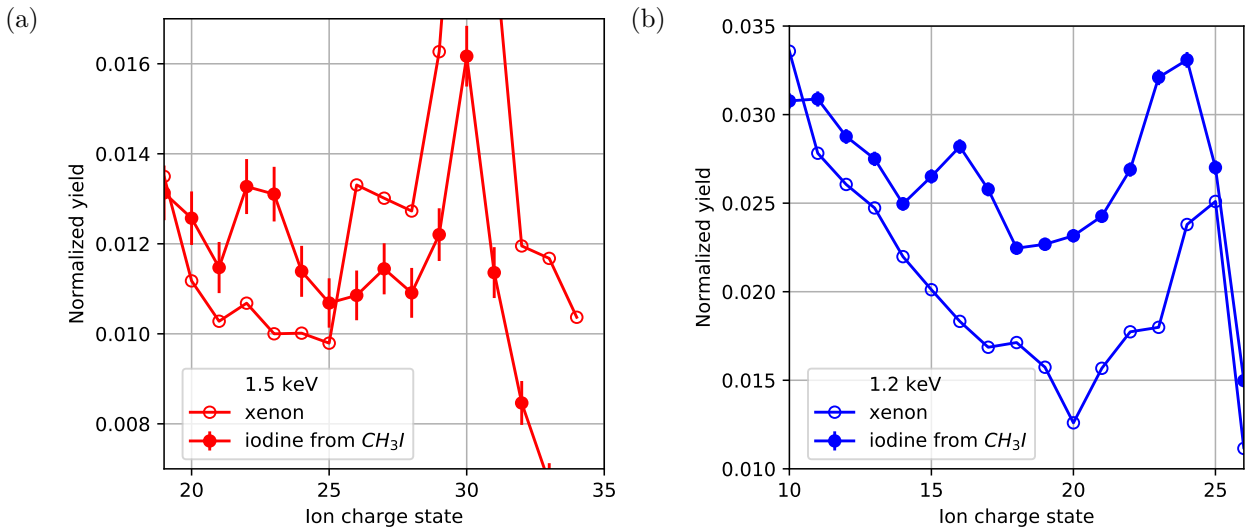

Figure 5.9: New resonance enhancement regions, present in the charge state distributions of the molecular case, but absent in the atomic case. (a) At 1.5 keV photon energy and for the molecular case, new enhancement region appears around I^{23+} which is 7 charge states lower than I^{30+} around which the major enhancement is located. (b) At 1.2 keV photon energy and for the molecular case, new enhancement region appears around I^{16+} which is 7 charge states lower than I^{23+} around which the major enhancement is located.

explained qualitatively with the charge transfer picture. 7 is the total number of electrons transferable from the the methyl group to iodine site. If iodine is not in the molecular environment, the bigger resonance enhancement only appears at around I^{30+} and I^{23+} for 1.5 keV and 1.2 keV respectively, but by transferring 7 electrons from methyl group to iodine, a bigger enhancement also appears at around $I^{23=}$ for 1.5 keV and I^{16+} for 1.2 keV.

5.2 Charge rearrangement

In general, x-rays mainly interact with a particular site in a molecules such as iodine site in CH_3I. With electrons ejected from the iodine site by sequential photoionizations discussed in the last section, a charge imbalance is created between the iodine site and its partner, the methyl group (CH_3). This charge imbalance can drive electron transfer from the methyl group to iodine. The charge transfer process depends on the number of charges on both sides, as well as their distance. For a particular ion pair with certain number of charges on each ion, the critical distance above which charge transfer is forbidden can be predicted by

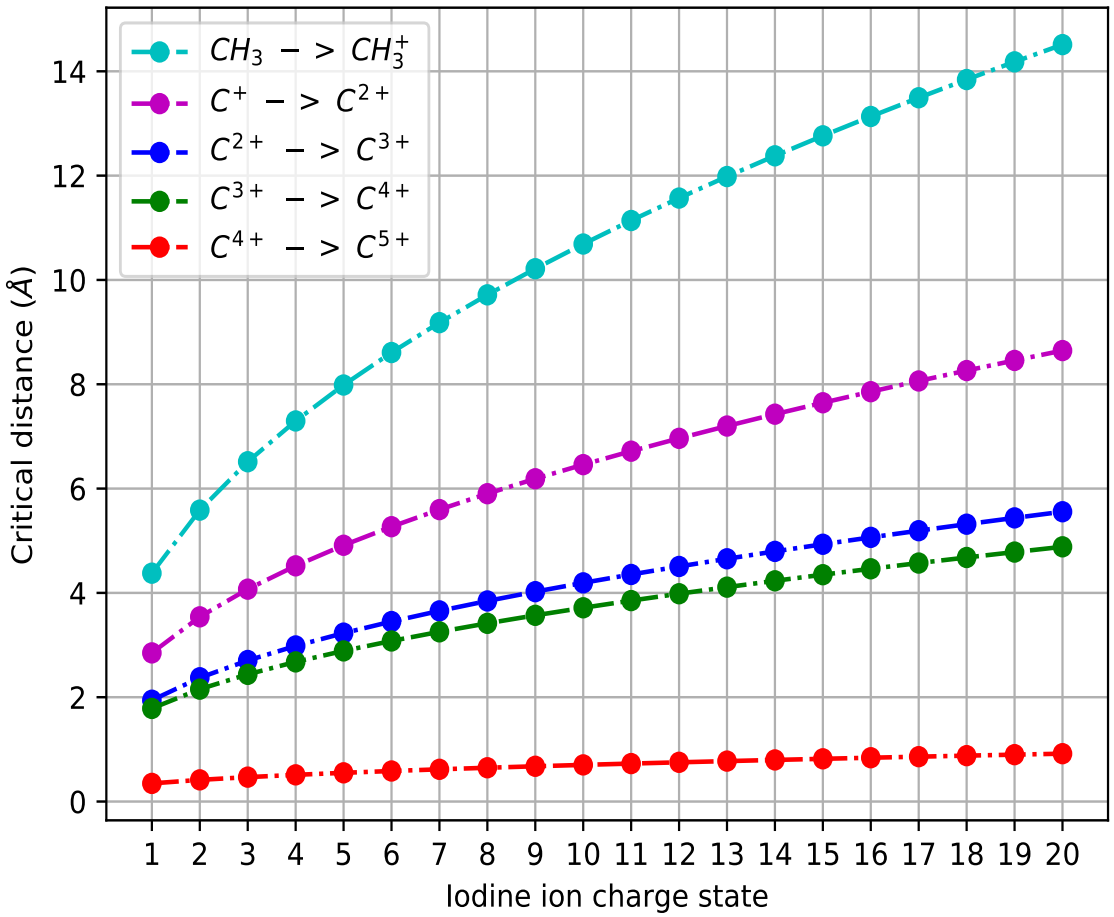

Figure 5.10: Critical distances predicted by the classical "over-the-barrier" model for electron transfers from CH_3, C^+, C^{2+}, C^{3+} and C^{4+} to iodine ions with charges ranging from 1 to 20. With each charge transfer, methyl group or carbon ions gain one more charge, as shown by the labels.

the classical "over-the-barrier" model discussed in subsection 2.4.7, and calculated with the formula

$$R_{DA,crit} = \frac{p + 1 + 2\sqrt{q(p+1)}}{E_{binding}}, \tag{5.5}$$

with p the charge of methyl group or carbon ion, q the iodine charge and $E_{binding}$ the electron binding energy of methyl group or carbon ion. With the electron binding energies [142, 143] 9.86 eV, 24.38 eV, 47.89 eV, 64.49 eV and 392.09 eV for CH_3, C^+, C^{2+}, C^{3+} and C^{4+}, respectively, the critical distances for electron transfer from them to iodine with charges

ranging from 1 to 20 are calculated and shown in Fig. 5.10. As expected, both higher iodine charge and lower carbon charge can make the critical distance larger. For electron transfer from C^{3+} to iodine to happen, the C-I distance has to be smaller than ~ 5 $\mathring{A}$ when iodine has 20 charges and ~ 2.16 $\mathring{A}$ when iodine has 2 charges. Given the equilibrium C-I distance ~ 2.14 $\mathring{A}$ [144], in order to make the electron transfer from C^{3+} to iodine more likely to happen, the sequential ionization of iodine must happen very fast so that iodine gain enough charges without the two nuclei moving too far apart. The charge transfer from C^{4+} to iodine site is classically forbidden because the corresponding critical distances are below the equilibrium C-I distance ~ 2.14 $\mathring{A}$, as shown by the red curve in Fig. 5.10. This is the reason why C^{5+} is not observed in the 8.3 keV x-ray experiment discussed in subsection 5.1.2. The presence of C^{5+} in the 2 keV x-ray experiment, as shown in Fig. 5.1, is due to the non-negligible direct x-ray ionization of carbon because of its increased photoabsorption cross sections at low photon energies.

5.3 Fragmentation and rate of ionization

With fast electron ejections from the iodine site and charge transfers to the methyl group, a CH_3I molecule can be rapidly charged up, leading to the fragmentation of the molecule. As will be discussed in the next chapter, due to the extremely rapid charge-up process enabled by the ultra-intense XFEL pulse, the fragmentation process can be well described by the Coulomb explosion model, making XFELs promising tools for Coulomb explosion imaging of ultrafast molecular dynamics.

In this section, how the fragmentation depends on pulse energy and pulse duration, and how such dependence reflects the ionization process (in particular, the ionization rate) will be discussed.

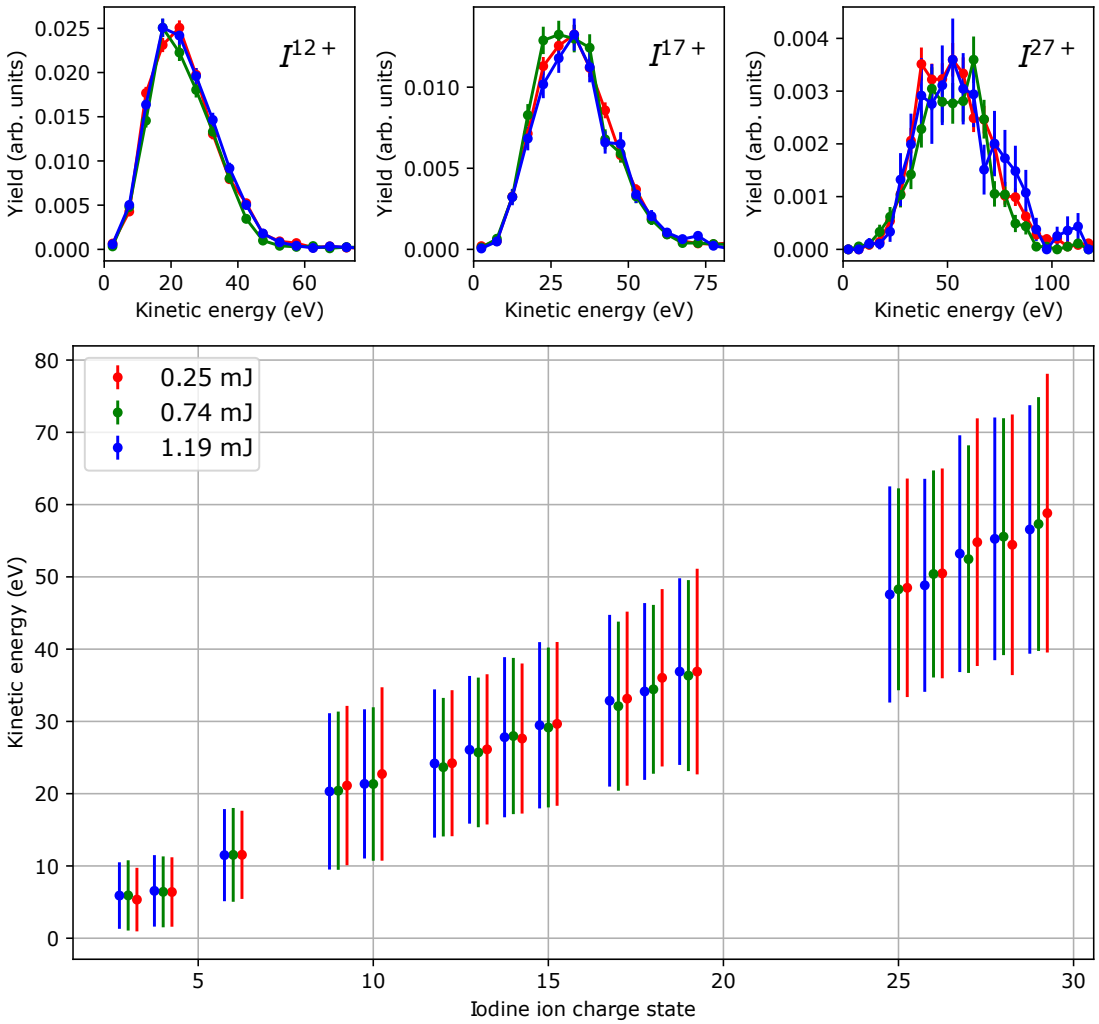

Figure 5.11: Kinetic energy of iodine ions from ionization of CH_3I molecules by x-rays at 3 different pulse energies (0.25 mJ, 0.74 mJ, and 1.19 mJ in the interaction region) and fixed pulse duration (30 fs). The top row displays kinetic energy distributions of 3 representative iodine ions. The bottom panel shows the average kinetic energy of iodine ions. The vertical bars in the bottom plot are the widths (standard deviations) of the ion kinetic energy distributions.

5.3.1 Fragmentation dependence on pulse energy and duration

To study the pulse energy and pulse duration dependence of fragmentation, the experiment with CH_3I molecules and 8.3 keV x-rays was repeated at varying pulse energies (0.25 mJ, 0.74 mJ, and 1.19 mJ in the interaction region) while keeping the pulse duration (30 fs) fixed, and at varying pulse durations (20 fs, 30 fs, and 60 fs) while keeping the pulse energy (0.37 mJ in the interaction region) fixed.

With increasing pulse energy and fixed pulse duration, the ion fragments on average are expected to reach higher kinetic energies due to the larger ionization rate, which results in shorter internuclear distances for a given ionization step and thus stronger Coulomb repulsion [145]. However, rather counterintuitively, the measured iodine ion kinetic energy plotted in Fig. 5.11 shows no dependence on the x-ray pulse energy.

This observation is the result of the interplay between photoionization, fragmentation and the pulse duration, which can be explained by the following qualitative picture. Because the rate for a single ionization increases with the intensity, a specific charge state is on average reached faster with the high-energy pulse. So this charge state is produced at an earlier time within the high-energy pulse. But on average, if this charge state is not the highest energetically reachable state, it will continue to be ionized to higher charge state until at the end of the pulse when there is no photon available anymore to get absorbed. So the time it takes to reach a certain final charge state is on average mainly determined by the pulse duration τ, which effectively set the ionization rate to be $\sim \frac{n}{\tau}$, with n the number of photonizations. Because the pulse duration is kept the same for the 3 cases in Fig. 5.11, even if they have different pulse energies, fluences and intensities, the corresponding kinetic energy distributions are still almost identical to one and another.

The pulse duration as an effective parameter to define the ionization rate and hence the fragment energy is further confirmed by Fig. 5.12, where the kinetic energy of iodine ions produced by x-rays of the same pulse energy (0.37 mJ) but different pulse durations are compared. It can be observed that for charge states above I^{9+}, which are created predominantly by absorption of more than one photon, shorter pulses produce higher-energy iodine ions. The larger kinetic energy of iodine ions and hence the larger ionization rate to produce such ions with shorter pulses than with longer ones are consistent with the conclusion reached from the qualitative picture that the average ionization rate leading to a certain interaction product is inversely proportional to the pulse duration.

In the next subsection, the pulse parameter dependence of fragmentation and average rate of ionization will be quantitatively discussed by continuing with the simple sequential ionization model introduced in section 5.1.1.

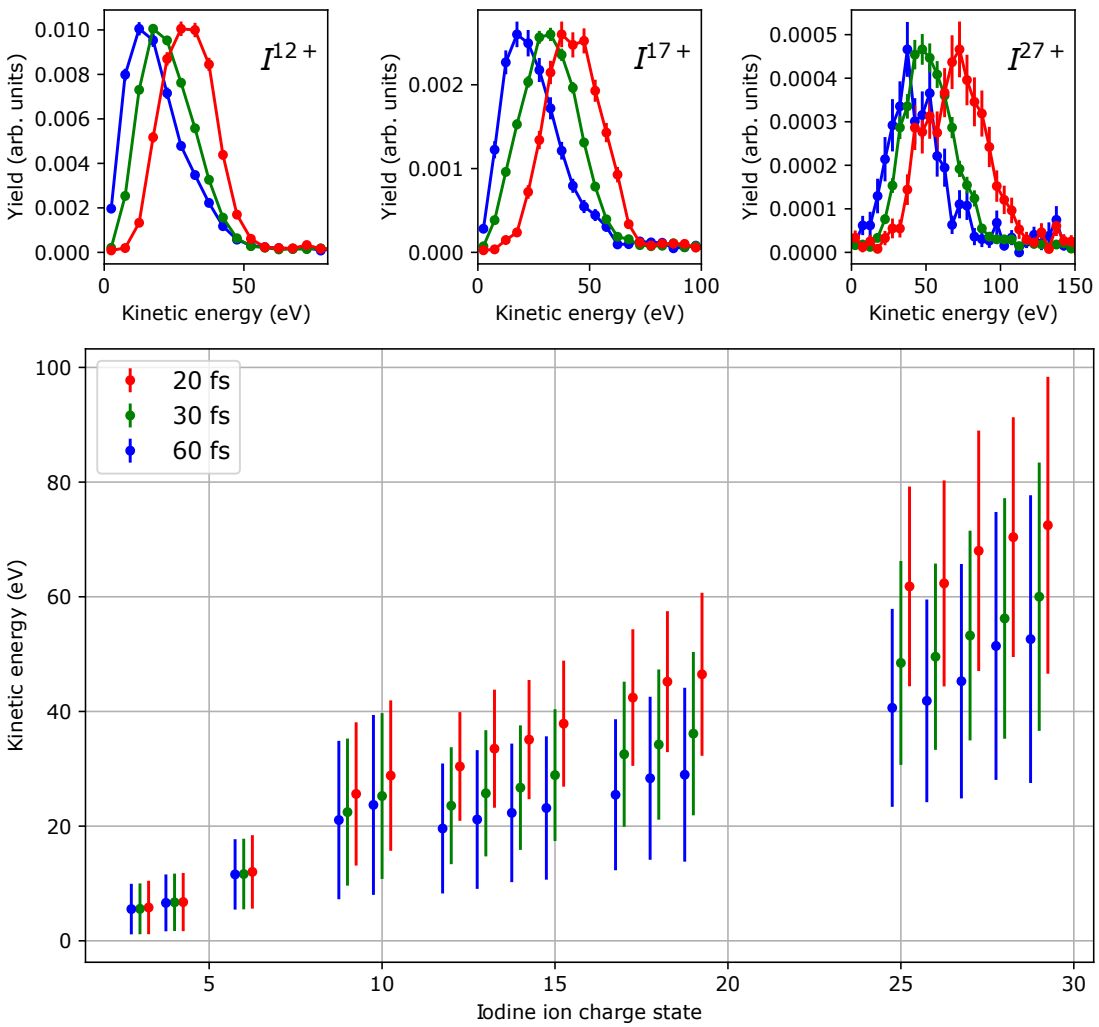

Figure 5.12: Kinetic energy of iodine ions from ionization of CH_3I molecules by x-rays at 3 different pulse durations (20 fs, 30 fs, and 60 fs) and fixed pulse energy (0.37 mJ in the interaction region). The top row displays kinetic energy distributions of 3 representative iodine ions. The bottom panel shows the average kinetic energy of iodine ions. The vertical bars in the bottom plot are the widths (standard deviations) of the ion kinetic energy distributions.

5.3.2 Average rate of ionization

Continuing with Eq. (5.2), and by normalizing $\frac{dP}{d\triangle t_{2,1} d\triangle t_{3,1} \cdots d\triangle t_{n,1}}$, such that

$$\begin{aligned}
&\int_0^{\infty} \int_0^{\triangle t_{n,1}} \cdots \int_0^{\triangle t_{3,1}} G_n \frac{dP}{d\triangle t_{2,1}\ d\triangle t_{3,1} \cdots d\triangle t_{n,1}} d\triangle t_{2,1} \cdots d\triangle t_{n-1,1} d\triangle t_{n,1} \\
&= \int_0^{\infty} \int_0^{\triangle t_{n,1}} \cdots \int_0^{\triangle t_{3,1}} C_n e^{4ln2 \frac{A^2 - nB}{n\tau^2}}\ d\triangle t_{2,1} \cdots d\triangle t_{n-1,1} d\triangle t_{n,1} \\
&= 1, \qquad (5.6)
\end{aligned}$$

the probability distribution $D_n(\triangle t_{2,1},\ \triangle t_{3,1},\ \cdots,\ \triangle t_{n,1})$ of the time interval sequence $\triangle t_{2,1}$, $\triangle t_{3,1}, \cdots, \triangle t_{n,1}$ can be obtained as

$$D_n(\triangle t_{2,1},\ \triangle t_{3,1},\ \cdots,\ \triangle t_{n,1}) = C_n e^{4ln2 \frac{A^2 - nB}{n\tau^2}}, \qquad (5.7)$$

where C_n is the normalization constant which does not depend on the peak intensity f and the cross section σ because they are only in the constant $e^{-\sqrt{\frac{\pi}{4ln2}}\sigma\tau f}\sigma^n f^n$ of the unnormalized Eq. (5.2) and are canceled out with the normalization procedure. So the probability distribution $D_n(\triangle t_{2,1},\ \triangle t_{3,1},\ \cdots,\ \triangle t_{n,1})$ in Eq. (5.12) only depends on the pulse duration τ, which makes the average ionization rate to be derived from this probability distribution only depends on the pulse duration as well, explaining the observations made in the last subsection. It's worth noting that $\frac{1}{G_n}$ is the probability for the n photoionizations to happen, which increases with the peak intensity f as discussed in section 5.1.1. So in summary, the sequential n-photon ionization becomes more likely with larger peak intensity, but the average ionization rate for n ionizations stays the same as long as the pulse duration is not changed.

In the following, Eq. (5.12) will be applied to the specific cases with two and three photoionizations. With two sequential photoionizations, the probability distribution for the

time interval $\triangle t_{2,1}$ is

$$D_2(\triangle t_{2,1}) \;=\; C_2 e^{-2ln2\frac{\triangle t_{2,1}^2}{\tau^2}}, \tag{5.8}$$

with the normalization constant $C_2 \;=\; \frac{2\sqrt{2ln2}}{\sqrt{\pi}\tau}$. From Eq. (5.8), the average time interval between the two photoionizations is

$$\begin{aligned}\overline{\triangle t_{2,1}} \;&=\; \int_0^\infty \triangle t_{2,1} D_2(\triangle t_{2,1})\; d\triangle t_{2,1} \\ &=\; \frac{\tau}{\sqrt{2\pi ln2}},\end{aligned} \tag{5.9}$$

which gives the ionization rate $\sqrt{2\pi ln2}\frac{1}{\tau}$. So if a certain interaction product is created with two photoionizations by a 30 fs XFEL pulse, the average time interval $\overline{\triangle t_{2,1}} \;=\; \frac{1}{\sqrt{2\pi ln2}} \;\times$ $30\ fs \approx\ 14\ fs$, with the corresponding average ionization rate about 0.07 fs^{-1}.

With three sequential photoionizations, the probability distribution for the time intervals $\triangle t_{2,1}$ and $\triangle t_{3,1}$ is

$$D_3(\triangle t_{2,1},\ \triangle t_{3,1}) \;=\; C_3 e^{-4ln2\frac{-2\triangle t_{2,1}^2\ +\ 2\triangle t_{2,1}\triangle t_{3,1}\ -\ 2\triangle t_{3,1}^2}{3\tau^2}}, \tag{5.10}$$

with the normalization constant $C_3 \;=\; \frac{48ln2}{\sqrt{3}\pi\tau^2}$. From Eq. (5.10), the average time interval between the first and last photoionizations can be calculated

$$\begin{aligned}\overline{\triangle t_{3,1}} \;&=\; \int_0^\infty \int_0^{\triangle t_{3,1}} \triangle t_{3,1} D_3(\triangle t_{2,1},\ \triangle t_{3,1})\; d\triangle t_{2,1} d\triangle t_{3,1} \\ &=\; \frac{3}{2\sqrt{2\pi ln2}}\tau,\end{aligned} \tag{5.11}$$

which gives the ionization rate $\frac{2\sqrt{2\pi ln2}}{3}\frac{2}{\tau}$. So if a certain interaction product is created with three photoionizations by a 30 fs XFEL pulse, the average time interval $\overline{\triangle t_{3,1}} \;=\; \frac{3}{2\sqrt{2\pi ln2}} \;\times$ $30fs \;\approx\; 22\ fs$, with the corresponding average ionization rate about 0.09 fs^{-1}.

The average time intervals and average ionization rate for larger number of sequential photoionizations can be calculated analogously as for the sequential three photoionization.

Without calculating $\overline{\triangle t_{n,1}}$, it can be shown in the following to be inversely proportional to the pulse duration τ.

Introducing the scaled time interval $\triangle t'_{i,1} = \frac{\triangle t_{i,1}}{\tau}$, with $i = 2,\ 3,\ \cdots,\ n$, the distribution for these scaled time intervals is

$$D'_n(\triangle t'_{2,1},\ \triangle t'_{3,1},\ \cdots,\ \triangle t'_{n,1}) = C'_n e^{4ln2\frac{A'^2 - nB'}{n}}, \tag{5.12}$$

where C'_n is the normalization constant which does not depend on τ, $A' = \triangle t'_{2,1} + \triangle t'_{3,1} + \cdots + \triangle t'_{n,1}$ and $B' = \triangle t'^2_{2,1} + \triangle t'^2_{3,1} + \cdots + \triangle t'^2_{n,1}$, with $\triangle t'_{2,1} \leq \triangle t'_{3,1} \leq \cdots \leq \triangle t'_{n,1}$. Since $D'_n(\triangle t'_{2,1},\ \triangle t'_{3,1},\ \cdots,\ \triangle t'_{n,1})$ doesn't depend on τ, so doesn't the average time interval $\overline{\triangle t'_{n,1}}$ which can be obtained with

$$\begin{aligned}\overline{\triangle t'_{n,1}} = \int_0^\infty \int_0^{\triangle t'_{n,1}} \cdots \int_0^{\triangle t'_{3,1}} \triangle t'_{n,1} D'_n(\triangle t'_{2,1},\ \triangle t'_{3,1},\ \cdots,\ \triangle t'_{n,1}) \\ d\triangle t'_{2,1} \cdots d\triangle t'_{n-1,1} d\triangle t'_{n,1}.\end{aligned} \tag{5.13}$$

The unscaled average time interval is then $\overline{\triangle t_{n,1}} = \overline{\triangle t'_{i,1}}\tau \propto \tau$. So the average ionization rate for the n-photon ionizations is proportional to $\frac{1}{\tau}$.

5.4 Interplay between ionization, fragmentation and charge rearrangement

In section 5.3, it was shown that the average kinetic energy of an ion fragment depended on the average ionization rate to reach it, which in turn had an inversely proportional relation with the pulse duration τ. This makes ions produced with shorter pulses have higher kinetic energies. In this section, charge rearrangement will join the interplay. The change of pulse duration is found to influence charge rearrangement efficiency as well, through the pulse duration effect on ionization and fragmentation discussed in the last section. In turn, the change of charge rearrangement efficiency can affect the ionization process.

5.4.1 Pulse duration dependence of charge rearrangement

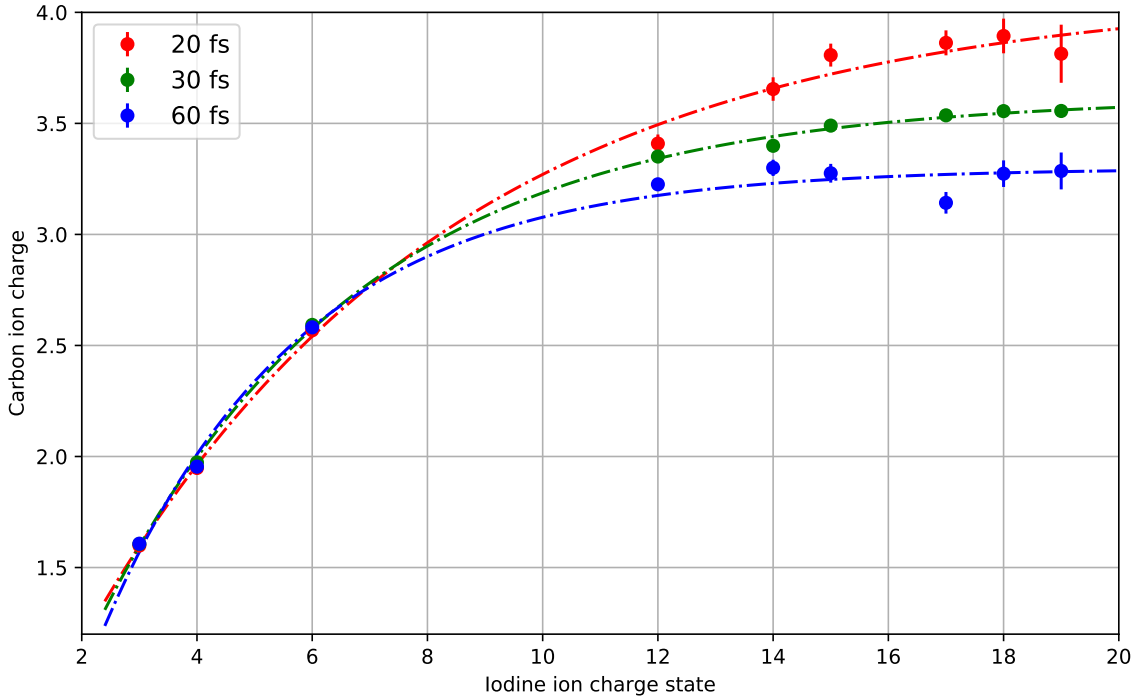

Figure 5.13: Charge of carbon ions detected in coincidence with a given iodine ion charge state for different pulse durations, with 0.37 mJ pulse energy in the interaction region. Dashed lines are exponential fits to guide the eye.

Since in the experiments at 8.3 keV described here carbon nearly exclusively gets charges through charge transfer from iodine, the charge transfer process can be studied by considering the average charge number of carbon ions detected in coincidence with particular iodine ions, as shown in Fig. 5.13 for x-rays with different pulse durations (20 fs, 30 fs and 60 fs) and fixed pulse energy (0.37 mJ in the interaction region). For a given iodine ion charge state with more than 6 charges, the average carbon charge is smaller for longer pulses, suggesting that the charge rearrangement is less efficient. This is because with longer pulses, the average ionization rate is smaller, such that a given total charge state is reached with longer times and at larger internuclear distances. And charge transfer probability decreases with increasing internuclear distance as discussed in subsection 2.4.7.

Fig. 5.14 shows the simulated average time evolution of the charges and internulcear distance of iodine and carbon for those interaction events which end up with iodine ion

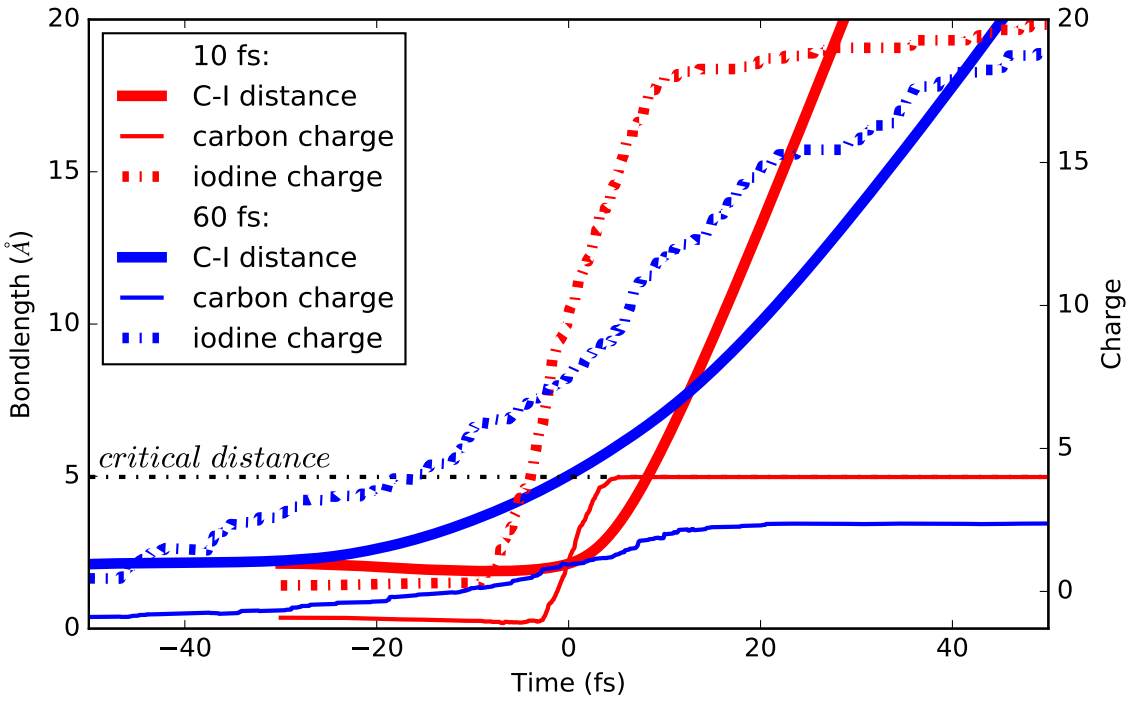

Figure 5.14: Average internuclear distance and charge evolution of carbon and iodine for those interaction events ending up with iodine ion charge of 20, and for pulse durations 10 fs and 60fs. The black dashed line is the critical distance (4.98 $\mathring{A}$) for the charge transfer from C^{3+} to I^{21+}. Adapted from [44].

charge of 20. The simulation was performed using the method as discussed in [43, 44]. The critical distance (4.98 $\mathring{A}$), above which the charge transfer from C^{3+} to I^{21+} is classically forbidden [16, 65, 66] is plotted as the black dashed line. For pulse duration of 10 fs, the C-I distance when carbon obtains 3 charges is about 3.97 $\mathring{A}$, smaller than the critical distance. On the other hand for 60 fs, the C-I distance is already much larger than the critical distance when the carbon charge increases to 3. This agrees reasonably well with the pulse duration dependence of charge transfer in Fig. 5.13, which shows the carbon charge reaches 4 with 20 fs pulse duration, but saturates at about 3.3 with 60 fs pulse duration. The charge transfer can also happen when iodine is at lower charge states than I^{21+}. I^{21+} is used here to get the largest possible critical distance allowing charge transfer to C^{3+}, because larger iodine ion charge results in larger critical distance according to the formula (5.5). In other words, if the C-I distance is above the calculated critical distance with I^{20+}, the charge transfer to C^{3+} is classically forbidden not only with I^{20+} but with all the lower iodine ion charge states

as well.

5.4.2 Extended charge-rearrangement-enhanced ionization

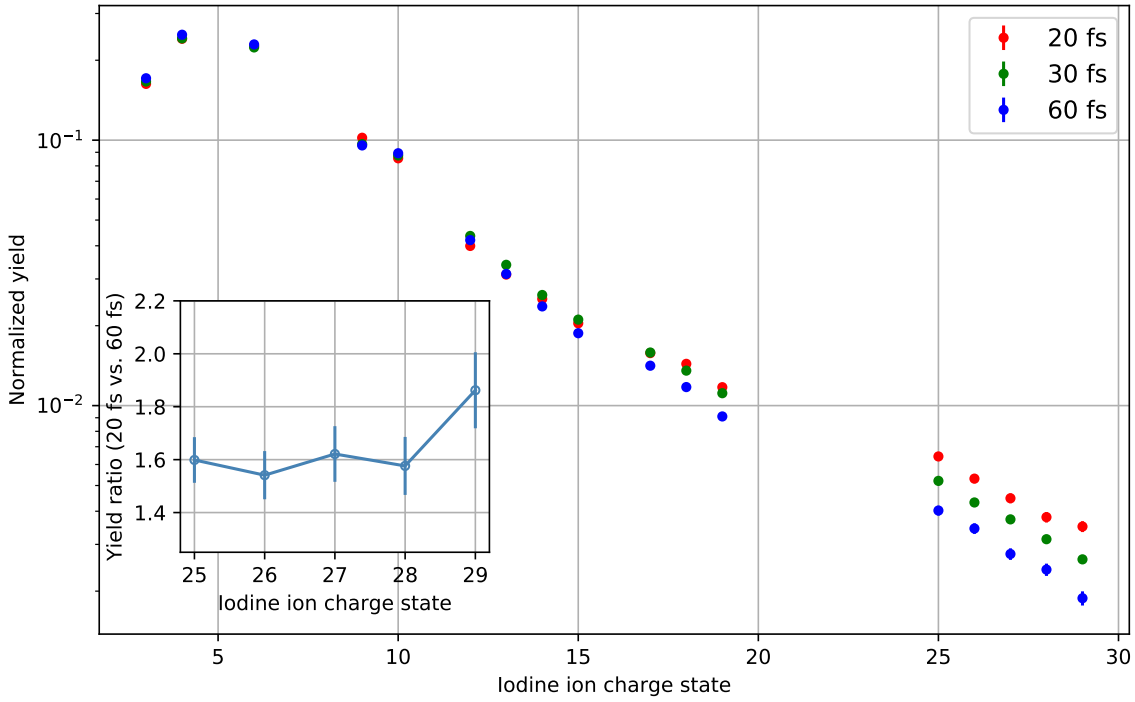

Figure 5.15: Iodine ion charge state distributions for different pulse durations, with 0.37 mJ pulse energy in the interaction region. The inset shows the yield ratio of high charge states between 20 fs and 60 fs cases.

It was shown in subsection 5.1.2 that the charge rearrangement could enhance the ionization of a molecule relative to the independent atoms among which no charge transfer was allowed. It will be shown in this subsection that the charge rearrangement can also enhance the ionization of an atom in a molecule relative to when it's not in the molecular environment.

Fig. 5.15 displays the iodine ion charge state distributions for three different pulse durations (20 fs, 30 fs and 60 fs), with 0.37 mJ pulse energy in the interaction region. Overall, similar ion charge state distributions are observed, because pulse energy, being the major factor in determining the degree of ionization as discussed in subsection 5.1.1, is the same for the 3 cases. Apart from this similarity, higher yield of high charge states is observed

with shorter pulses, in stark contrast with earlier experiments with ultra-intense soft x-ray ionization of neon atoms [1] and nitrogen molecules [141] which reported higher yield with longer pulses due to the effect of "intensity induced transparency' discussed in 5.1.1.

Another observation is that the iodine ions with charge states above I^{25+} are almost exclusively detected in coincidence with C^{4+} as shown in Fig. 5.6. It was shown in the last subsection that C^{4+} is easier to be reached with shorter pulses due to more efficient charge transfer.

These two observations suggest that the higher yield of high charge states with shorter pulses is due to more efficient charge transfer. And charge transfer can also enhance the ionization of an atom (I) in a molecule (CH_3I). Qualitatively, the ionization of such atom can be enhanced with the transferred electrons. They can participate in the decay processes which are otherwise not possible, and hence speed up the refilling of holes created by previous ionizations and Auger decays. The faster refilling effectively increases the instantaneous photoabsorption cross section due to the increased availability of electrons. With shorter pulses, the increase of the photoabsorption cross section is larger due to more efficient charge transfer, resulting in higher yield of high charge states.

Chapter 6

Coulomb explosion imaging of molecules with x-ray free-electron lasers

One of the major applications of x-ray free-electron lasers is the imaging of macromolecules [33], nanoparticles [38] and even molecules [23], with most of the techniques based on photon scattering. In this chapter, the "Coulomb explosion imaging" method [146, 147], which is a different imaging technique specific for molecules, will be discussed as a tool to study the structures of molecules exploded by XFEL pulses. This technique was originally developed for collisions of fast molecular beams with thin foils [146], and has been utilized for time-resolved studies of molecular structural dynamics in table-top laser experiments (see e.g. [147]). The advantage of combining "Coulomb explosion imaging" method with XFELs is that the ultra-intense and ultrashort (down to hundreds of attoseconds [97]) XFEL pulses can almost instantaneously charge up a molecule through the sequential photoionization and decay processes discussed in the last chapter, before the nuclei can move dramatically from the geometry right before the x-ray ionization, reminiscent of the "diffraction before destruction" concept in the imaging techniques based on photon scattering. It is interesting that this "destruction" which refers to the nulear rearrangement resulting from x-ray absorption

is also what makes "Coulomb explosion imaging" possible. By demonstrating that the relative momentum distributions of ion fragments from Coulomb explosion of a prototypical molecule (CH_3I) by 2 keV XFEL pulses, can indeed reflect the equilibrium structure of the molecule, this chapter aims to help set the stage for future XFEL experiments which will use the "Coulomb explosion imaging" method to capture not just the equilibrium structure, but also the transient molecular geometries. Most of the content in this chapter is adapted from [46].

6.1 Molecular explosion with XFEL pulses

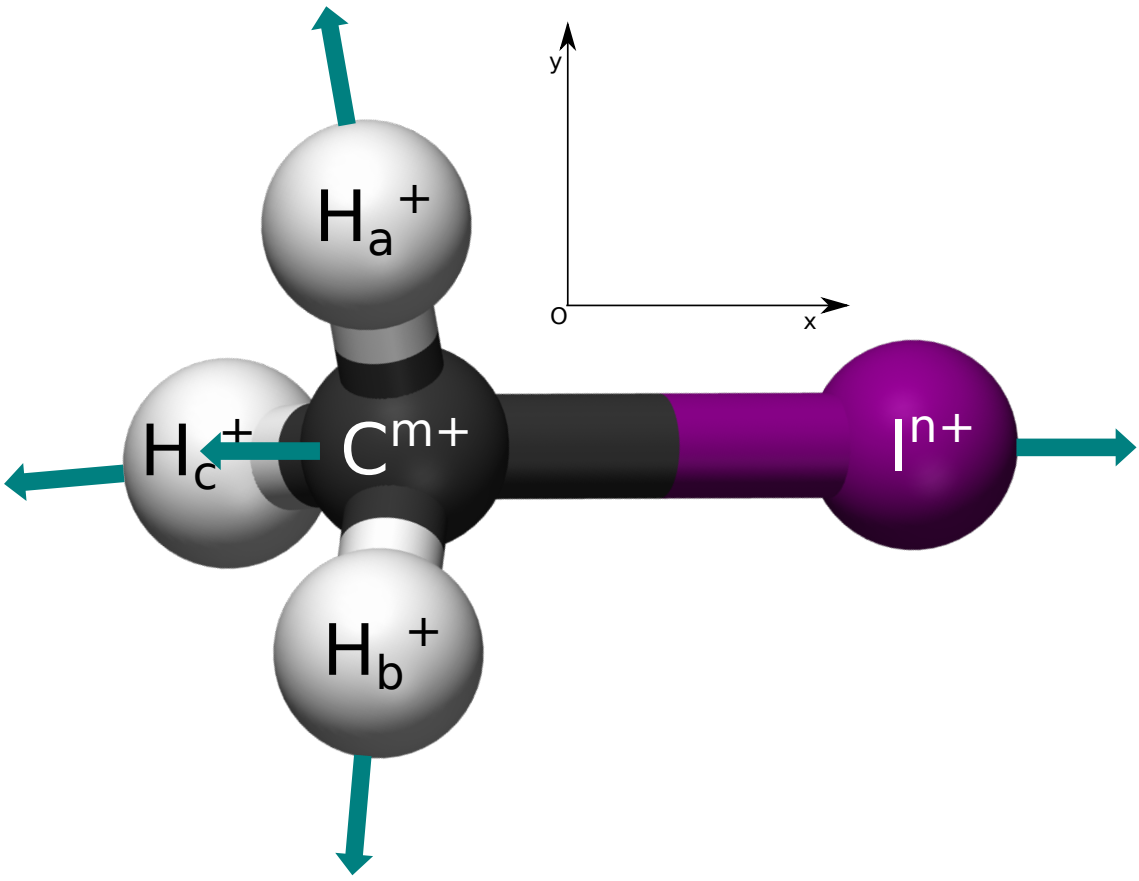

Figure 6.1: Illustration of the explosion of a CH_3I molecule from the equilibrium geometry after ionization by an XFEL pulse. $\boldsymbol{x}$ direction is defined as along the iodine ion flying direction. The CH_3I picture is adapted from [148].

Through the sequential photoionization by a XFEL pulse and charge rearrangement,

all the atoms in a molecule such as CH_3I shown in Fig. 6.1 can get charged up within the femtosecond or even attosecond pulse duration, before the nuclei can significantly move away from their positions before x-ray ionization. The charged-up molecule can therefore be assumed to explode by Coulomb repulsion from its initial geometry. The ion fragments (I^{n+}, C^{m+}, H_a^+, H_b^+, H_c^+, with a, b and c used here to specify the three hydrogen atoms.), after gaining momentum from the explosion process, are then detected in coincidence by the delay-line detector.

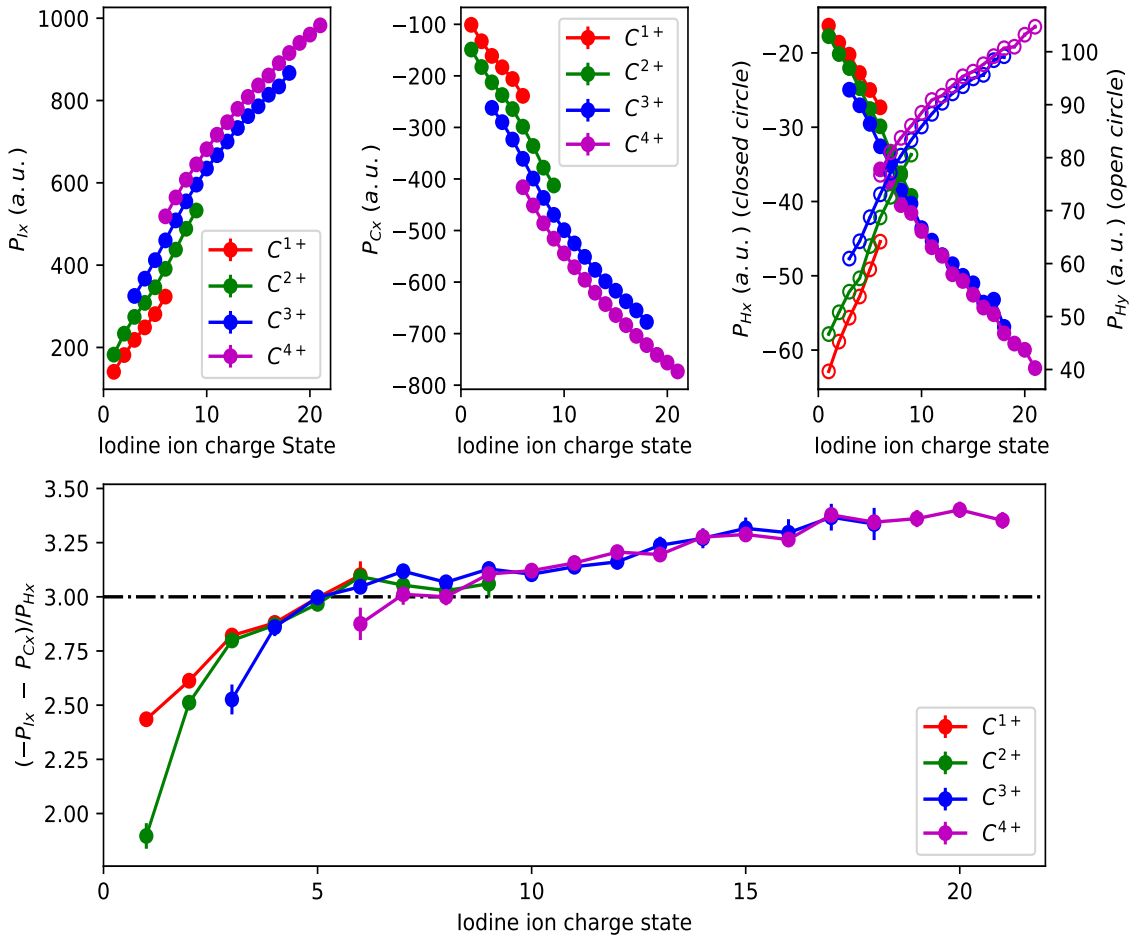

Figure 6.2: Top row: Average measured momentum of fragments (iodine, carbon and hydrogen, from left to right) from CH_3I explosion. $\boldsymbol{x}$ direction is defined as the iodine ion flying direction as shown in Fig. 6.1. The remaining momentum not along $\boldsymbol{x}$ is assigned as the $\boldsymbol{y}$ momentum. Bottom row: Average number of charged hydrogen ions for each fragmentation pair [C^{m+}, I^{n+}].

The yield of possible fragmentation pairs [I^{n+}, C^{m+}] measured at 2 keV photon energy

(pulse energy 1 mJ and pulse duration 25 fs) was shown in Fig. 5.1. The hydrogen atoms (either singly charged or neutral) are not displayed. For each group of detected coincident fragments [I^{n+}, C^{m+}, $H^{+}_{a/b/c}$], $\boldsymbol{x}$ axis is chosen in the direction of the I^{n+} momentum vector, and the remaining momentum for C^{m+} and $H^{+}_{a/b/c}$ not along $\boldsymbol{x}$ is defined as their $\boldsymbol{y}$ momentum. The resulting average ion fragment momentum is shown on the top row of Fig. 6.2. With iodine ion charge states increasing from 1 to 21, its momentum increases from about 100 to 1000 *a.u.*. Carbon $\boldsymbol{y}$ momentum is not plotted since it's negligible compared to its $\boldsymbol{x}$ momentum in the top middle subplot. Carbon $\boldsymbol{x}$ momentum is close in magnitude and opposite to that of iodine, with the difference making up by hydrogen $\boldsymbol{x}$ momentum shown as closed circles in the top right subplot. The hydrogen ion gets larger repulsion from its neighbors in $\boldsymbol{y}$ than in $\boldsymbol{x}$ as can be inferred from the observation that its $\boldsymbol{y}$ momentum (in open circles) magnitude is larger than that of $\boldsymbol{x}$.

As a result of the interaction between a CH_3I molecule and an XFEL pulse, the number of charged hydrogen fragments can range from 0 to 3. The average number of charged hydrogen for each fragmentation pair [I^{n+}, C^{m+}] can be estimated as $\frac{-P_{Ix} - P_{Cx}}{P_{Hx}}$ based on momentum conservation, which is shown in the bottom row of Fig. 6.2. For most of the fragmentation pairs except for [I^{+}, C^{+}], [I^{+}, C^{2+}], it can be seen that the average number of charged hydrogen is above 2.5. For coincident fragments with iodine ion having more than 6 charges, the number shows that all three hydrogen are charged. For higher charge states, the calculated average number increases above 3. This is because hydrogen gets more energetic with higher charge states, and high-energy hydrogen ions miss the detector more often than low-energy ones due to the limited spectrometer acceptance. This artifact makes the average momentum P_{Hx} smaller than reality, resulting in a larger calculated average number of charged hydrogen fragments.

6.2 "Visualization" of the molecular explosion

For 3-body fragmentations, the Newton diagram introduced in section 4.6.1 is a powerful tool for visualizing the molecular structure. To plot it, the coordinate frame is chosen such

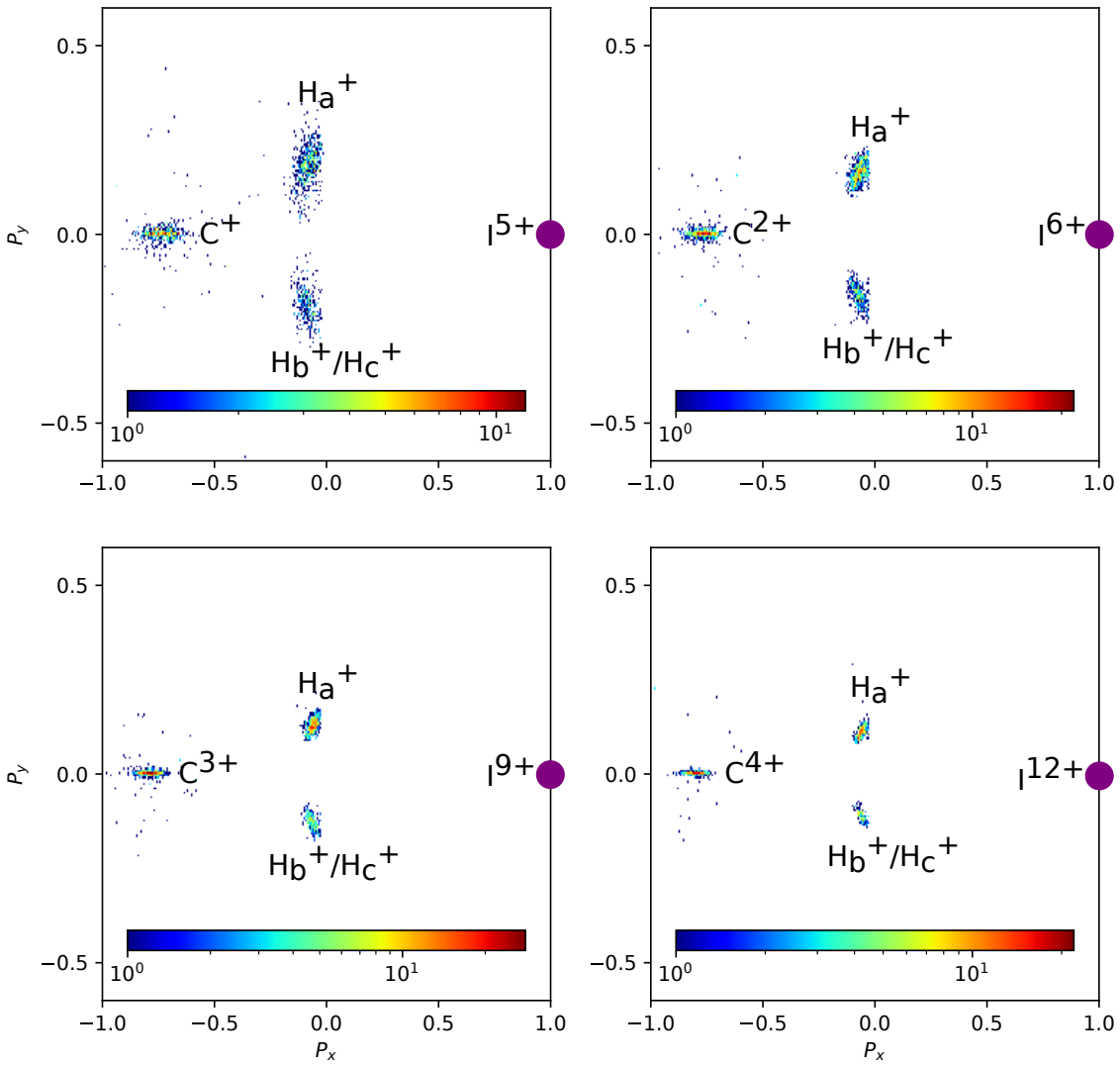

Figure 6.3: Newton diagrams for 4 representative fragmentations of CH_3I molecules ionized by 2 keV x-rays with 25 fs pulse duration and 1 mJ pulse energy.

that $\boldsymbol{x}$ direction is the momentum direction of one fragment and the momentum vector of this fragment is fixed at $P_x = 1$. The relative momenta of the other two fragments with respect to that of the first fragment are then plotted in this coordinate frame, with one fragment at the top of the plane and the other at the bottom.

For fragmentation in more than 3 bodies like a CH_3I molecule fragmenting into [I^{n+}, C^{m+}, H_a^+, H_b^+, H_c^+], the fragment momentum vectors typically do not lie within a plane, calling for either a 3D visualization [147] or a 2D variant of Newton diagram. Here the latter option is chosen to visualize the explosion of CH_3I molecules. As in the conventional 3-

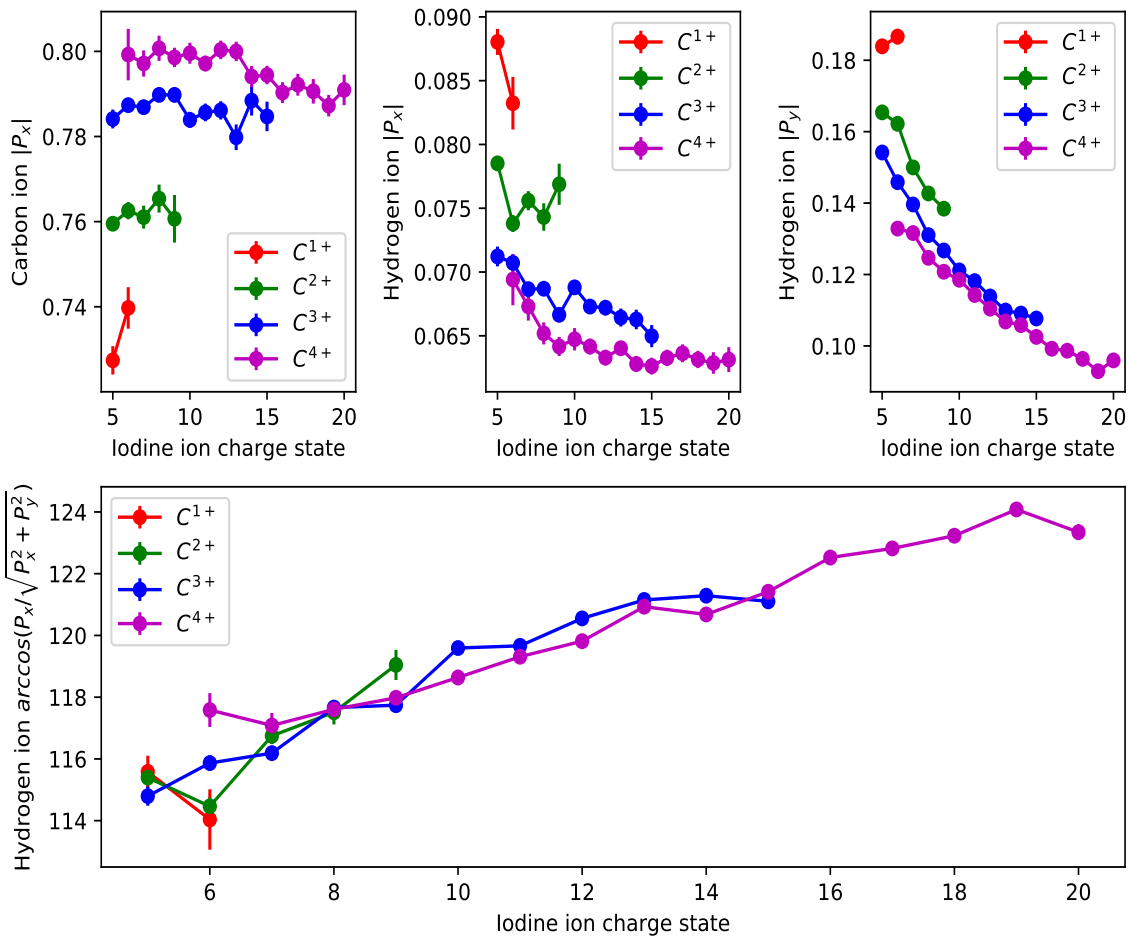

Figure 6.4: Relative absolute momenta of carbon and hydrogen ions with respect to the iodine momentum, (The $\boldsymbol{x}$ momenta of carbon and hydrogen ion are negative and their absolute values are used for the plot.) and the angles of hydrogen ion flying direction with respect to that of the iodine ion.

body Newton diagram, the coordinate frame is chosen such that $\boldsymbol{x}$ direction is the momentum direction of one fragment (I^{n+}) and the momentum vector of this fragment is fixed at $P_x = 1$. The following are required as the extra steps. $\boldsymbol{y}$ direction is defined such that the momentum vector of a second fragment lies within the top $x-y$ plane. For each of all the other fragments, the momentum is visualized after rotating with respect to $\boldsymbol{x}$ axis until it falls within the $x-y$ plane. Such modified Newton diagrams for 4 representative fragmentations of CH_3I molecules ionized by 2 keV x-rays with 25 fs pulse duration and 1 mJ pulse energy are displayed in Fig. 6.3. All four diagrams reflect the CH_3I equilibrium geometry as shown in Fig. 6.1. The connection between the molecular structure and fragment momenta will be

explored employing the Coulomb explosion simulation in the next subsection.

The top row of Fig. 6.4 shows the averaged relative ion momentum as shown in Fig. 6.3 for different fragmentations. In the top left subplot, for carbon charge states above C^+, carbon ion relative momentum increases in magnitude with increasing carbon ion charge state, but stays flat with increasing iodine ion charge state. Correspondingly, the top middle subplot shows that the hydrogen ion relative momentum decreases in magnitude with increasing carbon ion charge state. The increase of hydrogen ion relative momentum with iodine ion charge state for C^{3+} and C^{4+} is caused by the limited spectrometer acceptance for more energetic hydrogen ions. Otherwise they should also stay flat as those of carbon ions, which is required by momentum conservation. The change in magnitude of the relative momentum of carbon and hydrogen ions is due to the change of the time during which hydrogen ions are involved in the interaction with iodine and carbon ions, or in other words, how fast the hydrogen ions fly away relative to the interaction time scale of carbon and iodine ions. With increasing carbon ion charge state, hydrogen ions fly away relatively early, such that the carbon ions gain larger relative momentum from the repulsion of iodine ions. For a fixed carbon ion charge state above C^+, the flat relative momentum suggests that the relative time at which hydrogen ions fly away with respect to the time scale of carbon and iodine interactions, doesn't depend on the final iodine ion charge state. The qualitative conclusion is that the hydrogen ions tend to leave from the carbon ion before the carbon ion can increase its charge. The bottom of Fig. 6.4 shows the angles of hydrogen ion flying direction relative to that of the iodine ion for different carbon and iodine ion pairs. This angle is determined by both the equilibrium molecular geometry, and the charge buildup process of all the fragments from the molecule. Based on the equilibrium molecular geometry as illustrated in Fig. 6.1, hydrogen ions gain more momentum in $\boldsymbol{y}$ than in $\boldsymbol{x}$ from both the repulsion between hydrogen and carbon ions and that among hydrogen ions. On the other hand, the hydrogen ion gains more momentum in $\boldsymbol{x}$ than in $\boldsymbol{y}$ from the repulsion between it and the iodine ion. So if the iodine ion is at a higher charge state, a hydrogen ion is expected to gain more momentum in $\boldsymbol{x}$ than in $\boldsymbol{y}$, making the angle of the hydrogen ion momentum relative to that of iodine ion larger, as can be observed in the bottom plot of Fig. 6.4. The

observation that this angle doesn't show any systematic dependence on carbon ion charge state further confirms the previously reached conclusion that the hydrogen ions tend to leave from the carbon ion before the carbon ion can increase its charge.

6.3 Coulomb explosion simulation

6.3.1 Intantaneous charge-up model

If the molecule can be assumed to be instantaneously charged up, its structure before being ionized by the XFEL pulse is related to the fragments momentum as shown in Fig. 6.3 through Coulomb's law and Newton's second law. In this case, the ionic fragments, initially at locations $\boldsymbol{r}_{i0}$ with $i = 1, 2, \cdots, n$ and n being the label of the n^{th} fragment, start to move apart under the Coulomb repulsion between one and another, according to the coupled differential equations:

$$\frac{d^2\boldsymbol{r}_i}{dt^2} = \sum_{j\neq i} \frac{Q_i Q_j}{|\boldsymbol{r}_i - \boldsymbol{r}_j|^2} \frac{\boldsymbol{r}_j - \boldsymbol{r}_i}{|\boldsymbol{r}_i - \boldsymbol{r}_j|}, \tag{6.1}$$

with $i, j = 1, 2, \ldots, n$ being the label of the i^{th} and j^{th} fragment, and n being the number of fragments. Q_i and Q_j are the charges of the i^{th} and j^{th} fragments.

For a CH_3I molecule initially with $C-H$ bondlength 1.084 $\mathring{A}$, $C-I$ bondlength 2.136 $\mathring{A}$, $H-C-I$ angle 107.47 degrees and $H-C-H$ angle 111.4 degrees [144], and assuming the fragment charges are those shown in Fig. 6.3, the simulated fragments final momenta according Eq. (6.1) are shown as red triangles on top of the experimental momentum distributions in Fig. 6.5. Reasonably well visual agreement is achieved in all four representative fragmentation scenarios.

In a more quantitative consideration, there is a noticeable mismatch. The simulated carbon ion relative momenta in $\boldsymbol{x}$ are smaller in magnitude than those of corresponding experimental values and the simulated hydrogen ion relative momenta in $\boldsymbol{x}$ are larger. This discrepancy is due to the charge buildup and redistribution processes neglected in the instan-

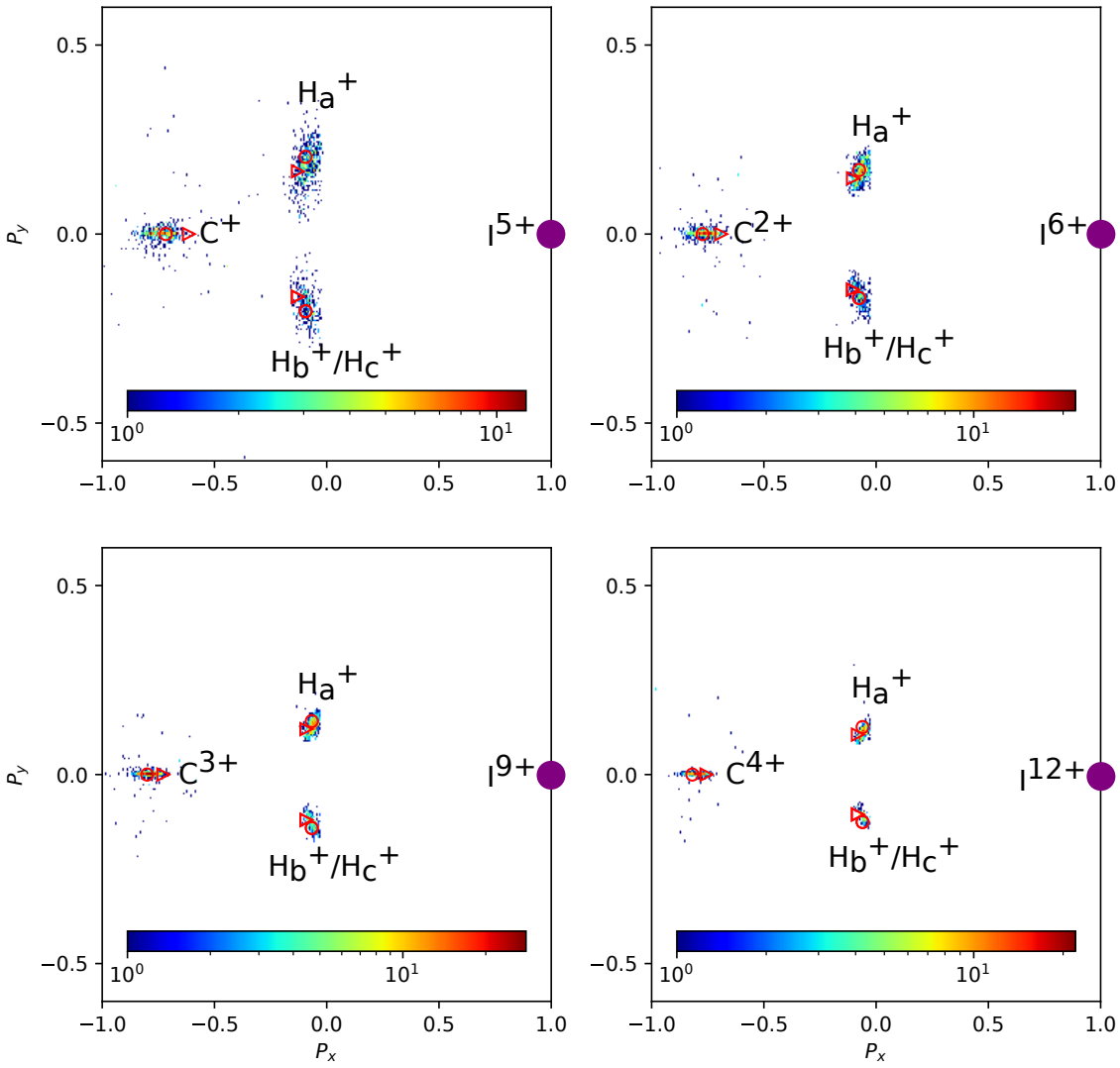

Figure 6.5: Newton diagrams for 4 representative fragmentations of CH_3I molecules ionized by 2 keV x-rays with 25 fs pulse duration and 1 mJ pulse energy (same as Fig. 6.3, but with the results of the simulations added). The red triangles are simulations with the instantaneous charge-up model. The red circles are simulations with the charge buildup model to be discussed in the next subsection.

taneous charge-up model. If these processes were taken into account, as will be discussed in the next subsection, the hydrogen ion would fly away from the vicinity of carbon and iodine ions before they are fully charged up, leaving only carbon and iodine ions interacting with each other during the rest of the charge-up process. This would make the hydrogen ion relative momenta smaller and carbon ion larger than in the instantaneous charge-up model.

6.3.2 A charge buildup model

To account for the charge buildup and redistribution processes, a model [18] developed by Motomura, Kukk and et al. is implemented in the Coulomb explosion simulation. In their model, the CH_3I molecule is not instantaneously charged up, instead the total charge Q_{total} increases according to an exponential function:

$$Q_{total}(t) \ = \ (m \ + \ n + 3)(1 \ - \ e^{-\frac{t}{a}}), \tag{6.2}$$

where m and n are respectively the final charges of carbon and iodine ions, and a is the time constant quantifying the time scale of the charge buildup process. The charge transfer from iodine site to methyl group is modeled by the differential equation

$$\frac{dQ_{CH_3(t)}}{dt} \ = \ bQ_I(t), \tag{6.3}$$

with the sum of methyl group charge $Q_{CH_3}(t)$ and iodine ion charge $Q_I(t)$ equal to the total charge $Q_{total}(t)$, and b the constant related to the rate of charge transfer.

Define the metric

$$\begin{aligned}\mathcal{M} \ = \ &(P_{Cx}^{(exp)} \ - \ P_{Cx}^{(sim)})^2 + \ (P_{Hx}^{(exp)} \ - \ P_{Hx}^{(sim)})^2 + \ (P_{Hy}^{(exp)} \ - \ P_{Hy}^{(sim)})^2 \\ &+ \ (|P_{Ix}^{(exp)}| \ - \ |P_{Ix}^{(sim)}|)^2,\end{aligned} \tag{6.4}$$

where the $P's$ are the fragment momenta in the molecular frame as defined in section 6.1. *exp* and *sim* represent experiment and Coulomb explosion simulation (with the above model included), respectively. The a and b values are determined to be 6.199 fs and 0.831 fs^{-1}, by minimizing the sum of the metrics for 4 different fragmentation scenarios in Fig. 6.5. The simulated momenta with these values are shown by red circles. A better match with experimental data is achieved with the current charge buildup model compared with the instantaneous one.

Chapter 7

Ion and electron coincidence measurement with x-ray free-electron lasers

Ion and electron coincidence measurement has been a powerful technique in the study of atomic and molecular dynamics with table-top lasers [116, 117, 149] and synchrotron facilities [150, 151]. Its application with free-electron lasers has been hindered by the their low repetition rates ($\sim$ 100 Hz), and only few such measurements have been reported up to now for sequential ionization of atoms [152–154] and autoionization of molecules [155] in the XUV domain. This limitation is being lifted with the new and upcoming high-repetition-rate (10^4 $-$ 10^6 Hz) free-electron lasers such as the EuXFEL and LCLS-II. The ion and electron coincidence measurement which requires low-interaction rate (less than one interaction event per laser shot) and such high-repetition-rate machines make a perfect combination for studying atomic and molecular physics in a new regime made possible by the XFEL-produced ultrashort and ultra-intense x-rays. In this chapter, the results from first ion-electron coincidence experiment with an x-ray free-electron laser (LCLS) will be presented. The interaction between N_2 molecules and 506 eV x-rays (pulse duration 100 fs and pulse energy $\sim$ 10 μJ) will be revealed through the coincidence measurement of the resulting photoelectrons and

ion fragments. Most of the paragraphs and figures are adapted from [47].

7.1 Ion and ion coincidence

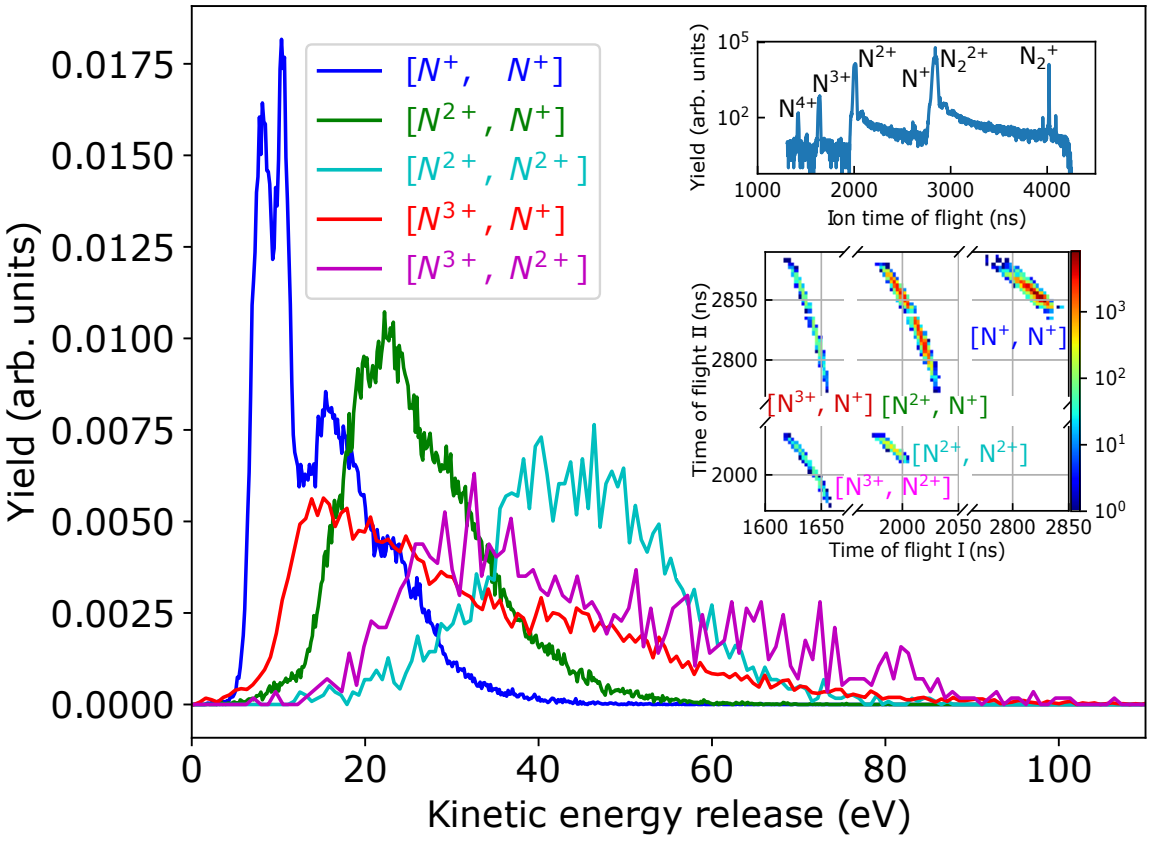

Figure 7.1: Kinetic energy release of ion-ion coincidence channels from 506 eV, 100 fs XFEL pulse interaction with N_2 molecules. Top inset is the ion time of flight spectrum. Bottom inset is the ion-ion coincidence map. Adapted from [47].

Extensive studies [125, 150, 151, 156–158] on x-ray interaction with N_2 molecules have been carried out with the ion-electron coincidence technique at synchrotron facilities, in which the one-photon absorption results in the production of $[N^+,\ N^+]$ and $[N^{2+},\ N^+]$ coincidence channels. With more intense x-rays from the LCLS, more than one photon can be absorbed by a N_2 molecule, resulting in higher charged ions than those from synchrotron experiments. Five ion-ion coincidence channels: $[N^+,\ N^+]$, $[N^{2+},\ N^+]$, $[N^{2+},\ N^{2+}]$, $[N^{3+},\ N^+]$ and $[N^{3+},\ N^{2+}]$ were detected in the present experiment as shown by Fig. 7.1. In

earlier synchrotron experiments, similar structures have been reported and identified for the kinetic energy releases of [N^+, N^+] and [N^{2+}, N^+] channels [125, 159]. As expected, the other three higher charged channels have higher kinetic energy releases due to the larger Coulomb repulsion. The steps that the interaction between x-rays and molecules takes to reach these five coincidence channels will be discussed in the next section with the help of the electron spectra detected in coincidence with different ion fragments.

7.2 Ion-ion and electron coincidence

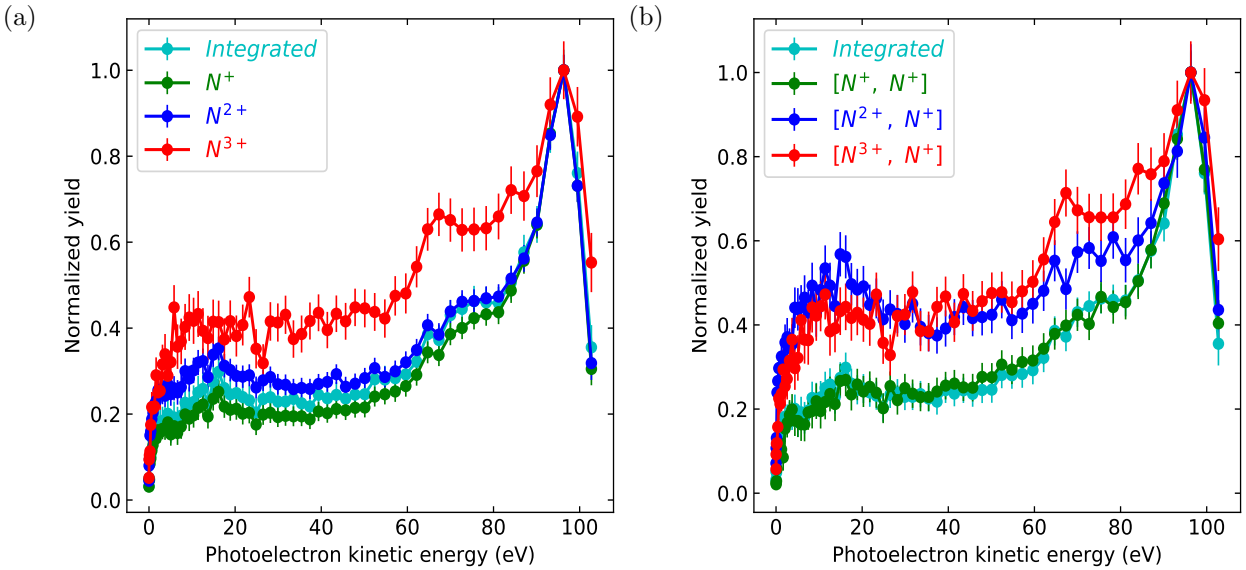

Figure 7.2: Photoelectron kinetic energy spectra, in coincidence with ions. (a) Ion-resolved photoelectron kinetic energy spectra. The spectra are obtained by integrating the VMI image over all angles at different radii and with the relation that the photoelectron energy is proportional to the square of the radius. (b) Ion-ion-coincidence-channel-resolved photoelectron kinetic energy spectra. The spectra are obtained by integrating the VMI image over all angles at different radii and with the relation that the photoelectron energy is proportional to the square of the radius. Adapted from [47].

The energy spectra of the electrons detected in coincidence with ions N^+, N^{2+} and N^{3+}, and three of the ionic channels [N^+, N^+], [N^{2+}, N^+] and [N^{3+}, N^+] are plotted respectively in Figs. 7.2a and 7.2b. Some of the Auger electrons ejected within a small angle relative to the spectrometer axis are also detected. In order to avoid the artefacts introduced by these

Auger electrons and stray electrons through the inversion procedure, non-inverted electron VMI images are used to obtain the electron energy spectra by integrating the image over the angles and using the relation that the energy of an electron is proportional to the square of the radius at which it is located in the VMI image. Each of the spectra has features distinct from one and another, which reflects the physical processes leading to the corresponding ionic channel. $[N^+, N^+]$ is mainly produced via single-photon absorption, with one electron ejected by inner-shell ionization and the other by Auger decay. Such photoelectrons are present as the major peak at around 96 eV in the $[N^+, N^+]$ electron spectrum. The broad shoulder on the left of the major peak is due to the photoelectrons generated from shake-up processes, where the photon energy is shared between the photoelectron and the remaining excited molecular ion. $[N^{2+}, N^+]$ can be produced by one-photon process as well. But different from that of $[N^+, N^+]$ channel, the production of $[N^{2+}, N^+]$ is dominated by the shake-off process [160], where one more electron is carried away during the process of ionization or Auger decay. The electrons thus produced have a lower energy than those by normal photoionization or Auger decay processes and they are present as the lifted tail in the low energy range of $[N^{2+}, N^+]$ electron spectrum relative to that of $[N^+, N^+]$. Apart from the shake-off process, one core-electron ionization followed by one outer-shell-electron ionization also contributes to the production of $[N^{2+}, N^+]$. For $[N^{3+}, N^+]$, its electron spectrum has two pronounced peaks, with one around 96 eV and the other 67 eV. The 96 eV peak is from the first photoionization which produces N_2^{2+} ions. The 67 eV peak is due to the photoelectrons from the subsequent ionization of N_2^{2+} ions. In addition to this two-step process, it is also possible to reach $[N^{3+}, N^+]$ channel by the production of double-core-hole states, where one photon is first absorbed, creating a core hole, and then a second photon gets absorbed, creating another core hole before the first core hole is filled [9–12]. Due to the much smaller probability to be produced with the 100 fs pulse (10 μJ), these states contribute to only a very small amount of $[N^{3+}, N^+]$ production.

7.3 KER-resolved ion-ion and electron coincidence

For ion fragments requiring more than one photoionizations, their kinetic energy release is related to how fast they are produced, as discussed in section 5.3. By inspecting the spectra of electrons coincident with ions with a certain KER value, it's possible to gain information on the transient state of molecular system at the time corresponding to that KER value. [N^{3+}, N^{+}] will be used in this section to illustrate how KER-resolved ion-ion and electron coincidence can help reveal the intermediate states. As discussed in the last section, overall it needs a sequential two-photon absorption process to reach [N^{3+}, N^{+}] channel from N_2 molecules. When the time delay between the two absorptions is shorter than the core hole life time, double-core-hole states are produced with a very high probability. For time delays longer than the core hole life time, which is more probable under our experimental conditions, [N^{3+}, N^{+}] is mainly obtained from N_2^{2+} molecular ions by the second photoabsorption. A manifold of states can be occupied by N_2^{2+}, of which about 20% remain quasi-bound and the other 80% are dissociative [161]. With different time delays, the second photoabsorption sees different evolution stages of those dissociating N_2^{2+} molecular ions. If the second photoabsorption occurs early, N_2^{2+} ions have short bond length and high-KER [N^{3+}, N^{+}] ion pairs are produced. So for [N^{3+}, N^{+}] ion pairs reached from dissociating N_2^{2+} molecular ions, the KER reflects the time delay between the two photoabsorptions. This relation between KER and time delay was also observed in a previous two-pulse x-ray-pump x-ray-probe experiment at the LCLS [32, 162]. By utilizing such relation and doing correlation analysis between KER and photoelectrons ejected by the probe photon, the change of core electron binding energy during the dissociation of N_2^{2+} ions can be observed.

7.3.1 Dynamic line shift

The [N^{3+}, N^{+}] ion pairs are divided into two categories, As shown in Fig. 7.3a, one is the low-KER region with KER below 27.4 eV and the other is the high-KER region with KER above 27.4 eV. The kinetic energy of photoelectrons detected in coincidence with the ion pairs falling into these two categories are displayed in Fig. 7.3b. The photoelectron peaks from

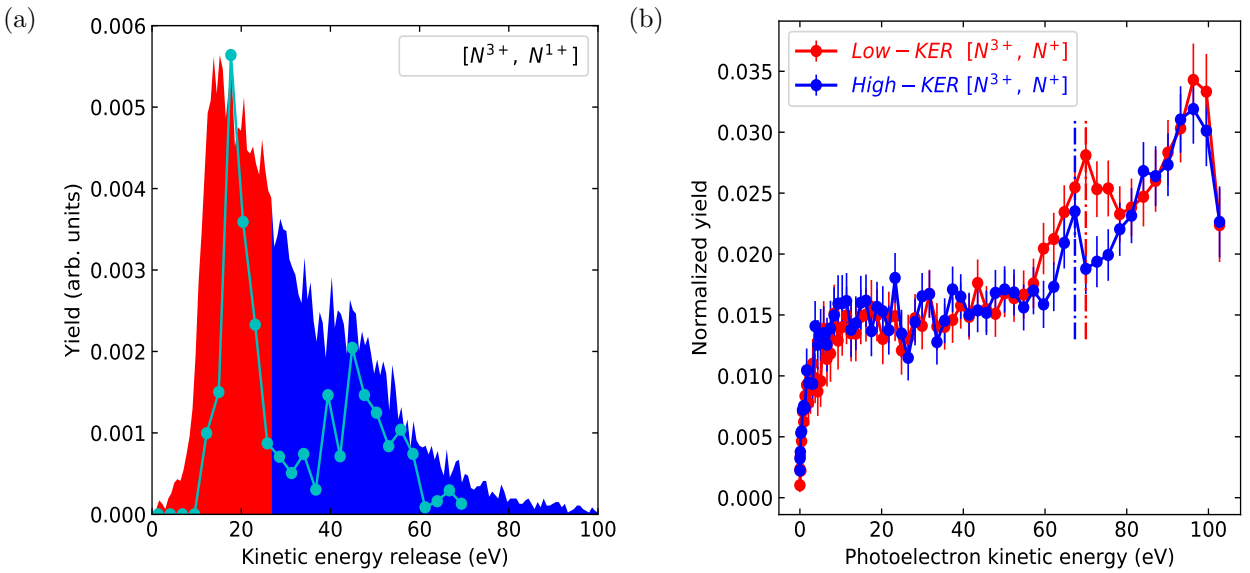

Figure 7.3: "Dynamic line shift" in the dissociating N_2^{2+} ion. (a) In red and blue is the experimental kinetic energy distribution of $[N^{3+}, N^{+}]$ coincidence channel, divided into 2 regions: low-KER region (0-27.4 eV, red) and high-KER region (27.4-100 eV, blue). The calculated kinetic energy release of $[N^{3+}, N^{+}]$ coincidence channel obtained by 60 fs pulses is shown by the cyan line with dots. (b)Experimental photoelectron energy spectra corresponding to the two regions in (a). The spectra are obtained by integrating the VMI image over all angles at different radii and with the relation that the photoelectron energy is proportional to the square of the radius. The blue and red dashed lines mark the peak positions 67.32 and 69.99 eV of electrons from the second photoionization. Adapted from [47].

the first photoabsorption appear in both spectra at about 96 eV. The photoelectron peaks at about 68 eV originating from the second photoionization, have different characteristics for the low-KER and high-KER cases. The peak maximum shifted from 67.32 eV to 69.99 eV when the ion pair KER changes from lower to higher region. Such shift is due to the core binding energy dependence on bond length, which shall be called "dynamic line shift". Since the low-KER ion pairs are mainly obtained from N_2^{2+} ions with larger "pump-probe" time delays when N_2^{2+} is at the later stage of its dissociation and has longer bond length, the corresponding higher photoelectron energy indicates that N_2^{2+} core electron binding energy becomes smaller as its internuclear distance gets longer.

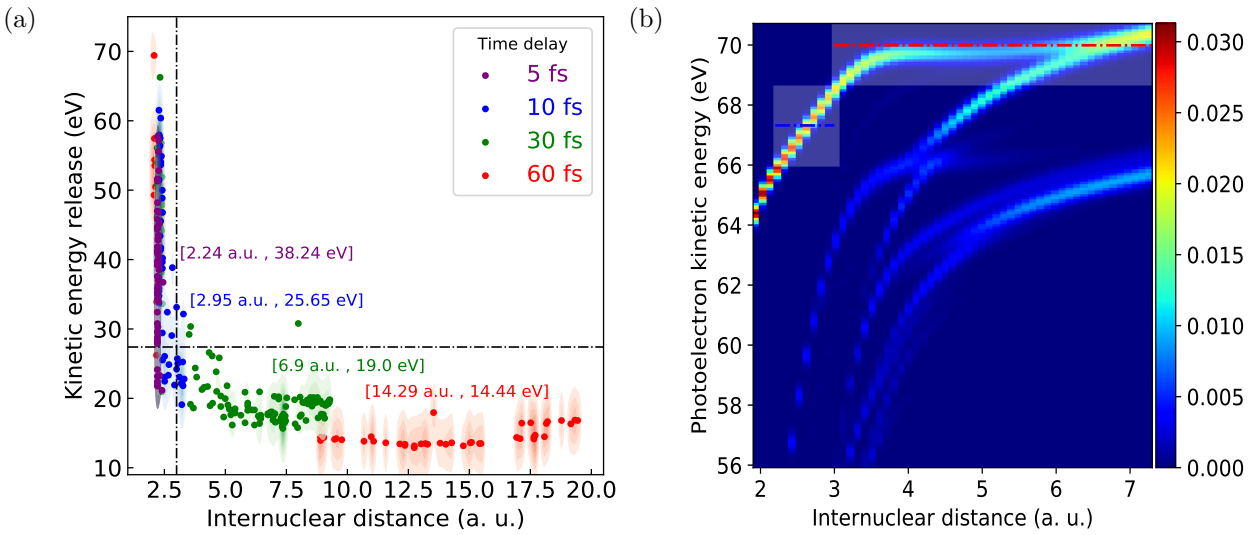

Figure 7.4: Calculated correlation of kinetic energy release with bond length at different time delays and calculated "dynamic line shift" of N_2^{2+} ($1^1\triangle_g$). (a) Theory plot of [N^{3+}, N^+] kinetic energy release and N_2^{2+} internuclear distance at the time of the probe photoabsorption for different time delays. The values in square brackets are the average internuclear distance and KER for each time delay. For time delays larger than 5 fs, only those points with internuclear distance larger than 2.5 a.u., which correspond to the dissociating wavepackets, are taken for calculating the average. The horizontal dashed line is the 27.4 eV boundary used in Fig. 4a. The vertical dashed line marks the bond length of 3 a.u.. (b) Theory plot of N_2^{2+} ($1^1\triangle_g$) photoelectron kinetic energy with its internuclear distance. The color encodes the relative probability for a N_2^{2+} photoelectron to have certain energy at different internuclear distances. The energy peak positions in Fig. 7.3b, of photoelectrons from the second photoionization and coincident with the high-KER and low-KER [N^{3+}, N^+] ion pairs, are shown respectively by the blue and red dashed lines in (d). The region 1.33 eV below and above the two lines are marked by white rectangles. Adapted from [47].

7.3.2 Comparison with calculations

Ab initio calculations have been carried out by Ludger Inhester from the Center for Free-ELectron Laser Science in Hamburg to support the "dynamic line shift" interpretation. In Fig. 7.4a, the calculated [N^{3+}, N^+] kinetic energy release with the corresponding N_2^{2+} bond length at the time of probe photoabsorption is plotted for time delays of 5 fs, 10 fs, 30 fs and 60 fs. At 5fs, the KER is distributed between 20 eV and 60 eV and the bond length ranges from 2 a.u. to 2.5 a.u.. For this time delay, N_2^{2+} ions are either remaining bound or at the very early stage of its dissociation, and the distributions of these two types of ions overlap with each other in the high-KER and short-bond-length region. For larger time delays, the

bound N_2^{2+} ion distributions continue to be present in the high-KER and short-bond-length region, whereas the distributions of dissociating N_2^{2+} ions are moving to regions of longer bond length (above 2.5 a.u.) and lower [N^{3+}, N^+] KER. The average values of kinetic energy releases and bond lengths are also shown for each delay. For time delays larger than 5 fs, only the dissociating N_2^{2+} ions are taken into account to get the averages, by excluding the distribution with bond length shorter than 2.5 a.u.. The time delays, average bond lengths and KERs are found to have a monotonic relation with one and another, which is as expected for ionization of a dissociating molecular ion. The 27.4 eV boundary in experimental Fig. 7.3a is marked by the horizontal dashed line in Fig.7.4a. The high-KER region above this line contains data points with time delays up to 10 fs and bond lengths up to about 3 a.u. (marked by the vertical dashed line), when N_2^{2+} ions either just started to dissociate or were bound. The low-KER region below the horizontal dashed line contains these data points with time delays larger than 10 fs. The N_2^{2+} ions for this region are mostly dissociating and ionized by the probe photon at larger internuclear distances.

To theoretically investigate the core electron binding energy of N_2^{2+} at different time delays and bond lengths, $1^1\triangle_g$ electronic state of N_2^{2+}, which accounts for $\sim 24\%$ [163] of the total population after the pump photoionization and Auger decay, is picked out. For N_2^{2+} ions populating this state, the relative probabilities of its photoelectrons having certain energy at different internuclear distances are plotted in Fig. 7.4b. At bond lengths around 2 a.u., there is a single photoelectron line, the energy of which increases with bond length. Above 2.5 a.u., several satellite photoelectron lines start to emerge at the lower region, due to shake up processes which, in addition to ejecting an electron from the core, leave the molecular ion with excited electronic configurations. The photoelectron energy increases with bond length in all the photoelectron lines. As N_2^{2+} further dissociates and has a longer bond length, it changes from a molecule with the ${}^1\pi_x^2{-}\pi_y^2$ configuration to two N^+ ions with 3P configuration. Beyond 7 a.u., the photoelectron lines converge into two separate photoelectron lines. They can be interpreted as due to the ionization of an atomic N^+ (3P) ion into a core-ionized N^{2+} ion with 4P and 2P configurations respectively. This interpretation becomes more accurate for much longer bond lengths at which the photoelectron energies are closer to those from

the ionization of isolated atomic ions.

The blue dashed line in Fig. 7.4b marks the experimental peak maximum position 67.32 eV in Fig. 7.3b of photoelectrons from the second ionization and in coincidence with the high-KER [N^{3+}, N^{+}] ion pairs. It crosses the photoelectron line in Fig. 7.4b at the internuclear distance 2.6 a.u.. The white rectangle under the dashed line is the region bounded by the electron energy 1.33 eV (half of the spacing between the peak maximum and its adjacent data points in Fig. 7.3b) below and above 67.32 eV and the bond length from 2.2 to 3 a.u.. This bond length range is consistent with the expected bond length of N_2^{2+} ion at time delays up to 10 fs as determined for the high-KER ion pairs.

For the photoelectrons from the second ionization detected in coincidence with the low-KER [N^{3+}, N^{+}] ion pairs, their peak maximum position 69.99 eV in Fig. 7.3b is marked by the red dashed line in Fig. 7.4b. The corresponding internuclear distance is 6.5 a.u.. The region confined by energy 1.33 eV below and above 69.9 eV and bond length from 3 to 12 a.u. goes out of the axis range of Fig. 7.4b and only part of it is shown by the white rectangle beneath the red dashed line. In Fig. 7.3b, the photoelectrons, of the low-KER case and with energy beyond the peak position and up to 75.39 eV, are from the probe photoionization of dissociating N_2^{2+} ions at larger time delays up to the full length of the XFEL pulse. These observations agree with the fact that the [N^{3+}, N^{+}] ion pairs in the low-KER region of Fig. 7.4a are from N_2^{2+} ions which have already dissociated for more than 10 fs and have bond lengths most likely longer than 3 a.u..

For the low-KER case, there are also photoelectrons to the left of the 69.9 eV electron peak in Fig. 7.3b. They most likely correspond to the less intense photoelectron lines below the topmost one in Fig. 7.4b, which mostly appears for N_2^{2+} ions with larger bond lengths and leading to low-KER ion pairs.

7.3.3 Discussion

In this experimental study, the KER is only divided into two regions, in order to get statistically more significant results from the ion-electron correlation analysis. More KER regions

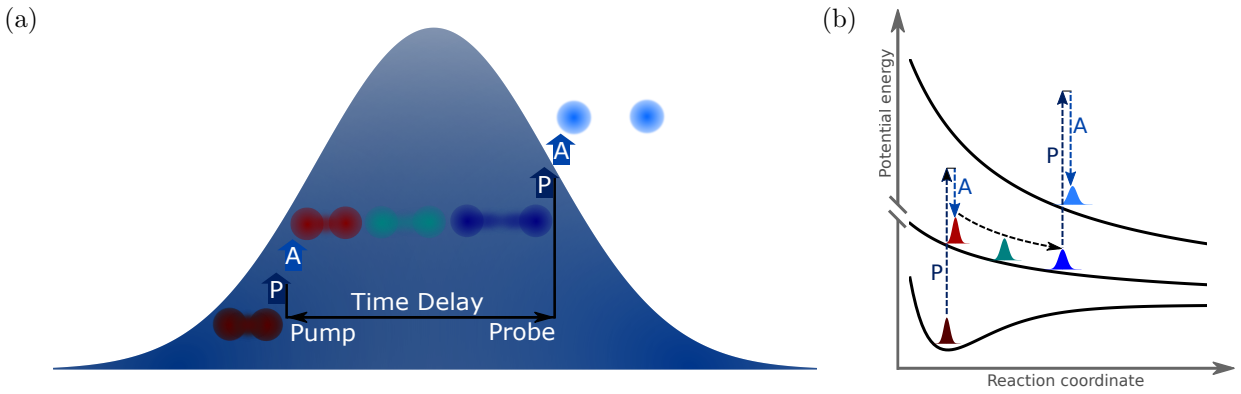

Figure 7.5: Illustration of the single-pulse x-ray-pump x-ray-probe scheme. (a) Sketch of a single XFEL pulse pump-probing molecular states. (b) Illustration of the propagation of wavepackets launched and probed by the absorption of two photons sequentially from a single XFEL pulse. The letters "P" and "A" represent photoionization and Auger decay processes. Adapted from publication [47].

and hence more refined time delays can be chosen for future studies at high-repetition-rate XFEL facilities such as the LCLS-II. This will allow a more detailed experimental mapping of core electron energy levels, as the one shown by the theory plot in Fig. 7.4b. In the theory study, only the dicationic state $1^1\triangle_g$ with 24% yield was picked out to study the core electron binding energy dependence on bond length. Other less populated dicationic states contribute to the photoelectrons in Fig 7.3b as well and cannot be disentangled in the current experiment. Given that the dissociative dicationic states show similar trend of core electron binding energy dependences especially at larger bond lengths, general insight shared by these states can be obtained by the comparison between Fig. 7.3b and 7.4b. A full disentanglement of these dicationic states requires future experiments, in which Auger electrons are detected in coincidence with photoelectrons and ions.

The observation of "dynamic line shift" described above is an exemplary case exploiting the single-pulse x-ray-pump x-ray-probe scheme enabled by the combination of ion-electron coincidence technique and XFELs as illustrated in Fig. 7.5. It is different from a previous single-pulse pump-probe experiment [164] at a synchrotron facility, in the sense that two photoabsorptions play the roles of "pump" and "probe" respectively, whereas the previous study used a single photoabsorption as "pump" and the Auger decay as "probe". In the current scheme, the pump and probe steps are realized by two time-delayed photoabsorptions

in a single XFEL pulse. A variable time delay can be achieved naturally through the interaction of intense x-rays with molecules. In a single pulse, the time delay between the pump and probe photoabsorptions can in principle vary from zero to the full pulse length thanks to the quantum mechanical nature of the photoabsorption process. Since the probability for a molecule to absorb a photon increases with the x-ray intensity, the time delay variability can be further enhanced by the pulse structure fluctuations due to the stochastic nature of the Self-Amplified Spontaneous Emission process for the XFEL pulse generation [81].

Unlike the conventional pump-probe experiments where the time delay is determined independently of the dynamics under study, the single-pulse experiment relies on the intrinsic correlation of different physical observables characterizing the same dynamical process. If a physical observable changes monotonically with the state evolution and a direct relation with the time delay can be established, the system evolution information can then be extracted by the correlation of this observable with the other quantities. It's therefore necessary to measure at least two physical quantities in coincidence for each interaction event.

When applicable, this scheme is a simple alternative to the two-pulse x-ray-pump x-ray-probe configuration [32]. For molecular studies, it can be used whenever the intermediate state is dissociative and the time delay is reflected in the KER of final ionic fragments, which is often the case for molecules after core electron ionization. By correlating the measured angular distribution of the second photoelectron with the KER, this concept has been recently applied to visualizing x-ray-induced dissociation of O_2 molecules via inner-shell photoelectron diffraction [165]. The single-pulse scheme is not limited to the two-photon absorption, and can be generalized to the study of other processes involving more than two photons. In that case, the pump photon is still the one which initiates the dissociation and the probe photon is the one which leads to the time-dependent signals such as photons, photoelectrons or Auger electrons.

Chapter 8

Summary and outlook

Molecular response to ultra-intense x-rays

X-ray interaction with a molecule is localized at particular sites of elements which have the largest photoabsorption cross sections. Through the sequential multiphoton ionization of inner-shell electrons and a sequence of Auger decays, these sites become highly charged. In the meantime, the localized interaction induces charge rearrangements and nuclear dynamics. The final interaction product is found to be determined by the interplay between these four key processes: photoabsorption, Auger decay, charge rearrangment and nulcear dynamics, unfolding on a time scale defined by the XFEL pulse duration.

From the simple sequential multiphoton ionization model derived based on the assumption of a average photoabsorption cross section for each ionization step, the probability to obtain a certain interaction product is found to be proportional to $e^{-dE_{pls}}E_{pls}^{n}$, with d being constant depending on the photon energy, photoabsorption cross section, focal area and beamline transmission coefficient, E_{pls} the pulse energy measured upstream of the experimental hall, and n the number of photoabsorptions needed to reach this interaction product. This proportion relation is successfully used to explain the experimental ion yield scaling with pulse energy. The model also predicts that the average ionization rate leading to a particular interaction product is inversely proportional to the pulse duration and independent of all other XFEL pulse parameters. The prediction is supported by the experimental ion

kinetic energies which show an increase with shorter pulses because of their larger ionization rate, and show no dependence on pulse energy or intensity.

However, this model can't account for the effects due to resonances and charge rearrangement. But such effects can still be qualitatively understood by analyzing the experimental data. Resonant excitations in molecules greatly increase the yield of high-charge-state ions which are otherwise unattainable, as previously reported for the atomic case [5]. But in contrast to the atomic case, new enhancement structures in the ion charge state distributions appear in the molecular case. For CH_3I, the structures are located about 7 charges lower than the common enhancement structure present in both the atomic and molecular cases. Such structures can be attributed to charge rearrangement which can decrease the charge state of these ions originally making up the common enhancement structure and create new enhancement structures at low charge states. It's worth noting that 7 is the total number of electrons transferable from the methyl group CH_3 to iodine site. Charge rearrangement is found to greatly enhance the ionization of molecules with respect to the independent-atom model when ultra-intense x-rays are used. This effect, which is called "Charge-Rearrangement-Enhanced X-ray Ionization of Molecules", can be explained by the electrons which, initially localized at the elements not interacting with x-rays, are transferred to the x-ray-absorbing site and then participate in the photoionization and decay processes, leading to more electrons ejected from the molecule. The interplay among the dominant processes (ionization, charge rearrangement and fragmentation) is revealed through their dependence on pulse duration. With shorter pulses, the average ionization rate is larger, a certain total charge state of the molecule is reached with a shorter time and hence at shorter internulcear distances before the atoms can move further apart through fragmentation. This shorter internuclear distance makes it easier for electrons to transfer from the other part of the molecule to the high-charged site, which is confirmed by the experimental data. The easier electron transfer in turn can influence the ionization, because the transferred electrons can participate in the decay processes which are otherwise not possible, and speed up the refilling of the holes created by previous ionizations and Auger decays. The faster refilling effectively increases the instantaneous photoabsorption cross section due to the increased

availability of electrons for x-ray interactions. This charge-rearrangement enhancement of ionization is different from CREXIM, in the sense that it is for the ionization of an atom in a molecular environment instead of for the ionization of the molecule as a whole as is the case for CREXIM. Such effect, dubbed "Extended-CREXIM", is used to explain the higher yield of high-charge-state ions produced by shorter pulses.

It needs to be pointed out that all the experimental observations match reasonably well with ab initio calculations 2.4.9, except the observation that shorter pulses produce higher yield of high-charge-state ions. This discrepancy can be caused by either the experiment or calculation. In the experiment, the enhanced yield of high-charge state ions can also be caused by a more focused x-ray spatial distribution in the interaction region when switching to a shorter pulse duration instead of by enhanced charge transfer, even if it's rather unlikely and to the best of our knowledge, there is no theory prediction for such x-ray spatial distribution dependence on pulse duration. As for the model calculation, the approximations made in the Hartree-Fock method may make it not accurate enough to describe the charge rearrangement process and its resulting ionization enhancement. In the future experiments, the charge rearrangement process shall be characterized in finer details, in order to establish a model for charge rearrangement which can accurately describe its dependence on the states of charge donor and acceptor, and the distance between the two. Such model can in turn improve the ab initio ionization calculations.

Coulomb explosion imaging of molecules with x-ray free electron lasers

Irradiated by ultra-intense XFEL pulses typically of tens of femtoseconds in duration, a molecule can be charged up before the nuclei can significantly move away from their original positions. Then the molecule starts to undergo Coulomb explosion. Because of this ultrafast charge-up, the relative momentum distribution of ion fragments from the explosion resembles the one expected from the explosion of a molecule which is instantaneously charged up. This makes "Coulomb Explosion Imaging" of molecules with XFEL pulses a promising complementary technique to x-ray [22, 23] or electron [24, 25] scattering-based imaging techniques as

well as to those based on photoelectron diffraction with table-top lasers [26–28] and XFELs [29–31]. The small discrepancy in the experimental relative momentum distribution with the one from the instantaneous charge-up model is due to the neglected charge buildup and redistribution processes. By incorporating a model [18] developed by Motomura, Kukk and et al., which takes into account these two processes, into the Coulomb explosion simulation, the obtained relative momentum distribution achieved a better match with experiment.

The current experiment has been performed with molecules (CH_3I) at their ground state and with the single pulse configuration, so only the molecular structure at equilibrium could be studied. In the future, such studies shall be extended to transient molecular structures at excited states. This can be done with an x-ray-pump x-ray-probe or external-light-pump x-ray-probe configuration, in which a molecule is first pumped to an excited state, initiating molecular structural changes through e.g. vibration and isomerization or dissociation. The transient molecular structures during such changes can then be imaged by a time delayed XFEL pulse through Coulomb explosion.

Ion and electron coincidence measurement with x-ray free-electron lasers

From the results of ion-ion and electron coincidence measurement of 506 eV x-ray pulses interacting with N_2 molecules, the physical processes leading to the production of certain ion fragments are revealed. For example with $[N^{3+},\ N^{+}]$ fragment pair, it typically takes one photoabsorption and an Auger decay to first reach N_2^{2+}, and from there a second photoabsorption and Auger decay to reach $[N^{3+},\ N^{+}]$. The kinetic energy release of $[N^{3+},\ N^{+}]$ reflects the internuclear distance of N_2^{2+} at which the second photoabsorption occurs, with lower KER corresponding to longer internuclear distance. Through KER-resolved ion-ion ($[N^{3+},\ N^{+}]$) and electron coincidence measurement, the second photoelectron kinetic energy is observed to be larger with smaller-KER $[N^{3+},\ N^{+}]$ ion pairs, indicating that the core electron binding energy of N_2^{2+} gets smaller when its internuclear distance gets larger during dissociation. Such "dynamical line shift" is observed with a single x-ray pulse, enabled by the combination of ion and electron coincidence measurement with an XFEL.

The current experiment only detected ions and photoelectrons in coincidence. In the future, all interaction products including ions, photoelectrons and Auger electrons shall be coincidently detected. In addition, more coincidence experiments will be implemented with the x-ray/external light-pump x-ray-probe configuration, which allow kinematically complete measurement of x-ray or external light induced dynamics in atoms or molecules. One example is to use the coincidence technique to study electronic dynamics in excited state molecules prepared by recently available attosecond XFEL pulses [97].

Bibliography

[1] L. Young, E. P. Kanter, B. Krässig, Y. Li, A. M. March, S. T. Pratt, R. Santra, S. H. Southworth, N. Rohringer, L. F. DiMauro, G. Doumy, C. A. Roedig, N. Berrah, L. Fang, M. Hoener, P. H. Bucksbaum, J. P. Cryan, S. Ghimire, J. M. Glownia, D. A. Reis, J. D. Bozek, C. Bostedt, and M. Messerschmidt. Femtosecond electronic response of atoms to ultra-intense x-rays. *Nature*, 466:56–61, 2010. URL https://www.nature.com/articles/nature09177.

[2] G. Doumy, C. Roedig, S.-K. Son, C. I. Blaga, A. D. DiChiara, R. Santra, N. Berrah, C. Bostedt, J. D. Bozek, P. H. Bucksbaum, J. P. Cryan, L. Fang, S. Ghimire, J. M. Glownia, M. Hoener, E. P. Kanter, B. Krässig, M. Kuebel, M. Messerschmidt, G. G. Paulus, D. A. Reis, N. Rohringer, L. Young, P. Agostini, and L. F. DiMauro. Nonlinear atomic response to intense ultrashort x rays. *Physical Review Letters*, 106:083002, 2011. URL https://link.aps.org/doi/10.1103/PhysRevLett.106.083002.

[3] C. Weninger, M. Purvis, D. Ryan, R. A. London, J. D. Bozek, C. Bostedt, A. Graf, G. Brown, J. J. Rocca, and N. Rohringer. Stimulated electronic x-ray Raman scattering. *Physical Review Letters*, 111:233902, 2013. URL https://link.aps.org/doi/10.1103/PhysRevLett.111.233902.

[4] M. Fuchs, M. Trigo, J. Chen, S. Ghimire, S. Shwartz, M. Kozina, M. Jiang, T. Henighan, C. Bray, G. Ndabashimiye, P. H. Bucksbaum, Y. Feng, S. Herrmann, G. A. Carini, J. Pines, P. Hart, C. Kenney, S. Guillet, S. Boutet, G. J. Williams, M. Messerschmidt, M. M. Seibert, S. Moeller, J. B. Hastings, and D. A. Reis. Anomalous nonlinear x-ray Compton scattering. *Nature Physics*, 11:964–970, 2015. URL https://www.nature.com/articles/nphys3452.

[5] B. Rudek, S.-K. Son, L. Foucar, S. W. Epp, B. Erk, R. Hartmann, M. Adolph, R. An-

dritschke, A. Aquila, N. Berrah, C. Bostedt, J. Bozek, N. Coppola, F. Filsinger, H. Gorke, T. Gorkhover, H. Graafsma, L. Gumprecht, A. Hartmann, G. Hauser, S. Herrmann, H. Hirsemann, P. Holl, A. Hömke, L. Journel, C. Kaiser, N. Kimmel, F. Krasniqi, K.-U. Kühnel, M. Matysek, M. Messerschmidt, D. Miesner, T. Möller, R. Moshammer, K. Nagaya, B. Nilsson, G. Potdevin, D. Pietschner, C. Reich, D. Rupp, G. Schaller, I. Schlichting, C. Schmidt, F. Schopper, S. Schorb, C.-D. Schröter, J. Schulz, M. Simon, H. Soltau, L. Strüder, K. Ueda, G. Weidenspointner, R. Santra, J. Ullrich, A. Rudenko, and D. Rolles. Ultra-efficient ionization of heavy atoms by intense x-ray free-electron laser pulses. *Nature Photonics*, 6:858–865, 2012. URL https://www.nature.com/articles/nphoton.2012.261.

[6] B. Rudek. *Multiple Ionization of Heavy Atoms by Intense X-Ray Free-Electron Laser Pulses*. PhD thesis, The Ruperto-Carola-University of Heidelberg, 2012.

[7] B. Rudek, D. Rolles, S.-K. Son, L. Foucar, B. Erk, S. Epp, R. Boll, D. Anielski, C. Bostedt, S. Schorb, R. Coffee, J. Bozek, S. Trippel, T. Marchenko, M. Simon, L. Christensen, S. De, S.-i. Wada, K. Ueda, I. Schlichting, R. Santra, J. Ullrich, and A. Rudenko. Resonance-enhanced multiple ionization of krypton at an x-ray free-electron laser. *Physical Review A*, 87:023413, 2013. URL https://link.aps.org/doi/10.1103/PhysRevA.87.023413.

[8] B. Rudek, K. Toyota, L. Foucar, B. Erk, R. Boll, C. Bomme, J. Correa, S. Carron, S. Boutet, G. J. Williams, K. R. Ferguson, R. Alonso-Mori, J. E. Koglin, T. Gorkhover, M. Bucher, C. S. Lehmann, B. Krässig, S. H. Southworth, L. Young, C. Bostedt, K. Ueda, T. Marchenko, M. Simon, Z. Jurek, R. Santra, A. Rudenko, S.-K. Son, and D. Rolles. Relativistic and resonant effects in the ionization of heavy atoms by ultra-intense hard x-rays. *Nature Communications*, 9:4200, 2018. URL https://www.nature.com/articles/s41467-018-06745-6.

[9] L. S. Cederbaum, F. Tarantelli, A. Sgamellotti, and J. Schirmer. On double vacancies

in the core. *The Journal of Chemical Physics*, 85:6513–6523, 1986. URL https://aip.scitation.org/doi/10.1063/1.451432.

[10] J. P. Cryan, J. M. Glownia, J. Andreasson, A. Belkacem, N. Berrah, C. I. Blaga, C. Bostedt, J. Bozek, C. Buth, L. F. DiMauro, L. Fang, O. Gessner, M. Guehr, J. Hajdu, M. P. Hertlein, M. Hoener, O. Kornilov, J. P. Marangos, A. M. March, B. K. McFarland, H. Merdji, V. S. Petrović, C. Raman, D. Ray, D. Reis, F. Tarantelli, M. Trigo, J. L. White, W. White, L. Young, P. H. Bucksbaum, and R. N. Coffee. Auger electron angular distribution of double core-hole states in the molecular reference frame. *Physical Review Letters*, 105:083004, 2010. URL https://link.aps.org/doi/10.1103/PhysRevLett.105.083004.

[11] L. Fang, M. Hoener, O. Gessner, F. Tarantelli, S. T. Pratt, O. Kornilov, C. Buth, M. Gühr, E. P. Kanter, C. Bostedt, J. D. Bozek, P. H. Bucksbaum, M. Chen, R. Coffee, J. Cryan, M. Glownia, E. Kukk, S. R. Leone, and N. Berrah. Double core-hole production in N_2: beating the Auger clock. *Physical Review Letters*, 105:083005, 2010. URL https://link.aps.org/doi/10.1103/PhysRevLett.105.083005.

[12] N. Berrah, L. Fang, B. Murphy, T. Osipov, K. Ueda, E. Kukk, R. Feifel, P. v. d. Meulen, P. Salen, H. T. Schmidt, R. D. Thomas, M. Larsson, R. Richter, K. C. Prince, J. D. Bozek, C. Bostedt, S.-i. Wada, M. N. Piancastelli, M. Tashiro, and M. Ehara. Double-core-hole spectroscopy for chemical analysis with an intense x-ray femtosecond laser. *Proceedings of the National Academy of Sciences*, 108:16912–16915, 2011. URL https://www.pnas.org/content/108/41/16912.

[13] B. Erk, D. Rolles, L. Foucar, B. Rudek, S. W. Epp, M. Cryle, C. Bostedt, S. Schorb, J. Bozek, A. Rouzee, A. Hundertmark, T. Marchenko, M. Simon, F. Filsinger, L. Christensen, S. De, S. Trippel, J. Küpper, H. Stapelfeldt, S. Wada, K. Ueda, M. Swiggers, M. Messerschmidt, C. D. Schröter, R. Moshammer, I. Schlichting, J. Ullrich, and A. Rudenko. Ultrafast charge rearrangement and nuclear dynamics upon inner-shell

multiple ionization of small polyatomic molecules. *Physical Review Letters*, 110:053003, 2013. URL https://link.aps.org/doi/10.1103/PhysRevLett.110.053003.

[14] B. Erk, D. Rolles, L. Foucar, B. Rudek, S. W. Epp, M. Cryle, C. Bostedt, S. Schorb, J. Bozek, A. Rouzee, A. Hundertmark, T. Marchenko, M. Simon, F. Filsinger, L. Christensen, S. De, S. Trippel, J. Küpper, H. Stapelfeldt, S. Wada, K. Ueda, M. Swiggers, M. Messerschmidt, C. D. Schröter, R. Moshammer, I. Schlichting, J. Ullrich, and A. Rudenko. Inner-shell multiple ionization of polyatomic molecules with an intense x-ray free-electron laser studied by coincident ion momentum imaging. *Journal of Physics B: Atomic, Molecular and Optical Physics*, 46:164031, 2013. URL https://iopscience.iop.org/article/10.1088/0953-4075/46/16/164031/meta.

[15] B. Erk. *Fragmentation Dynamics of Small Molecules upon Multiple Ionization by X-Ray Free-Electron Laser Pulses*. PhD thesis, The Ruperto-Carola-University of Heidelberg, 2013.

[16] B. Erk, R. Boll, S. Trippel, D. Anielski, L. Foucar, B. Rudek, S. W. Epp, R. Coffee, S. Carron, S. Schorb, K. R. Ferguson, M. Swiggers, J. D. Bozek, M. Simon, T. Marchenko, J. Kupper, I. Schlichting, J. Ullrich, C. Bostedt, D. Rolles, and A. Rudenko. Imaging charge transfer in iodomethane upon x-ray photoabsorption. *Science*, 345:288–291, 2014. URL http://www.sciencemag.org/cgi/doi/10.1126/science.1253607.

[17] R. Boll, B. Erk, R. Coffee, S. Trippel, T. Kierspel, C. Bomme, J. D. Bozek, M. Burkett, S. Carron, K. R. Ferguson, L. Foucar, J. Küpper, T. Marchenko, C. Miron, M. Patanen, T. Osipov, S. Schorb, M. Simon, M. Swiggers, S. Techert, K. Ueda, C. Bostedt, D. Rolles, and A. Rudenko. Charge transfer in dissociating iodomethane and fluoromethane molecules ionized by intense femtosecond x-ray pulses. *Structural Dynamics*, 3:043207, 2016. URL http://aip.scitation.org/doi/10.1063/1.4944344.

[18] K. Motomura, E. Kukk, H. Fukuzawa, S.-I. Wada, K. Nagaya, S. Ohmura, S. Mondal, T. Tachibana, Y. Ito, R. Koga, T. Sakai, K. Matsunami, A. Rudenko, C. Nicolas,

X.-J. Liu, C. Miron, Y. Zhang, Y. Jiang, J. Chen, M. Anand, D. E. Kim, K. Tono, M. Yabashi, M. Yao, and K. Ueda. Charge and nuclear dynamics induced by deep inner-shell multiphoton ionization of CH_3I molecules by intense x-ray free-electron laser pulses. *The Journal of Physical Chemistry Letters*, 6:2944–2949, 2015. URL https://doi.org/10.1021/acs.jpclett.5b01205.

[19] K. Nagaya, K. Motomura, E. Kukk, H. Fukuzawa, S. Wada, T. Tachibana, Y. Ito, S. Mondal, T. Sakai, K. Matsunami, R. Koga, S. Ohmura, Y. Takahashi, M. Kanno, A. Rudenko, C. Nicolas, X.-J. Liu, Y. Zhang, J. Chen, M. Anand, Y. H. Jiang, D.-E. Kim, K. Tono, M. Yabashi, H. Kono, C. Miron, M. Yao, and K. Ueda. Ultrafast dynamics of a nucleobase analogue illuminated by a short intense x-ray free electron laser pulse. *Physical Review X*, 6:021035, 2016. URL https://link.aps.org/doi/10.1103/PhysRevX.6.021035.

[20] B. F. Murphy, T. Osipov, Z. Jurek, L. Fang, S.-K. Son, M. Mucke, J. H. D. Eland, V. Zhaunerchyk, R. Feifel, L. Avaldi, P. Bolognesi, C. Bostedt, J. D. Bozek, J. Grilj, M. Guehr, L. J. Frasinski, J. Glownia, D. T. Ha, K. Hoffmann, E. Kukk, B. K. McFarland, C. Miron, E. Sistrunk, R. J. Squibb, K. Ueda, R. Santra, and N. Berrah. Femtosecond x-ray-induced explosion of C_{60} at extreme intensity. *Nature Communications*, 5:1–9, 2014. URL https://www.nature.com/articles/ncomms5281.

[21] N. Berrah, A. Sanchez-Gonzalez, Z. Jurek, R. Obaid, H. Xiong, R. J. Squibb, T. Osipov, A. Lutman, L. Fang, T. Barillot, J. D. Bozek, J. Cryan, T. J. A. Wolf, D. Rolles, R. Coffee, K. Schnorr, S. Augustin, H. Fukuzawa, K. Motomura, N. Niebuhr, L. J. Frasinski, R. Feifel, C. P. Schulz, K. Toyota, S.-K. Son, K. Ueda, T. Pfeifer, J. P. Marangos, and R. Santra. Femtosecond-resolved observation of the fragmentation of buckminsterfullerene following x-ray multiphoton ionization. *Nature Physics*, pages 1–5, 2019. URL https://www.nature.com/articles/s41567-019-0665-7.

[22] J. Küpper, S. Stern, L. Holmegaard, F. Filsinger, A. Rouzée, A. Rudenko, P. Johnsson, A. V. Martin, M. Adolph, A. Aquila, S. Bajt, A. Barty, C. Bostedt, J. Bozek, C. Cale-

man, R. Coffee, N. Coppola, T. Delmas, S. Epp, B. Erk, L. Foucar, T. Gorkhover, L. Gumprecht, A. Hartmann, R. Hartmann, G. Hauser, P. Holl, A. Hömke, N. Kimmel, F. Krasniqi, K.-U. Kühnel, J. Maurer, M. Messerschmidt, R. Moshammer, C. Reich, B. Rudek, R. Santra, I. Schlichting, C. Schmidt, S. Schorb, J. Schulz, H. Soltau, J. C. H. Spence, D. Starodub, L. Strüder, J. Thøgersen, M. J. J. Vrakking, G. Weidenspointner, T. A. White, C. Wunderer, G. Meijer, J. Ullrich, H. Stapelfeldt, D. Rolles, and H. N. Chapman. X-ray diffraction from isolated and strongly aligned gas-phase molecules with a free-electron laser. *Physical Review Letters*, 112:083002, 2014. URL https://link.aps.org/doi/10.1103/PhysRevLett.112.083002.

[23] M. P. Minitti, J. M. Budarz, A. Kirrander, J. S. Robinson, D. Ratner, T. J. Lane, D. Zhu, J. M. Glownia, M. Kozina, H. T. Lemke, M. Sikorski, Y. Feng, S. Nelson, K. Saita, B. Stankus, T. Northey, J. B. Hastings, and P. M. Weber. Imaging molecular motion: femtosecond x-ray scattering of an electrocyclic chemical reaction. *Physical Review Letters*, 114:255501, 2015. URL https://link.aps.org/doi/10.1103/PhysRevLett.114.255501.

[24] J. Yang, X. Zhu, T. J. A. Wolf, Z. Li, J. P. F. Nunes, R. Coffee, J. P. Cryan, M. Gühr, K. Hegazy, T. F. Heinz, K. Jobe, R. Li, X. Shen, T. Veccione, S. Weathersby, K. J. Wilkin, C. Yoneda, Q. Zheng, T. J. Martinez, M. Centurion, and X. Wang. Imaging CF_3I conical intersection and photodissociation dynamics with ultrafast electron diffraction. *Science*, 361:64–67, 2018. URL https://science.sciencemag.org/content/361/6397/64.

[25] T. J. A. Wolf, D. M. Sanchez, J. Yang, R. M. Parrish, J. P. F. Nunes, M. Centurion, R. Coffee, J. P. Cryan, M. Gühr, K. Hegazy, A. Kirrander, R. K. Li, J. Ruddock, X. Shen, T. Vecchione, S. P. Weathersby, P. M. Weber, K. Wilkin, H. Yong, Q. Zheng, X. J. Wang, M. P. Minitti, and T. J. Martínez. The photochemical ring-opening of 1,3-cyclohexadiene imaged by ultrafast electron diffraction. *Nature Chemistry*, 11:504–509, 2019. URL https://www.nature.com/articles/s41557-019-0252-7.

[26] J. Xu. *Ultrafast Imaging: Laser Induced Electron Diffraction*. PhD thesis, Kansas State University, 2012.

[27] C. I. Blaga, J. Xu, A. D. DiChiara, E. Sistrunk, K. Zhang, P. Agostini, T. A. Miller, L. F. DiMauro, and C. D. Lin. Imaging ultrafast molecular dynamics with laser-induced electron diffraction. *Nature*, 483:194–197, 2012. URL https://www.nature.com/articles/nature10820.

[28] M. G. Pullen, B. Wolter, A.-T. Le, M. Baudisch, M. Hemmer, A. Senftleben, C. D. Schröter, J. Ullrich, R. Moshammer, C. D. Lin, and J. Biegert. Imaging an aligned polyatomic molecule with laser-induced electron diffraction. *Nature Communications*, 6:1–6, 2015. URL https://www.nature.com/articles/ncomms8262.

[29] R. Boll, D. Anielski, C. Bostedt, J. D. Bozek, L. Christensen, R. Coffee, S. De, P. Decleva, S. W. Epp, B. Erk, L. Foucar, F. Krasniqi, J. Küpper, A. Rouzée, B. Rudek, A. Rudenko, S. Schorb, H. Stapelfeldt, M. Stener, S. Stern, S. Techert, S. Trippel, M. J. J. Vrakking, J. Ullrich, and D. Rolles. Femtosecond photoelectron diffraction on laser-aligned molecules: towards time-resolved imaging of molecular structure. *Physical Review A*, 88:061402, 2013. URL https://link.aps.org/doi/10.1103/PhysRevA.88.061402.

[30] D. Rolles, R. Boll, M. Adolph, A. Aquila, C. Bostedt, J. D. Bozek, H. N. Chapman, R. Coffee, N. Coppola, P. Decleva, T. Delmas, S. W. Epp, B. Erk, F. Filsinger, L. Foucar, L. Gumprecht, A. Hömke, T. Gorkhover, L. Holmegaard, P. Johnsson, C. Kaiser, F. Krasniqi, K.-U. Kühnel, J. Maurer, M. Messerschmidt, R. Moshammer, W. Quevedo, I. Rajkovic, A. Rouzée, B. Rudek, I. Schlichting, C. Schmidt, S. Schorb, C. D. Schröter, J. Schulz, H. Stapelfeldt, M. Stener, S. Stern, S. Techert, J. Thøgersen, M. J. J. Vrakking, A. Rudenko, J. Küpper, and J. Ullrich. Femtosecond x-ray photoelectron diffraction on gas-phase dibromobenzene molecules. *Journal of Physics B: Atomic, Molecular and Optical Physics*, 47:124035, 2014. URL https://iopscience.iop.org/article/10.1088/0953-4075/47/12/124035/meta.

[31] R. Boll. *Imaging Molecular Structure with Photoelectron Diffraction*. PhD thesis, The Ruperto-Carola-University of Heidelberg, 2014.

[32] A. Picón, C. S. Lehmann, C. Bostedt, A. Rudenko, A. Marinelli, T. Osipov, D. Rolles, N. Berrah, C. Bomme, M. Bucher, G. Doumy, B. Erk, K. R. Ferguson, T. Gorkhover, P. J. Ho, E. P. Kanter, B. Krässig, J. Krzywinski, A. A. Lutman, A. M. March, D. Moonshiram, D. Ray, L. Young, S. T. Pratt, and S. H. Southworth. Hetero-site-specific x-ray pump-probe spectroscopy for femtosecond intramolecular dynamics. *Nature Communications*, 7:11652, 2016. URL https://www.nature.com/articles/ncomms11652.

[33] H. N. Chapman. X-ray free-electron lasers for the structure and dynamics of macromolecules. *Annual Review of Biochemistry*, 88:35–58, 2019. URL https://doi.org/10.1146/annurev-biochem-013118-110744.

[34] H. N. Chapman, P. Fromme, A. Barty, T. A. White, R. A. Kirian, A. Aquila, M. S. Hunter, J. Schulz, D. P. DePonte, U. Weierstall, R. B. Doak, Filipe R. N. C. Maia, A. V. Martin, I. Schlichting, L. Lomb, N. Coppola, R. L. Shoeman, S. W. Epp, R. Hartmann, D. Rolles, A. Rudenko, L. Foucar, N. Kimmel, G. Weidenspointner, P. Holl, M. Liang, M. Barthelmess, C. Caleman, S. Boutet, M. J. Bogan, J. Krzywinski, C. Bostedt, S. Bajt, L. Gumprecht, B. Rudek, B. Erk, C. Schmidt, A. Hömke, C. Reich, D. Pietschner, L. Strüder, G. Hauser, H. Gorke, J. Ullrich, S. Herrmann, G. Schaller, F. Schopper, H. Soltau, K.-U. Kühnel, M. Messerschmidt, J. D. Bozek, S. P. Hau-Riege, M. Frank, C. Y. Hampton, R. G. Sierra, D. Starodub, G. J. Williams, J. Hajdu, N. Timneanu, M. M. Seibert, J. Andreasson, A. Rocker, O. Jönsson, M. Svenda, S. Stern, K. Nass, R. Andritschke, C.-D. Schröter, F. Krasniqi, M. Bott, K. E. Schmidt, X. Wang, I. Grotjohann, J. M. Holton, T. R. M. Barends, R. Neutze, S. Marchesini, R. Fromme, S. Schorb, D. Rupp, M. Adolph, T. Gorkhover, I. Andersson, H. Hirsemann, G. Potdevin, H. Graafsma, B. Nilsson, and J. C. H

Spence. Femtosecond x-ray protein nanocrystallography. *Nature*, 470:73–77, 2011. URL https://www.nature.com/articles/nature09750.

[35] M. M. Seibert, T. Ekeberg, Filipe R. N. C. Maia, M. Svenda, J. Andreasson, O. Jönsson, D. Odić, B. Iwan, A. Rocker, D. Westphal, M. Hantke, D. P. DePonte, A. Barty, J. Schulz, L. Gumprecht, N. Coppola, A. Aquila, M. Liang, T. A. White, A. Martin, C. Caleman, S. Stern, C. Abergel, V. Seltzer, J.-M. Claverie, C. Bostedt, J. D. Bozek, S. Boutet, A. A. Miahnahri, M. Messerschmidt, J. Krzywinski, G. Williams, K. O. Hodgson, M. J. Bogan, C. Y. Hampton, R. G. Sierra, D. Starodub, I. Andersson, S. Bajt, M. Barthelmess, J. C. H. Spence, P. Fromme, U. Weierstall, R. Kirian, M. Hunter, R. B. Doak, S. Marchesini, S. P. Hau-Riege, M. Frank, R. L. Shoeman, L. Lomb, S. W. Epp, R. Hartmann, D. Rolles, A. Rudenko, C. Schmidt, L. Foucar, N. Kimmel, P. Holl, B. Rudek, B. Erk, A. Hömke, C. Reich, D. Pietschner, G. Weidenspointner, L. Strüder, G. Hauser, H. Gorke, J. Ullrich, I. Schlichting, S. Herrmann, G. Schaller, F. Schopper, H. Soltau, K.-U. Kühnel, R. Andritschke, C.-D. Schröter, F. Krasniqi, M. Bott, S. Schorb, D. Rupp, M. Adolph, T. Gorkhover, H. Hirsemann, G. Potdevin, H. Graafsma, B. Nilsson, H. N. Chapman, and J. Hajdu. Single mimivirus particles intercepted and imaged with an x-ray laser. *Nature*, 470:78–81, 2011. URL https://www.nature.com/articles/nature09748.

[36] T. Gorkhover, M. Adolph, D. Rupp, S. Schorb, S. W. Epp, B. Erk, L. Foucar, R. Hartmann, N. Kimmel, K.-U. Kühnel, D. Rolles, B. Rudek, A. Rudenko, R. Andritschke, A. Aquila, J. D. Bozek, N. Coppola, T. Erke, F. Filsinger, H. Gorke, H. Graafsma, L. Gumprecht, G. Hauser, S. Herrmann, H. Hirsemann, A. Hömke, P. Holl, C. Kaiser, F. Krasniqi, J.-H. Meyer, M. Matysek, M. Messerschmidt, D. Miessner, B. Nilsson, D. Pietschner, G. Potdevin, C. Reich, G. Schaller, C. Schmidt, F. Schopper, C. D. Schröter, J. Schulz, H. Soltau, G. Weidenspointner, I. Schlichting, L. Strüder, J. Ullrich, T. Möller, and C. Bostedt. Nanoplasma dynamics of single large xenon clusters irradiated with superintense x-ray pulses from the Linac Coher-

ent Light Source free-electron laser. *Physical Review Letters*, 108:245005, 2012. URL https://link.aps.org/doi/10.1103/PhysRevLett.108.245005.

[37] T. Gorkhover, S. Schorb, R. Coffee, M. Adolph, L. Foucar, D. Rupp, A. Aquila, J. D. Bozek, S. W. Epp, B. Erk, L. Gumprecht, L. Holmegaard, A. Hartmann, R. Hartmann, G. Hauser, P. Holl, A. Hömke, P. Johnsson, N. Kimmel, K.-U. Kühnel, M. Messerschmidt, C. Reich, A. Rouzée, B. Rudek, C. Schmidt, J. Schulz, H. Soltau, S. Stern, G. Weidenspointner, B. White, J. Küpper, L. Strüder, I. Schlichting, J. Ullrich, D. Rolles, A. Rudenko, T. Möller, and C. Bostedt. Femtosecond and nanometre visualization of structural dynamics in superheated nanoparticles. *Nature Photonics*, 10:93–97, 2016. URL https://www.nature.com/articles/nphoton.2015.264.

[38] T. Gorkhover, A. Ulmer, K. Ferguson, M. Bucher, Filipe R. N. C. Maia, J. Bielecki, T. Ekeberg, M. F. Hantke, B. J. Daurer, C. Nettelblad, J. Andreasson, A. Barty, P. Bruza, S. Carron, D. Hasse, J. Krzywinski, D. S. D. Larsson, A. Morgan, K. Mühlig, M. Müller, K. Okamoto, A. Pietrini, D. Rupp, M. Sauppe, G. v. d. Schot, M. Seibert, J. A. Sellberg, M. Svenda, M. Swiggers, N. Timneanu, D. Westphal, G. Williams, A. Zani, H. N. Chapman, G. Faigel, T. Möller, J. Hajdu, and C. Bostedt. Femtosecond x-ray Fourier holography imaging of free-flying nanoparticles. *Nature Photonics*, 12: 150, 2018. URL https://www.nature.com/articles/s41566-018-0110-y.

[39] L. F. Gomez, K. R. Ferguson, J. P. Cryan, C. Bacellar, R. M. P. Tanyag, C. Jones, S. Schorb, D. Anielski, A. Belkacem, C. Bernando, R. Boll, J. Bozek, S. Carron, G. Chen, T. Delmas, L. Englert, S. W. Epp, B. Erk, L. Foucar, R. Hartmann, A. Hexemer, M. Huth, J. Kwok, S. R. Leone, J. H. S. Ma, Filipe R. N. C. Maia, E. Malmerberg, S. Marchesini, D. M. Neumark, B. Poon, J. Prell, D. Rolles, B. Rudek, A. Rudenko, M. Seifrid, K. R. Siefermann, F. P. Sturm, M. Swiggers, J. Ullrich, F. Weise, P. Zwart, C. Bostedt, O. Gessner, and A. F. Vilesov. Shapes and vorticities of superfluid helium nanodroplets. *Science*, 345:906–909, 2014. URL https://science.sciencemag.org/content/345/6199/906.

[40] R. Neutze, R. Wouts, D. V. D. Spoel, E. Weckert, and J. Hajdu. Potential for biomolecular imaging with femtosecond x-ray pulses. *Nature*, 406:752–757, 2000. URL https://www.nature.com/articles/35021099.

[41] K. Nass, L. Foucar, T. R. M. Barends, E. Hartmann, S. Botha, R. L. Shoeman, R. B. Doak, R. Alonso-Mori, A. Aquila, S. Bajt, A. Barty, R. Bean, K. R. Beyerlein, M. Bublitz, N. Drachmann, J. Gregersen, H. O. Jönsson, W. Kabsch, S. Kassemeyer, J. E. Koglin, M. Krumrey, D. Mattle, M. Messerschmidt, P. Nissen, L. Reinhard, O. Sitsel, D. Sokaras, G. J. Williams, S. Hau-Riege, N. Timneanu, C. Caleman, H. N. Chapman, S. Boutet, and I. Schlichting. Indications of radiation damage in ferredoxin microcrystals using high-intensity x-FEL beams. *Journal of Synchrotron Radiation*, 22:225–238, 2015. URL https://www.ncbi.nlm.nih.gov/pubmed/25723924.

[42] L. Galli, S.-K. Son, M. Klinge, S. Bajt, A. Barty, R. Bean, C. Betzel, K. R. Beyerlein, C. Caleman, R. B. Doak, M. Duszenko, H. Fleckenstein, C. Gati, B. Hunt, R. A. Kirian, M. Liang, M. H. Nanao, K. Nass, D. Oberthür, L. Redecke, R. Shoeman, F. Stellato, C. H. Yoon, T. A. White, O. Yefanov, J. Spence, and H. N. Chapman. Electronic damage in s atoms in a native protein crystal induced by an intense x-ray free-electron laser pulse. *Structural Dynamics*, 2, 2015. URL https://www.ncbi.nlm.nih.gov/pmc/articles/PMC4711609/.

[43] A. Rudenko, L. Inhester, K. Hanasaki, X. Li, S. J. Robatjazi, B. Erk, R. Boll, K. Toyota, Y. Hao, O. Vendrell, C. Bomme, E. Savelyev, B. Rudek, L. Foucar, S. H. Southworth, C. S. Lehmann, B. Kraessig, T. Marchenko, M. Simon, K. Ueda, K. R. Ferguson, M. Bucher, T. Gorkhover, S. Carron, R. Alonso-Mori, J. E. Koglin, J. Correa, G. J. Williams, S. Boutet, L. Young, C. Bostedt, S.-K. Son, R. Santra, and D. Rolles. Femtosecond response of polyatomic molecules to ultra-intense hard x-rays. *Nature*, 546: 129–132, 2017. URL https://www.nature.com/articles/nature22373.

[44] X. Li, L. Inhester, S. J. Robatjazi, B. Erk, R. Boll, K. Hanasaki, K. Toyota, Y. Hao, C. Bomme, B. Rudek, L. Foucar, S. H. Southworth, C.S. Lehmann, B. Kraessig,

T. Marchenko, M. Simon, K. Ueda, K. R. Ferguson, M. Bucher, T. Gorkhover, S. Carron, R. Alonso-Mori, J. E. Koglin, J. Correa, G. J. Williams, S. Boutet, L. Young, C. Bostedt, S.-K. Son, R. Santra, D. Rolles, and A. Rudenko. Pulse energy and pulse duration effects in the ionization and fragmentation of polyatomic molecules by ultraintense hard x-rays, in review.

[45] X. Li et al. Resonance-enabled x-ray multiple ionization of a molecule, to be submitted.

[46] X. Li et al. Coulomb explosion imaging of iodomethane with an x-ray free-electron laser, to be submitted.

[47] X. Li et al. Single-pulse x-ray pump-probing of molecular dynamics, to be submitted.

[48] B. E. A. Saleh and M. C. Teich. *Fundamentals of Photonics*. John Wiley and Sons Inc, 2007.

[49] G. M. Wysin. Quantization of the Free Electromagnetic Field: Photons and Operators. URL https://www.phys.ksu.edu/personal/wysin/notes/quantumEM.pdf.

[50] E. Merzbacher. *Quantum Mechanics*. John Wiley and Sons Inc, 1998.

[51] V. May and O. Kühn. *Charge and Energy Transfer Dynamics in Molecular Systems*. WILEY-VCHVerlag GmbH and Co. KGaA, 2011.

[52] M. Berger, J. H. Hubbell, S. M. Seltzer, J. Chang, J. S. Coursey, R. Sukumar, D. S. Zucker, and K. Olsen. XCOM: Photon Cross Sections Database. URL https://www.nist.gov/pml/xcom-photon-cross-sections-database.

[53] B. H. Bransden and C. J. Joachain. *Physics of Atoms and Molecules*. New York: Prentice-Hall, 2003.

[54] P. Lambropoulos and X. Tang. Multiple excitation and ionization of atoms by strong lasers. *JOSA B*, 4:821–832, 1987. URL https://www.osapublishing.org/josab/abstract.cfm?uri=josab-4-5-821.

[55] K. Tamasaku, E. Shigemasa, Y. Inubushi, T. Katayama, K. Sawada, H. Yumoto, H. Ohashi, H. Mimura, M. Yabashi, K. Yamauchi, and T. Ishikawa. X-ray two-photon absorption competing against single and sequential multiphoton processes. *Nature Photonics*, 8:313–316, 2014. URL https://www.nature.com/articles/nphoton.2014.10.

[56] *X-Ray Data Booklet*. Lawrence Berkeley National Laboratory, 2009.

[57] S. Mukamel, D. Healion, Y. Zhang, and J. D. Biggs. Multidimensional attosecond resonant x-ray spectroscopy of molecules: lessons from the optical regime. *Annual Review of Physical Chemistry*, 64:101–127, 2013. URL https://doi.org/10.1146/annurev-physchem-040412-110021.

[58] J. T. O'Neal and J. P. Cryan et al. submitted.

[59] L. S. Cederbaum, J. Zobeley, and F. Tarantelli. Giant intermolecular decay and fragmentation of clusters. *Physical Review Letters*, 79:4778–4781, 1997. URL https://link.aps.org/doi/10.1103/PhysRevLett.79.4778.

[60] S. Marburger, O. Kugeler, U. Hergenhahn, and T. Möller. Experimental evidence for interatomic Coulombic decay in Ne clusters. *Physical Review Letters*, 90:203401, 2003. URL https://link.aps.org/doi/10.1103/PhysRevLett.90.203401.

[61] T. Jahnke, A. Czasch, M. S. Schöffler, S. Schössler, A. Knapp, M. Käsz, J. Titze, C. Wimmer, K. Kreidi, R. E. Grisenti, A. Staudte, O. Jagutzki, U. Hergenhahn, H. Schmidt-Böcking, and R. Dörner. Experimental observation of interatomic Coulombic decay in neon dimers. *Physical Review Letters*, 93:163401, 2004. URL https://link.aps.org/doi/10.1103/PhysRevLett.93.163401.

[62] K. Schnorr, A. Senftleben, M. Kurka, A. Rudenko, L. Foucar, G. Schmid, A. Broska, T. Pfeifer, K. Meyer, D. Anielski, R. Boll, D. Rolles, M. Kübel, M. F. Kling, Y. H. Jiang, S. Mondal, T. Tachibana, K. Ueda, T. Marchenko, M. Simon, G. Brenner, R. Treusch, S. Scheit, V. Averbukh, J. Ullrich, C. D. Schröter, and R. Moshammer.

Time-resolved measurement of interatomic Coulombic decay in Ne_2. *Physical Review Letters*, 111:093402, 2013. URL https://link.aps.org/doi/10.1103/PhysRevLett.111.093402.

[63] K. Schnorr. *XUV Pump-Probe Experiments on Electron Rearrangement and Interatomic Coulombic Decay in Diatomic Molecules*. PhD thesis, The Ruperto-Carola-University of Heidelberg, 2014.

[64] A. I. Kuleff, N. V. Kryzhevoi, M. Pernpointner, and L. S. Cederbaum. Core ionization initiates subfemtosecond charge migration in the valence shell of molecules. *Physical Review Letters*, 117:093002, 2016. URL https://link.aps.org/doi/10.1103/PhysRevLett.117.093002.

[65] H. Ryufuku, K. Sasaki, and T. Watanabe. Oscillatory behavior of charge transfer cross sections as a function of the charge of projectiles in low-energy collisions. *Physical Review A*, 21:745–750, 1980. URL https://link.aps.org/doi/10.1103/PhysRevA.21.745.

[66] A. Niehaus. A classical model for multiple-electron capture in slow collisions of highly charged ions with atoms. *Journal of Physics B: Atomic and Molecular Physics*, 19: 2925–2937, 1986. URL http://stacks.iop.org/0022-3700/19/i=18/a=021?key=crossref.10cba3df250dd59759a1b7fdde008391.

[67] L.D. Landau. Assotsiatsiya dvukhatomnykh molekul. *Sovetskii Fizicheskii Zhurnal*, 2: 46–52, 1932.

[68] C. Zener and R. H. Fowler. Non-adiabatic crossing of energy levels. *Proceedings of the Royal Society of London. Series A, Containing Papers of a Mathematical and Physical Character*, 137:696–702, 1932. URL https://royalsocietypublishing.org/doi/abs/10.1098/rspa.1932.0165.

[69] A. Salop and R. E. Olson. Charge exchange between H (1s) and fully stripped heavy

ions at low-keV impact energies. *Physical Review A*, 13:1312–1320, 1976. URL https://link.aps.org/doi/10.1103/PhysRevA.13.1312.

[70] R. E. Olson and A. Salop. Electron transfer between multicharged ions and neutral species. *Physical Review A*, 14:579–585, 1976. URL https://link.aps.org/doi/10.1103/PhysRevA.14.579.

[71] K. Schnorr, A. Senftleben, M. Kurka, A. Rudenko, G. Schmid, T. Pfeifer, K. Meyer, M. Kübel, M. F. Kling, Y. H. Jiang, R. Treusch, S. Düsterer, B. Siemer, M. Wöstmann, H. Zacharias, R. Mitzner, T. J. M. Zouros, J. Ullrich, C. D. Schröter, and R. Moshammer. Electron rearrangement dynamics in dissociating I_2^{n+} molecules accessed by extreme ultraviolet pump-probe experiments. *Physical Review Letters*, 113:073001, 2014. URL https://link.aps.org/doi/10.1103/PhysRevLett.113.073001.

[72] N. Rohringer and R. Santra. X-ray nonlinear optical processes using a self-amplified spontaneous emission free-electron laser. *Physical Review A*, 76:033416, 2007. URL https://link.aps.org/doi/10.1103/PhysRevA.76.033416.

[73] S.-K. Son and R. Santra. Monte carlo calculation of ion, electron, and photon spectra of xenon atoms in x-ray free-electron laser pulses. *Physical Review A*, 85:063415, 2012. URL https://link.aps.org/doi/10.1103/PhysRevA.85.063415.

[74] P. J. Ho, C. Bostedt, S. Schorb, and L. Young. Theoretical tracking of resonance-enhanced multiple ionization pathways in x-ray free-electron laser pulses. *Physical Review Letters*, 113:253001, 2014. URL https://link.aps.org/doi/10.1103/PhysRevLett.113.253001.

[75] Y. Hao, L. Inhester, K. Hanasaki, S.-K. Son, and R. Santra. Efficient electronic structure calculation for molecular ionization dynamics at high x-ray intensity. *Structural Dynamics*, 2:041707, 2015. URL https://aca.scitation.org/doi/abs/10.1063/1.4919794.

[76] L. Inhester, K. Hanasaki, Y. Hao, S.-K. Son, and R. Santra. X-ray multiphoton ionization dynamics of a water molecule irradiated by an x-ray free-electron laser pulse. *Physical Review A*, 94:023422, 2016. URL https://link.aps.org/doi/10.1103/PhysRevA.94.023422.

[77] H. Fukuzawa, S.-K. Son, K. Motomura, S. Mondal, K. Nagaya, S. Wada, X.-J. Liu, R. Feifel, T. Tachibana, Y. Ito, M. Kimura, T. Sakai, K. Matsunami, H. Hayashita, J. Kajikawa, P. Johnsson, M. Siano, E. Kukk, B. Rudek, B. Erk, L. Foucar, E. Robert, C. Miron, K. Tono, Y. Inubushi, T. Hatsui, M. Yabashi, M. Yao, R. Santra, and K. Ueda. Deep inner-shell multiphoton ionization by intense x-ray free-electron laser pulses. *Physical Review Letters*, 110:173005, 2013. URL https://link.aps.org/doi/10.1103/PhysRevLett.110.173005.

[78] C. Bostedt, S. Boutet, D. M. Fritz, Z. Huang, H. J. Lee, H. T. Lemke, A. Robert, W. F. Schlotter, J. J. Turner, and G. J. Williams. Linac Coherent Light Source: the first five years. *Reviews of Modern Physics*, 88:015007, 2016. URL https://link.aps.org/doi/10.1103/RevModPhys.88.015007.

[79] J. M. J Madey. Stimulated emission of bremsstrahlung in a periodic magnetic field. *Journal of Applied Physics*, 42:1906–1913, 1971. URL https://aip.scitation.org/doi/10.1063/1.1660466.

[80] D. A. G. Deacon, L. R. Elias, J. M. J. Madey, G. J. Ramian, H. A. Schwettman, and T. I. Smith. First operation of a free-electron laser. *Physical Review Letters*, 38: 892–894, 1977. URL https://link.aps.org/doi/10.1103/PhysRevLett.38.892.

[81] C. Pellegrini, A. Marinelli, and S. Reiche. The physics of x-ray free-electron lasers. *Reviews of Modern Physics*, 88:015006, 2016. URL https://link.aps.org/doi/10.1103/RevModPhys.88.015006.

[82] P. Emma, R. Akre, J. Arthur, R. Bionta, C. Bostedt, J. Bozek, A. Brachmann, P. Bucksbaum, R. Coffee, F.-J. Decker, Y. Ding, D. Dowell, S. Edstrom, A. Fisher,

J. Frisch, S. Gilevich, J. Hastings, G. Hays, P. Hering, Z. Huang, R. Iverson, H. Loos, M. Messerschmidt, A. Miahnahri, S. Moeller, H.-D. Nuhn, G. Pile, D. Ratner, J. Rzepiela, D. Schultz, T. Smith, P. Stefan, H. Tompkins, J. Turner, J. Welch, W. White, J. Wu, G. Yocky, and J. Galayda. First lasing and operation of an ångstrom-wavelength free-electron laser. *Nature Photonics*, 4:641–647, 2010. URL https://www.nature.com/articles/nphoton.2010.176.

[83] R. Bonifacio, C. Pellegrini, and L. M. Narducci. Collective instabilities and high-gain regime in a free electron laser. *Optics Communications*, 50:373–378, 1984. URL http://www.sciencedirect.com/science/article/pii/0030401884901056.

[84] J. Amann, W. Berg, V. Blank, F.-J. Decker, Y. Ding, P. Emma, Y. Feng, J. Frisch, D. Fritz, J. Hastings, Z. Huang, J. Krzywinski, R. Lindberg, H. Loos, A. Lutman, H.-D. Nuhn, D. Ratner, J. Rzepiela, D. Shu, Y. Shvyd'ko, S. Spampinati, S. Stoupin, S. Terentyev, E. Trakhtenberg, D. Walz, J. Welch, J. Wu, A. Zholents, and D. Zhu. Demonstration of self-seeding in a hard-x-ray free-electron laser. *Nature Photonics*, 6: 693–698, 2012. URL https://www.nature.com/articles/nphoton.2012.180.

[85] L. H. Yu. Generation of intense uv radiation by subharmonically seeded single-pass free-electron lasers. *Physical Review A*, 44:5178–5193, 1991. URL https://link.aps.org/doi/10.1103/PhysRevA.44.5178.

[86] G. Stupakov. Using the beam-echo effect for generation of short-wavelength radiation. *Physical Review Letters*, 102:074801, 2009. URL https://link.aps.org/doi/10.1103/PhysRevLett.102.074801.

[87] J. Feldhaus, E. L. Saldin, J. R. Schneider, E. A. Schneidmiller, and M. V. Yurkov. Possible application of x-ray optical elements for reducing the spectral bandwidth of an x-ray SASE FEL. *Optics Communications*, 140:341–352, 1997. URL http://www.sciencedirect.com/science/article/pii/S0030401897001636.

[88] E. L. Saldin, E. A. Schneidmiller, Y. V. Shvyd'ko, and M. V. Yurkov. X-ray FEL with

a meV bandwidth. *Nuclear Instruments and Methods in Physics Research Section A: Accelerators, Spectrometers, Detectors and Associated Equipment*, 475:357–362, 2001. URL http://www.sciencedirect.com/science/article/pii/S016890020101539X.

[89] A. A. Lutman, J. P. MacArthur, M. Ilchen, A. O. Lindahl, J. Buck, R. N. Coffee, G. L. Dakovski, L. Dammann, Y. Ding, H. A. Dürr, L. Glaser, J. Grünert, G. Hartmann, N. Hartmann, D. Higley, K. Hirsch, Y. I. Levashov, A. Marinelli, T. Maxwell, A. Mitra, S. Moeller, T. Osipov, F. Peters, M. Planas, I. Shevchuk, W. F. Schlotter, F. Scholz, J. Seltmann, J. Viefhaus, P. Walter, Z. R. Wolf, Z. Huang, and H.-D. Nuhn. Polarization control in an x-ray free-electron laser. *Nature Photonics*, 10:468–472, 2016. URL https://www.nature.com/articles/nphoton.2016.79.

[90] T. Hara, Y. Inubushi, T. Katayama, T. Sato, H. Tanaka, T. Tanaka, T. Togashi, K. Togawa, K. Tono, M. Yabashi, and T. Ishikawa. Two-colour hard x-ray free-electron laser with wide tunability. *Nature Communications*, 4:1–5, 2013. URL https://www.nature.com/articles/ncomms3919.

[91] A. A. Lutman, R. Coffee, Y. Ding, Z. Huang, J. Krzywinski, T. Maxwell, M. Messerschmidt, and H.-D. Nuhn. Experimental demonstration of femtosecond two-color x-ray free-electron lasers. *Physical Review Letters*, 110:134801, 2013. URL https://link.aps.org/doi/10.1103/PhysRevLett.110.134801.

[92] Y. Ding, A. Brachmann, F.-J. Decker, D. Dowell, P. Emma, J. Frisch, S. Gilevich, G. Hays, P. Hering, Z. Huang, R. Iverson, H. Loos, A. Miahnahri, H.-D. Nuhn, D. Ratner, J. Turner, J. Welch, W. White, and J. Wu. Measurements and simulations of ultralow emittance and ultrashort electron beams in the Linac Coherent Light Source. *Physical Review Letters*, 102:254801, 2009. URL https://link.aps.org/doi/10.1103/PhysRevLett.102.254801.

[93] P. Emma, K. Bane, M. Cornacchia, Z. Huang, H. Schlarb, G. Stupakov, and D. Walz. Femtosecond and subfemtosecond x-ray pulses from a self-amplified spontaneous-

emission–based free-electron laser. *Physical Review Letters*, 92:074801, 2004. URL https://link.aps.org/doi/10.1103/PhysRevLett.92.074801.

[94] S. Huang, Y. Ding, Y. Feng, E. Hemsing, Z. Huang, J. Krzywinski, A. A. Lutman, A. Marinelli, T. J. Maxwell, and D. Zhu. Generating single-spike hard x-ray pulses with nonlinear bunch compression in free-electron lasers. *Physical Review Letters*, 119:154801, 2017. URL https://link.aps.org/doi/10.1103/PhysRevLett.119.154801.

[95] A. A. Zholents. Method of an enhanced self-amplified spontaneous emission for x-ray free electron lasers. *Physical Review Special Topics - Accelerators and Beams*, 8:040701, 2005. URL https://link.aps.org/doi/10.1103/PhysRevSTAB.8.040701.

[96] E. L. Saldin, E. A. Schneidmiller, and M. V. Yurkov. Self-amplified spontaneous emission FEL with energy-chirped electron beam and its application for generation of attosecond x-ray pulses. *Physical Review Special Topics - Accelerators and Beams*, 9: 050702, 2006. URL https://link.aps.org/doi/10.1103/PhysRevSTAB.9.050702.

[97] J. Duris, S. Li, T. Driver, E. G. Champenois, J. P. MacArthur, A. A. Lutman, Z. Zhang, P. Rosenberger, J. W. Aldrich, R. Coffee, G. Coslovich, F.-J. Decker, J. M. Glownia, G. Hartmann, W. Helml, A. Kamalov, J. Knurr, J. Krzywinski, M.-F. Lin, M. Nantel, A. Natan, J. O'Neal, N. Shivaram, P. Walter, A. Wang, J. J. Welch, T. J. A. Wolf, J. Z. Xu, M. F. Kling, P. H. Bucksbaum, A. Zholents, Z. Huang, J. P. Cryan, and A. Marinelli. Tunable isolated attosecond x-ray pulses with gigawatt peak power from a free-electron laser. *arXiv:1906.10649 [physics]*, 2019. URL http://arxiv.org/abs/1906.10649.

[98] X-Ray Parameters of the LCLS. URL https://lcls.slac.stanford.edu/parameters.

[99] X-Ray Parameters of the EuXFEL. URL https://www.xfel.eu/facility/overview/facts_amp_figures/index_eng.html.

[100] X-Ray Parameters Available to the SQS Instrument at the EuXFEL. URL https://www.xfel.eu/facility/instruments/sqs/index_eng.html.

[101] S. P. Hau-Riege, R. M. Bionta, D. D. Ryutov, R. A. London, E. Ables, K. I. Kishiyama, S. Shen, M. A. McKernan, D. H. McMahon, M. Messerschmidt, J. Krzywinski, P. Stefan, J. Turner, and B. Ziaja. Near-ultraviolet luminescence of N_2 irradiated by short x-ray pulses. *Physical Review Letters*, 105:043003, 2010. URL https://link.aps.org/doi/10.1103/PhysRevLett.105.043003.

[102] C. Behrens, F.-J. Decker, Y. Ding, V. A. Dolgashev, J. Frisch, Z. Huang, P. Krejcik, H. Loos, A. Lutman, T. J. Maxwell, J. Turner, J. Wang, M.-H. Wang, J. Welch, and J. Wu. Few-femtosecond time-resolved measurements of x-ray free-electron lasers. *Nature Communications*, 5:1–7, 2014. URL https://www.nature.com/articles/ncomms4762.

[103] S. Düsterer, P. Radcliffe, C. Bostedt, J. Bozek, A. L. Cavalieri, R. Coffee, J. T. Costello, D. Cubaynes, L. F. DiMauro, Y. Ding, G. Doumy, F. Grüner, W. Helml, W. Schweinberger, R. Kienberger, A. R. Maier, M. Messerschmidt, V. Richardson, C. Roedig, T. Tschentscher, and M. Meyer. Femtosecond x-ray pulse length characterization at the Linac Coherent Light Source free-electron laser. *New Journal of Physics*, 13: 093024, 2011. URL https://iopscience.iop.org/article/10.1088/1367-2630/13/9/093024.

[104] S. Schorb, T. Gorkhover, J. P. Cryan, J. M. Glownia, M. R. Bionta, R. N. Coffee, B. Erk, R. Boll, C. Schmidt, D. Rolles, A. Rudenko, A. Rouzee, M. Swiggers, S. Carron, J.-C. Castagna, J. D. Bozek, M. Messerschmidt, W. F. Schlotter, and C. Bostedt. X-ray–optical cross-correlator for gas-phase experiments at the Linac Coherent Light Source free-electron laser. *Applied Physics Letters*, 100:121107, 2012. URL https://aip.scitation.org/doi/10.1063/1.3695163.

[105] Y. Ding, C. Behrens, P. Emma, J. Frisch, Z. Huang, H. Loos, P. Krejcik, and M.-H. Wang. Femtosecond x-ray pulse temporal characterization in free-electron lasers using

a transverse deflector. *Physical Review Special Topics - Accelerators and Beams*, 14: 120701, 2011. URL https://link.aps.org/doi/10.1103/PhysRevSTAB.14.120701.

[106] I. Grguraš, A. R. Maier, C. Behrens, T. Mazza, T. J. Kelly, P. Radcliffe, S. Düsterer, A. K. Kazansky, N. M. Kabachnik, T. Tschentscher, J. T. Costello, M. Meyer, M. C. Hoffmann, H. Schlarb, and A. L. Cavalieri. Ultrafast x-ray pulse characterization at free-electron lasers. *Nature Photonics*, 6:852–857, 2012. URL https://www.nature.com/articles/nphoton.2012.276.

[107] W. Helml, A. R. Maier, W. Schweinberger, I. Grguraš, P. Radcliffe, G. Doumy, C. Roedig, J. Gagnon, M. Messerschmidt, S. Schorb, C. Bostedt, F. Grüner, L. F. DiMauro, D. Cubaynes, J. D. Bozek, T. Tschentscher, J. T. Costello, M. Meyer, R. Coffee, S. Düsterer, A. L. Cavalieri, and R. Kienberger. Measuring the temporal structure of few-femtosecond free-electron laser x-ray pulses directly in the time domain. *Nature Photonics*, 8:950–957, 2014. URL https://www.nature.com/articles/nphoton.2014.278.

[108] N. Hartmann, G. Hartmann, R. Heider, M. S. Wagner, M. Ilchen, J. Buck, A. O. Lindahl, C. Benko, J. Grünert, J. Krzywinski, J. Liu, A. A. Lutman, A. Marinelli, T. Maxwell, A. A. Miahnahri, S. P. Moeller, M. Planas, J. Robinson, A. K. Kazansky, N. M. Kabachnik, J. Viefhaus, T. Feurer, R. Kienberger, R. N. Coffee, and W. Helml. Attosecond time–energy structure of x-ray free-electron laser pulses. *Nature Photonics*, 12:215–220, 2018. URL https://www.nature.com/articles/s41566-018-0107-6.

[109] S. Li, Z. Guo, R. N. Coffee, K. Hegazy, Z. Huang, A. Natan, T. Osipov, D. Ray, A. Marinelli, and J. P. Cryan. Characterizing isolated attosecond pulses with angular streaking. *Optics Express*, 26:4531–4547, 2018. URL https://www.osapublishing.org/oe/abstract.cfm?uri=oe-26-4-4531.

[110] T. Maxwell, C. Behrens, Y. Ding, Z. Huang, A. Lutman, and P. Krejcik. The LCLS XTCAV: Manual for Users. URL https://confluence.slac.stanford.

edu/display/PSDM/New+XTCAV+Documentation?preview=/235380371/240275438/xtcav-users-v0p4.pdf.

[111] Z. Huang, K. Bane, Y. Cai, A. Chao, R. Hettel, and C. Pellegrini. Steady-state analysis of short-wavelength, high-gain FELs in a large storage ring. *Nuclear Instruments and Methods in Physics Research Section A: Accelerators, Spectrometers, Detectors and Associated Equipment*, 593:120–124, 2008. URL https://linkinghub.elsevier.com/retrieve/pii/S0168900208006372.

[112] K. Toyota, Z. Jurek, S.-K. Son, H. Fukuzawa, K. Ueda, N. Berrah, B. Rudek, D. Rolles, A. Rudenko, and R. Santra. XCALIB: a focal spot calibrator for intense x-ray free-electron laser pulses based on the charge state distributions of light atoms. *Journal of Synchrotron Radiation*, 26:1017–1030, 2019. URL https://journals.iucr.org/s/issues/2019/04/00/ig5068/.

[113] D. R. Miller. *"Free Jet Sources" in Atomic and Molecular Beam Methods edited by G. Scoles*. Oxford University Press, 1988.

[114] S. Wolf and H. Helm. Ion-recoil momentum spectroscopy in a laser-cooled atomic sample. *Physical Review A*, 62:043408, 2000. URL https://link.aps.org/doi/10.1103/PhysRevA.62.043408.

[115] X. Flechard, H. Nguyen, E. Wells, I. Ben-Itzhak, and B. D. DePaola. Kinematically complete charge exchange experiment in the Cs^+ + Rb collision system using a MOT target. *Physical Review Letters*, 87:123203, 2001. URL https://link.aps.org/doi/10.1103/PhysRevLett.87.123203.

[116] R. Dörner, V. Mergel, O. Jagutzki, L. Spielberger, J. Ullrich, R. Moshammer, and H. Schmidt-Böcking. Cold Target Recoil Ion Momentum Spectroscopy: a 'momentum microscope' to view atomic collision dynamics. *Physics Reports*, 330:95–192, 2000. URL https://linkinghub.elsevier.com/retrieve/pii/S037015739900109X.

[117] J. Ullrich, R. Moshammer, A. Dorn, R. Dörner, L. P. H. Schmidt, and H. Schmidt-Böcking. Recoil-ion and electron momentum spectroscopy: reaction-microscopes. *Reports on Progress in Physics*, 66:1463–1545, 2003. URL http://stacks.iop.org/0034-4885/66/i=9/a=203?key=crossref.4f0ed0c11253bbad6096727290d95871.

[118] T. Osipov, C. Bostedt, J.-C. Castagna, K. R. Ferguson, M. Bucher, S. C. Montero, M. L. Swiggers, R. Obaid, D. Rolles, A. Rudenko, J. D. Bozek, and N. Berrah. The LAMP instrument at the Linac Coherent Light Source free-electron laser. *Review of Scientific Instruments*, 89:035112, 2018. URL https://aip.scitation.org/doi/10.1063/1.5017727.

[119] A. T. J. B. Eppink and D. H. Parker. Velocity map imaging of ions and electrons using electrostatic lenses: application in photoelectron and photofragment ion imaging of molecular oxygen. *Review of Scientific Instruments*, 68:3477–3484, 1997. URL https://aip.scitation.org/doi/10.1063/1.1148310.

[120] D. Rolles, Z. D. Pešić, M. Perri, R. C. Bilodeau, G. D. Ackerman, B. S. Rude, A. L. D. Kilcoyne, J. D. Bozek, and N. Berrah. A velocity map imaging spectrometer for electron–ion and ion–ion coincidence experiments with synchrotron radiation. *Nuclear Instruments and Methods in Physics Research Section B: Beam Interactions with Materials and Atoms*, 261:170–174, 2007. URL http://www.sciencedirect.com/science/article/pii/S0168583X07009949.

[121] Simion Software. URL https://simion.com.

[122] Hamamatsu Photonics. MCP (MicroChannel Plate) and MCP Assembly. URL https://www.hamamatsu.com/resources/pdf/etd/MCP_TMCP0002E.pdf.

[123] Peak Finding Algorithms in the LCLS Data Analysis Page. URL https://confluence.slac.stanford.edu/display/PSDM/Peak+Finding.

[124] RoentDek CFD Manual. The Constant Fraction Discriminators CFD8c, CFD7x,

CFD4c, CFD1c and CFD1x. URL https://www.roentdek.com/manuals/CFD%20Manual.pdf.

[125] T. Weber, O. Jagutzki, M. Hattass, A. Staudte, A. Nauert, L. Schmidt, M. H. Prior, A. L. Landers, A. Bräuning-Demian, H. Bräuning, C. L. Cocke, T. Osipov, I. Ali, R. D. Muiño, D. Rolles, F J García de Abajo, C. S. Fadley, M. A. V. Hove, A. Cassimi, H. Schmidt-Böcking, and R. Dörner. K-shell photoionization of CO and N_2 : is there a link between the photoelectron angular distribution and the molecular decay dynamics? *Journal of Physics B: Atomic, Molecular and Optical Physics*, 34: 3669–3678, 2001. URL http://stacks.iop.org/0953-4075/34/i=18/a=305?key=crossref.ec3eccff01d5c90f47b602196a9febc8.

[126] R. Moshammer, D. Fischer, and H. Kollmus. Recoil-ion momentum spectroscopy and "reaction microscopes". In Joachim Ullrich and Viatcheslav Shevelko, editors, *Many-Particle Quantum Dynamics in Atomic and Molecular Fragmentation*, Springer Series on Atomic, Optical, and Plasma Physics, pages 33–58. Springer Berlin Heidelberg, 2003. doi: 10.1007/978-3-662-08492-2_2. URL https://doi.org/10.1007/978-3-662-08492-2_2.

[127] U. Ablikim. *Coulomb Explosion Imaging of Polyatomic Molecules after Photoionization with X-Rays and Strong Laser Fields*. PhD thesis, Kansas State University, 2017.

[128] L. Montgomery Smith, D. R. Keefer, and S. I. Sudharsanan. Abel inversion using transform techniques. *Journal of Quantitative Spectroscopy and Radiative Transfer*, 39:367–373, 1988. URL http://www.sciencedirect.com/science/article/pii/002240738890101X.

[129] V. Dribinski, A. Ossadtchi, V. A. Mandelshtam, and H. Reisler. Reconstruction of Abel-transformable images: the Gaussian basis-set expansion Abel transform method. *Review of Scientific Instruments*, 73:2634–2642, 2002. URL https://aip.scitation.org/doi/10.1063/1.1482156.

[130] G. A. Garcia, L. Nahon, and I. Powis. Two-dimensional charged particle image inversion using a polar basis function expansion. *Review of Scientific Instruments*, 75: 4989–4996, 2004. URL https://aip.scitation.org/doi/10.1063/1.1807578.

[131] C. J. Dasch. One-dimensional tomography: a comparison of Abel, onion-peeling, and filtered backprojection methods. *Applied Optics*, 31:1146–1152, 1992. URL https://www.osapublishing.org/ao/abstract.cfm?uri=ao-31-8-1146.

[132] C. Bordas, F. Paulig, H. Helm, and D. L. Huestis. Photoelectron imaging spectrometry: principle and inversion method. *Review of Scientific Instruments*, 67:2257–2268, 1996. URL https://aip.scitation.org/doi/10.1063/1.1147044.

[133] K. Zhao, T. Colvin, W. T. Hill, and G. Zhang. Deconvolving two-dimensional images of three-dimensional momentum trajectories. *Review of Scientific Instruments*, 73: 3044–3050, 2002. URL https://aip.scitation.org/doi/10.1063/1.1493231.

[134] G. M. Roberts, J. L. Nixon, J. Lecointre, E. Wrede, and J. R. R Verlet. Toward real-time charged-particle image reconstruction using polar onion-peeling. *Review of Scientific Instruments*, 80:053104, 2009. URL https://aip.scitation.org/doi/10.1063/1.3126527.

[135] M. J. J Vrakking. An iterative procedure for the inversion of two-dimensional ion/photoelectron imaging experiments. *Review of Scientific Instruments*, 72:4084–4089, 2001. URL https://aip.scitation.org/doi/10.1063/1.1406923.

[136] S. Hsieh and J. H. D Eland. Reaction dynamics of three-body dissociations in triatomic molecules from single-photon double ionization studied by a time- and position-sensitive coincidence method. *Journal of Physics B: Atomic, Molecular and Optical Physics*, 30:4515–4534, 1997. URL https://doi.org/10.1088%2F0953-4075%2F30%2F20%2F015.

[137] N. Neumann, D. Hant, L. P. H. Schmidt, J. Titze, T. Jahnke, A. Czasch, M. S. Schöffler, K. Kreidi, O. Jagutzki, H. Schmidt-Böcking, and R. Dörner. Fragmentation dynamics

of CO_2^{3+} investigated by multiple electron capture in collisions with slow highly charged ions. *Physical Review Letters*, 104:103201, 2010. URL https://link.aps.org/doi/10.1103/PhysRevLett.104.103201.

[138] R. H. Dalitz. On the analysis of tau-meson data and the nature of the tau-meson. *Phil. Mag. Ser.7*, 44:1068–1080, 1953.

[139] R. D. Cowan. Atomic Structure Codes. URL https://www.tcd.ie/Physics/people/Cormac.McGuinness/Cowan/.

[140] R. D. Cowan. *The Theory of Atomic Structure and Spectra*. University of California Press, Berkeley, CA, 1981.

[141] M. Hoener, L. Fang, O. Kornilov, O. Gessner, S. T. Pratt, M. Gühr, E. P. Kanter, C. Blaga, C. Bostedt, J. D. Bozek, P. H. Bucksbaum, C. Buth, M. Chen, R. Coffee, J. Cryan, L. DiMauro, M. Glownia, E. Hosler, E. Kukk, S. R. Leone, B. McFarland, M. Messerschmidt, B. Murphy, V. Petrovic, D. Rolles, and N. Berrah. Ultraintense x-ray induced ionization, dissociation, and frustrated absorption in molecular nitrogen. *Physical Review Letters*, 104:253002, 2010. URL https://link.aps.org/doi/10.1103/PhysRevLett.104.253002.

[142] S. N. Foner and R. L. Hudson. Ionization potential of the CH_2 free radical by mass spectrometry. *The Journal of Chemical Physics*, 45:49–51, 1966. URL https://aip.scitation.org/doi/10.1063/1.1727353.

[143] A. Kramida, Yu. Ralchenko, J. Reader, and NIST ASD Team. NIST Atomic Spectra Database (ver. 5.7.1), [Online]. URL https://physics.nist.gov/asd.

[144] NIST Standard Reference Database 101. URL https://cccbdb.nist.gov/expgeom2.asp?casno=74884&charge=0.

[145] L. Fang, T. Osipov, B. Murphy, F. Tarantelli, E. Kukk, J. P. Cryan, M. Glownia, P. H. Bucksbaum, R. N. Coffee, M. Chen, C. Buth, and N. Berrah. Multiphoton ionization

as a clock to reveal molecular dynamics with intense short x-ray free electron laser pulses. *Physical Review Letters*, 109:263001, 2012. URL https://link.aps.org/doi/10.1103/PhysRevLett.109.263001.

[146] Z. Vager, R. Naaman, and E. P. Kanter. Coulomb explosion imaging of small molecules. *Science*, 244:426–431, 1989. URL https://www.jstor.org/stable/1703084.

[147] M. Pitzer, M. Kunitski, A. S. Johnson, T. Jahnke, H. Sann, F. Sturm, L. P. H. Schmidt, H. Schmidt-Böcking, R. Dörner, J. Stohner, J. Kiedrowski, M. Reggelin, S. Marquardt, A. Schießer, R. Berger, and M. S. Schöffler. Direct determination of absolute molecular stereochemistry in gas phase by Coulomb explosion imaging. *Science*, 341:1096–1100, 2013. URL https://science.sciencemag.org/content/341/6150/1096.

[148] CH_3I Picture. URL https://en.wikipedia.org/wiki/Methyl_iodide#/media/File:Iodomethane-3D-balls.png.

[149] L. Cattaneo, J. Vos, R. Y. Bello, A. Palacios, S. Heuser, L. Pedrelli, M. Lucchini, C. Cirelli, F. Martín, and U. Keller. Attosecond coupled electron and nuclear dynamics in dissociative ionization of H_2. *Nature Physics*, 14:733–738, 2018. URL https://www.nature.com/articles/s41567-018-0103-2.

[150] W. Eberhardt, E. W. Plummer, I. W. Lyo, R. Carr, and W. K. Ford. Auger-electron ion coincidence studies of soft-x-ray-induced fragmentation of N_2. *Physical Review Letters*, 58:207–210, 1987. URL https://link.aps.org/doi/10.1103/PhysRevLett.58.207.

[151] M. S. Schöffler, J. Titze, N. Petridis, T. Jahnke, K. Cole, L. P. H. Schmidt, A. Czasch, D. Akoury, O. Jagutzki, J. B. Williams, N. A. Cherepkov, S. K. Semenov, C. W. McCurdy, T. N. Rescigno, C. L. Cocke, T. Osipov, S. Lee, M. H. Prior, A. Belkacem, A. L. Landers, H. Schmidt-Böcking, T. Weber, and R. Dörner. Ultrafast probing of core hole localization in N_2. *Science*, 320:920–923, 2008. URL https://science.sciencemag.org/content/320/5878/920.

[152] M. Kurka, A. Rudenko, L. Foucar, K. U. Kühnel, Y. H. Jiang, Th Ergler, T. Havermeier, M. Smolarski, S. Schössler, K. Cole, M. Schöffler, R. Dörner, M. Gensch, S. Düsterer, R. Treusch, S. Fritzsche, A. N. Grum-Grzhimailo, E. V. Gryzlova, N. M. Kabachnik, C. D. Schröter, R. Moshammer, and J. Ullrich. Two-photon double ionization of Ne by free-electron laser radiation: a kinematically complete experiment. *Journal of Physics B: Atomic, Molecular and Optical Physics*, 42:141002, 2009. URL https://doi.org/10.1088%2F0953-4075%2F42%2F14%2F141002.

[153] A. Rudenko, Y. H. Jiang, M. Kurka, K. U. Kühnel, L. Foucar, O. Herrwerth, M. Lezius, M. F. Kling, C. D. Schröter, R. Moshammer, and J. Ullrich. Exploring few-photon, few-electron reactions at FLASH: from ion yield and momentum measurements to time-resolved and kinematically complete experiments. *Journal of Physics B: Atomic, Molecular and Optical Physics*, 43:194004, 2010. URL https://doi.org/10.1088%2F0953-4075%2F43%2F19%2F194004.

[154] S. Augustin, M. Schulz, G. Schmid, K. Schnorr, E. V. Gryzlova, H. Lindenblatt, S. Meister, Y. F. Liu, F. Trost, L. Fechner, A. N. Grum-Grzhimailo, S. M. Burkov, M. Braune, R. Treusch, M. Gisselbrecht, C. D. Schröter, T. Pfeifer, and R. Moshammer. Signatures of autoionization in the angular electron distribution in two-photon double ionization of Ar. *Physical Review A*, 98:033408, 2018. URL https://link.aps.org/doi/10.1103/PhysRevA.98.033408.

[155] Y. Liu. *Two-Color Pump-Probe Experiments on O_2 and N_2 at the Free-Electron Laser in Hamburg*. PhD thesis, The Ruperto-Carola-University of Heidelberg, 2019.

[156] T. Weber, M. Weckenbrock, M. Balser, L. Schmidt, O. Jagutzki, W. Arnold, O. Hohn, M. Schöffler, E. Arenholz, T. Young, T. Osipov, L. Foucar, A. D. Fanis, R. Díez Muiño, H. Schmidt-Böcking, C. L. Cocke, M. H. Prior, and R. Dörner. Auger electron emission from fixed-in-space CO. *Physical Review Letters*, 90:153003, 2003. URL https://link.aps.org/doi/10.1103/PhysRevLett.90.153003.

[157] S. K. Semenov, M. S. Schöffler, J. Titze, N. Petridis, T. Jahnke, K. Cole, L. Ph. H.

Schmidt, A. Czasch, D. Akoury, O. Jagutzki, J. B. Williams, T. Osipov, S. Lee, M. H. Prior, A. Belkacem, A. L. Landers, H. Schmidt-Böcking, Th. Weber, N. A. Cherepkov, and R. Dörner. Auger decay of $1\sigma_g$ and $1\sigma_u$ hole states of the N_2 molecule: disentangling decay routes from coincidence measurements. *Physical Review A*, 81:043426, 2010. URL https://link.aps.org/doi/10.1103/PhysRevA.81.043426.

[158] H. Iwayama, T. Kaneyasu, Y. Hikosaka, and E. Shigemasa. Stability and dissociation dynamics of N_2^{++} ions following core ionization studied by an Auger-electron–photoion coincidence method. *The Journal of Chemical Physics*, 145:034305, 2016. URL https://aip.scitation.org/doi/10.1063/1.4958620.

[159] M. Lundqvist, D. Edvardsson, P. Baltzer, and B. Wannberg. Doppler-free kinetic energy release spectrum of N_2^{2+}. *Journal of Physics B: Atomic, Molecular and Optical Physics*, 29:1489–1499, 1996. URL https://doi.org/10.1088%2F0953-4075%2F29%2F8%2F013.

[160] T. Kaneyasu, Y. Hikosaka, E. Shigemasa, P. Lablanquie, F. Penent, and K. Ito. Auger decays of 1s shake-up and shake-off states in N_2 molecules. *Journal of Physics B: Atomic, Molecular and Optical Physics*, 41:135101, 2008. URL https://doi.org/10.1088%2F0953-4075%2F41%2F13%2F135101.

[161] A. M. Hanna, O. Vendrell, A. Ourmazd, and R. Santra. Laser control over the ultrafast Coulomb explosion of N_2^{2+} after Auger decay: a quantum-dynamics investigation. *Physical Review A*, 95:043419, 2017. URL https://link.aps.org/doi/10.1103/PhysRevA.95.043419.

[162] C. S. Lehmann, A. Picón, C. Bostedt, A. Rudenko, A. Marinelli, D. Moonshiram, T. Osipov, D. Rolles, N. Berrah, C. Bomme, M. Bucher, G. Doumy, B. Erk, K. R. Ferguson, T. Gorkhover, P. J. Ho, E. P. Kanter, B. Krässig, J. Krzywinski, A. A. Lutman, A. M. March, D. Ray, L. Young, S. T. Pratt, and S. H. Southworth. Ultrafast x-ray-induced nuclear dynamics in diatomic molecules using femtosecond x-ray-pump–

x-ray-probe spectroscopy. *Physical Review A*, 94:013426, 2016. URL https://link.aps.org/doi/10.1103/PhysRevA.94.013426.

[163] J. P. Cryan, J. M. Glownia, J. Andreasson, A. Belkacem, N. Berrah, C. I. Blaga, C. Bostedt, J. Bozek, N. A. Cherepkov, L. F. DiMauro, L. Fang, O. Gessner, M. Gühr, J. Hajdu, M. P. Hertlein, M. Hoener, O. Kornilov, J. P. Marangos, A. M. March, B. K. McFarland, H. Merdji, M. Messerschmidt, V. S. Petrović, C. Raman, D. Ray, D. A. Reis, S. K. Semenov, M. Trigo, J. L. White, W. White, L. Young, P. H. Bucksbaum, and R. N. Coffee. Molecular frame Auger electron energy spectrum from N_2. *Journal of Physics B: Atomic, Molecular and Optical Physics*, 45:055601, 2012. URL https://doi.org/10.1088%2F0953-4075%2F45%2F5%2F055601.

[164] H. Sann, T. Havermeier, C. Müller, H.-K. Kim, F. Trinter, M. Waitz, J. Voigtsberger, F. Sturm, T. Bauer, R. Wallauer, D. Schneider, M. Weller, C. Goihl, J. Tross, K. Cole, J. Wu, M. S. Schöffler, H. Schmidt-Böcking, T. Jahnke, M. Simon, and R. Dörner. Imaging the temporal evolution of molecular orbitals during ultrafast dissociation. *Physical Review Letters*, 117:243002, 2016. URL https://link.aps.org/doi/10.1103/PhysRevLett.117.243002.

[165] G. Kastirke, M. Schöffler, M. Weller, J. Rist, R. Boll, N. Anders, Th. M. Baumann, S. Eckart, B. Erk, A. De Fanis, K. Fehre, A. Gatton, S. Grundmann, P. Grychtol, A. Hartung, M. Hofmann, M. Ilchen, Ch. Janke, M. Kircher, M. Kunitski, X. Li, T. Mazza, N. Melzer, J. Montano, V. Music, G. Nalin, Y. Ovcharenko, A. Pier, N. Rennhack, D. E. Rivas, R. Dörner, D. Rolles, A. Rudenko, P. Schmidt, J. Siebert, N. Strenger, D. Trabert, I. Vela-Perez, R. Wagner, Th. Weber, J. B. Williams, P. Ziolkowski, L. Ph. H. Schmidt, A. Czasch, F. Trinter, M. Meyer, K. Ueda, P. V. Demekhin, and T. Jahnke. Photoelectron diffraction imaging of a molecular break-up using an X-ray free-electron laser, in review.

Appendix A

Derivation of the approximate momentum formula for spectrometers with one homogeneous field region

When the spectrometer has a homogeneous field configuration with one acceleration region (with or without the drift region) and ion fragments gain much more energy from the spectrometer field than their initial energy acquired from the reaction, an approximate formula for the momentum along the spectrometer axis can be derived. If there is no drift region, according to Newton's second law, the time of flight t of an ion with mass m, charge q and its initial **z** direction energy E_z satisfy the equation

$$\frac{1}{2}\frac{qU}{ml}t^2 \pm \sqrt{\frac{2E_z}{m}}t = l, \tag{A.1}$$

where U and l are the voltage and length across the spectrometer respectively, and the plus or minus sign corresponds to ions initially flying towards or away from the detector. From Eq. (A.1) and the condition that $qU >> E_z$, the time of flight is

$$t = \frac{\sqrt{2ml}}{\sqrt{qU + E_z} \pm \sqrt{E_z}} \approx \frac{\sqrt{2ml}}{\sqrt{qU} \pm \sqrt{E_z}} \approx \sqrt{\frac{2m}{qU}}l(1 \pm \sqrt{\frac{E_z}{qU}}). \tag{A.2}$$

The plus or minus sign in A.2 corresponds to ions flying away from or towards the detector. The time of flight difference $(t\ -\ t_0)$ between an ion with **z** momentum P_z and the one with zero **z** momentum is

$$\begin{aligned} t\ -\ t_0 &= \left[\frac{dt}{d_{E_z}}\frac{dE_z}{dP_z}\right]_{P_z=0} P_z \\ &= \left[\frac{\sqrt{2m}}{qU}\frac{l}{2\sqrt{E_z}}\sqrt{\frac{2E_z}{m}}\right]_{P_z=0} P_z \\ &= \frac{l}{qU}P_z. \end{aligned} \tag{A.3}$$

From Eq. (A.3), P_z is given by

$$P_z = \frac{qU}{l}(t-t_0) = (8.04\ \times\ 10^{-3}\frac{cm\ a.u.}{eV\ ns})\ \cdot\ \frac{qU}{l}(t-t_0). \tag{A.4}$$

If there is in addition a drift region of length d, based on Eq. (A.2), the time of flight becomes

$$t = \frac{\sqrt{2m}l}{\sqrt{qU\ +\ E_z}\ \pm\ \sqrt{E_z}}\ +\frac{\sqrt{\frac{m}{2}}d}{\sqrt{qU\ +\ E_z}}. \tag{A.5}$$

Similar derivations can be made and the resulting P_z formula is the same as Eq. (A.4).

Appendix B

Ion time of flight with arbitrary electric field configurations

Based on Eq. (A.2), which is the ion time of flight for spectrometers with a single homogeneous electric field region, the ion time of flight for a spectrometer with an arbitrary combination of $(length, voltage)$ regions $[(l_1,\ U_1),\ (l_2,\ U_2),\ \cdots,\ (l_i,\ U_i),\ \cdots,\ (l_n,\ U_n)]$ is given by

$$\begin{aligned} t\ =\ & \frac{\sqrt{2m}l_1}{\sqrt{qU_1\ +\ E_z}\ \pm\ \sqrt{E_z}}\ +\ \frac{\sqrt{2m}l_2}{\sqrt{qU_2\ +qU_1\ +\ E_z}\ \pm\ \sqrt{qU_1\ +E_z}}\ +\ \cdots \\ & +\ \frac{\sqrt{2m}l_i}{\sqrt{qU_i\ +\ \cdots\ +\ qU_2\ +qU_1\ +\ E_z}\ \pm\ \sqrt{qU_{i-1}\ +\ \cdots\ +qU_2\ +qU_1\ +E_z}}\ +\ \cdots \\ & +\ \frac{\sqrt{2m}l_n}{\sqrt{qU_n\ +\ \cdots\ +qU_2\ +qU_1\ +\ E_z}\ \pm\ \sqrt{qU_{n-1}\ +\ \cdots\ +qU_2\ +qU_1\ +E_z}}. \end{aligned} \tag{B.1}$$

The center value t_c of the time of flight peak for an ion species is then obtained from Eq. (B.1) by setting $E_z = 0$,

$$\begin{aligned} t_c &= \frac{\sqrt{2m}l_1}{\sqrt{qU_1}} + \frac{\sqrt{2m}l_2}{\sqrt{qU_2 + qU_1} \pm \sqrt{qU_1}} + \cdots \\ &\quad + \frac{\sqrt{2m}l_i}{\sqrt{qU_i + \cdots + qU_2 + qU_1} \pm \sqrt{qU_{i-1} + \cdots + qU_2 + qU_1}} + \cdots \\ &\quad + \frac{\sqrt{2m}l_n}{\sqrt{qU_n + \cdots + qU_2 + qU_1} \pm \sqrt{qU_{n-1} + \cdots + qU_2 + qU_1}} \\ &\propto \sqrt{\frac{m}{q}}. \end{aligned} \tag{B.2}$$

Given the time of flight spectrum, the relation in Eq. (B.2) can be used to identify ion species by their characteristic mass and charge ratios.